Insights into Abnormal Combustion in Advanced Gasoline Engines

Matthew John McAllister

Exeter College

University of Oxford

A Thesis submitted for the degree of

Doctor of Philosophy

Trinity 2025

To Dawn, Michael and Niamh, thank you for your sacrifice and support in allowing me to pursue this dream.

To my late parents, sorry you weren't around to see this.

Acknowledgements

The author would like to acknowledge the following for there support through this research project:

- Dr Martin Davy, University of Oxford, DPhil supervisor. I couldn't have done this without you. A sincere thank you for your continued patience and support throughout my time as an Exeter college student
- Dr Martin Gold, Dr Paul Howarth and Dr Andrew Smith. BP Castrol UK, thank you for your financial support and the continued challenge to deliver the best results
- Dr Luke Doherty, Dr Laurent Le Page, Dr Rowland Penty Geraets and Mr Christopher Wheeler. Oxford Thermal Institute (OTI) for your patience, continued help and assistance with the CDST
- Mr Jonathan Harris, Jaguar Land Rover and Dr Sashi Balakrishnan, BP Castrol. For permission to use the multi-cylinder raw data collected during a long standing joint research project
- Mr Ricardo Santos, Jaguar Land Rover. For your help with MATLAB, my nemesis
- Dr Felix Leach, Prof Richard Stone and Dr Ben Williams, University of Oxford. For your help and for the useful discussions on a range of topics throughout this work
- The Advanced Propulsion Centre (APC), for the feasibility studies grant funding
- Dr Mark Barrow and Latifa Alostad (PhD student), Department of Chemistry Warwick University, for the advanced oil analysis. This work was funded via Seedcorn Access (funded by EPSRC grant EP/V007688/1) and also the funding for the instrumentation (EPSRC grant EP/V007718/1)

Abstract

Abnormal combustion has been a significant problem for engine manufacturers and owners for the last century. This has taken several forms, aggressive normal knock, pre-ignition and mega-knock. It has had severe impacts throughout engine development programmes and in production, impacting timing, cost and warranty. Abnormal combustion continues to be a problem in world markets, with potential risks to future engines due to in-market exposure to 'bad fuels', varying lubricant properties, ambient conditions and driving style. Researchers have made significant steps in the understanding of the causal mechanisms surrounding abnormal combustion. Detection controls have been implemented in the form of dedicated test cycles. There has also been research regarding the role of the lubricant, in particular detergent packs containing alkaline metallic compounds. However there are still significant gaps in the knowledge. One such gap identified was 'why does calcium promote abnormal combustion, whilst magnesium doesn't?'. This thesis presents the findings of investigations relating to the impact of specific fuel and lubricant properties. A cold driven shock tube was used to visualise interactions between metal oxide (calcium and magnesium) powers and (carbon dioxide, nitrogen and argon) gasses. Results suggest a new mechanism for Low Speed Pre-Ignition (LSPI) via a previously unseen reaction between CaO and N_2. It was noted that typical end of compression temperature would be insufficient to provoke the observed response, suggesting a contributory factor from internal residual gasses. Fuel and lubricant from the top land crevice volume of a single cylinder gasoline engine were collected and analysed to establish an understanding of the in-service composition of the top land crevice material. This study included the use of advanced diagnostic techniques (Petroleomics) carried out in collaboration researchers at the University of Warwick. The results indicate the presence of new chemical compounds present in the top land crevice not present in the new fuel and oil. Multi-cylinder engine testing of LSPI promoting fuels, with the addition of Methylcyclopentadienyl Manganese Tricarbonyl, with a lubricant containing calcium detergent was also conducted to determine the abnormal combustion characteristics. The results show previously unseen levels of abnormal combustion, so severe that it led to terminal engine damage not previously

seen in the public domain.

Contents

List of Figures

List of Tables

Chapter 1

Introduction, Drivers for Change, and Thesis Structure

1.1 Introduction

The available propulsion options for transportation, particularly personal transportation, have increased significantly in recent years. In a market previously dominated by the internal combustion engine (ICE), the most significant change has been an increase in the level of vehicle electrification. This started with the introduction of micro hybrids e.g. vehicles with a basic stop-start features and this has increased significantly to include: (1) Mild hybrids – an ICE vehicle that utilises a belt driven or crank integrated starter/generator that can enable regenerative braking, coasting or stop-on-the-move strategies, (2) Plug-in Hybrid Electric Vehicles – a vehicle capable of being driven in a full electric drive mode for a certain range, but where an integrated ICE is also available to drive the vehicle for the majority of operation, and (3) Battery Electric Vehicles (BEV) – whereby the vehicle consists of battery pack and motor as the only means of propulsion, this is charged via a cable, but there are no alternative drive or charging options on the vehicle. So-called 'range extenders' offer a solution to increase the range of a BEV, with the addition of a small ICE powered generator, however the inclusion of a combustion engine is currently unpopular due to the creation of tailpipe emissions [1]. The UK and Europe have sought to 'lead the way' in clean transportation creating new legislation banning the internal combustion engine, potentially as soon as 2030 [2]. The ICE is however not the problem as any harmful emissions and generation of carbon dioxide are the result

of the fuel burned. Whilst auto makers have supported the transition to electrification, and there was an initial surge in sales of BEV's in recent years by early adopters, this has levelled off due to the day to day usage experience, lack of available charging infrastructure, availability of green electricity and issues with the resale value of the vehicle. For ICE powered vehicles the mileage and service history provided the next owner of a used vehicle with an indication of its health. Whilst not perfect, it has been satisfactory for many years. In contrast, it is not yet possible to gauge the health of the BEV battery, as this is a function of driving style, ambient operating conditions and the number of fast charges [3]. Globally, the drive for change has been slower and factors such as energy security, for example due to war, have overtaken the potential environmental crisis of global warming. This has led to more strategic thinking regarding the availability of 'green' alternatives to an 'electrification only' solution, and consideration of the availability of local energy sources that can be used to produce carbon neutral fuels. Although there are niche markets, such as Brazil for example, whereby alternative liquid fuels (primarily ethanol) are available to the consumer, and gaseous fuels have been around for a number of years on fuel station forecourts, the majority of ICE's in use today use conventional fossil fuels (gasoline and diesel). Unfortunately, whilst being the most versatile and efficient choice, diesel fuel used in the compression ignition engine has unfairly fallen out of favour as it is perceived as the most 'dirty' form of propulsion due to higher NOx and soot emissions, despite meeting the legal homologation limits specified by legislators. The added cost of the battery and motor made hybridisation uneconomical for diesel engine vehicles due to the high initial cost of the engine and complex after-treatment system, therefore the spark ignited engine was the obvious choice. Additionally, whilst some alternative fuels (natural gas, hydrogen and alcohols), can be ignited by a diesel pilot injection which requires a secondary fuel storage and injection system, they more readily lend themselves to ignition via a spark. This has led to renewed interest in spark ignited (SI) engines [3].

1.2 Drivers for change

Despite over a century of development, there remains more that can be done to improve the base SI engine. Over the years steady progress has been made – mostly through the availability of new technology, materials or manufacturing processes. The three main areas that have driven, and that

continue to drive, the development of ICE technology are as follows; (1) emissions legislation, (2) customer demand for increased specific performance, and (3) CO_2 reduction.

(1) Emissions legislation: Figure 1.1 illustrates the reductions in emissions legislative limits since the introduction of EU1 in 1992. It can be seen that the limits for hydrocarbons (HC) and oxides of nitrogen (NOx) have reduced by 95 percent from EU1 to EU6. As the legislative limits have reduced, the test cycle and boundary conditions have become tougher with the introduction of real-world driving emissions (RDE) meaning that driver aggressiveness, payload, altitude and ambient temperature are included, in conjunction with vehicle mounted real-time measurements. EU7, due to be enacted in 2025, seeks to align emissions limits for both gasoline and diesel fuelled vehicles. Test boundary conditions are to become more challenging, extended to lower engine starting temperatures and more aggressive driving. This emission standard is the first to consider non-fuel related particle emissions from tyres and brakes. The intention is to include battery electric vehicles (BEV's) which tend to have higher mass than their ICE equivalent vehicle, which can result in higher particle emissions from tyres, but potential reductions from brakes if regenerative braking is optimised [4] [5]. Battery durability will also be included to help customers evaluate the condition of the vehicle for used BEV's [6].

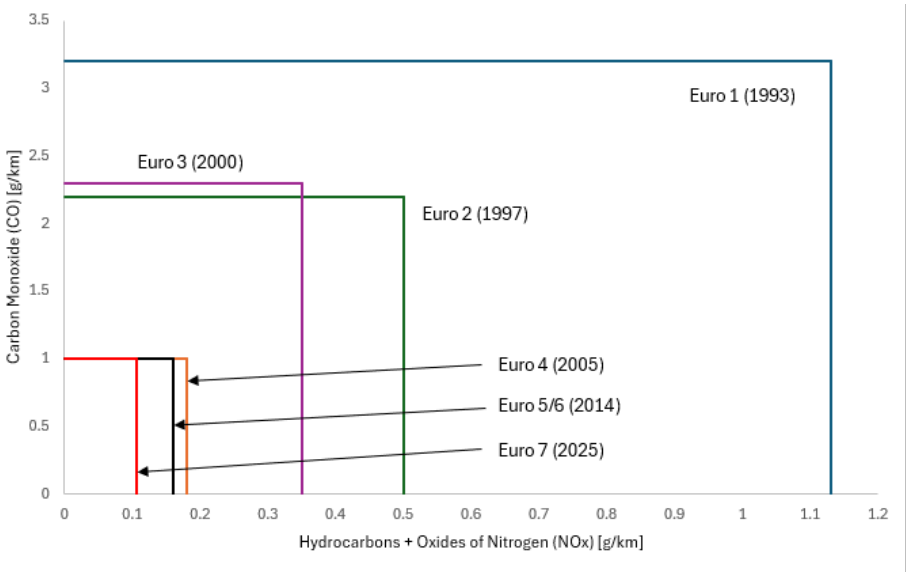

Figure 1.1: The evolution of gaseous EU emission limits, adapted from [7]

(2) Customer demand for increased specific performance: Specific power (P_s) [kW/l] is the brake

power (P_b) [kW] that the engine can generate divided by the displacement of the engine (V_d) [l].

$$P_b = 2\pi NT \times 10^{-3} \tag{1.1}$$

Where P_b is the brake power [kW], N is the rotational speed [rev/s] of the engine and T [Nm] is the torque.

$$V_d = n \times \frac{\pi}{4} B^2 L \tag{1.2}$$

Where n is the number of engine cylinders, V_d is the volume displaced by the engine [l], B is the bore diameter [m] and L [m] is the length of the stroke.

$$P_s = \frac{P_b}{V_d} \tag{1.3}$$

Gasoline engines can be split into two groups; naturally aspirated, which breathe air directly at atmospheric pressure; and pressure charged, which increases the density of the air by some form of compressor. It can be seen from Figure 1.2 that the specific performance of naturally aspirated engines is approximately 60 - 70 kW/l and 60 - 140 kW/l for boosted engines. There are several ways to pressure charge an engine, examples include: turbocharger (TC), roots blower or supercharger (SC), combinations of TC and SC and finally electric supercharger (eSC).

Naturally aspirated engine specific power has remained fairly constant over the last thirty years and could actually be reducing since 2010. Conversely the specific power of boosted engines has increased significantly since 2010, peaking at 140 kW/l in 2017. Also related are increases in specific torque T_s [Nm/l]. Brake torque is measured using a dynamometer defined as:

$$T = Fb \tag{1.4}$$

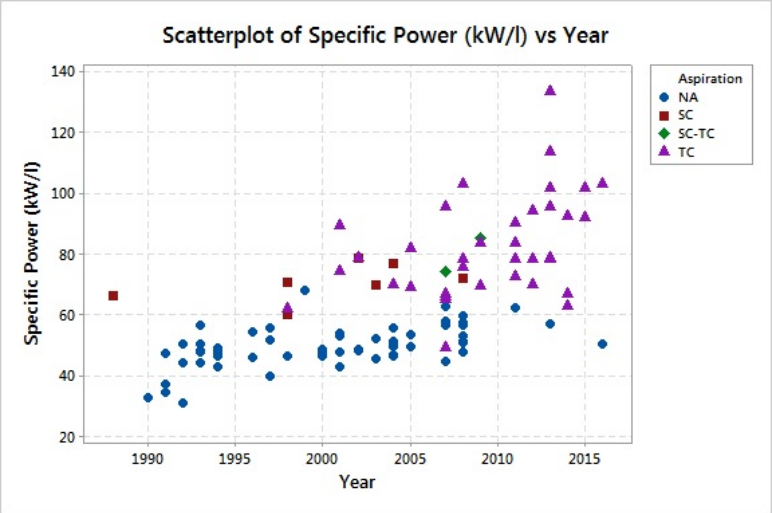

Figure 1.2: The evolution of specific power vs. year [8]. Naturally Aspirated (NA), Supercharged (SC), Supercharger plus Turbocharger (SC-TC) and Turbocharger (TC).

Where F is the force applied to load cell on the dynamometer [N] and b is the distance from the centre of the crank shaft to the dynamometer load cell [m]. Taking the measured brake torque T_b [Nm] and dividing by the volume displaced by the engine V_d [l], gives the specific torque T_s [Nm]:

$$T_s = \frac{T_b}{V_d} \tag{1.5}$$

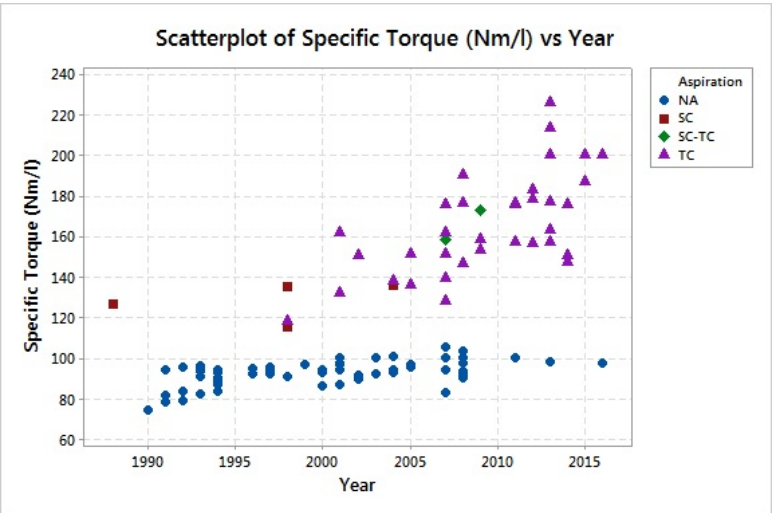

Figure 1.3: The evolution of specific torque vs. year [8]. Naturally Aspirated (NA), Supercharged (SC), Supercharger plus Turbocharger (SC-TC) and Turbocharger (TC).

Figure 1.3 shows the trend of specific torque from the early nineties until 2016. Whilst naturally aspirated specific torque has remained fairly constant, the specific torque of boosted engines has been steadily rising. This has been largely driven by downsizing and pressure charging [9]. The increasing levels of specific torque from smaller displacement engines has seen dramatic rises in brake mean effective pressure (*BMEP*) [kPa], Figure 1.4.

$$\text{BMEP} = \frac{6.28 \times n_R \times T_b}{V_d} \tag{1.6}$$

Where n_R is the number of crank revolutions per power stroke (two for four-stroke and one for two-stroke), T_b is the brake torque [Nm] and V_d is displaced volume [l].

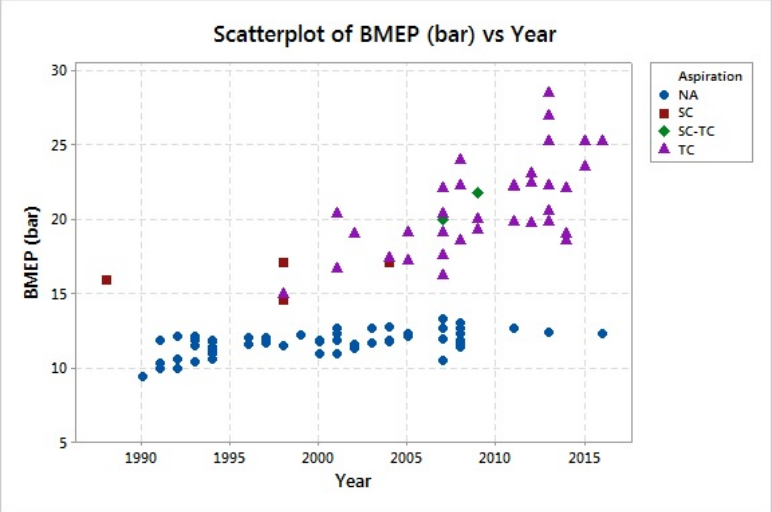

Figure 1.4: Maximum BMEP vs. year [8]. Naturally Aspirated (NA), Supercharged (SC), Supercharger plus Turbocharger (SC-TC) and Turbocharger (TC).

(3) CO_2 reduction: By 2021 the fleet average to be achieved by all new cars within the EU was 95 grammes of CO_2 per kilometre [10]. Failure to comply with this fleet average limit attracted a fine of 95 Euros per gramme over the limit. In a gasoline engine, reductions in CO_2 are directly linked to reducing fuel consumption. The rate of introduction of new technology designed to reduce fuel consumption has been unprecedented in the last 10 years. There are four key loss areas that provide opportunities to increase efficiency and thereby reduce fuel consumption in gasoline engines; (a) pumping losses, (b) friction losses, (c) combustion losses, and (d) heat losses.

(a) Pumping loss reduction: The term 'pumping losses' refers to work done in pumping air and

exhaust gases through the throttle and intake/exhaust valves, Accordingly, any restriction in the flow path will induce some level of pumping loss. A gasoline engine typically employs a physical throttle (usually a simple butterfly valve) to control the mass of the induced charge and thereby control the load, often referred to as quantity governed [11], as shown in Figure 1.5.

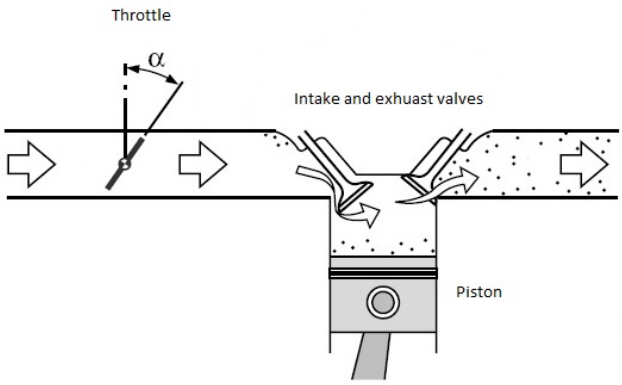

Figure 1.5: Basic load control of a gasoline engine, adapted from [12]

Other aspects of the engine design that create pumping losses, are the details of the inlet and exhaust systems (e.g. ports, cam profile, manifolds, system pipework and, where fitted, a turbocharger). There are several ways to reduce pumping losses by de-throttling for a given intake air mass, the most recognised of which are: the use of complex valve-trains to remove the need for the intake throttle by effectively throttling at the valve [13], the use of air dilution (lean operation) [14] [15], exhaust gas recirculation (EGR) displacing air with exhaust gas [16], load point shifting or operating at a higher load than previously [17], and downsizing (another form of load point shifting) [18].

(b) Friction reduction: The reduction of engine friction may be achieved in two ways; the first is to optimise conventional engine designs – optimising the mechanics and tribology to meet the specific performance and peak firing pressure of the engine. The second way is to add new technology, e.g. to replace a plain cam bearing with a roller type bearing [19]. Low friction coatings or production techniques to improve the installed roundness of the cylinder [20] also provide opportunities for reducing frictional losses without the loss of other attributes.

(c) Combustion control: Gasoline combustion in engines is a highly cyclically variable process [21]. The combustion process relies on pre-mixing of the air and the fuel at the desired air to fuel ratio to achieve stable, repeatable combustion performance. Gasoline combustion, in addition to the

quantity of air and fuel in the cylinder, is governed by the spark timing. The lowest possible fuel consumption for a given speed and load will be at the point of optimum spark timing, typically 50% mass fraction burned (MFB 50) of 8°CA +/- 2°CA [11]. Modern engine control units employ automatically adaptive combustion control, whereby the controller seeks to achieve the optimal combustion phasing unless this is not possible. One such reason is knocking combustion, detected using a knock sensor (this phenomenon which will be explored in more detail in Chapter 2, is an undesirable feature of SI combustion).

(d) Reduction of heat loss: Heat transfer to the wall of the combustion chamber and piston during combustion and expansion of the working fluid results in lost work to the piston and ultimately the crankshaft. An engine design that's optimal for fuel consumption will have a different layout to that of a high specific power racing engine. The objective to minimise heat transfer is to achieve the minimum surface area to the volume of the cylinder, or surface to volume ratio. Alternative methods to insulate the cylinder during combustion, so-called thermal swing coatings [22], could potentially provide benefits but are in the early stages of research for passenger car applications.

1.3 Introducing Abnormal Combustion

Each of the four areas (a – d) identified as directly relevant to CO_2 reduction are worthy of further study in themselves. However, this thesis will focus on a limiting phenomenon common to all – abnormal combustion, and in particular the phenomena of low-speed pre-ignition (LSPI). Abnormal combustion, a catch-all term which includes 'normal' knocking combustion, heavy knock, pre-ignition, low speed pre-ignition and mega-knock, can prevent the use of the 'optimum' ignition timing – in which case the operating point is typically described as 'knock limited', and can limit boosting and downsizing – through increases in in-cylinder temperature and pressure, and therefore increased 'criticality' of the charge associated with increased BMEP. High levels of BMEP (>20 bar) at low engine speed present a significant challenge in this regard and while operating conditions between 1000 and 2500 rpm engine speed and wide open throttle are known to promote LSPI, the fundamental causes of the phenomenon are not well understood.

1.4 Thesis Structure

This thesis, structured as follows, will explore this issue in detail:

- Chapter 1 – Drivers for change and Thesis Structure, (the current chapter) presents a brief general introduction to the work and details the thesis workflow and structure
- Chapter 2 – Abnormal Combustion, presents a detailed background describing in turn, abnormal combustion in it's various forms, factors known to affect it, classification methods and characterisation tests.
- Chapter 3 – Research topics, introduces the three areas for investigation in relation to cause of abnormal combustion
- Chapter 4 – Fundamental Investigation into Oil Detergent as the Cause of LSPI, this chapter introduces the Chiba hypothesis and shock tube experiments aimed at investigating this further via shock heating of metal oxide powers
- Chapter 5 – Top Land Crevice Sampling, describes the process of collecting and analysing oil samples from the top land crevice zone of a fired engine using oils with different detergents
- Chapter 6 – Multi-cylinder Testing of Methylcyclopentadienyl-Manganese-Tricarbonyl (MMT), concludes with testing fuels known to promote abnormal combustion with the addition of MMT, a metal oxide octane booster
- Chapter 7 – Conclusions, Claims for Originality and Future Work
- Appendices
- Nomenclature
- References

1.5 Published Works and Presentations

1.5.1 Conference Oral Presentations

- UnICE3G, 21st April 2022, University College London; Understanding Low-speed Pre-ignition Promoting Mechanisms of Calcium. (APC Feasibility Study)
- Society of Automotive Engineers (SAE) World Congress, April 2024, Detroit, Michigan; Understanding the low-speed pre-ignition promoting mechanisms of Calcium
- American Society of Mechanical Engineers (ASME) Internal Combustion Engine Forward (ICEF) 20 – 23 Oct 2024, San Antonio, Texas.

1.5.2 Conference Publications

American Society of Mechanical Engineers (ASME) Internal Combustion Engine Forward (ICEF) 20 – 23 Oct 2024, San Antonio, Texas. **ICEF2024-140006 – A Fundamental study on the potential LSPI promoting mechanisms of Ca and Mg based oil detergents.** Matthew J. McAllister[1,2,*], Martin H. Davy[2,*], Luke J. Doherty[2], Laurent M. LePage[2], Christopher Wheeler[2]. [1] Caterpillar Inc., Peterborough, United Kingdom. [2] University of Oxford, Oxford, United Kingdom. [*] Joint first authors

1.5.3 Future Publications

A number of potential publications are in preparation or planned to be generated from this thesis. Details are yet to be confirmed, however the outline is as follows:

- Journal paper, based on the work in (ASME) ICEF paper, with additional material not included in the primary publication
- Conference paper – Top land crevice sampling with calcium and magnesium detergents. Joint publication with University of Warwick
- Journal Paper – Petroleomics analysis of new oil and fuel vs. a top land crevice sample. Joint publication with University of Warwick

- Conference paper – The effect on LSPI of adding MMT to LSPI promoting fuels

Chapter 2

Abnormal Combustion in SI Engines

2.1 Introduction

Combustion of a premixed fuel and oxidiser causes a wave to propagate through the unburned mixture. The rate that the wave progresses is dependant upon heat transfer via conduction and the diffusion of radicals. This 'wave' is more commonly referred to as a flame. Deflagration describes the subsonic process of combustion, where the burning flame proceeds through a combustible substance at velocities less than the speed of sound. Detonation is supersonic and propagates through shock waves. The rate of combustion is no longer controlled by the heat conduction and diffusion of radicals; rather the shock wave structure of the developing flame front compresses the mixture in the unburned zone, rapidly increasing its temperature and pressure and resulting in an explosive reaction. In the context of an SI ICE, normal combustion refers the propagation of a sub-subsonic flame through a premixed air-fuel mixture. Detonative combustion in an SI engine generates an audible noise – commonly referred to as knock – due to the shock waves resulting from explosive reactions in the unburned zone or 'end-gas'. While knock is by far the most commonly referenced abnormal combustion phenomenon associated with SI combustion engines other significant forms of abnormal combustion exist. The following section of this work categorises and details the different types of abnormal combustion events that may be found in SI engine operation.

2.2 Classes of abnormal combustion

As a first approximation, abnormal combustion events in an SI engine can be divided into two broad classifications – those occurring pre-spark (or pre-ignition) and those occurring post-ignition. Pre-ignition, as the name suggests, describes the ignition of the pre-mixed charge in the cylinder before the spark has ignited it. Post-ignition events refer to the uncontrolled combustion of some (or all) of the unburned mixture ahead of an approaching flame front. As will be described below, the two classifications may be linked in that a pre-ignition abnormal combustion event may be the trigger for post-ignition abnormal combustion and vice-versa.

2.2.1 Post-ignition abnormal combustion

Normal knock and auto-ignition

As the premixed charge in an SI engine is ignited, an expanding flame fills the combustion chamber driving the piston downwards and converting the chemical energy contained in the fuel to kinetic energy, which, in turn, drives the crankshaft and ultimately the driving wheels of a vehicle. 'Knock' is the common term used to describe the noise generated when uncontrolled auto-ignition of the unburned in-cylinder charge (the end-gas) occurs ahead of the arrival of the flame front. The tendency of an engine to knock is largely the result of the temperature and pressure history of the end gas (which is isentropically compressed by the expanding flame), but is also influenced by the design detail of the combustion system, the operating conditions of the engine and the chemical properties of the fuel [11]. The auto-ignition of the end-gas is a kinetically controlled process. There is, therefore, a significant temporal affect on knocking tendency – a finite time is required for the relevant reaction processes to occur. Accordingly, faster burn rates (flame speeds), which can be promoted by appropriately controlled levels of in-cylinder turbulence, reduce the tendency to knock. The most widely used form of in-cylinder charge motion in SI engines is 'tumble', so-called as it describes the bulk motion of the air as it enters the cylinder [11] [21], see Figure 2.1. As the piston moves upward during the compression stroke, the bulk tumble motion breaks down into smaller-scale turbulent structures, in accordance with the principle of conservation of angular momentum.

Figure 2.1: In-cylinder 'tumble' bulk motion, adapted from [23]

Modern SI engines employ high levels of tumble in order to promote fast burn rates for improved efficiency and knock resistance [13]. The inherent variability of intake process results in high cyclic variability of combustion [21] [24] and a wide range of burn rates for each cylinder, for each cycle of engine operation. Given the above discussion, it is interesting to note that, for a fixed spark timing, the very fastest burning cycles can result in heavy knock. This is due to those cycles behaving in a way similar to advancing the spark timing. In theses cycles, the rise in bulk in-cylinder temperature due to the earlier heat release increases the reactivity of the end gas to the extent that the potential temporal benefits of the faster flame speed are completely offset.

Figure 2.2 shows a cylinder pressure vs crank angle trace for what might be described as 'normal' knocking combustion. Knocking combustion is characterised by the 'spiky' pressure trace that can be seen in the cylinder pressure diagram. Typical acoustic frequencies for knock are in the range 5 – 10 kHz [11]. A favourable feature of knocking combustion is that it is to some extent predictable and can also be actively controlled by a suitable control system using accelerometers mounted to the engine block. This allows an engine to run at its most efficient 'knock limited' ignition timing throughout the speed and load range via control of the spark advance. If controlled properly, knock will not damage the piston or combustion chamber components. However uncontrolled knocking initially leads to audible combustion, an annoyance to the driver of the vehicle, but can also damage the piston surface [11]. Whilst a single uncontrolled knock event is unlikely to cause much damage,

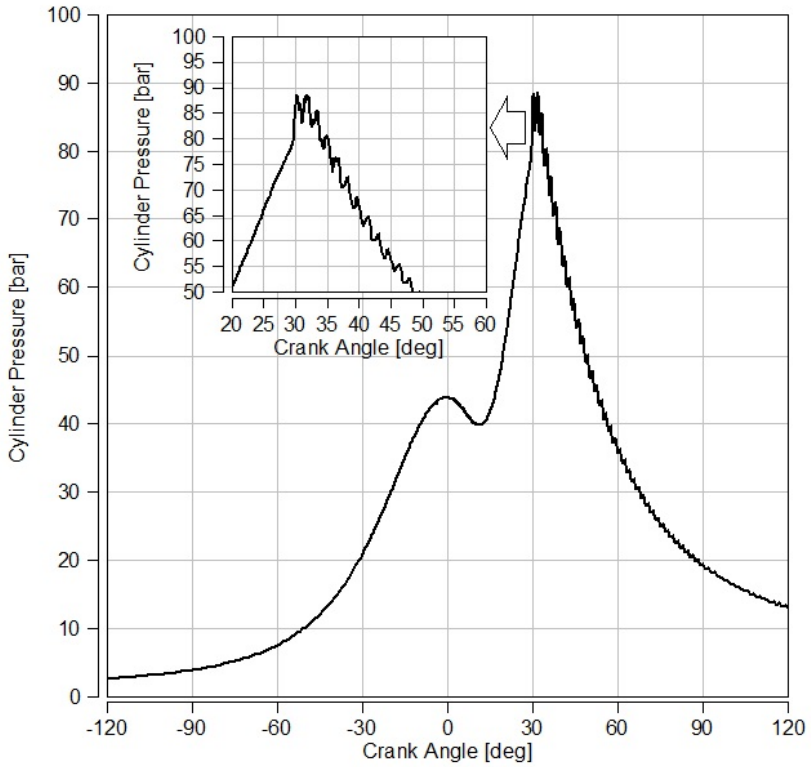

Figure 2.2: Normal Knock. 1750 rpm, WOT, $\lambda = 1$, 98 Ron fuel, spark timing 7°CA ATDC

repeated uncontrolled events lead to erosion of the piston [11].

Surface Ignition, rumble and 'wild ping'

In 1954, the Coordinating Research Council (CRC) defined 'surface ignition' as the "initiation of a flame front by any hot surface other than the spark discharge prior to the arrival of the flame front", i.e. 'surface ignition' was originally defined as a post-ignition event. Moreover, the flame front or fronts established by surface ignition were said to propagate at normal velocities [25], that is to say the resultant end gas reactions are not detonative in nature thereby distinguishing the phenomenon from knocking combustion. More recently however, Chapman and Costanzo [26] have suggested the term "surface ignition" is both too general a description and that it could be misleading if ignition of the charge were due to a particle of deposit or oil. It is likely that early use of the term "surface ignition" was the result of a lack of understanding of the mechanisms behind certain aspects of abnormal combustion or that the problem was one of hot-spot pre-ignition rather than that which is now known to be particle or droplet based pre-ignition. Interestingly, the primary terms used to refer to fuel/lubricant derived abnormal combustion that were observed in the 1950's and 1960's

were 'rumble' and 'wild ping' [27]. These terms were derived from the sounds that were heard from the engine when these forms of abnormal combustion occurred. In this context, rumble was defined as a low pitched noise with an approximate frequency range of 800 to 1400 Hz [27]. The noise was ultimately found to be linked with bending vibration of the crankshaft due to abnormally high rates of pressure rise near to top dead centre (TDC). These high rates of pressure rise were correlated with a repetitive pattern of single or multiple abnormal ignitions occurring immediately before or after normal spark discharge [28]. Wild ping is no longer used to the best of the author's knowledge.

2.2.2 Pre-ignition abnormal combustion

Hot spot ignition

Hot spot pre-ignition occurs when a localised high-temperature energy source ignites the in-cylinder charge before spark. Hot spots may occur in the form of overheated combustion chamber components, most commonly the spark plug, exhaust valves, and piston crown, or combustion chamber deposits – hard carbonaceous material created from the combustion of fuel and possibly small amounts of lubricating oil (if these deposits become excessive and if suitably placed they can retain heat to the point where they can provide sufficient temperature to ignite the charge [26]). Hot spot pre-ignition is often the consequence of post-ignition abnormal combustion. Poorly controlled knock may cause the spark plug to overheat. Further, an increased frequency of knock amplitude and occurrence may disrupt the thermal boundary layer protecting the piston allowing the hot combustion gasses to reach the piston crown and form a hot spot. Accordingly, pre-ignition is more likely at low speed high load or under operating conditions where prolonged knocking combustion can occur, for example repeated transients or under leaner than desired lambda where chamber temperatures are higher than normal. Lambda (λ) is defined in Equation (2.1)

$$\lambda = \frac{\text{Actual Air-Fuel Ratio}}{\text{Stoichiometric Air-Fuel Ratio}} \tag{2.1}$$

Where the actual air to fuel ratio (AFR) is measured using an emissions analyser or lambda sensor. The stoichiometric AFR ratio is ideal amount of air required to completely burn all of the fuel.

Stoichiometric AFR is specific for each fuel, for example a typically gasoline is 14.7:1. A lambda less than 1 is 'rich', whereas a lambda greater than 1 is 'lean'.

Low Speed Pre-ignition (LSPI)

LSPI is the term used to describe low speed, (in the approximate region 1000 - 2500 rpm) pre-ignition of the in-cylinder charge. This form of pre-ignition differs to that of the hot-spot pre-ignition due to that fact that the pre-mixed charge is ignited by mobile oil droplets or detached particles from in-cylinder deposits. As a result of the particle mobility, the LSPI ignition sites are randomly distributed within the cylinder [29]. The literature suggests two primary mechanisms by which LSPI can occur:

1. Oil and fuel accumulate in the top land of the piston and during a transient increase in engine speed, a droplet is released into the pre-mixed charge containing sufficient energy to ignite the mixture before the spark [29] (Figure 2.3).

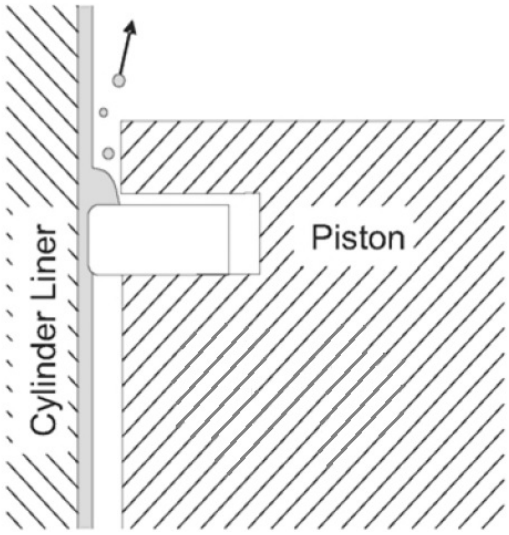

Figure 2.3: Oil Release from the Top Piston Land [29] [30]

2. A hot deposit particle or particles become detached from the surface of the combustion chamber and ignite the mixture in cylinder [31] [32] [33]. Figure 2.4 illustates the various phases that lead to LSPI via this mechanism. They are as follows:

   A. Deposits formed by cylinder liner wall wetting accumulate above the top ring reversal and on the top of the piston

B. Deposits form on the piston crown over time due to operation at low engine speed and load

C. A particle or particles from A or B are dislodged and move around the chamber

D. A particle moves through the propagating normal flame kernel

E. The particle is not completely consumed, but continues to oxidise and gets hotter

F. In the next cycle, the glowing particle enters and ignites the premixed charge before the spark initiates combustion

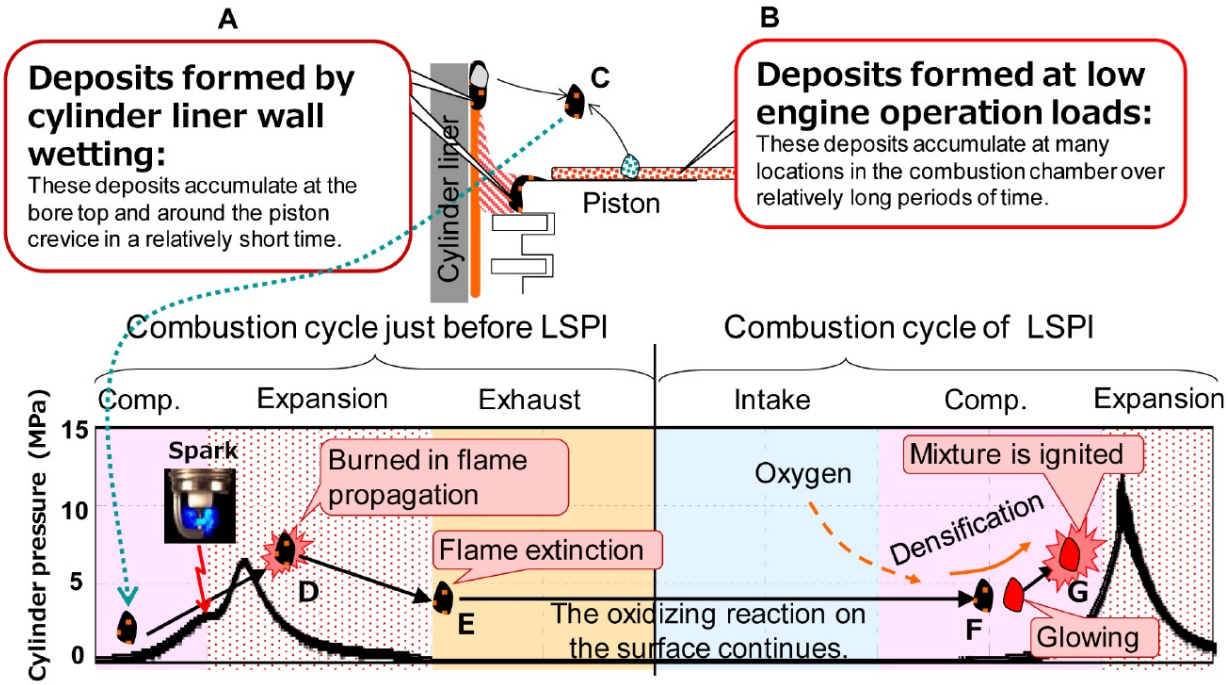

Figure 2.4: Particle release as a cause of LSPI [31]

In addition to these two primary LSPI mechanisms, an important secondary LSPI mechanism, an interaction between the oil release and deposit release mechanisms, has also been demonstrated within the literature [29][31]. It has been shown that pre-ignition caused by oil being released from the top land crevice can result in a further pre-ignition due to the pressure waves in the cylinder dislodging particles which go on to cause further pre-ignitions. This pattern of pre-ignition can be referred to as runaway pre-ignition and can lead to severe engine damage if not controlled quickly [29][31]. Figure 2.5 (a) shows a recording of cylinder pressure in 4500 engine cycles, with an occurrence of LSPI. Figure 2.5 (b) is an exploded view of the LSPI on a time basis, showing that this 'event' was in fact 5 LSPI events with normal combustion cycles in between.

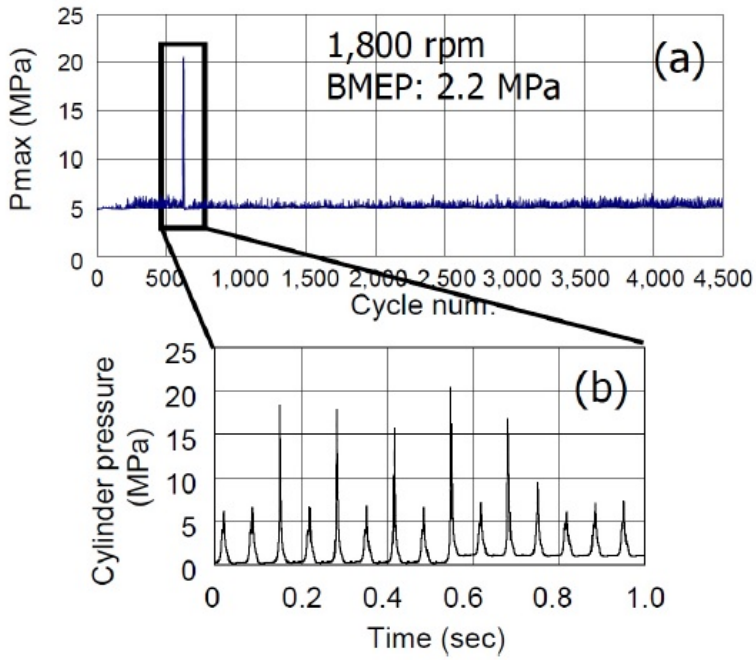

Figure 2.5: Pattern of repeated LSPI with normal combustion in between, 1800 rpm 2.2 MPa BMEP [29]

Industry concerns over the tendency towards, and the potentially serious negative effects of LSPI in modern boosted and downsized gasoline engines has led to the development of dedicated test cycles to evaluate the phenomenon, for example, the Toyota LSPI test, the AVL LSPI test and the GM Dexos test [34]. Each of these tests has its own advantages and disadvantages, for example the Dexos test is the most transient, whereas the AVL test covers the LSPI tendency of a 'clean' vs. 'dirty' state of the combustion chamber. The Toyota test is steady state and spends most of the test at peak torque. Jaguar Land Rover (JLR) developed a test cycle specifically designed to evaluate both LSPI mechanisms (oil droplet and deposit initiated LSPI) in a single test, Figure 2.6. Further details are unavailable due to confidentiality.

Figure 2.7 shows examples of both normal and abnormal combustion cylinder pressure data captured during the JLR LSPI test cycle from an engine operating at at 1750 rpm wide open throttle (WOT). It can be seen that the LSPI cycle shown within the figure results in a very high peak amplitude knock (so-called 'mega-knock'), with the highest peak reaching approximately 270 bar. Although it is difficult to determine the exact pressure that the rotating engine components (piston, gudgeon pin, con-rod and big end crank-shaft pin) are exposed to due to the acoustic 'ringing' on the cylinder pressure trace, these extreme abnormal combustion events may lead to engine failure if, (1) it is not accounted for in the design process [34], or (2) the number of occurrences exceeds the design limits.

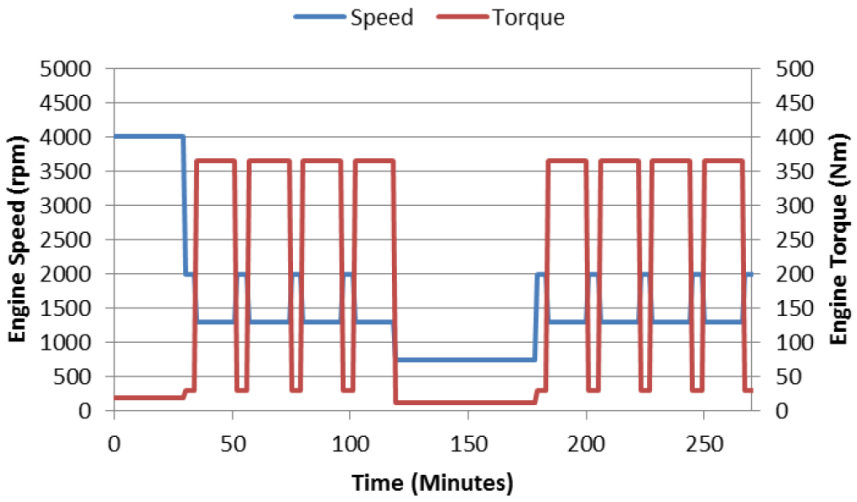

Figure 2.6: Jaguar Land Rover LSPI Test [34]

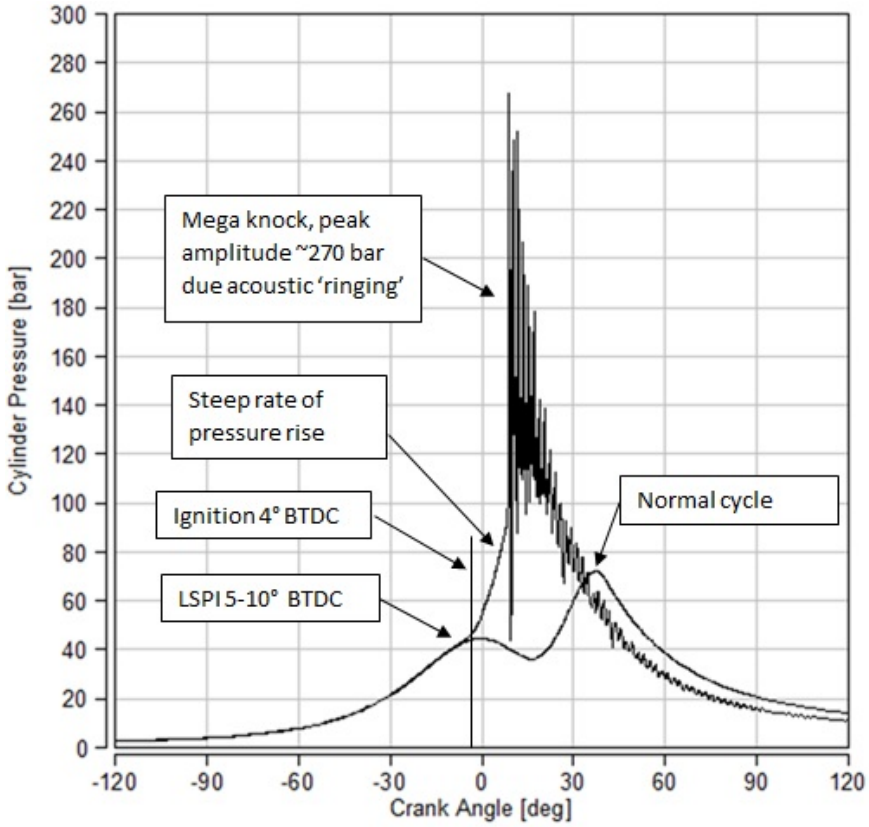

Figure 2.7: Pre-ignition and Mega-knock. 1750 rpm, WOT, $\lambda = 1$, 98 RON fuel, spark timing 4°CA BTDC

Mega-knock and super-knock

The terms 'mega-knock' and 'super-knock' are used frequently within the literature to describe extreme knocking events [35–39]. However, quantitative definitions of super-knock/mega-knock are lacking. The author believes that both terms refer to the same phenomenon, a view supported by

[40]. Accordingly, the term mega-knock will be used exclusively throughout this thesis to describe these extreme events.

Origins of mega-knock

Kalghatgi [40] states that from optical engine testing, that a turbulent flame front occurs after pre-ignition. It is also suggested that the increase in temperature due to the pre-ignition could intensify the reaction process. The end-gas is typically heterogeneous and there will always be variation in temperature and ϕ (equivalence ratio). When fuel and air are pre-mixed in an SI engine the reactivity gradient can be assumed to be the temperature gradient [40]. The autoignition flame front will move through the chamber at a velocity relative to the unburned gas given by U_a, where

$$U_a = \left(\frac{\partial \tau}{\partial r}\right)^{-1} = \left(\frac{\partial \tau}{\partial T}\right)^{-1} \left(\frac{\partial T}{\partial r}\right)^{-1} \tag{2.2}$$

Where τ is the autoignition delay time, T is temperature and r is radius of the flame [40] [41]. The autoignition time can be given for a homogeneous mixutre as; $\tau(T,p)$ where T is the temperature and p the pressure of the end gas at which it must remain to auto-ignite [41]. However, for an SI engine in practice, the temperature and pressure of the end gas are constantly changing, therefore an alternative relationship is required. The Livengood-Wu (l) integral can be used to calculate the likelihood that auto-ignition will occur after time $\tau^{'}$ using the equation [41]:

$$l = \int_0^{\tau^{'}} \frac{dt}{\tau(T,p)} \tag{2.3}$$

Where $\tau^{'}$ is the time available for autoignition and t is time. The amplitude of the pressure wave generated by autoignition is dependant upon U_a. The pressure wave above the ambient pressure caused by the propagating reaction front through a hotspot, in the absence of shock waves, can be related to a non-dimensional resonance parameter ξ, defined as:

$$\xi = \frac{a}{U_a} \tag{2.4}$$

Where a the acoustic speed is given by;

$$a = \sqrt{\frac{\gamma p}{\rho}} \tag{2.5}$$

Where γ is the ratio of specific heats.

The developing detonation depends not just on ξ but also on a dimensionless reactivity parameter ϵ, given by

$$\epsilon = \frac{r_o}{a\tau_e} \tag{2.6}$$

Where r_o is the radius of the hotspot (or oil droplet) and τ_e is the excitation time for autoignition heat release. Therefore ϵ describes the the reactivity of the hotspot.

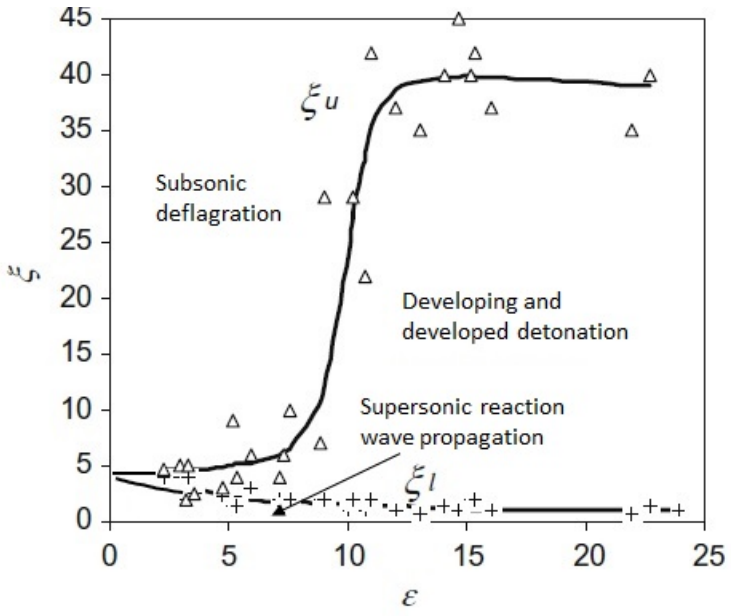

Figure 2.8: Developing Detonation Peninsula, adapted from [41]

The pressure wave created by the hotspot can couple with the autoignition reaction front resulting in a high pressure spike propagating at high velocity into the unburned zone at the speed of sound. Bradley and Kalghatgi [41], computed values of ξ and ϵ using CO + H_2 mixtures as the reaction kinetics were well known. The result was a developing detonating peninsula as shown in Figure 2.8. Kalghatgi [40] goes on to describe 'modes' of propagation within the hotspot, with an upper bound of ξ_u and lower bound of ξ_l, shown in Figure 2.8, as follows:

a. *ξ = 1, chemical resonance.*

b. *ξ = 0, thermal explosion.*

c. *$0<\xi<\xi_l$, supersonic autoignitive deflagration. The autoignitive wave is ahead of the acoustic wave.*

d. *$\xi_l \leqslant \xi < \xi_u$, developing and developed detonation.*

e. *$\xi_l \leqslant \xi < aS_1^{-1}$, subsonic autoignitive deflagration, where S_1 is the laminar burning velocity.*

f. *$\xi \geqslant aS_1^{-1}$, laminar burning deflagration at the laminar burning velocity.*

Therefore if some assumptions are made, as certain data is not available from physical experiments e.g. for the radius of the hotspot, values can be calculated for ξ and ϵ and plotted onto Figure 2.8. This allows for an estimation of the nature of the hotspot and the likelihood of mega-knock, to be calculated. It can therefore be assumed that pre-ignition raises the temperature and pressure ahead of the propagating flame front that could cause a migrant oil/fuel droplet to ignite the unburned mixture and result in the extreme pressure peaks due to acoustic coupling. If multiple migrant droplets are moving through the un-burnt end-gas this effect will be amplified, leading to higher and higher peak pressures and ultimately engine damage. Finally, Kalghatgi confirms the authors experience that pre-ignition does not always result in mega-knock. Also, that pre-ignition in a previous cycle could increases the temperature and pressure, leading to increased probability that mega-knock will occur in subsequent cycles. In summary, the hot spot or oil droplet or glowing particle may be the cause of the pre-ignition, whether this develops into mega-knock is a function of multiple factors. This phenomena is not well known, but its consequences can be significant.

The negative consequences of mega-knock

Mega-knock events may lead to extreme in-cylinder pressures far exceeding the design intent of combustion chamber components. Rumours exist within the Powertrain community as to the highest amplitude mega-knock pressure ever recorded (1000 bar) and the author has personally observed mega-knock amplitudes of up to 350 bar. Repeated mega-knock events in an ICE can lead to catastrophic mechanical failures. Figure 2.9 shows typical damage that can result from mega knock. The piston damage shown in Figure 2.9(a) is a classical mega knock failure of the second and third piston lands that have broken as the result of mega knock induced ignition of fuel and air in the top land area. Figure 2.9(b) shows the failure of the spark plug centre electrode insulator, the picture compares a damaged spark plug with an undamaged part. The insulator failure can be the result of a single mega knock event that mechanically overloads the ceramic which leads to it shearing off. An alternative failure mode is the result of excessive spark plug gap growth which increases the required voltage to make the spark jump the gap. When this voltage gets close to the dielectric strength of the insulator (typically 38 - 40 kV), the spark can break through the insulator leaving “pin holes" in the ceramic, Figure 2.10 [42]. Over time these compromise the structural integrity of the insulator leading to failure. Further damage to the engine can result from this spark plug insulator failure. As the spark plug is no longer as design intent, the unprotected centre electrode can get hot to the point where it becomes a hot spot itself, which in turn may lead to a hot spot pre-ignition failure melting the spark plug centre and ground electrodes [43], [44].

(a) Piston damage (b) Spark plug damage

Figure 2.9: Typical Mega Knock Damage [45].

Figure 2.10: Insulator with dielectric puncture. Images courtesy of Jaguar Land Rover.

2.3 The effects of fuel composition

A typical gasoline has in excess of 200 different hydrocarbon components, the characteristics and relative proportions of which influence the fuel's behaviour through all elements of the ICE mixture preparation and combustion processes [46]. Hydrocarbons are typically classified as: saturated, unsaturated, or aromatic. As described by Richards [47], the term saturated refers to the fact that carbon atoms can only accept a maximum of 4 bonds and the bonding consists of a single sigma bond (see Figure 2.11). Alkanes are saturated hydrocarbons with single bonds to the hydrogen atoms. Carbon atoms attached by sigma bonds can rotate around the bond freely. Alkenes and alkynes are unsaturated hydrocarbons which means they can have double or triple bonds. Alkenes have double bonds consisting of 1 sigma bond and 1 pi bond. Alkynes have triple bonds consisting of 1 sigma bond and 2 pi bonds. The pi bonds lock the atoms in the sigma bond which stops movement around the bonds. The general principle of atomic bonding can be seen in Figure 2.11. Pi bonds are significantly less stable than sigma bonds and are therefore easier to break. Chemical reactions can break the bonds via a metallic catalyst, such as platinum, and introduce more hydrogen atoms in a process called hydrogenation.

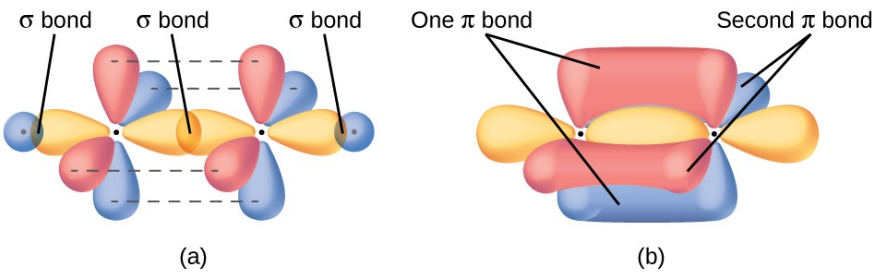

Figure 2.11: Sigma and Pi Bonding [48], (a) σ bonds, (b) π bonds.

The process of hydrogenation is an addition reaction, where the hydrogen atoms introduced can form single bonds with available carbon atoms. Alternative addition reactions are the introduction of a water molecule (hydration) or oxygen atom (oxygenation). This means that alkynes can become alkenes and alkenes can become alkanes, also hydrocarbons can bond with each other to form chains in a process called polymerisation. The term alkane has replaced paraffin as the term to describe acyclic branched or unbranched saturated hydrocarbons and has the general chemical formula C_nH_{2n+2}. Figure 2.13 is a historical chart showing the boiling point temperature ranges of hydrocarbons [49]. The terms; n-paraffin means 'normal', straight-chain, saturated hydrocarbon molecule. The term 'iso' or i-paraffins are the branched chain hydrocarbon molecules. Naphthenes are a class of cyclic aliphatic hydrocarbons obtained from petroleum and have the general formula C_nH_{2n}. Aromatic hydrocarbons are so-called due to the fact that they have distinctive smells. Aromatics are cyclic unsaturated alkenes as they typically have double bonds. The most recognised aromatic with regard to gasoline fuel is benzene C_6H_6, as its this which give the fuel its sweet aroma.

2.3.1 Distillation and Volatility

The boiling/distillation behaviour of a hydrocarbon blend is heavily dependent its composition. Fuel volatility is quantified by the volumetric percentage that is distilled at a given temperature. A fuel's volatility curve has a significant contribution to its ability to start the engine at low temperatures and the likelihood of vapour bubbles to form in the low pressure fuel system. UK and European fuels have to meet a fixed specification; BS EN 228. This standard specifies, amongst many other things, the fuel's volatility (typically expressed in terms of Reid Vapour Pressure (RVP) and final boiling point). Reid vapour pressure is measured using a specially designed test rig [21]. The fuel sample to be tested is cooled in a refrigerator to 0 - 1°C, and held in a 'test bomb'. The test rig contains an air chamber with fitted with a very accurate pressure gauge (to within 0.25% of point) which is heated in a water bath to 37.8 °C. When the sample is to be measured the bomb is attached to the air chamber making a sealed measurement volume. The sample is agitated, warming the fuel and it is placed in the water bath. The resulting measured vapour pressure is the Reid vapour pressure. As typical pump gasoline has both summer and winter blends, adjusting the RVP is a means to

help with ignitability in winter (increased volatility) and reduce evaporative emissions in summer (reduced volatility). The details of the test method can be found in the test standard ASTM-D-323.

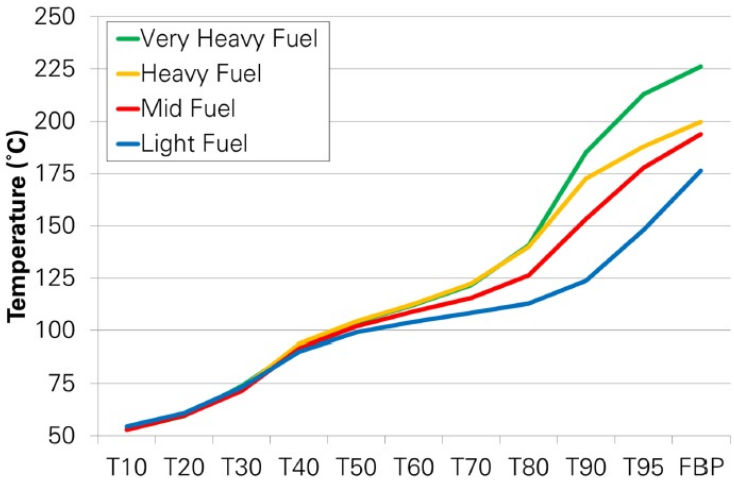

Figure 2.12: Fuel % evaporated [38]

Figure 2.12 shows some example distillation curves for a range of fuel properties [38]. The x-axis of the chart shows the temperature at which that percentage of the fuel evaporates e.g T60 is the temperature at which 60 % of the fuel has evaporated and so on. The legend refers the boiling characteristics of the fuel, for example the 'light' fuel will evaporate easily. In contrast the very heavy fuel requires significantly higher temperatures to evaporate and has a very high final boiling point. EN 228 specifies a maximum final boiling point of 210 °C, typical European fuels have a final boiling point of approximately 195 °C. It can be seen in Figure 2.12 that the curves diverge from approximately T40 and there is a wide spread in T90 and final boiling points. These aspects of the curves are commonly referred to as the 'mid' and 'back-end' distillation characteristics.

2.3.2 Octane number and resistance to knock

The octane number (ON) of a gasoline quantifies the anti-knock resistance of the fuel. There are two tests used to quantify the octane rating; namely the research octane number (RON) ASTM D-2699[1] and the motor octane number (MON) ASTM D-2700. Both tests are conducted on the single cylinder CFR engine, developed by the Co-operative Fuels Research Committee. The engine has an 82.6 mm bore and 114.3 mm stroke and can vary compression ratio between 3 and 30 dynamically whilst the engine is running. This achieved by moving the cylinder head relative to the cylinder

[1]ASTM denotes the American Society for Testing and Materials; the letters and numbers denote the test standard.

block [11]. The test conditions are specified in Table 2.1.

Table 2.1: RON and Mon Test Conditions [11]

Test	**Research Method**	**Motor Method**
Inlet Temperature [°C]	52	149
Inlet Pressure [mbar]	Prevailing atmospheric pressure (typically 1013 mbar at sea level)	
Humidity [kg/kg dry air]	0.0036 – 0.0072	
Coolant Temperature [°C]	100	
Engine Speed [rpm]	600	900
Spark Advance [°CA BTDC]	13 (constant)	19 - 26 (varies with compression ratio)
Air/Fuel Ratio [AFR]	Adjusted for maximum knock	
Compression Ratio [:1]	4 – 18	

Due to the higher intake temperature and more advanced ignition timing, the MON rating is lower than the RON. The numerical difference between the RON and the MON is called the fuel sensitivity, equation (2.7) [11].

$$\text{Sensitivity} = RON - MON \tag{2.7}$$

The RON test is analogous to operating an engine at low speeds and loads, whereas the MON test is more like operating the engine at higher loads. The octane number (ON) scale is defined by 2 primary reference fuels; normal heptane n-C_7H_{16} is a straight chain alkane (paraffin) and it describes the 0 end of the octane scale due to its explosive behaviour in spark ignition engines. Conversely isooctane i-C_8H_{18} defines the 100 on the ON scale, due to its knock resistance. Blends of these fuels can be used to describe fuels between the ends of the ON scale, therefore a fuel's ON is defined by comparing its antiknock behaviour to blends of these primary reference fuels. For fuels above 100 RON a further octane boosting element is required as isooctane in not the highest RON fuel available. In the past tetra-ethyl lead was added to isooctane, however as lead is no longer used in road fuel alternative components are required. For modern high octane fuels Ethanol is used in the RON test as 100% ethanol or E100 has a RON of 120 -135 and a MON of 100 - 106 [50]. Forecourt fuel

pumps in the UK and Europe only display the RON of a fuel and are not required to display MON. In the USA, RON and MON values are sometimes combined to give the antiknock index (AKI), where

$$AKI = \frac{(RON + MON)}{2} \tag{2.8}$$

2.3.3 Metallic octane boosters

Octane boosters are chemical additives used to increase the RON of a fuel. According to local fuel standards it is typical to specify a minimum RON for forecourt pump gasoline. Where the minimum RON cannot be met by the base fuel, octane boosters are added to achieve this. As stated in §2.2.1 tetra-ethyl lead has historically proven to be an excellent octane booster for use in gasoline fuels but, due to the public health concerns of metallic compounds in exhaust gases [51–53], largely has been banned from forecourt fuels [54] [55]. However, alternative metallic octane boosters do exist and are in use in some regions, in particular Methylcyclopentadienyl Manganese Tricarbonyl (MMT), others include Aniline and Ferrocene. The highest concentrations of MMT in commercial fuels (140 parts per million (PPM) from a 2016 survey) are seen in Africa, Asia and to a lesser extent in central and South America [56].

2.3.4 Links to abnormal combustion and LSPI

Figure 2.13 illustates the relationship between common hydrocarbon structural groups, their boiling temperatures and RON, demonstrating the potential influence of blend composition on a fuels evaporation and combustion characteristics.

Fuels that contain the heavier alkane molecules tend to have a lower RON (therefore low knock resistance) and higher boiling temperature, while naphthenes tend to influence the mid-boiling temperature of a blend and have low to mid-range RON values. Aromatics have a high RON and would, on first inspection, seem to be attractive way to improve the overall RON of a fuel blend. The drawback is that the aromatics have a high final boiling point. Fuels that have a high mid and back-end distillation temperature tend to be more prone to LSPI [38], [57]. This is thought to be due to the tendency of the fuel not to completely evaporate leaving the heavy-ends of the fuel in liquid form in the piston top land crevice. This fuel will readily strip the oil from the liner and the resulting

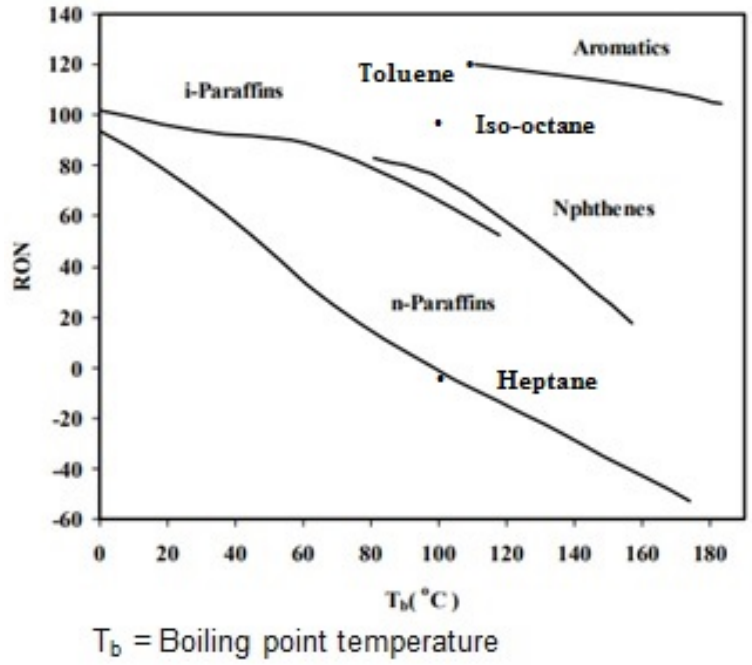

Figure 2.13: RON and boiling temperature of hydrocarbons, adapted from [49]

mixture can be released from the piston land, typically during an aggressive transient acceleration manoeuvres, see Figure 2.3 [29] [30]. Moreover, fuels high in aromatics tend to have high particulate forming potential. This particle generation effect can be quantified using either the particle matter (PM) index and/or the particle number (PN) index, which is calculated using the double bond equivalent and vapour pressure of the fuel [58]. The higher the Pn index, the higher the likelihood of high particle emissions.

$$\text{Pn Index} = \frac{\sum_{i=1}^{n}[DBE_i + 1]V_i}{DVPE(kPa)}(kPa^{-1}) \tag{2.9}$$

Increasing aromatic content tends to increase unburned particle emissions, which, in turn, may lead to a higher tendency to LSPI through the glowing particle as an ignition source mechanism described in §2.2.2 [46]. The suitability of RON and MON test methods is often questioned due to the low engine speed, high inlet air temperature, variation in air to fuel ratio (AFR) and significance of K [59].

$$\text{Octane Index (OI)} = RON - KS \tag{2.10}$$

Where S is the sensitivity (2.7) and K is a constant for that condition. High OI indicates high knock resistance, and K is typically assumed to 0.5 (2.8). The work of Kalghatgi [60], determined that K varies with operating condition and can actually become negative. Also in terms of end-gas thermal properties, K decreases as the temperature decreases for a given in-cylinder pressure. Moreover, the experimental work in this paper confirms that the value of K also changes between engines, with constant fuel properties. It has been shown also that provided that the base fuel stock is of a good quality, changing the RON doesn't increase or decrease the likelihood for LSPI occurrence [61–63]. It does however have an effect on mega-knock – the lower the RON the higher the mega-knock amplitude as shown by [38], [64] and the observations of the Author in multiple tests (the data cannot be shared for confidentiality reasons). The previous paragraphs link fuel structure to octane number and abnormal combustion. Kalghatgi [40] demonstrates a link between a fuel's laminar burning velocity, which is a fundamental fuel property and its propensity to pre-ignite. The work of Zeldovich [65] is introduced to provide an initiation criterion for the ignition of oil/fuel droplets. This work describes the concept of a flame ball with a critical radius, R_f. A spherical flame with radius greater than R_f propagates, whereas as a flame with a radius smaller than R_f extinguishes. The term R_f is related to the laminar flame thickness, δ, Equation (2.11) [65]:

$$\frac{R_f}{\delta} = \exp \frac{1}{2}\beta(1 - \frac{1}{Le}) \tag{2.11}$$

Where: β is the Zeldovich number and Le is the Lewis number. The Zeldovich number is given by Equation (2.12) [65]:

$$\beta = E\frac{(T_b - T_u)}{RT_b^2} \tag{2.12}$$

Where: E is the activation energy, T_b is the temperature of the burned gas, T_u is the temperature

of the unburned gas, R is the universal gas constant. The Lewis number is dimensionless and is the ratio of thermal diffusivity to mass diffusivity and is given by Equation (2.13) [66]:

$$Le = \frac{\alpha}{D} \tag{2.13}$$

D (mass diffusivity), can be calculated using Equation (2.14) [40]:

$$D = \frac{\mu}{\rho} \tag{2.14}$$

Finally, in cases where poorer base fuels are used, with an octane booster such as MMT, there could be case where a nominally 'high RON fuel' could have an high LSPI/mega-knock propensity and intensity. Where MMT is used, the problem is thought to be two-fold; firstly the base fuel properties are typically poor (heavy carbons, high mid, back end and final boiling point) and would potentially increase the propensity for LSPI due to accumulation and release of oil/fuel from to top land crevice [29] §2.2.2; and secondly, MMT is known to readily build chamber deposits with low oxidation temperature, which could be plausibly linked to the alternative LSPI trigger mechanism §2.2.2 (deposit release), albeit due to a different deposit formation mechanism (manganese oxide deposit formation) [56].

2.4 The effects of lubricating oil composition

The main functions of lubricating oil are as follows [11] to: lubricate the engine components and prevent wear; reduce friction to ensure maximum mechanical efficiency is achieved; collect wear particles, soot and other impurities for removal by the oil filter; transfer heat; e.g. cooling or heating of the pistons depending upon the operating condition of the engine. The lubricating oil is subject to extremes of temperature, contamination by water, fuel, soot particles, acid build up and is continually sheared by its interaction with the mechanical components in the engine. During use,

its initial composition undergoes continuous evolution due to fuel dilution and exposure to high-temperature/pressure, and combustion gases. The following subsections consider the composition of the base oils and its additive pack, and the influence of the oil on abnormal combustion and LSPI.

2.4.1 Base Stock

Base stock describes the major component of the lubricant and is divided into five groups. Groups I - III (1 to 3) are produced by refining crude oil and represent the mineral oils, where Group I have low saturates and high volatility and Group III have high saturates and low volatility. The higher the group the more refined or higher quality of the base oil. Group IV (4) oils are said to be synthetic as they are processed. Group III oils that have been heavily 'hydro-cracked' can also be referred to a synthetic. Hydro-cracking is a chemical process where unsaturated and aromatic molecules are broken apart and, by the addition of hydrogen, are refined into more desirable saturated hydrocarbon chains. The last group, Group V (5) cover all other types of base stocks. The trend is a decline in Group I, in favour of higher quality group II & III base stocks [67]. Hydro-finishing is part of the refining process, whereby the properties of the oil are modified by the addition of hydrogen. This process can be used to reduce the acidity and stabilise the colour of the base oil. It is used to remove sulphur, nitrogen and oxygen, however there will be some oxidation or hydrogenation of the unsaturated hydrocarbon compounds [67]. In terms of composition, the base stock makes upon approximately 75% of the final oil with the remainder being a combination of viscosity modifiers and the detergent pack. These figures are indicative only, as the blend will be modified depending upon the application.

2.4.2 Oil Additives

Base oil (mineral or synthetic) alone is unable to lubricate an engine consistently and for a sufficiently long time period. If left untreated the oil would deteriorate rapidly and result in the engine not being correctly lubricated leading to accelerated wear, chemical attack and/or heavy deposit formation. Additives are introduced to minimise the effect of the destructive processes that degrade the engine and oil. They also provide positive effects by enhancing the performance of the lubricant, e.g. reduce friction, therefore reducing fuel consumption [67]. As lubricating oil is a hydrocarbon

blend, its molecules are subject to oxidation due to the operating temperatures and exposure to air in the engine. General oil sump temperatures are typically below 140°C, however local temperatures in certain areas can reach 250°C; for example in the piston top land. The oil contains antioxidants to prevent lubrication oil forming excessive deposits, as deposits can cause problems such as ring sticking if not dealt with correctly. Exposure to elevated temperature could also cause acids to form in the oil, therefore anti-corrosive additives are also added to prevent corrosion of bearings etc [11].

Detergents

The detergent pack is a blend of chemicals that counteract some of the problems faced by the oil detailed above, namely oxidation and acid/deposit build up. The detergent aspect of the additive pack tend to be alkaline metals typically present as hydroxide or carbonate, stabilised in solution lipophilic soap molecules forming micelles [38]. Metal detergents neutralise acidic species, namely sulphur oxides and organic acids. By definition, the detergent properties reduce the formation of deposits (carbon, varnish deposits and lacquers) [67].

Anti-wear Additives - Zinc Dialkyldithiophosphate

Advanced lubricants have an anti-wear additive as part of the oil additive pack. Zinc Dialkyldithiophosphate (ZDDP) is a popular anti-wear additive that has been added to oil since 1941. The mechanism that describes how ZDDP works is as follows: [68]; ZDDP is a hydrocarbon solution that undergoes a thermally activated, catalytic decomposition. The products are volatile and mainly comprise; mercaptides, alkyl sulphides, hydrogen sulphide (H_2S) and olefins. The alkyl sulphates and mercaptides are formed directly and not due to a reaction between the H_2S and olefins. No olefins are produced that are of higher molecular weight than the original alkyl chain on the ZDDP. The other main product is glassy, insoluble and contains zinc, oxygen, phosphorus and some sulphur. The thermal decomposition of ZDDP is acid-catalysed and not accelerated by oxygen. ZDDP's were recognised to be highly effective oxidation inhibitors in engines in the early 1940's. In the 1960's it was found that ZDDP's also decompose peroxyl radicals. This combined effect makes them effective at quenching the peroxide oxidation cycle, which is at the heart of hydrocarbon oxidation chain reaction.

Dispersants

Dispersants are additives that suspend carbonaceous soot particles, inhibit sludge formation and to reduce the formation of deposits on metal surfaces. Typical compositions are ash-less (metal free) polyisobutene succinimide (PIBSA PAM) [67].

2.4.3 Viscosity and the effects of degradation and ageing

Viscosity

Dynamic viscosity is a fluid dynamic term that describes resistance to flow of a fluid. Kinematic viscosity is the dynamic viscosity divided by the fluid density. Oil viscosity is important in the ICE as its the correct viscosity that forms the correct oil film thickness on mechanical moving components to lubricate them without being excessively thick and result in losses from the fluid. The viscosity index (VI) describes the relationship between viscosity and temperature. Oils with high VI change kinematic viscosity less with increasing temperature than low VI oils. Viscosity modifier additives can be used to reduce the influence of temperature on oil viscosity [67].

Total Base and Total Acid Number

Total base number (TBN) is an indicator of the lubricating oils ability to resist degradation from combustion and acid formation. The TBN will be highest when the oil is new and has the greatest ability to neutralise acids and will degrade as the oil is aged. The TBN is therefore an indicator of the alkaline additives in the oil. When designing the lubricant the TBN is targeted depending upon the application e.g gasoline lubricating oil will have a lower TBN when new compared to diesel lubricating oil due to the exposure to soot and sulphur. When the TBN has reached a level that can no longer protect the engine the oil must be changed to prevent chemical attack of the components [69]. Acidification of lubricant oil is an undesirable result of the combustion process and exposure to acid producing components in the fuel. As a lubricant degrades acidic by-products will be formed as the base stock and additives being exposed to air and heat. The total acid number (TAN) is a measure of the amount of acid present in the oil. The TAN should be used in conjunction with the TBN as a means of assessing the ‘health’ of the lubricating oil [69].

Oil Ageing

Oil ageing or evolution, is the natural process of the lubricating oil in the sump becoming 'aged' as the hours or miles increase. However, as the oil ages between oil change periods (services), other factors begin to come into play. The TBN reduces as the detergent is consumed to counteract the acidity of the oil due to combustion, in contrast the TAN increases to reflect the increased acidity. The quality of oil in the engine sump will degrade, due to increasing contaminant concentration in the remaining oil. As not all of the fuel in the engine is burnt or evaporates, certain parts of the fuel will make its way into the oil sump. The fuel components will be those who evaporate above 150°C, as discussed in §2.3.1.

Nitration

The combustion of fuel and air in a ICE produces oxides of nitrogen (NO_x) as a result of the combustion process. When lubricating oil comes into contact with NO_x, nitration of the oil occurs. Nitration is undesirable as it indicates that the oil has be come saturated with soluble or insoluble NO_x compounds. The nitration process forms organic nitrates and nitro compounds in the oil dependant upon whether the oil contacts combustion gasses on the cylinder liner or via blowby gasses in the crankcase. Nitration is separate degradation to the process of oxidation caused by exposure to oxygen [70]. Despite nitration being linked to oil degradation and potential corrosion and wear of engine components, there is new interest in role of nitrogen and nitration based on the work of Splitter *et al* [71]. This will be discussed in detail with respect to the current work in Chapter 4 and Chapter 5.

2.4.4 Links to abnormal combustion and LSPI

In a comprehensive literature review paper Chapman *et al.* [26], summarise the findings of 90 significant papers in the field of LSPI. Figure 2.14 examines key factors highlighted by the body of work in terms of current knowledge and the trends with respect to each factor. However there are still many gaps in the knowledge of this phenomenon leaving open 'technical questions' as yet unanswered.

Of significance are the base compositions of both fuels and oils, similarly the additive types and

Factor	Proposed Future Work and Technical Questions:	
	Confirm Previous Trends That Increased Fuel/Lubricant Derivative Ignition Tendency:	Other Technical Questions
Fuel – base composition	• Aromatic content (volume %) ↑ • Higher boiling fraction components ↑ – *especially problematic were heavy molecular weight aromatics*	• Are all aromatics problematic for abnormal fuel/lubricant derivative ignition?
Fuel – additives	• Phosphorus, Boron, compounds ↓ • *(Lead had no consistent effect, but mostly ↑)*	• Detergent additives in fuel: are type and concentration important to mitigate modern issues?
Oil – base composition	• Higher boiling fraction components (use of Bright Stock/ API Grade 1 as blending component) ↑ • Viscosity Improver ?	• Is base oil composition a factor for modern lubricants? • Do viscosity improvers increase the rate of modern problems?
Oil – additives	• Metallic detergent content (% weight) ↑ -- *impact of varying degrees based on the specific metal; calcium had the strongest impact* • Phosphorus and sulfur content ↓ • Presence of zinc inhibitors ↓ • *(Total sulfated ash content does not correlate)*	• Low ash or ashless additives: is there a solution that works for modern engines? Do ashless additives or detergents "solve this problem"?
Operating Conditions and Hardware	• In general, any factor that promotes combustion (higher temperatures and higher oxygen partial pressures) ↑ • Compression ratio ↑, Intake pressure ↑, Intake temperature ↑, Engine speed ↑ • Oil consumption rate↑ • Soot production (due to specific operating conditions) ↑ • Low Speed operation to generate deposits in the engine, followed by a transient acceleration↑	• What role does fuel injection spray shape, timing and location of spray play? • Can adjusting liner wall temperatures impact initiation mechanisms for modern problems? • Does more carefully controlled piston cooling via modulating piston oil squirter jets at particular engine loads help mitigate modern problems via an impact on deposit formation? • Can piston and ring designs to manage deposits, oil and residual liquid fuel in the crevice reduce modern problems?
Deposit Properties	• Size of particles ↑ • Temperature at which the deposit ignites ↓ • Temperature at which the deposit melts ↑	• Can deposit morphology and/or physical properties be affected in a way to reduce modern problems (if deposits are the root cause)?
Fundamental Root Cause	• Is the attributed cause from the past (deposits) the same issue with current technology?	• Are there other causes than deposits, like oil droplets? • What is the impact of oil consumption rate and oil vapor in the intake air?

Figure 2.14: Possible areas for future examination[26]

concentrations. Some additives have abnormal combustion promoting and others have calming effects. Engine operating condition, injection strategy and certain hardware configurations can influence LSPI tendency (promoting and reducing). The most widely accepted causal mechanisms are based on deposits and/or oil droplets creating hot spots that can lead to LSPI. The fundamental root causes have not yet been conclusively proven. In a similar literature review paper, Wang *et al.* [72] collated the findings of 332 papers in the field of knocking combustion in SI engines. This included the latest understanding of knocking combustion, LSPI and mega-knock and relates this to the key mechanisms and known countermeasures. Tamura *et al.*[33] explored the role of metal oil additives on combustion chamber deposits with respect to LSPI tendency in an air cooled single cylinder engine. This work found that calcium based deposits facilitated knock and auto-ignition, whereas molybdenum did neither. Following deposition of the metallic additives on the combustion chamber surfaces, the metallic atoms remained, but sulphur and phosphorous were depleted. In a similar study, Hayakawa *et al.* [73], investigated the effects of ZnDTP and MoDTC blended into primary reference fuel (PRF50) on abnormal combustion using spark plug washer temperature as an indicator of knock intensity. It was found that spark plug washer temperature increased with higher levels of knock intensity, and neither additive had a promoting effect for abnormal combustion.

The same group at Nihon University, Japan, conducted further experiments with typical metallic oil additives, blended into PRF50 fuel. Miura *et al.*[74], Miyasaka *et al.* [75] and Shimizu *et al.* [76]: found that PRF50 fuel containing 2000 ppm Ca resulted in higher occurrence of abnormal combustion vs. PRF50 without additive. The results also showed that PRF50 fuel containing Na and Mg did not have a promoting effect on abnormal combustion. Lubricating oil and the chemistry of detergent packs have been linked to abnormal combustion by many researchers: [77–81] represent a small selection, chosen due to common findings. Namely, the composition of the oils' additive pack has a confirmed linkage to the LSPI performance of the engine. Calcium, iron and copper are deemed to promote LSPI, whereas magnesium, Zinc (and ZDDP) and molybdenum are moderators or don't take part in LSPI. All have observed a link between calcium treat rate in the detergent as the 'bad actor' and a primary cause of pre-ignition. The causes hypothesised are either; oxidation of the calcium particle once it has been stripped from the surface of the cylinder liner resulting in sufficient heat being released to ignite the premixed charge ahead of the spark; or, some form of catalytic reaction of the calcium in the cylinder leading to a similar mechanism of ignition. Whilst studies such as those conducted by Leach *et al.* [38] conclude a measurable link to calcium concentration and LSPI tendency as shown in Figure 2.15, indicating that the presence of calcium is a prerequisite for LSPI, no explanation as to why calcium has this effect was given.

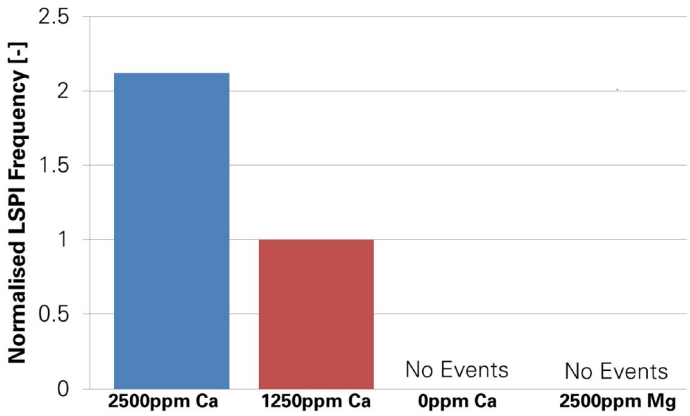

Figure 2.15: Effect of lubricant calcium concentration on LSPI [38]

It is also suggested that an alternative magnesium based or mixed metal detergent, behaves, from an LSPI perspective, in a way similar to a lubricant with no calcium additive. Moreover, that reduction in the calcium treat rate to reduce LSPI must be compensated to maintain the anti-wear and detergent role of the additive pack. Why one metallic additive can be a prerequisite to LSPI and

another appear to have no reactivity or be in fact preventative remains unclear. Fletcher *et al.* [77], completed a more comprehensive study into the effects of different types of metallic detergents in combination and at a range of treat rates. The results with respect to calcium and magnesium effects on LSPI are consistent with the findings of Leach *et al.*. However, no explanation as to the reason 'why' was provided. The 'natural' ageing of oil has also been linked to increased LSPI tendency. Figure 2.16 shows an oil analysis of new and two used oil samples of the same 0W 20 oil formulation [38]. The chart shows key indicators of the condition of the oil when comparing the new oil to the two used samples, which are considered typical of oils within their service interval. The two indicators of viscosity; kinematic viscosity at 100°C and 40°C, show that the aged samples viscosity has reduced, probably as a function of the gasoline dilution which has risen from 0% in the new oil to 2 - 3% in the aged samples. The TBN has reduced in the used samples showing that there has been a level of degradation of the additive pack. The TAN shows that the detergent is working and that the oil doesn't contain levels of acid that would cause problems to the engine as they are lower than that of the new oil. The nitration and oxidation show that there is difference in the way the engine has been run whilst ageing the oils, as the nitration and oxidation in oil A is lower for both parameters compared to oil B.

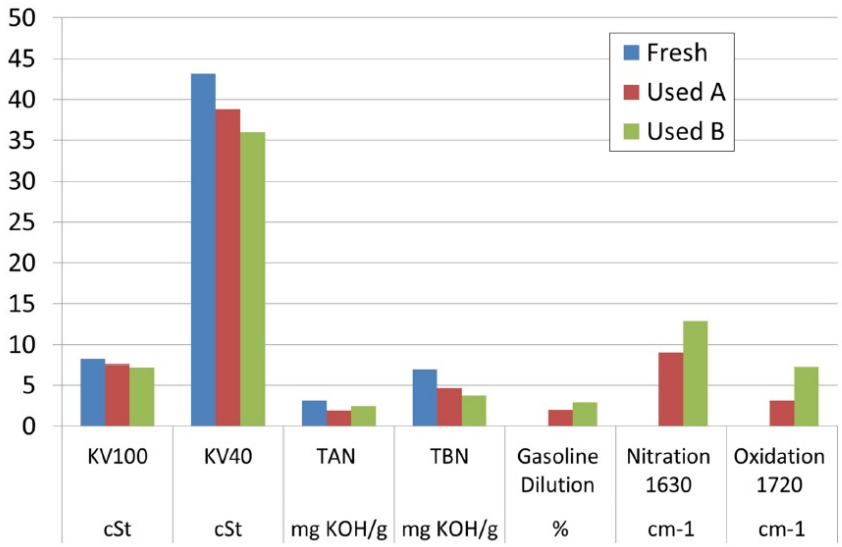

Figure 2.16: Analysis of new vs. used oil (2 used samples) [38]

Of interest is the LSPI behaviour of the used oil samples. Figure 2.17 shows the normalised LSPI frequency of two used oil samples compared to the same new oil sample in the same engine.
The LSPI tendency is approximately double for used oil compared to new [38]. This is interesting

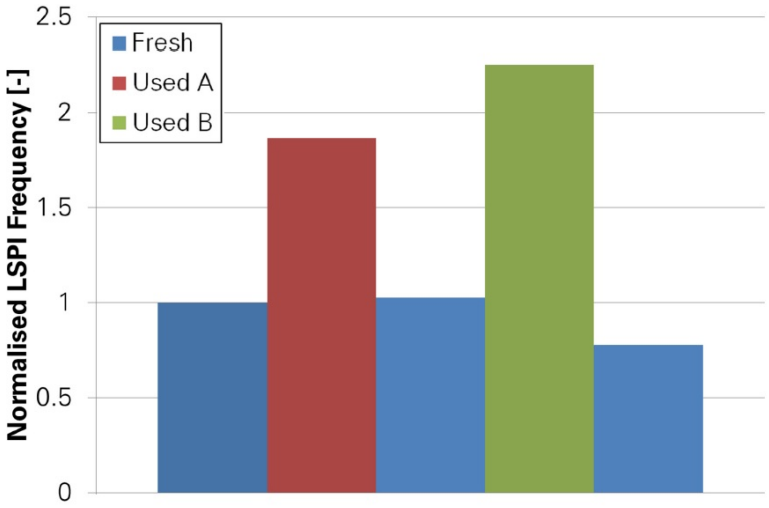

Figure 2.17: LSPI tendency of new vs. used oil (2 samples used) [38]

as most of the published literature studies have used new oil and focussed on the detergent treat rate rather than the condition of the oil in the actual operating condition of the engine in service. The fact that the oil now has an interaction with the fuel, in particular the likelihood that these fuel components are of the 'heavy back end', is not interrogated by Leach *et al.* [38] or [77] and therefore remains a topic of interest for this current work. Finally, with respect to the additive pack, previous studies have indicated a potential positive impact of ZDDP on LSPI. Fletcher *et al.* [77] tested oils with ZDDP and increased levels of phosphorus and zinc. By a process of elimination they were able to show that a statistically significant reduction in LSPI occurred with phosphorus, whereas the oils with elevated zinc showed a minor reduction. However, practically this is not a solution to LSPI reduction, as phosphorus levels are limited to avoid damage to three-way catalysts used in engine after-treatment systems. There was no suggestions in literature of a link between dispersants and LSPI.

2.5 Conclusions

In conclusion it can be seen that: a review of the key indicators and properties of base fuel and oil, and additives, was undertaken with respect to their potential affects on LSPI. A review of the underlying theoretical mechanisms relating to knock, pre-ignition, mega-knock and developing detonation was undertaken. Comprehensive review papers were used to direct the Author to a 'state of the art' understanding of LSPI and identification of the gaps and areas for further enquiry. Looking

specifically at the additive pack in the oil (and in some fuel tests), calcium has been unequivocally confirmed as a 'bad actor' for abnormal combustion. Magnesium detergent appears to be either a moderator or takes no part in LSPI. ZDDP has a LSPI reducing tendency, confirmed in the work of multiple researchers. To date, no explanation as why magnesium is good and calcium is bad, with respect to LSPI has been presented in the, now significant, body of research in this field of combustion.

Chapter 3

Research Topics

3.1 Introduction

The previous chapter provides the reader with the necessary background to the research that will be presented in the body of this work. The different types of abnormal combustion in gasoline engines, their causes (as far as is known in the literature), and their consequences are described, and the links between fuel and lubricant composition and abnormal combustion, particularly LSPI, were reviewed. This review identified the key gaps in the knowledge that will be examined further in this thesis.

3.1.1 How does a calcium based detergent pack promote LSPI?

Although a clear link between the use of calcium in a lubricant's detergent pack and LSPI has been demonstrated by numerous researchers and research groups, the precise mechanism by which calcium leads to increased LSPI tendency remains unknown. Research published by Moriyoshi *et al.* [82] [83] (Chiba University, Japan), hypothesises that the cause relates to a carbonation reaction of the calcium detergent in the oil with carbon dioxide (CO_2) leading to an exothermic reaction of sufficient energy as to act as an ignition source for the surrounding charge.

The 'Chiba' hypothesis

As stated in §2.4.2, lubricating oils require detergents to maintain the oil quality, resist deposit formation and the acidification that results from exposure to combustion. The detergents tend to be

alkaline metals typically present as a hydroxide, carbonate or sulphonate. The detergent is usually in the form of a colloid with the base oil to form a lubricant suitable for use in the ICE. The detergent in the lubricating oil of interest here is calcium carbonate ($CaCO_3$). The LSPI mechanism proposed by Moriyoshi *et al.* [83] is as follows;

- Oil in the top land crevice of the piston containing calcium carbonate $CaCO_3$ detergent and possibly fuel, is released into the combustion chamber as a droplet or droplets from the oil film build up in the top land crevice being released by the inertia of the piston.
- This mixture is heated to in excess of 900 K during the combustion and exhaust process and thermally decomposes into calcium oxide (CaO) and carbon dioxide (CO_2), but remains in the combustion chamber.
- During the next compression stroke this droplet is heated to in excess of 1000 K in the presence of CO_2.
- The exothermic reaction resulting from the carbonation of CaO and CO_2 to form $CaCO_3$ has sufficient energy to ignite the premixed charge leading to LSPI.
- The probability of all of these phenomena occurring together in this way is rare, thus the behaviour of LSPI can be described as stochastic.

The current work will examine the Chiba hypothesis in detail, initially focusing on the replication of the proposed chemical mechanism under carefully controlled, i.e. non-engine, conditions of temperature, pressure and gas composition. Equation 3.1 [84] describes the formation of carbon dioxide by oxidation of carbon, naturally present in the hydrocarbon fuel, with oxygen. The characters in brackets refer to the state of each chemical element, solid (s), liquid (l) and gas (g) respectively. The CO_2 is the product of complete combustion and therefore formed during each combustion cycle in an ICE. Some quantity of CO_2 will also be present in the trapped cylinder gases between combustion strokes. The basic oxidation reaction is as follows:

$$C_{(l)} + O_{2(g)} \longrightarrow CO_{2(g)} \tag{3.1}$$

Equation 3.2 shows the carbonation of CaO detergent, when the oil is exposed to CO_2 in the cylinder

to form $CaCO_3$. The change in enthalpy (H) is -178 kJ/mol, at the boundary conditions of 298 K and CO_2 partial pressure of 1 bar [84]. The negative sign indicates that the reaction is exothermic, where heat is released during the chemical reaction. This process is reversible through calcination, Equation 3.3.

$$CaO_{(s)} + CO_{2(g)} \longrightarrow CaCO_{3(s)} \qquad \Delta H_{298K} = \text{-178 kJ/mol} \tag{3.2}$$

$$CaCO_{3(s)} \longrightarrow CaO_{(s)} + CO_{2_{(g)}} \qquad \Delta H_{298K} = 178 \text{ kJ/mol} \tag{3.3}$$

It has been noted in the literature that, in direct contrast to calcium containing detergent packs, magnesium detergent does not promote LSPI [38, 77]. The Chiba hypothesis does not directly address this issue. The general formation equation and enthalpy can be determined for magnesium carbonate [85], Equation (3.4):

$$MgO_{(s)} + CO_{2(g)} \longrightarrow MgCO_{3(s)} \qquad \Delta H_{298K} = \text{-118 kJ/mol} \tag{3.4}$$

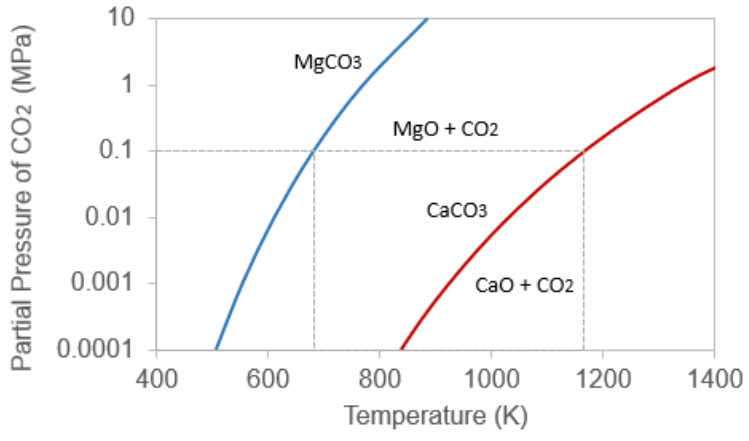

Figure 3.1: Thermodynamic equilibrium plots for calcium oxide (red) and magnesium oxide (blue).

As with the calcium carbonation reaction it too is exothermic, however the level of heat released to form magnesium carbonate is 60 kJ/mol lower. This process is also reversible, again through

calcination. Figure 3.1 compares the theoretical thermodynamic equilibrium of the products and reactants of the chemicals of interest. The solid blue and red lines indicate the equilibrium conditions where all three chemical elements can exist. In both cases (MgO and CaO), if the temperature and partial pressure of CO_2 are to the left hand side of the equilibrium line, then this will favour the carbonation reaction and $CaCO_3$ or $MgCO_3$ will be created respectively. Similarly, if the temperature and partial pressure of CO_2 are to the right hand side of the equilibrium line this will favour the reactants and the carbonates will calcinate into the metal oxide and CO_2. The partial pressure of a gas is analogous to its concentration (according to Dalton's law, the partial pressure of a gas is the sum of the partial pressures of the individual gasses in the mixture). It can be seen from Figure 3.1, that the carbonation of MgO occurs at conditions of temperature and pressure within the combustion chamber which are potentially not high enough for inducing LSPI. The heat released during carbonation of MgO is therefore potentially insufficient for inducing LSPI. Chapter 4 explores the Chiba hypothesis and shock tube experiments aimed at investigating this further via shock heating of metal oxide powers. In order to evaluate the Chiba hypothesis CaO and MgO were shock-heated in the Oxford CDST, in a range of gasses (carbon dioxide, nitrogen and argon) to capture any light emitted from these metal oxide/gas combinations at a range of temperatures and pressures

3.1.2 Why does a used lubricant tend to promote LSPI?

As noted in §2.4.4, it has been observed in the literature that used oil has a significantly higher propensity towards LSPI than new oil under the same operating conditions [38]. However, the root cause of the increased LSPI tendency has not been demonstrated. A particular challenge lays in determining the chemical composition and physical properties of the used oil found within the combustion chamber. Traditionally, the analysis of used oil properties is performed on samples collected from engine's sump oil. It is reasonable to expect that the composition and physical properties of the lubricant oil found in-cylinder will differ from the sump oil due to its exposure to high pressures and temperatures and the products of combustion. Previous studies that successfully collected piston crevice oil samples were mostly focussed on tribology or rheology and not on the local chemical mechanisms relating to LSPI. Chapter 5 will present the results of a detailed investigation into the chemical composition of aged (approximately 50 hours of operation) lubricant oil collected from the

piston top land crevice (TLC) volume on a single cylinder research engine. TLC samples from both Ca and Mg detergent pack lubricants were collected and analysed for comparison with the known composition of the new oil and used oil samples collected from the engine sump.

3.1.3 What are the effects of MMT on LSPI?

Abnormal combustion linked to metal oxide oil detergents has been widely investigated. Thus, the body of research was mainly focussed on the oil, with some limited work adding oil additives to fuel, as discussed in §2.4.4. The objective of this experimental campaign was to characterise the behaviour of fuels containing varying quantities of alkaline metal octane booster (MMT), whilst allowing the RON of the fuel to vary naturally with MMT concentration. Allowing the effect of MMT to be quantified and sampling of the deposit that results from burning fuel containing MMT to be collected from a fuel injector tip. The objective of this work is to answer the question "Is the effect on LSPI of metal oxides in the fuel the same as metal oxide detergents in the oil?". Chapter 6 will present the results of a multi-cylinder engine testing using fuel blends known to promote LSPI, with the addition of MMT in quantities determined via in market fuel sampling. A dedicated LSPI test was used to characterise the LSPI behaviour. Samples of the in-cylinder deposits were analysed to understand the mechanisms with respect to LSPI

3.2 Conclusions

This chapter has laid out the three linked research studies that aim to investigate the fundamentals of LSPI via: shock heating metallic oxide powders, dynamic oil sampling of the TLC and multi-cylinder testing of LSPI prone fuels containing MMT. Significant advanced analysis techniques will be applied to investigate the various samples, with the objective of explaining the fundamentals. The following chapter 4 begins the current work with fundamental shock tube experiments conduced using the University of Oxford cold driven shock tube.

Chapter 4

Fundamental Investigation into Oil Detergent as the Cause of LSPI

4.1 Introduction

As described in Chapter 3, the so-called 'Chiba hypothesis' — whereby the carbonation reaction of calcium oxide is proposed to be a fundamental cause of LSPI — is unproven. Moriyoshi and co-workers have shown image sequences that point to a visible light discharge from particles in the combustion chamber during an LSPI event, however the precise mechanism by which this occurs and the key reactions leading to phenomenon have not been demonstrated – not least due to the complex turbulent combustion environment of an ICE. The objective of the experimental work described in this chapter was then to move the investigation of the Chiba hypothesis away from the ICE to a more closely controlled environment where it could be investigated at a more fundamental level. This chapter will present the results of a fundamental study on the behaviour of metallic oil detergent derivatives, CaO and MgO, under engine-like conditions of temperature and pressure in a quiescent environment provided by a reflected shock facility.

Note on authorship and collaborative working

The experimental work described in this chapter is a result of the collaborative efforts of the author, Dr Rowland Penty-Gearats, Dr Laurent Le Page, Mr Christopher Wheeler, and Dr Luke Doherty. Due to the high pressures and large volumes of gases involved with the operation of the

shock-tube facility it is considered too dangerous for DPhil students to operate alone. The author contributed significantly to the experimental set-up and participated in a substantial number of 'fired shots' during all three campaigns, and was solely responsible for the definition of the test matrix, cleaning methodology, data analysis and interpretation of the results presented in this chapter.

4.2 The Oxford Cold Driven Shock Tube (CDST)

The University of Oxford CDST is a bespoke, reflected shock, facility designed for characterisation of fuel sprays and the investigation of chemical kinetics under controlled engine-representative condition of temperature and pressure in a quiescent charge, Figure 4.1 [86]. The basic principle of operation, described in detail in §4.2.1 is to generate a reflected shock in the driven section of the tube using a relatively low cost, unheated (hence cold driven) driver gas, typically compressed air. The final temperature and pressure properties of the gas in the working section of the CDST are a function of the initial gas composition and the experimental setup. Table 4.1 and Figure 4.2 detail the specification of the CDST, describing both its geometric features and design boundary conditions. The configuration used in this research was the area change mode, whereby the diameter of the driver section is larger than the driven section.

The CDST has optical access via quartz windows located at the end farthest away from the driver as shown in Figure 4.2. There are horizontal windows on either side and vertical window on the top only. For this experiment the optical section was accessed from the LH side when viewed from the driven end of the CDST. At the end of the driven section there was an injector mounting point or end cap. This was modified to hold a knife blade to carry the test powders, more detail is contained in §4.3.1 and in Figure 4.3. The CDST can be operated in either a single or double diaphragm mode. In single diaphragm mode, the driver pressure is gradually increased until the diaphragm ruptures.

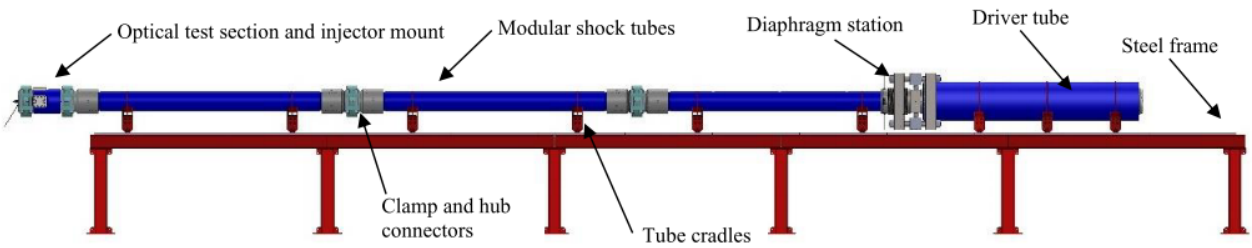

Figure 4.1: Cold Driven Shock Tube (CDST) [86]

Table 4.1: Oxford Cold Driven Shock Tube Specification [86]

	Value	Unit
Driver section internal diameter	250	mm
Driven section internal diameter	100	mm
Overall length (area change mode)	10.9	m
Nominal design test condition:	60	bar
	900	K
	3	ms
Maximum pressure capability	150	bar
Maximum temperature capability	1500	K

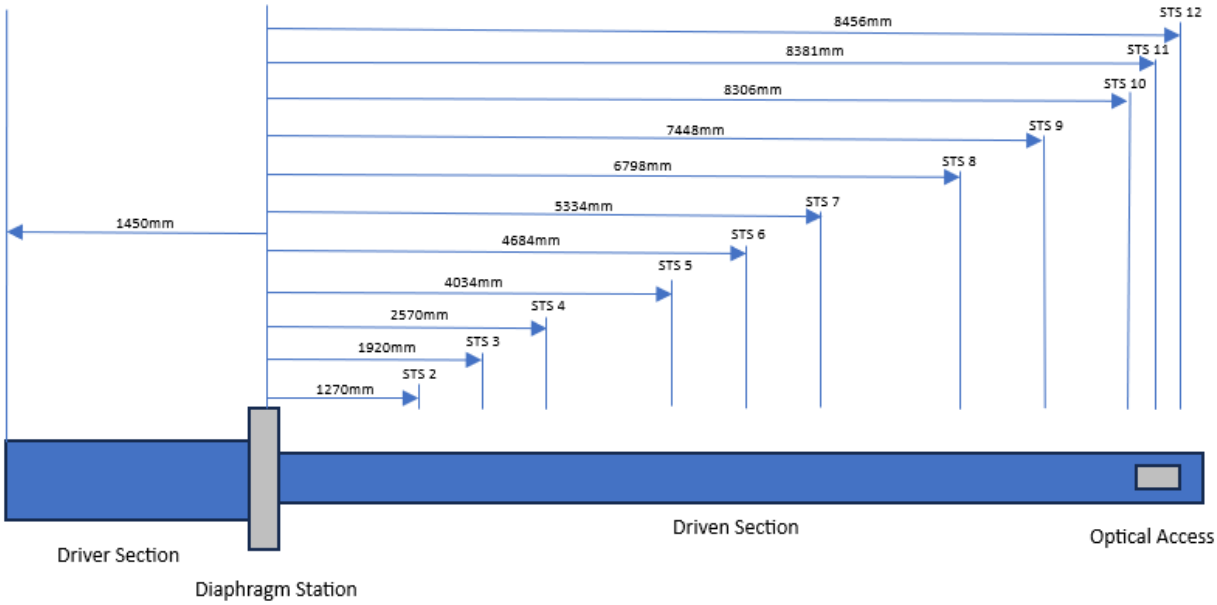

Figure 4.2: CDST Schematic. STS signifies 'shock tube station', the numbered locations of each pressure sensor point. The pressure signal from STS 9 was used to enact a TTL trigger for connected devices each time a shot was fired.

Although this is a simple arrangement, which is adequate for some purposes, it does not provide a sufficiently high level of control over the shock triggering, final test conditions or repeatability. Minor variations in the diaphragm material or its machining can significantly affect its rupture behaviour and thereby introduce substantial variability in the subsequent shock strength and speed. In double diaphragm mode, the use of two diaphragms with an intermediate volume filled to an

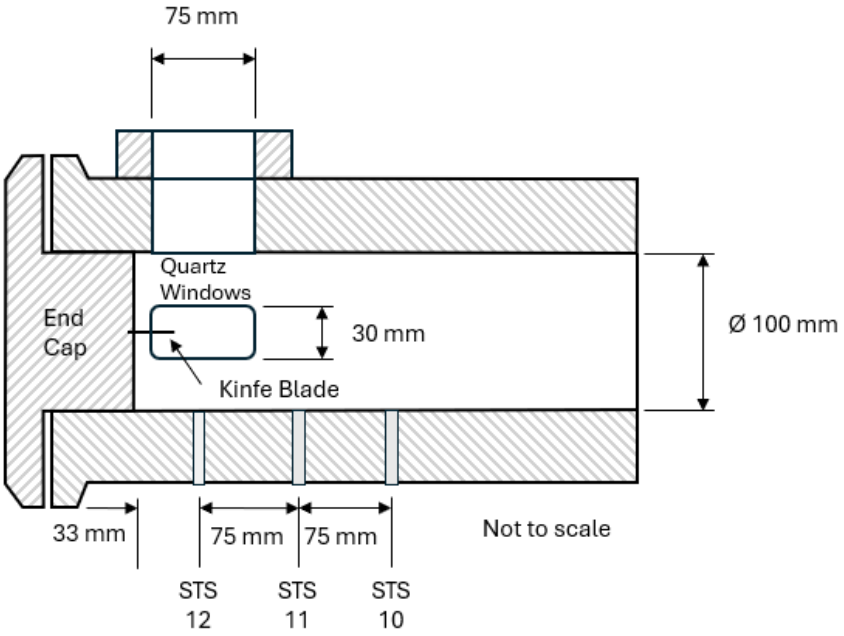

Figure 4.3: CDST detailed schematic of the optical section.

intermediate pressure, allows both the driven and driver sections to be filled to the target pressure. A vacuum pump is then used to rapidly evacuate the space between the diaphragms causing the first diaphragm to rupture, which in-turn causes the second diaphragm to rupture. The result is a more readily repeatable incident shock wave in the driven section, as the driver pressure is fixed rather than a variable as is the case of single diaphragm mode. Accurate pressure measurement is vital to calculate the experimental conditions and determine the shock speed. Table 4.2 details the type, location and description of each sensor. The sensors used to fill the tunnel with gasses were absolute sensors, the STS sensors were relative. The sensors were calibrated using a dead weight tester prior to fitment and were checked and recalibrated in accordance with the schedule defined by Oxford Thermal Institute (OTI).

4.2.1 Principles of operation

The CDST is a ‘reflected’ shock facility, which utilises a high pressure gas in the driver section, to shock-heat the gas in the driven section to a ‘design’ temperature and pressure ’condition’. The numbered states of the conditions described in Figure 4.4 are explained as follows: (1) is the initial state of the driven gas, based on the desired boundary conditions. State (4) describes the initial condition of the driver gas at the start of the experiment. As stated in §4.2, the gasses are separated

Table 4.2: CDST Instrumentation. Pressure sensor type, location and description.

Sensor Name	Unit	Brand	Model	Serial Number	Comment
K1	Pa	Kulite	XTL-190LM-140-BARA	8226-12-501	Driver reservoir
K2	Pa	Kulite	XTL-190LM-140-BARA	8226-12-500	Driven fill pressure
STS07	Pa	PCB	113B26	LW45516	Shock pressure
STS09	Pa	PCB	113B21	LW54072	Shock pressure
STS10	Pa	PCB	113B21	LW54094	Shock pressure
STS11	Pa	PCB	113B21	LW54096	Shock pressure
STS12	Pa	PCB	113B21	LW54095	Shock pressure

by either a single or double diaphragm depending upon the experiment. (3) is the result of the unsteady expansion of gas following the rupture of the diaphragm which causes gas to flow into the driven section. State (2) is the result of the 'normal' shock-wave leaving the driver and following the gas flowing into the driven section, which compresses the upstream gas. This shock-wave is called the 'incident shock'. Once the shock wave reaches the end of the driven section it is reflected. As the reflected shock moves in the direction of the driver, the gas behind the shock wave is brought to rest and further compressed, state (5). It is state (5) that is the desired test condition, which is typically designed to last for 3 ms.

4.2.2 Shock speed, gas temperature and pressure

The following section details the governing principles and equations for shock tube experimentation. These equations were used to calculate the shock speed and the temperature and pressure conditions in the CDST. The fundamentals that describe the working principle of the shock tube were taken from Anderson [87]. The 's' term in each equation refers to the 'state' and number relates to the properties of the gasses during the experiment. The initial states, prior to the shock, are shown in Figure 4.5 and are referenced to the laboratory i.e. standing at the driver and looking towards the driven or optical access end of the CDST. This is significant as later it was necessary to

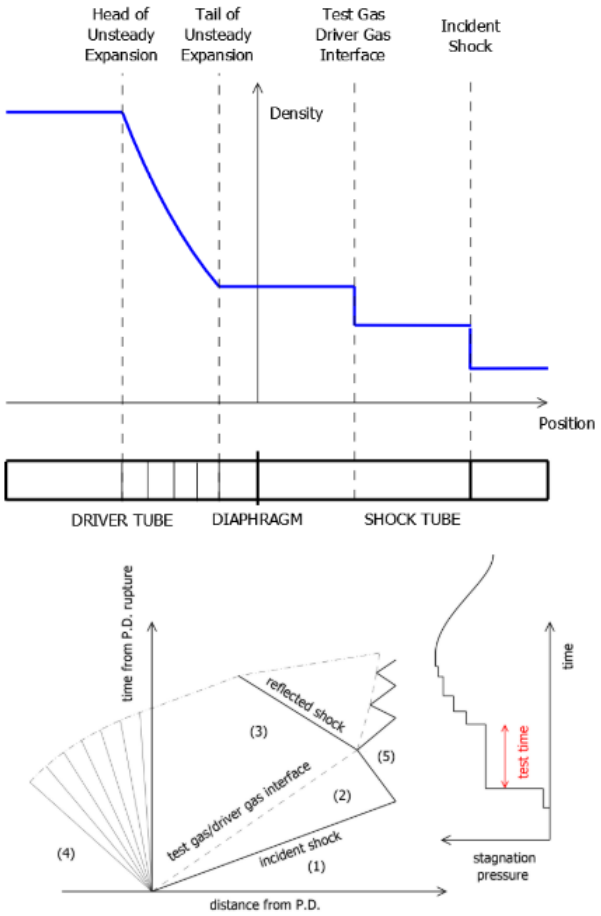

Figure 4.4: Top: Density distribution in the specific regions of the CDST following a burst diaphragm. Bottom: *x-t* schematic diagram showing the pressures in the CDST, PD refers to the primary diaphragm. The numbered regions are described in the text. [86]

switch to a shock based reference to calculate the gas properties moving in and out of the shock.

The driver gas was compressed air for all but the argon gas tests in the driven section, where a mixture of argon and nitrogen was used as the driver gas. For each test the data was recorded at a frequency of 2 MHz using a National Instruments data acquisition system, and controlled by the LabVIEW programming software T4NIDAQ. These data was subsequently post-processed using MATLAB script containing Equations (4.1 - 4.18) to calculate the average shock speed the gas properties for each gas state.

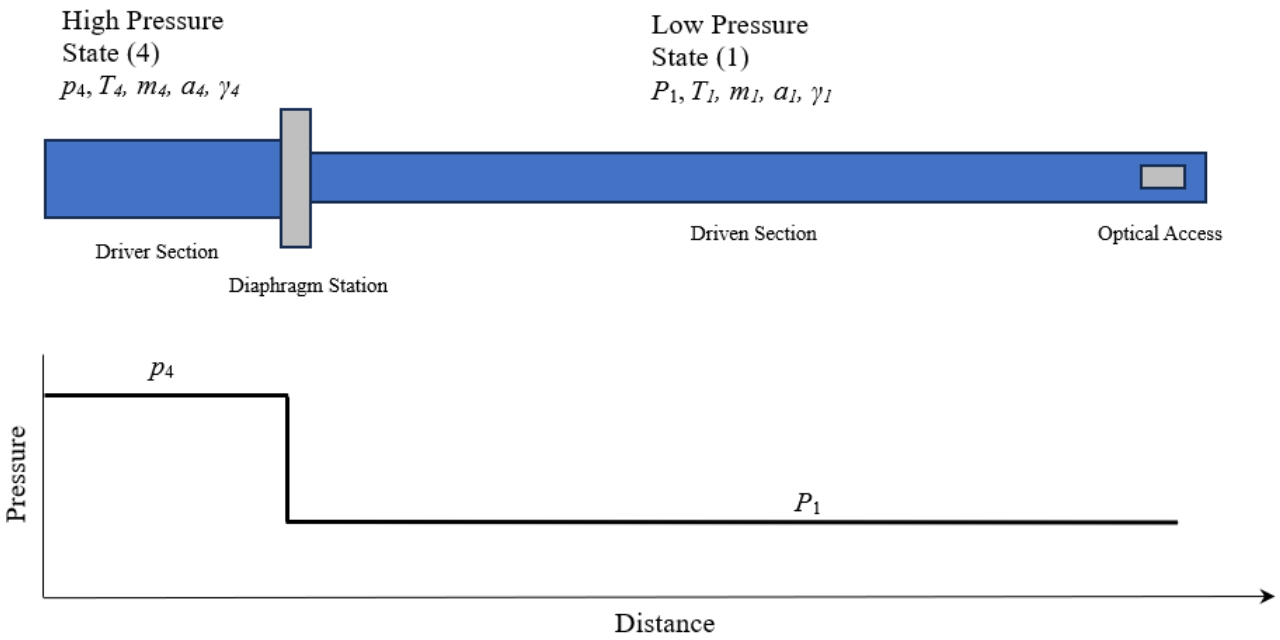

Figure 4.5: CDST Initial conditions, adapted from [87]

The first step calculates the initial gas properties for s(1) and s(4):

s(1).T = the initial temperature of driven gas, 23°, 296K.

s(1).p = The initial pressure of the driven gas measured using a dedicated pressure sensor, in Pa.

s(1).γ = Ratio of specific heats for the driven gas.

s(1).R = driven gas constant, CO_2 = 189 J/kg K, N_2 = 297 J/kg K.

s(4).T = the initial temperature of driver gas, 23°, 296K.

s(4).p = The initial pressure of the driver gas measured using a dedicated pressure sensor, in Pa.

s(4).γ = Ratio of specific heats for the driver gas.

s(1).R = driver gas constant, Air = 287 J/kg K.

The physical dimensions of the shock tube:

L = length of the driven section (8.456m), L1 = Length of the driver section (1.45m).

The differential pressure across the diaphragm:

$$dP = s(4).p - s(1).p \tag{4.1}$$

The density of the gas ρ was calculated as follows:

$$s(1).\rho = \frac{s(1).p}{s(1).R\, s(1).T} \tag{4.2}$$

Equation 4.2 was also used to calculate s(4).ρ, substituting for s(4).; T, p and R.

The speed of sound was calculated as follows:

$$s(1).a = \sqrt{s(1).\gamma\, s(1).R\, s(1).T} \tag{4.3}$$

Equation 4.3 was also used to calculate s(4).a, substituting s(4).; γ, p and R.

s(1).u = initial velocity of the driver gas, which is 0 as the gas is initially at rest.

s(4).u = initial velocity of the driven gas, which is 0 as the gas is initially at rest.

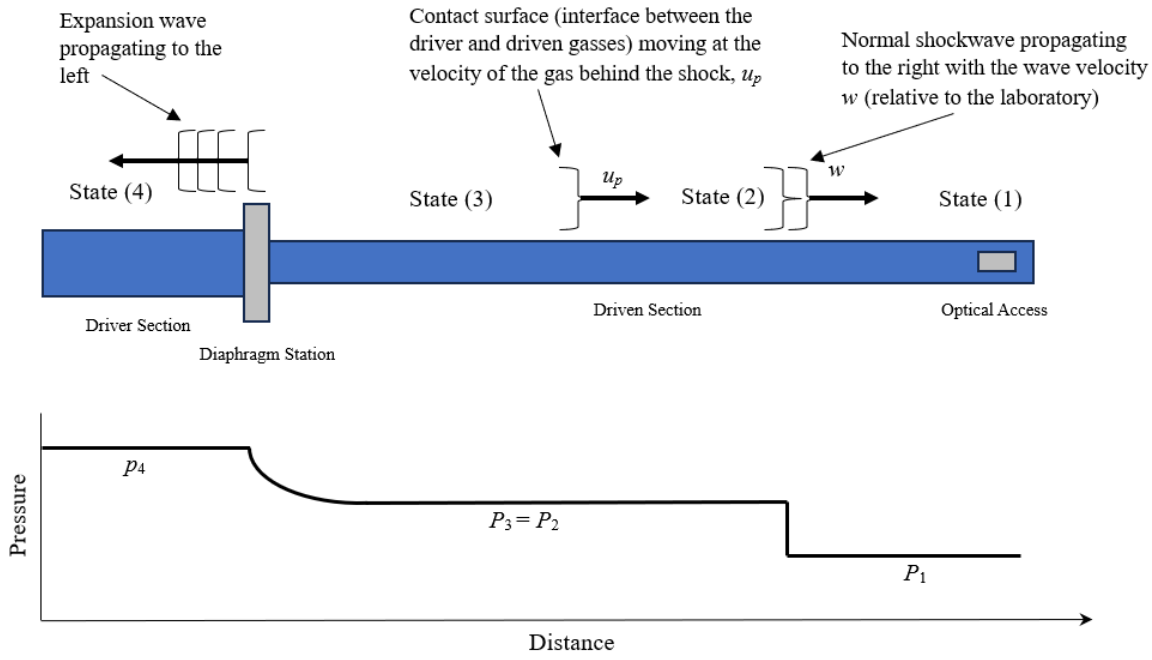

Figure 4.6: CDST Incident Shock Wave, adapted from [87]

When the diaphragm or diaphragms rupture, a shock wave propagates along the driven section of the CDST. Figure 4.6 shows this diagrammatically and introduces two new 'states' which describe the properties of the driver gas (state 3) and driven gas (state 2) with the contact surface in-between. The incident shock wave develops upstream in the driver gas.

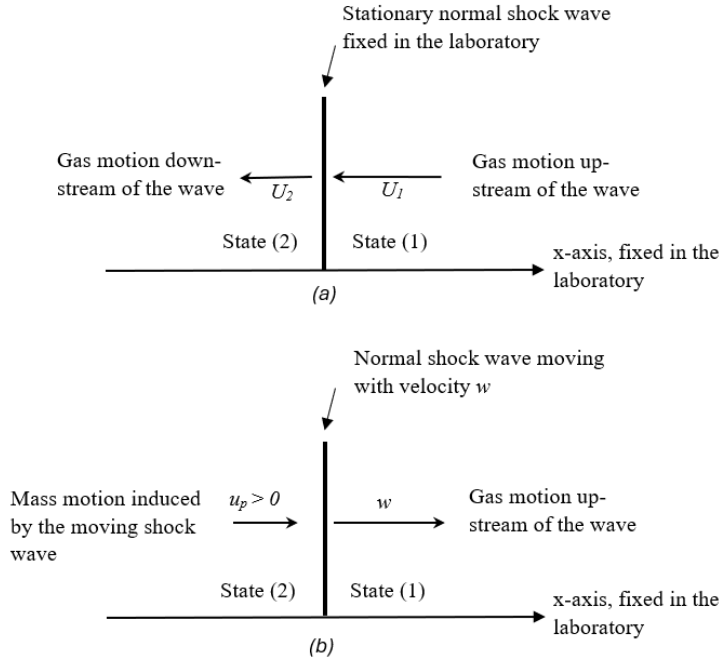

Figure 4.7: Referencing; fixed vs. moving shock wave, adapted from [87]

Next it was necessary to switch to shock based frame of reference to calculate Mach number. Consider $u_s(1)$, the velocity of the gas *ahead* of the shock wave, relative the wave. Also u_a, which was the velocity of the gas *behind* the wave, relative to the wave. Where $u_s(1) = u_a$, for reference purposes 'state a'. The Mach number for 'state a' M_a was calculated using Equation (4.4).

$$M_a = \frac{u_s(1)}{s(1).a} \tag{4.4}$$

State 'b' describes the properties of the gas behind the shock, relative to the shock, where (4.5);

$$u_b = u_s(1) - s(2).u \tag{4.5}$$

The velocity of 'state b' can also be calculated using Equation (4.6) ;

$$u_b = M_b\, s(2).a \tag{4.6}$$

M_b is determined by Equation (4.7);

$$M_b = \frac{\left(\frac{2}{(\gamma-1)} + M_a^2\right)}{\left(\frac{(2\gamma)}{(\gamma-1)} \times M_a^2 - 1\right)} \tag{4.7}$$

It is known that; p_a = s(1).a, T_a = s(1).T, ρ_a = s(1).ρ, γ_a = s(1).γ. Therefore, knowing p_a, p_b can be calculated using (4.8);

$$p_b = p_a(2\,\gamma)M_a^2 - \frac{(\gamma-1)}{(\gamma+1)} \tag{4.8}$$

Similarly knowing T_a, T_b can be calculated, Equation (4.9);

$$T_b = T_a\left(\frac{1+(\gamma-1)}{2\,M_a^2}\right)\frac{\left(\frac{2\,\gamma}{(\gamma-1)}M_a^2 - 1\right)}{\left(\frac{(\gamma+1)^2}{2\,(\gamma-1)\,M_a^2}\right)} \tag{4.9}$$

Finally ρ_b can be calculated using, Equation (4.10)

$$\rho_b = \rho_a\frac{(\gamma+1)\,M_a^2}{((\gamma-1)\,M_a^2+2)} \tag{4.10}$$

It was then necessary to return to the lab based frame of reference; s(2).γ = s(1).γ, s(2).R = s(1).R, the speed of sound and velocity of state (2) are obtained from Equation (4.11);

$$s(2).a = \sqrt{s(2).\gamma\,s(2).T\,s(2).R} \tag{4.11}$$

and Equation (4.12);

$$s(2).u = u_s 1 - u_b \tag{4.12}$$

The pressure, velocity, gamma and gas constants of state 2 and 3 are the same, hence: s(3).p = s(2).p, s(3).u = s(2).u, s(3).γ = s(2).γ and s(3).R = s(2).R. Finally, the most significant aspect of this experimental rig was the reflected shock. It's this, coupled with the properties of the gas in the incident shock that generates the test condition. To calculate the properties of the reflected shock its was again necessary to move to a shock based frame of reference.

The Mach number of the shock is calculated using Equation (4.13).

$$M_s = \frac{u_s 1}{s(1).a} \tag{4.13}$$

And the Mach number of the reflected shock, using Equation (4.14)

$$M_r = -\left(\frac{M_s}{M_s^2 - 1}\right)^{-1} . \sqrt{1 + 2.(s(2).\gamma - 1).(M_s^2 - 1).(s(2).\gamma + 1)^{-2}} \tag{4.14}$$

The pressure, temperature and rho of state 5 and 2 are the same, hence: s(5).p = s(2).p, s(5).T = s(2).T and s(5).ρ = s(2).ρ. M_b was calculated using Equation (4.7), M_r from (4.14) incorporating s(2).γ. It was then necessary to return back to the lab based from of reference to calculate u_a using (4.15) as follows:

$$u_a = s2.a\, M_r \tag{4.15}$$

And finally the reflected shock absolute velocity s(5).a;

$$s(5).a = \sqrt{s(5)\gamma\, s(5).T\, s(5).R} \tag{4.16}$$

$$u_b = M_b\, s(5).a \tag{4.17}$$

$$u_r = u_b \tag{4.18}$$

The gas is stagnant after the reflected shock therefore s(5).u = 0.

4.3 Experimental methodology, set-up, and test plan

The primary objective of the experimental campaign presented in this chapter was to examine the so-called 'Chiba hypothesis' [82] [83] in which the exothermic recombination of the thermally decomposed calcium detergent in the oil with carbon dioxide is suggested as a trigger for LSPI at a fundamental level — see §3.1.1 for details of the proposed reaction mechanism. The current work extends the experimental study to include magnesium detergent as it is unclear from the literature as to why magnesium detergent packs do not promote LSPI in the same way as calcium based detergents. As a starting point for the current work, it was assumed that the first steps of Moriyoshi's proposed mechanism, the release of carbonate containing particles into the combustion chamber and their subsequent thermal decomposition into their respective metal oxides and carbon dioxide had occurred. A series of fundamental shock-tube experiments were then designed and performed in which quantities of the metal oxides CaO and MgO (in powder form) were exposed to elevated temperatures and pressures in the presence of CO_2, N_2, and argon (Ar) bath gases and their visible light emissions observed.

4.3.1 Powder delivery

Powder delivery was undertaken following the work of Bazyn *et al.* [88], who used a simple knife-blade arrangement as a means of dispersing aluminium and nanocomposite thermite powders in a reflected shock tube in order to observe their combustion reactions (see Figure 4.8). A plug was manufactured that fitted the optical section of the Oxford CDST, sealed via an 'O-ring', and containing a knife blade secured in place with a grub screw. Figure 4.9 illustrates the finished component and its installed position in the end of the CDST.

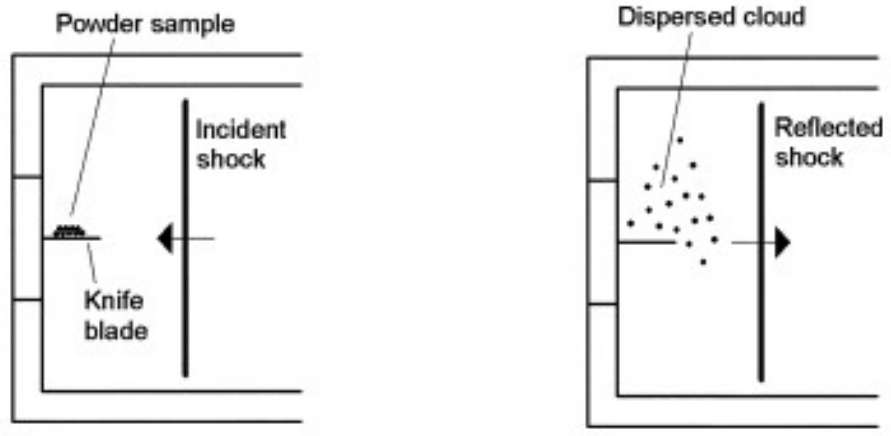

(a) Powder sample and incident shock (b) Dispersed powder and reflected Shock

Figure 4.8: Knife blade method for testing powder in a CDST - modified from [88]

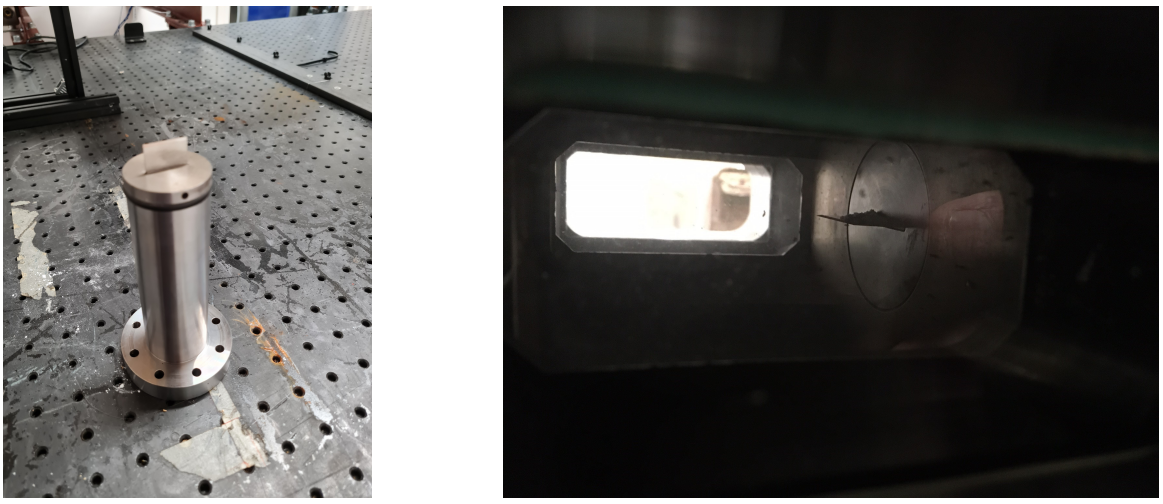

(a) CDST Sealing Plug and knife blade (b) Knife blade – installed position in the end wall of the CDST

Figure 4.9: Knife blade design and installation within the optical section of the CDST

4.3.2 Data acquisition

The triggering and data logging of the CDST was carried out using a National Instruments T4NIDAQ Data Acquisition System or DAQ. The logging system was configured as follows: Pre-trigger of 25 milliseconds (ms) and post-trigger of 150 ms, the logging rate in between triggers was in 0.5 micro second (μs) steps. Details of the connected channels and pressure sensor type and location can be found in §4.2.

4.3.3 Imaging system(s)

The dispersed powder was monitored for visible light emission through the quartz-windows of the CDST's optical test section using high-speed naturally backlit photography via a high-speed camera system, as per Figure 4.10. A photodiode positioned as shown in Figure 4.10, was also included to detect very low level light or light emissions outside the visible spectrum. The full test campaign, detailed in Appendix A, was divided into three discrete campaigns carried out over a period of 1 year 7 months. The imaging system used for the first campaign was a Photron mini UX100 and a Nikon AF (auto focus) NIKKOR lens with a 50 mm focal length, f/1.8 minimum aperture and 46°field of view. The settings of the camera and lens are important as they determine the exposure. The shutter speed is how fast the lens shutter opens and closes, the aperture is what varied the amount of light into the lens and the ISO is the cameras sensitivity to light. The frame rate was 10,000 frames per second, and the resolution of captured image was 1280 x 480 pixels. Campaign two and three also used a different model high speed camera and lens; Photron Mini AX200 and a Tamron ultrasonic silent drive. For campaigns 2 and 3 the camera and lens set up was the same as campaign 1, shutter speed 10,000 frames per second, however the captured image resolution was slightly different, 1024 x 672 pixels, full details are provided in Table 4.3. The camera was set in a continuous buffering mode prior to each shot and subsequently triggered, through the DAQ, by the incident shock reaching shock tube station 9 (STS 9). The resultant image files were analysed using bespoke Photron Fast-camera Viewer PFV4(x64) software provided by the camera manufacturer. Each image file was centred around the trigger point, and can be viewed retrospectively at different frame rates. The software also had the ability to export each frame as an individual photo image, examples of which will be shown in the results section.

Table 4.3: Optical Systems

Campaign(s)	1	2&3
Camera	Photron FASTCAM Mini UX100	Photron FASTCAM Mini AX200
Sensor	1280 x 480	1024 x 672
Type	CMOS	CMOS
Pixel (μm)	10 x 10	20 x20
Range (ADC)	12-bit	12-bit
Speed (fps)	10,000	10,000
Lens	NIKKOR	Tamron

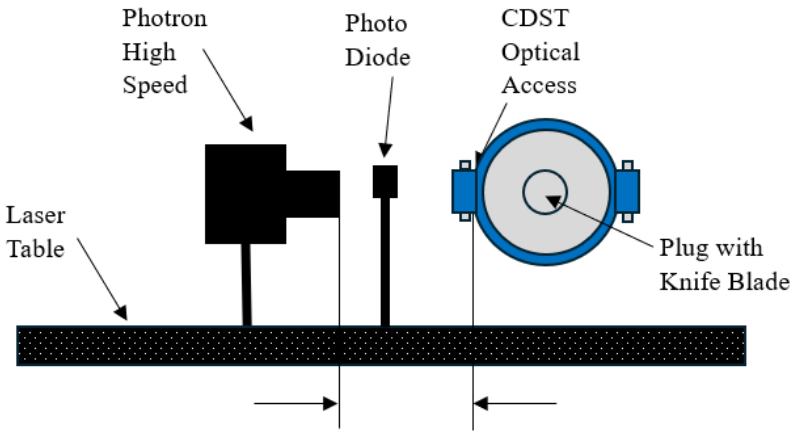

Figure 4.10: Schematic of high speed camera set-up and photodiode. Distance between the camera and quartz window: campaign 1, 300mm, campaigns 2 and 3, 100mm.

4.3.4 CDST test procedure

Prior to starting the experimental campaign, the initial boundary conditions – driver and driven gas compositions and their respective initial pressures – required to produce the target conditions of temperature and pressure were calculated using L1d4 [89]. L1d4 is an open-source quasi-one-dimensional gas dynamics code developed by the University of Queensland for the simulation of shock-tube or expansion-tube facilities [90] [91]. The CDST L1d4 model was created and maintained by the OTI team, the driver and driven pressure and gas composition condition for each test was provided by the same team.

Having identified the desired boundary conditions, the standard method for operating the CDST was as follows:

- The 'plug' containing the knife edge was removed and the CDST was rigorously cleaned using a foam 'cleaning pig' and alcohol spray
- New diaphragm(s) were installed in the 'diaphragm section' of the CDST (note that both single and double diaphragm configurations were used at times during testing)
- The predetermined quantity of metal oxide powder was placed on the knife blade and the plug was then reinstalled into the CDST
- The driven section of the CDST was evacuated using a vacuum pump
- The driven section was filled with the test gas to the desired predetermined pressure
- The driver section was then filled with the driver gas of the desired gas type to the predetermined fill pressure
- The diaphragm was ruptured by increasing the driver pressure (single diaphragm mode) or by evacuation of the space between the diaphragms (double diaphragm mode), which in turn triggered the DAQ and the imaging systems, when the incident shock reached STS 9.
- The captured pressure data was post-processed to calculate the test's temperature and pressure for each 'state'

4.3.5 Data post processing

The data files collected by the DAQ contain temporal pressure information logged by each pressue sensor at known positions along the shock tube. The sensor locations, known as shock tube stations, were previously defined and numbered in §4.2. For this project STS7, STS9, STS10 - 12 were used. The raw pressure data files (typically 38.7 Mb in size) and their accompanying high speed camera files were aligned using the STS-9 trigger signal generated from the first arrival of the incident shock. A MATLAB script was provided by the team at the Oxford Thermal Institute, which contained the outline of how to post process shock tube data, the original being authored

by Doherty *et al.* and modified by the author to suit this experiment. MATLAB contains bespoke functions the can interpret NI DAQ data and read this in to the software for further analysis. The primary objective of the first stage of data post processing was to extract the pressure in the driver and driven section and to calculate the mean shock speed.

Mean Shock Speed

Using bespoke code, MATLAB aligned the vertical dashed red lines to the pressure at each STS and by measuring the time between each rise in pressure, the shock speed can be calculated in m/s, Figure 4.11. The trigger (STS 9), defines the 0 point in terms of a reference time. STS7 to the left of the trigger and STS10 - 12 to the right.

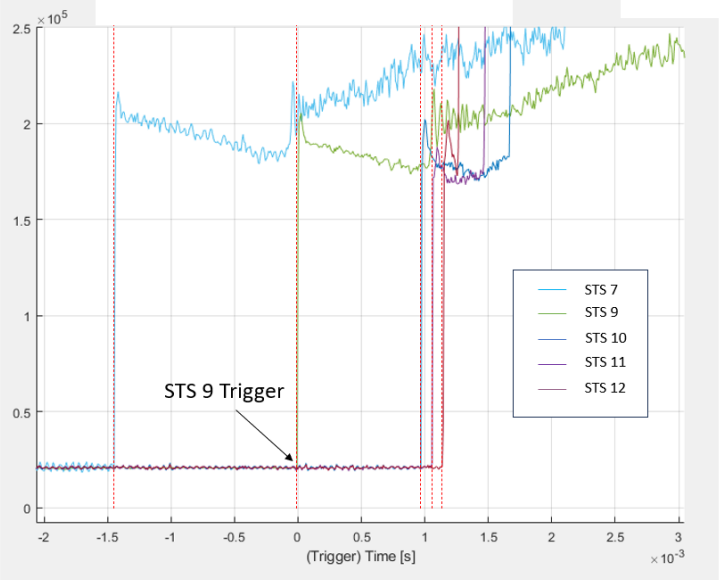

Figure 4.11: Example Shock Speed Determination, shot 110.

The first visual check is that the shocks speeds are similar, repeatability checks will be covered in a later section. The shock speed between timing stations were then averaged in order to report a mean shock speed. It is desirable to use the maximum number of shock speed measurements possible (in this case 5 sensors were available), as the lower the number of measurements the higher the potential error. For example, shot 110; if only STS 11 and STS 12 are averaged the shock speed is 18.7 m/s slower than if STS 7, 9, 10, 11 and 12 are used.

4.3.6 Experimental test plan

The starting point for the study was the desire to examine the 'Chiba hypothesis' which proposes the exothermic carbonation reaction of calcium oxide as a trigger for LSPI, at a fundamental level. Accordingly, the combination of pressure and temperature initially considered for the shock-tube experiments were derived from 3D CFD simulations of an engine operating condition known to promote LSPI as shown in Figure 4.12. This simulation shows the end of compression pressure is approximately 4.1 MPa and the temperature is 750 K for this engine operating condition.

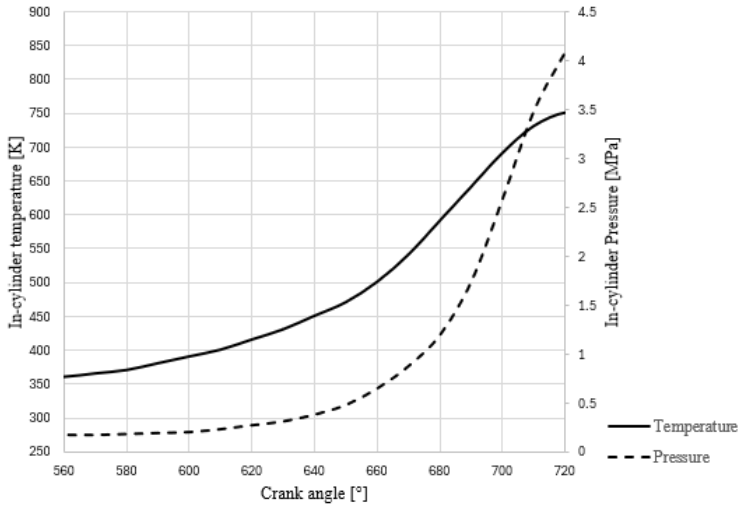

Figure 4.12: Siemens Star-CD CFD simulation (provided by the CFD team of Jaguar Land Rover) - 1500 RPM, WOT (25 bar BMEP); LSPI conditions. Approximate in-cylinder temperature and pressure, used to identify 'engine-like' conditions. 4-cylinder gasoline engine, 10.5:1 compression ratio.

The hypothesis proposed by Chiba University suggests that a temperature in excess of 1000 K and an in-cylinder pressure of approximately 4 – 5 MPa is required for the thermal carbonation reaction to occur and the corresponding exothermic heat release to trigger LSPI [82]. Although this pressure range corresponds well with the predicted end of compression pressure for the LSPI operating condition shown in Figure 4.12, the simulations predict a substantially lower in-cylinder bulk temperature at the time that LSPI would be expected to occur (5–10°CAD BTDC - see Figure 2.7 for a representative example). Accordingly, the lower temperature range of the test matrix for this study was set at a more 'engine-like' value of 773 K. Table 4.4 details the nominal test conditions examined during the study in order of increasing ambient gas temperature. Note here that, assuming an engine speed of 1500 rpm, the complete compression stroke of the 4-stroke engine (180 deg crank angle) corresponds to 20ms and that the ignition event either by spark or LSPI occurs in less that

Table 4.4: Experimental test matrix for nominal conditions

Temperature [K]	Pressure [MPa]	Powder 0.20g ± 0.025g	Driven gases
773	1.90	CaO, MgO	CO_2, N_2
873	0.85	CaO	N_2
1058	0.62	CaO, MgO	CO_2, N_2, Ar
1173	0.97	CaO, MgO	CO_2

20 degrees CA equates to approximately 2.2 ms. The shock-tube conditions, detailed in Appendix A, were designed accordingly to target a minimum of 3 ms at the desired constant temperature and pressure. Figure 4.12 illustrates a typical end of compression pressure at which LSPI can occur, approximately 4.1 MPa. When the shock tube was configured for this work, limits were placed on the experiment in terms of the pressures that were allowed. The initial testing in campaign 1 commenced at engine like temperature and lower pressure conditions where no light emissions were visible or detected on the photo diode. It is typical in chemical reaction kinetics for temperature to dominate, due to the additional energy imparted into the reactants. A practical way to achieve this in the CDST was to increase the fill pressure, hence density of the driven gas, in order to explore increased temperature. The result of this approach was that the test pressure reduced as the temperature increased. The first test where a light emission was observed was with CaO + CO_2, 1173 K and the resultant pressure was 0.97 MPa, in contrast to 753 K and 1.9 MPa in the fired engine. The occurrence of a light emission at lower pressure and high temperature validates the dominance of thermal effects in lieu of pressure. On that basis the author placed emphasis on exploring the effect of temperature, rather than matching the varying pressure in the engine. The experiments were performed in three pure gas environments: CO_2 – the particular gas of interest with respect to the Chiba hypothesis, and N_2 and Ar – both assumed to be inert with respect to the proposed reaction mechanism. Two metal oxide powders were used, both sourced from Sigma Aldrich; Calcium Oxide ReagentPlus 99.9% and Magnesium Oxide 99.99% trace base metals, powder. The quantity of powder used in each experiment was 0.2g +/- 0.025g. An aspect of the Chiba hypothesis not investigated in the current work was the impact of particle size.

4.3.7 Image Processing

As previously stated in §4.3.3, the images were captured using Photron high-speed camera(s) in 12-bit .mraw format, and viewed/edited using bespoke Photron PFV4 (x64) software. This software was used to sub-divide the files and export individual frames. Additional post-processing was undertaken using Fiji (ImageJ), allowing the images to be cropped to the dimensions (75mm x 30 mm) of the optical window of the CDST, and converted to 8-bit grey scale prior to applying a histogram normalisation to enhance the contrast. In some cases, where the image was too dark or contained faint particles, further post-processing was necessary to sharpen and/or brighten the image. The photographs in the following sections were extracted as representative, specifically selected individual frames, for each condition of interest. Where enhancements were required this will be stated, as not all images required this additional level of post-processing.

4.4 Results

4.4.1 Powder dispersal

In order to verify the efficacy of the powder dispersal via the knife-blade method, the target quantity of powder was placed on the blade while the CDST was fired. The measurement region was simply illuminated by a suitable light source to observe the powder moving. Figure 4.13, shows four frames from the high-speed camera file. Starting with the incident shock arrival, (a), the powder is pushed to the back of the knife edge. The reflected shock, (b) and (c), disperses the powder into the field of view. The residual powder is entrained by the shock wave and is shown to be well dispersed in the CDST, (d).

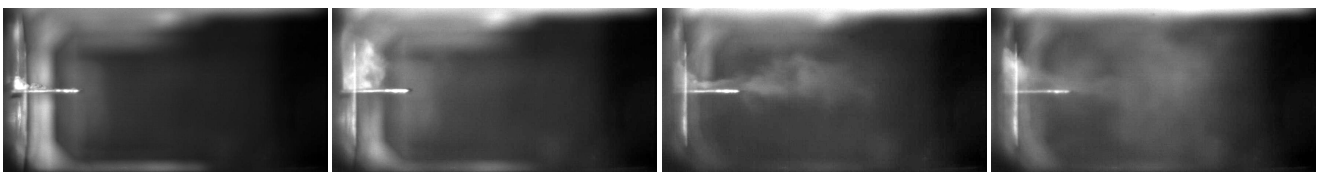

(a) t=-0.25 ms (b) t=0.5 ms (c) t=3.0 ms (d) t=5.0 ms

Figure 4.13: Shock induced powder dispersal – Test #34, 4000 FPS. The test section was externally illuminated. The timing refers to the arrival of the incident shock at the knife blade. The images were brightened to enhance the visibility of the powder.

4.4.2 Repeatability of test conditions

As noted in §4.2, the CDST was operated in both single and double diaphragm modes over the full course of the experimental study described in this chapter. In both instances repeat tests under nominally identical operating conditions (driver and driven gas compositions, temperatures and pressures) were performed to establish the repeatability of these test conditions. The overall repeatability in shock speed for campaigns one and two (a) in Figure 4.14 was within ± 4% of the mean using a single diaphragm, which was deemed 'good'. This was improved further for campaign three to ± 2.3% of the mean, with a double diaphragm arrangement, (b) in Figure 4.14.

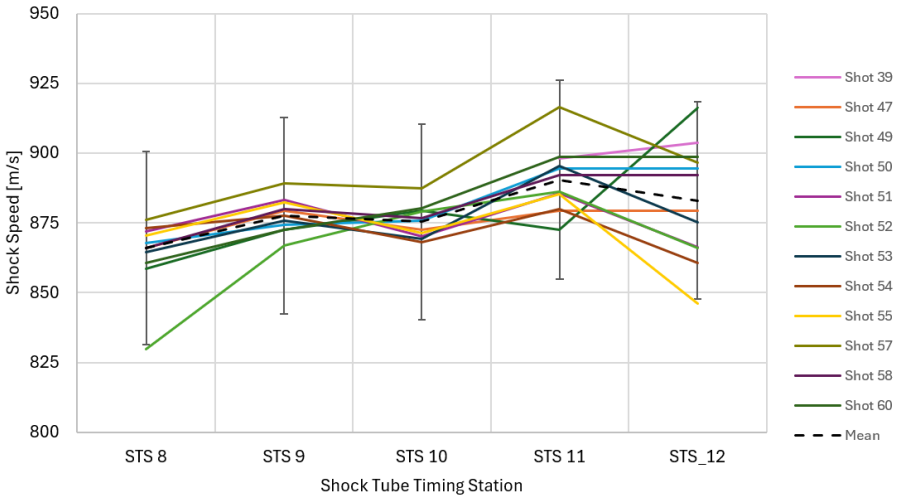

(a) Campaigns 1 and 2.

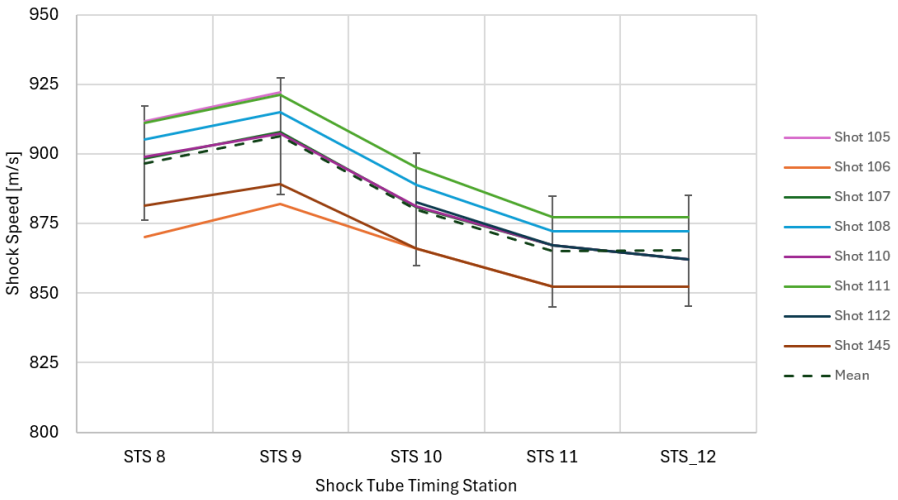

(b) Campaign 3.

Figure 4.14: Improved shock speed repeatability, single diaphragm (a) and double diaphragm (b). All target test conditions N_2 + CaO, target 1058 K and 6.2 bar. The error bars for (a) represent ± 4% of the mean, similarly for (b) represent ± 2.3% of the mean.

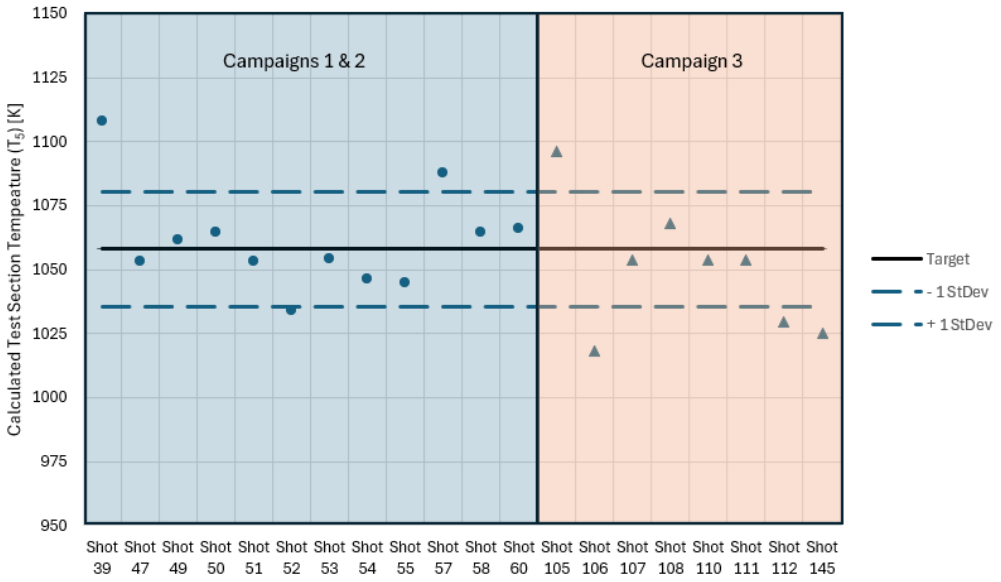

Figure 4.15: Desired test section gas temperature

It was found after multiple tests during campaigns 1 and 2 that the variation in burst pressure of the single diaphragm led to larger than desired variation in shock speed, Figure 4.14. This was illustrated in Figure 4.15, for shot 57, it can be seen that it has the fastest shock speed which in turn leads to the second highest test (T_5) temperature. In campaign 1, T_5 temperatures ranged from 1034 – 1108 K. Switching to a double diaphragm set-up led to a significant reduction in shock speed variation, however this did not translate into lower variation in (T_5) temperature. Figure 4.15, contains dashed lines indicating $\pm$ one standard deviation (σ) or (22 K). The change to double diaphragm changed to a more consistent profile of the shock speed vs. timing station, however as the (T_5) is calculated from the mean shock speed, this did not significantly improve the overall variation. This may be due to the lack of 'tailoring' of the test condition. More refinement or 'tailoring' could have reduced the variation further, but this was not pursued in the current work. In a paper on chemical kinetics modelling and shock tube study, Ning *et al.* [92], quote a shock tube test temperature uncertainty of $\pm$ 1 % over a test time of 1 - 2 ms. In a similar experiment to this research, using piezo-electric transduces, Ferris *et al.* [93], quoted a 1- σ uncertainty of $\pm$ 0.5 % of T_5 (desired test section temperature). The expected uncertainty of this experiment, as it used a similar both similar sensors and normal shock relation equations to calculate the temperature from pressure, would be similar $\pm$ 0.5 %. Overall, a very small value of uncertainty in comparison to the levels of temperatures assessed.

4.4.3 Engine relevant temperatures (T < 750 K)

Following the proposed reaction mechanism of the Chiba hypothesis and the end of compression gas temperatures for typical LSPI operating conditions as shown in Figure 4.12 and as evidenced in the literature [94] , an initial set of 20 tests were performed with CaO in a 100% CO_2 environment at a target gas temperature of 763 - 773 K. It is notable that that no visible light emissions were captured at the lowest temperatures examined with CaO in CO_2 or N_2 test gasses. It is also significant than no light emissions were captured for MgO in any test gasses, at any temperatures examined.

4.4.4 In-cylinder gas hot spot temperatures (800 < T < 1100 K)

After running multiple shots at T < 750 K the temperature was increased. This was done in stages, but it was necessary to raise the temperature to in excess of 1173 K to observe an output visible on the high speed camera. As no light emissions occurred at end of compression temperature and it was necessary to significantly increase the temperature in the CDST, this points at an alternative source of temperature in the engine being required to trigger pre-ignition. Literature suggests internal residual temperatures in the range of 800 – 1100 K in SI engines, at the typical speed and load that LSPI occurs [95], [96], [97].

4.4.5 Temperatures where light emissions occurred (873 < T < 1173 K)

The first clearly visible light emission was diffuse in form and appeared to last for a very short duration, at approximately 2 ms. Further inspection of the camera images later identified faint glowing particles, resulting in an overall duration of light emitted of approximately 30 ms.

Figure 4.17 charts the data collected from the STS's in the CDST. The dashed line is STS09 which was used to time all of the elements of the experiment. The solid line is STS12, the pressure measurement in the optical section of the CDST. The grey shaded area of the figure illustrates the start, end and timing of the light emission relative to the pressure signals. The legend is consistent for all of the result charts in the following section. The inset table shows the target test conditions and the measured results. Accordingly, T_5 and P_5 are the temperature and pressure during the test time calculated using normal shock relations.

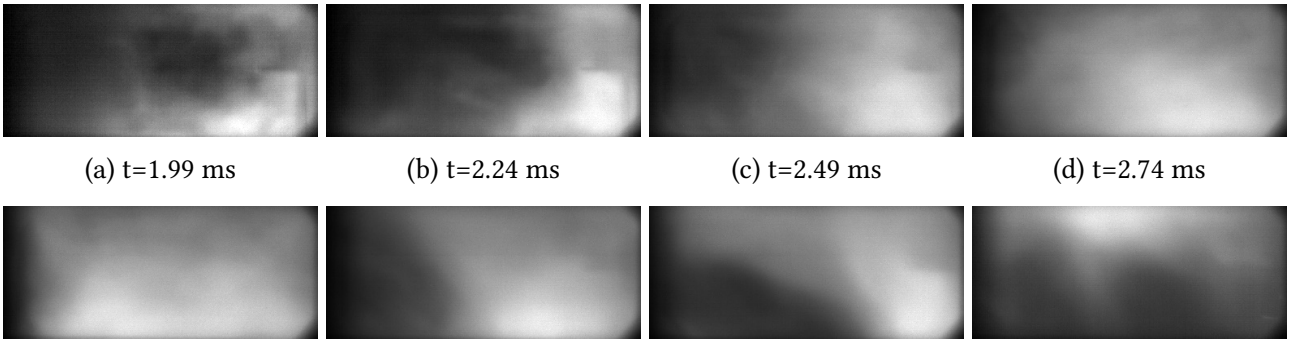

(a) t=1.99 ms (b) t=2.24 ms (c) t=2.49 ms (d) t=2.74 ms

(e) t=2.99 ms (f) t=3.24 ms (g) t=3.49 ms (h) t=3.74 ms

Figure 4.16: High speed images, CaO + CO_2, T_5 = 1185 K, P_5 = 0.98 MPa, campaign 1, Test #37, frame speed 4,000 FPS, (all times were relative to the first visible light emission). The images were brightened to enhance the visibility of the light emission.

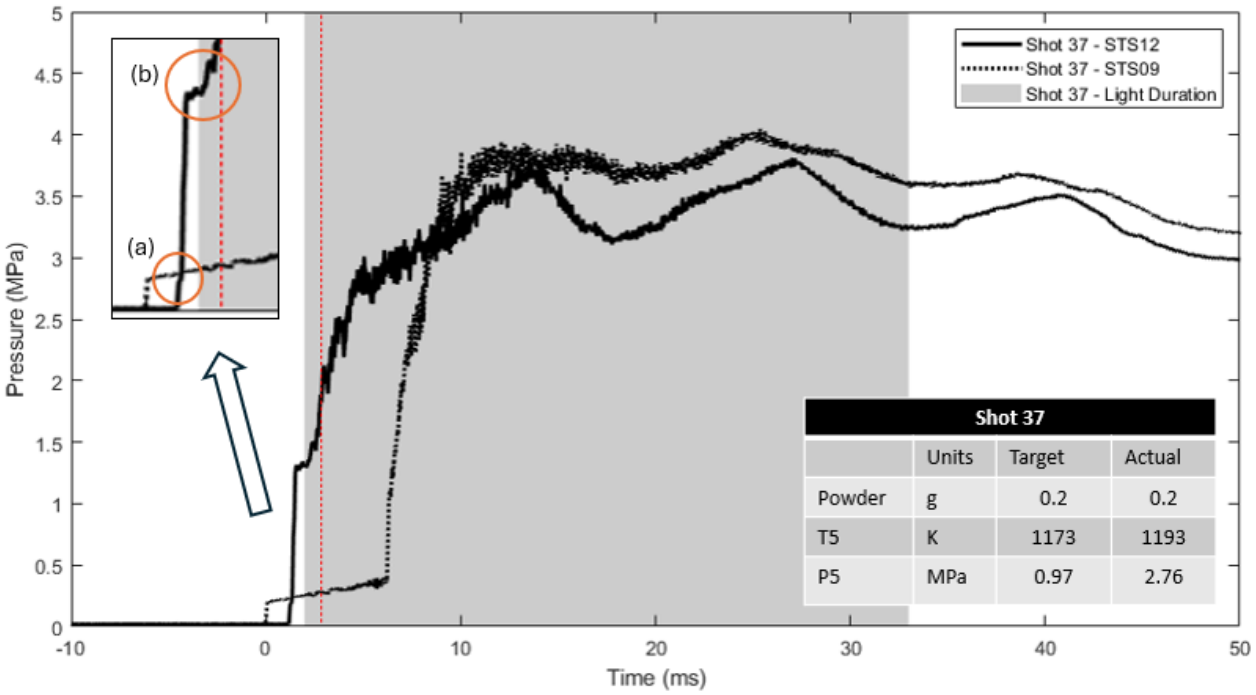

Figure 4.17: Shot #37, CaO + CO_2, 1173 K, 0.97 MPa. Camera speed 10,000 FPS. The dashed red line indicates the period of the displayed images in Figure 4.16. The in-set image is zoomed in on STS12; The orange circles (a) shows the incident shock, (b) shows the reflected shock/test time.

It can be seen that the light emission starts during the test time, in this case where the temperature reaches 1193 K. The desired test time, in a well tailored shock tube experiment, would be flat for the duration of the target test time (3 ms). There was initially a flat portion to the test time, then a rise in pressure around 1 ms after the shock is reflected. Tailoring will be discussed in more detail later in the chapter, however it can already be stated that this is not a well tailored condition. Of note is that there was a significant rise in pressure during the test time which will also be examined

in more depth later. Under the same fill conditions, the bath gas was changed to Nitrogen (N_2). As N_2 is considered to be an inert gas below 1600 K and low pressure, the expectation was that the no visible light emission would be observed. What was actually captured was unexpected.

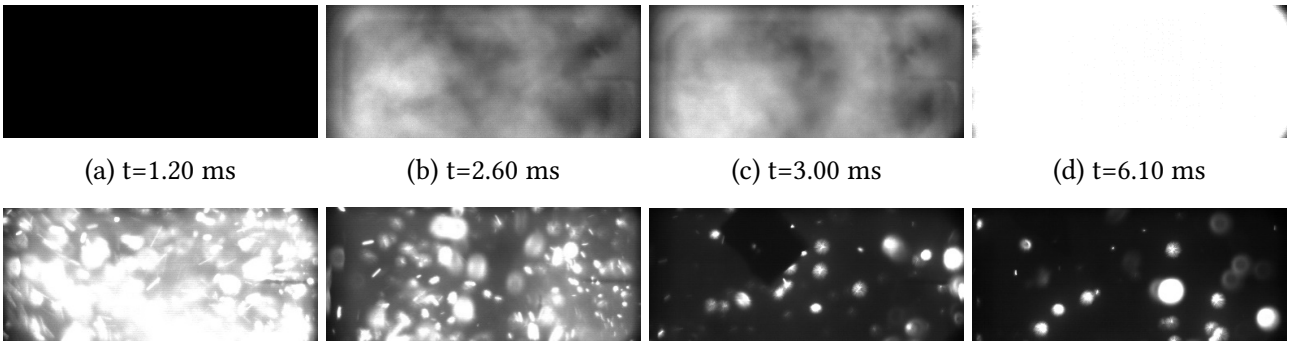

(a) t=1.20 ms (b) t=2.60 ms (c) t=3.00 ms (d) t=6.10 ms

(e) t=8.80 ms (f) t=11.20 ms (g) t=15.90 ms (h) t=17.70 ms

Figure 4.18: High speed images, CaO + N_2, T_5 = 1108 K, P_5 = 0.82 MPa, campaign 1, Test #39, frame speed 10,000 FPS, (all times were relative to the first visible light emission). The images were brightened to enhance the visibility of the light emission.

Figure 4.18 highlights an extremely bright and energetic light emission, so bright in fact that by 6.1 ms the CMOS chip in the high-speed camera was completely saturated. This condition was initially not well adjusted for the differing gas properties between CO_2 and N_2, hence the T_5 and P_5 were both above target, Figure 4.19. The early images in Figure 4.18 were similar to the CO_2 + CaO, diffuse and cloud-like. It was not possible to describe the characteristics during the saturation due to the extreme brightness levels. Thereafter, a particle like appearance dominated for an extended period of time (47 ms), until the last particle disappeared. It can be seen from Figure 4.19 that the start of the light emission was co-incident, possibly just in advance of the reflected shock reaching the pressure transducer STS12. This indicated that the initiation of this 'reaction' resulting in a light emission, may be occurring at a lower temperature. Of note in shot #39, is the absence of plateau during the test time, with the rise in pressure following the early light emission, occurring immediately after the reflected shock arrived. The behaviour of CaO + N_2 was investigated further, with a double diaphragm set-up of the CDST. It should also be noted that the piezo-electric pressure transducers were replaced and recalibrated. The range of the new sensors was targetted at improved resolution in the test time region of the trace, lower that those previously fitted. The result was saturation of the pressure transducers above 2.8 - 3 MPa, characterised by a horizontal line as shown in Figure 4.21.

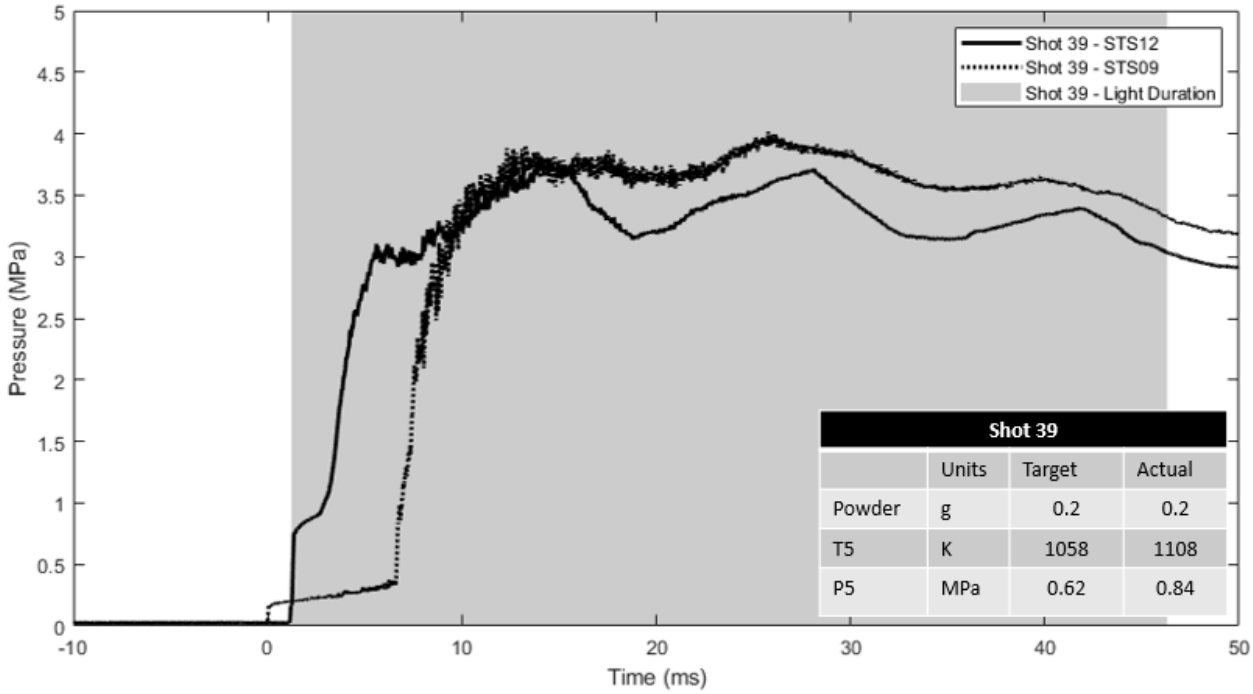

Figure 4.19: Shot #39, CaO + N_2, 1108 K, 0.84 MPa. Camera speed 10,000 FPS.

The fill pressures were similar to the previous condition, but the introduction of two diaphragms meant that rather than the driver pressure being a variable to burst the diaphragm, it was fixed at 4 MPa and the evacuation of the breech controlled the firing of the CDST. Shot #145 was the clearest example of the apparent reaction between CaO + N_2, Figure 4.20. The images in Figure 4.20 behave is a manner very similar to the lower temperature back-lit images of the powder being displaced rearward then entrained by the incident and reflected shock, Figure 4.13. As soon at the temperature and pressure conditions reach a sufficient level, 1025 K in the case the CaO particles emit light. Of particular note, in the case of shot #145, was that no diffuse or cloud-like light preceded the glowing

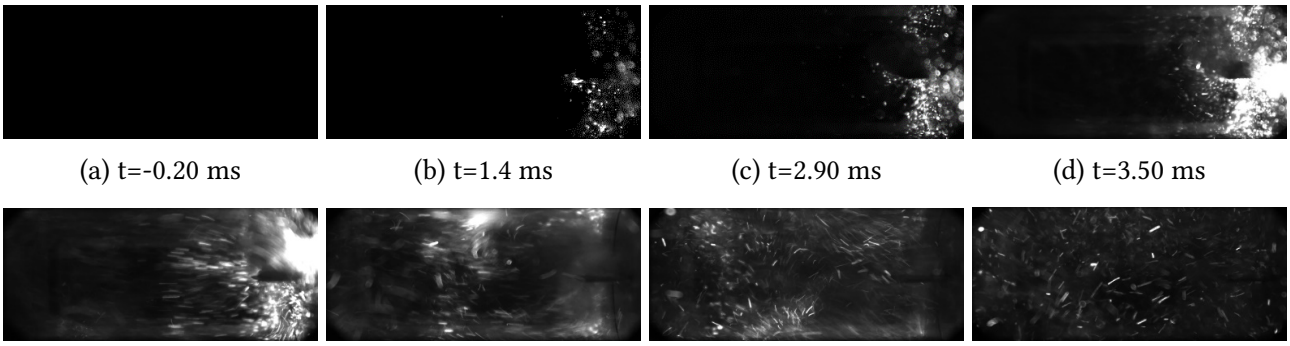

(a) t=-0.20 ms (b) t=1.4 ms (c) t=2.90 ms (d) t=3.50 ms

(e) t=4.10 ms (f) t=4.70 ms (g) t=5.50 ms (h) t=8.10 ms

Figure 4.20: High speed images, CaO + N_2, T_5 = 1025 K, P_5 = 0.66 MPa, campaign 3, Test #145, frame speed 10,000 FPS, (all times were relative to the first visible light emission). The images were brightened to enhance the visibility of the light emission.

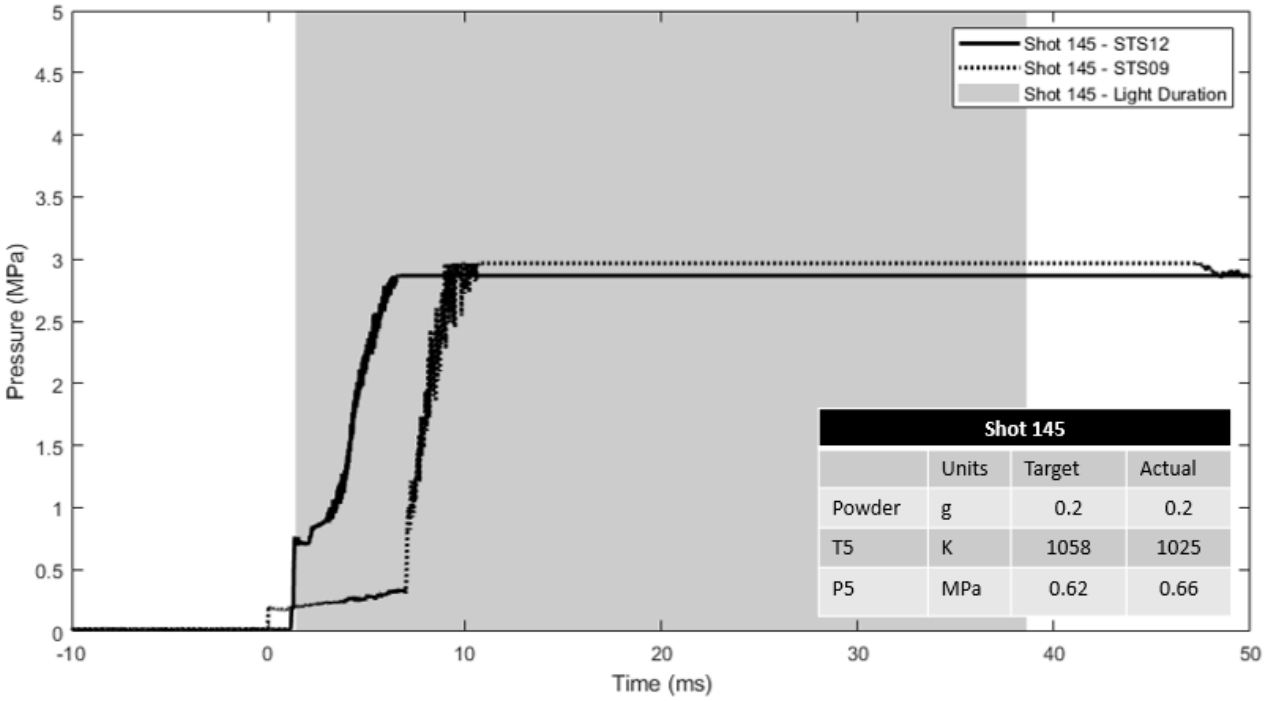

Figure 4.21: Shot #145, CaO + N_2, 1025 K, 0.66 MPa. Camera speed 10,000 FPS. The flat region of the pressure signal is due to saturation of the pressure sensor.

particle phase. Individual or glowing groups of particles can be seen as the incident shock arrives, then they glow very brightly as the reflected shock moves them through the optical section of the CDST. As noted for shot #39, there is a significant rise in pressure during the test time, in this case the rise was preceded by an initial pressure plateau, this will be explored further later in the chapter. To investigate the significance of temperature on this occurrence further, the next condition investigated was at a target of 873 K, Figure 4.22.

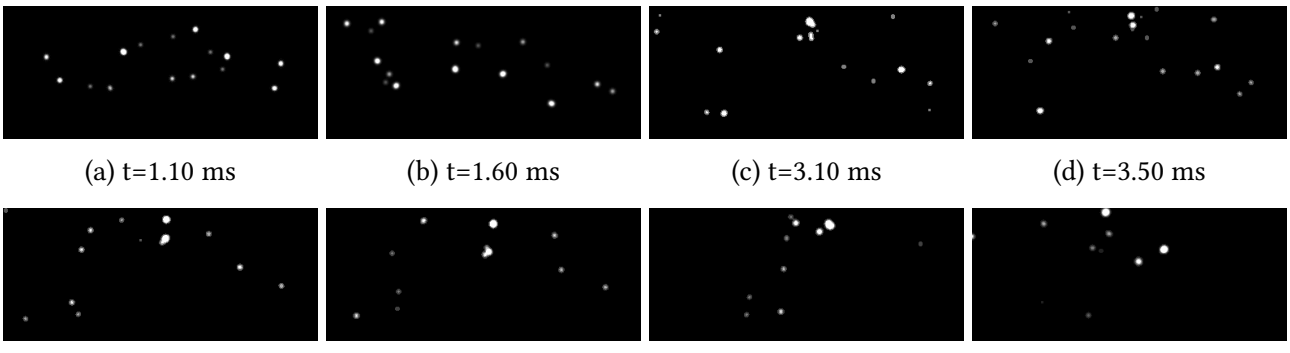

(a) t=1.10 ms (b) t=1.60 ms (c) t=3.10 ms (d) t=3.50 ms

(e) t=4.10 ms (f) t=4.60 ms (g) t=8.30 ms (h) t=10.20 ms

Figure 4.22: High speed images, CaO + N_2, T_5 = 869 K, P_5 = 0.85 MPa, campaign 3, Test #154, frame speed 10,000 FPS, (all times were relative to the first visible light emission). The images were brightened to enhance the visibility of the light emission.

The last test conducted with CaO + N_2 was targeting 873 K and approaching 'engine-like' conditions,

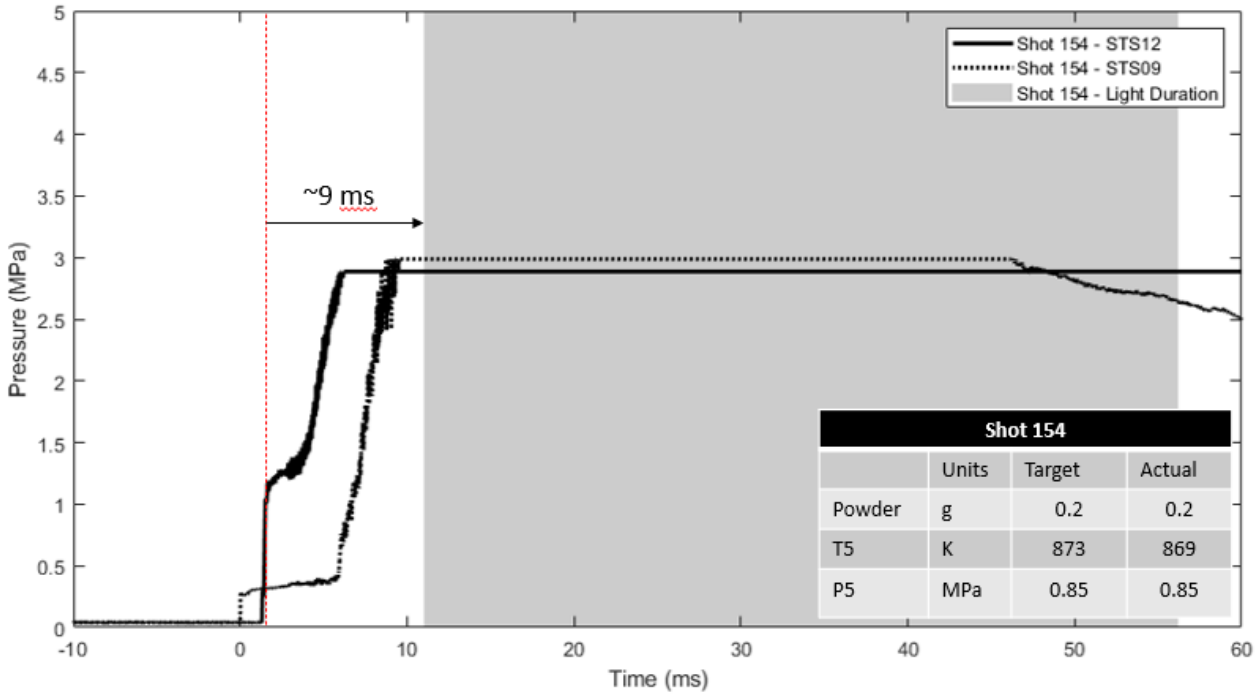

Figure 4.23: Shot #154, CaO + N_2, 869 K, 0.85 MPa. The flat region of the pressure signal is due to saturation of the pressure sensor.

but still approximately 125 K above the end of compression temperature referenced in Figure 4.12. From the timing of the light emission shown in Figure 4.23, it can be seen that light wasn't visible until approximately 9 ms after the test time. The significance being that the temperature was too low during the test time to initiate a light emission. The increasing pressure and hence temperature post-test in the CDST must have reached a level where light was able to be emitted. The particles themselves were very dull, such that they would be very difficult to see without a level of image brightness increase conducted in Fiji. The x-axis of this plot was increased to 60 ms, to allow for the delayed start to light being emitted and the long duration of emission 45.2 ms.

4.4.6 Testing with Argon (Temperature Target = 1058 K)

A unexpected apparent 'reaction' between calcium oxide and an inert gas (N_2) at a temperature at which it should be 'unreactive' led to many questions. It was decided to test with a truly inert gas, Argon (Ar). Known as the 'lazy gas' Ar is know to be unreactive with all known chemicals in the temperature region of this experiment. A new condition to replicate the CaO + N_2 temperature and pressure was designed using L1d4. This required a change to the diaphragm material from aluminium to Mylar due to the lower pressure conditions of the driver and fill condition. The nature

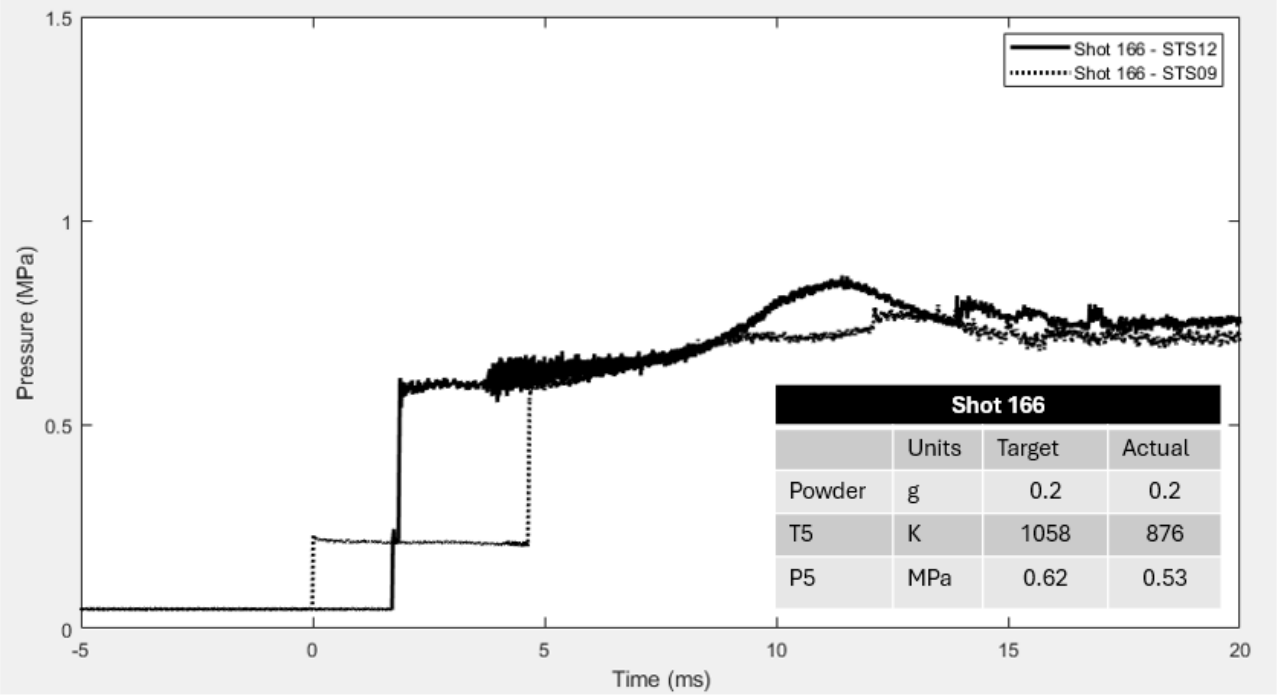

Figure 4.24: Shot #166, CaO + Ar, 876 K, 0.53 MPa.

of Mylar diaphragm rupture creates additional debris in the shock tube, leading to more extensive cleaning requirements between tests. Unfortunately, despite L1d4 suggesting that 1058 K would be achieved, the actual calculated temperature for these tests was lower, 876 K. This was due to the shock speed being lower than predicted and this resulted in the temperature not reaching the target. However, as 876 K is in the vicinity of test 154 (869 K), a condition where a light emission occurred, it can be confirmed that no light was emitted with CaO + Ar. If Figure 4.24 is examined and number of different artefacts can be evaluated. Firstly the test time was a more defined plateau and the test time was at target, approximately 3 ms. Moreover, the absence of a large rise in pressure and no light emission under similar conditions to shot #154 is significant. The x and y axes we changed for the Ar condition as the pressure was significantly lower for this shot. The time axis was similarly shortened as the pressure after 20 ms was reducing and unremarkable. Limited time and opportunity for further testing was available, had this not been the case and certainly for future work, this condition could be examined further to match the precise conditions for a more extensive comparison at this condition.

4.4.7 Testing with MgO (Temperature Target = 1058 K)

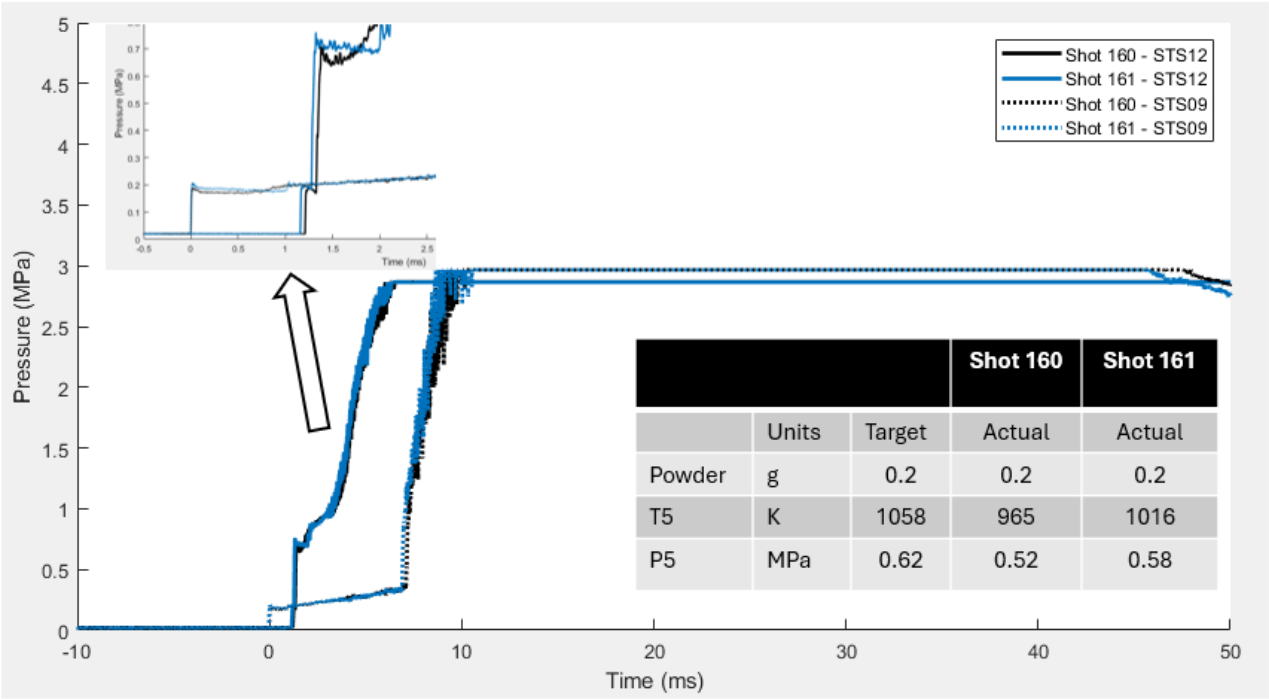

Figure 4.25: Shot #160 and #161, MgO + N_2, 968 and 1016 K, 0.53 and 0.58 MPa. Inset, zoomed in to; -0.5 – 2.5 ms and 0 – 0.7 MPa. The flat region of the pressure signal is due to saturation of the pressure sensor.

To test the hypothesis MgO does not emit light under the same conditions as CaO, this condition was repeated with MgO powder. Figure 4.25 shows two tests at the same target condition. Firstly, it can be seen that neither test met the target closely, test #160 at 965 K was 93 K below target despite being a double diaphragm test with the same fill conditions. Similarly, but to a lesser extent, test #161 was also below target by 42 K. This behaviour can be partially attributed to slower shock speed in both cases, in CaO + N_2 tests close to target, the average shock speed was approximately 900 m/s, whereas tests #160 and #161 were 836 and 864 m/s respectively. The inset chart in Figure 4.25, shows that although the timing of the incident shock arrival at STS09 was identical for both tests, there was a difference in the reflected shock time of 0.05 ms at STS12, with #160 being slower. The exact reason for this is unknown, but is most likely to be related to differences in the rupture characteristics of the diaphragms and any non-ideal flow behaviour. The absence of images is the result of there being no light emissions to examine, hence it was confirmed that MgO powder did not emit light under similar conditions as CaO. For future work this condition should be examined further to achieve fully comparable test conditions, and with many more repeat tests.

4.4.8 Testing With and Without CaO Powder

To confirm if what had previously been observed as light emissions in the preceding subsections was in fact not a light emission from CaO powder, instead the result of N_2 gas emitting visible light in some way that Ar gas does not, two tests were conducted without CaO powder in the CDST. Figure 4.26 compares the 'no-powder' tests to several notable tests 'with powder' under nominally identical test conditions (driver and driven gas compositions, pressure, temperature, targeting 1058 K and 0.62 MPa). It is immediately apparent from tests # 57 and 58, that they differ significantly from the other tests, despite on first impressions that the absence of powder was the only difference. Examining the driver pressure, this was significantly higher than the other tests, at 5.0 and 4.9 MPa for shots #57 and #58 respectively. This was most likely due to differences in the material properties or scoring of the single diaphragm. The rupture characteristics have a significant effect on the flow field of the shock wave. Figure 4.27 show an example of a new and fired diaphragms. Whilst the machining process was as identical as it can be for a manual process, the behaviour of the diaphragms vary. The fired diaphragm, illustrates the non-ideal behaviour seen in this experimental campaign. An ideal result would have been for all 4 'petals' to open equally and symmetrically. This was not achieved in this testing, which could have led to undesirable variability in addition to the varying rupture pressure. What is significant was that the calculated shock speed and P_5 pressure were close to the target, however the temperature was 50 - 117 K higher in the case of shots # 57 and #58. Moreover, the reflected shock and post-shock pressure was very different to what should have been similar. If the characteristics of the repeat tests, plus confirmed 'no light emission' MgO #160 and #161 are added (all zoomed into the test time region), the following observations were made, figure 4.28. Firstly, the variability in the arrival time of the incident and reflected shocks can been seen via the different timings of each pressure rise. Starting with the shots that included powder; shot 39 (black line), explored in detail 4.18 and 4.19, had no pressure plateau, rather a steady rise in pressure throughout the test time.

Shots #106 and #108 are interesting as they display different pressure characteristics. Shot #106 (purple line), behaved similarly to shot #39, no defined plateau, followed by a steady rise in pressure. This test had the lowest shock speed (865 m/s) , P_5 (0.58 MPa) and T_5 (1018 K) of the CaO tests. In contrast, shot #108 (green line) had a defined plateau at the start of the test time, followed by a small

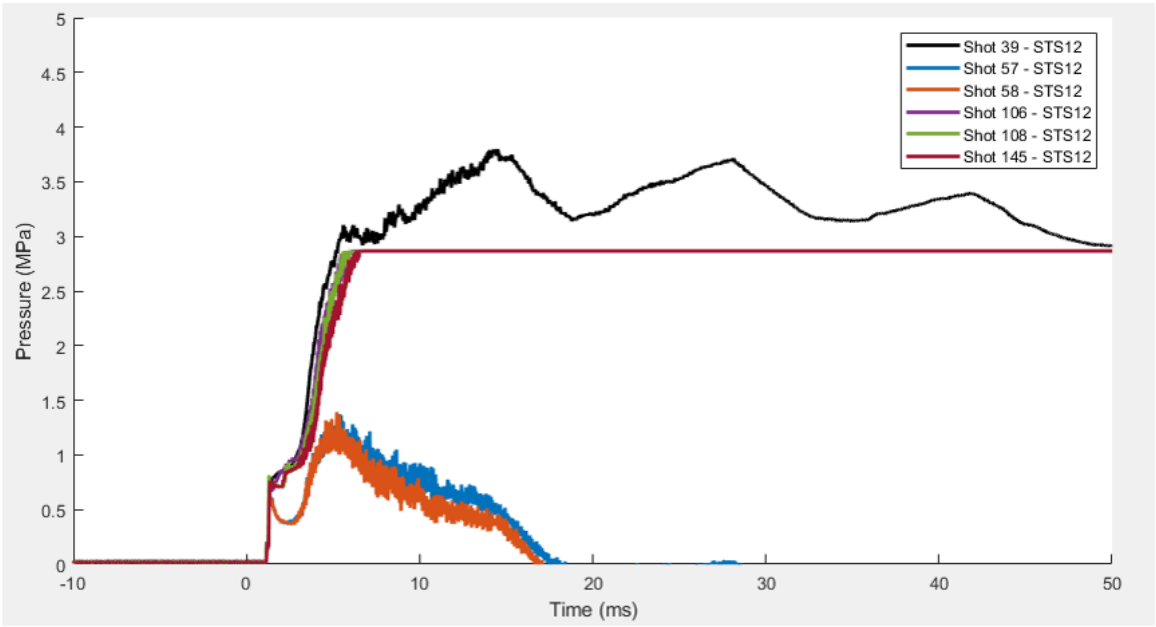

	Units	Target	Shot 39	Shot 57	Shot 58	Shot 106	Shot 107	Shot 108	Shot 145
Powder			Yes	No	No	Yes	Yes	Yes	Yes
T5	K	1058	1108	1165	1064	1018	1054	1068	1025
P5	MPa	0.62	0.84	0.66	0.61	0.58	0.65	0.67	0.59
Shock Speed	m/s	n/a	896	893	881	865	883	890	868
Driver pressure	MPa	4.0*	4.3*	5.0*	4.9*	4.0	4.0	4.0	4.0

Figure 4.26: Shots; #39, #57, #58, #106, #108, #145 CaO + N_2, 1058 K, 0.62 MPa.The flat region of the pressure signal is due to saturation of the pressure sensor. Driver pressures marked * represent single diaphragm tests from campaigns 1 and 2, where the burst pressure was variable. Later (campaign 3) double diaphragm tests had fixed driver fill pressure.

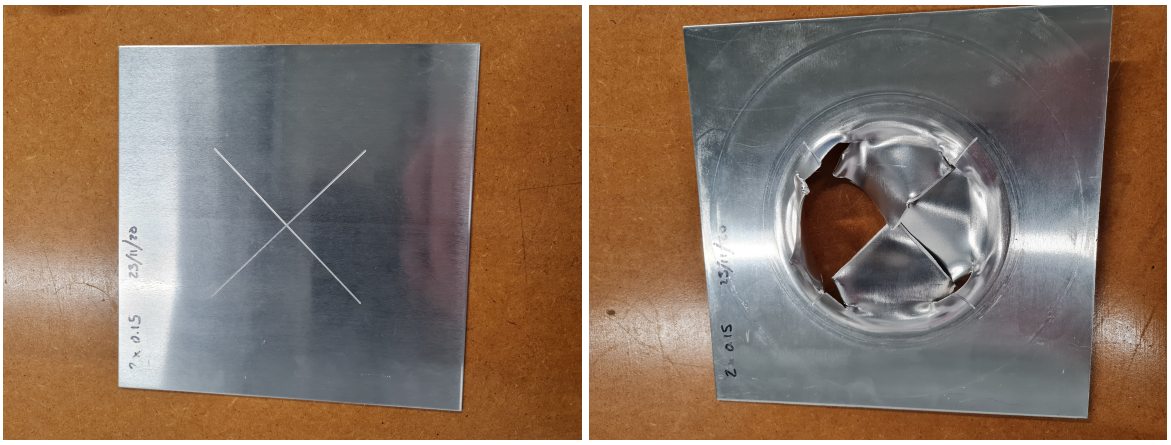

(a) New diaphragm, 2 x 0.15mm crossing scores (b) Fired diaphragm

Figure 4.27: Comparison of new and fired diaphragms

rise in pressure approximately 1 ms after the start. The results for this test have faster shock speed (890 m/s), higher P_5 (0.67 MPa) and higher T_5 (1068 K). Similarly shot #145 (brown line) exhibited almost identical behaviour to shot #108, including the small rise in pressure after 1 ms. It was also

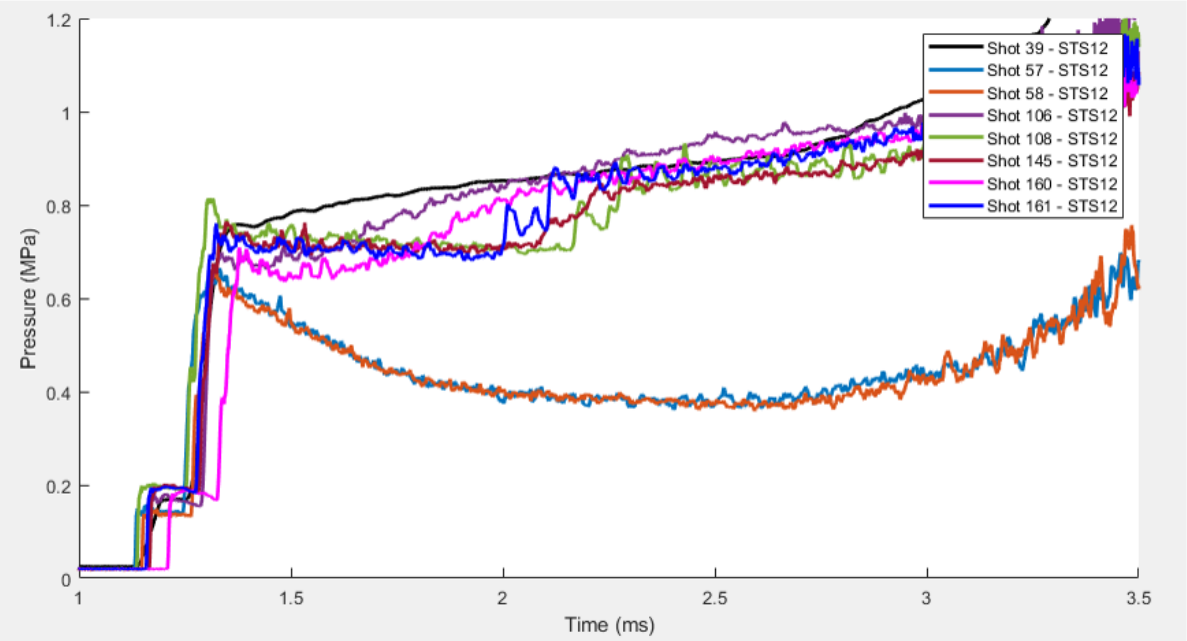

	Units	Target	Shot 39	Shot 57	Shot 58	Shot 106	Shot 108	Shot 145	Shot 160	Shot 161
Powder			CaO	No	No	CaO	CaO	CaO	MgO	MgO
T5	K	1058	1108	1165	1064	1018	1068	1025	965	1016
P5	MPa	0.62	0.84	0.66	0.61	0.58	0.67	0.59	0.52	0.58
Shock Speed	m/s	n/a	896	893	881	865	890	868	836	864
Driver pressure	MPa	4.0*	4.3*	5.0*	4.9*	4.0	4.0	4.0	4.0	4.0

Figure 4.28: Shots; #39, #57, #58, #106, #108, #145, CaO + N_2, nominal conditions 1058 K, 0.62 MPa. Shots; #160 and #161 MgO + N_2, nominal conditions 1058 K, 0.62 MPa. The flat region of the pressure signal is due to saturation of the pressure sensor. Driver pressures marked * represent single diaphragm tests from campaigns 1 and 2, where the burst pressure was variable. Later (campaign 3) double diaphragm tests had fixed driver fill pressure.

considered, if the light emission was coincident with the small pressure rise after 1 ms, however this was quickly disproved as it can be seen in 4.21 that the start of the light emission was coincident with the start of the test time, not the small rise in pressure. To investigate if this observed pressure behaviour was the result of an apparent reaction or simply an artefact of the flow and aerodynamic behaviour of the experimental design, two additional tests with confirmed 'no light emissions', were overlaid. Shots #160 and #161 (MgO), were examined in detail in figure 4.25 and can be seen to follow characteristics previously described in the CaO tests earlier in this subsection. In fact, they are different in a similar way to shots #106 and #108, in that shot #160 (magenta line) had no real plateau and a steady pressure rise during the test time, whereas shot #161 (royal blue line), had a plateau and a more defined pressure rise after 1 ms. It is therefore most likely that the variation in incident and reflected shocks, hence shock speed, P_5, T_5 and plateau vs. steady pressure rise, must there be the

result of test to test thermo-fluid differences and not the result of a chemical reaction. Finally, the tests conducted without powder were revisited, namely shots #57 and #58. It was first thought that as these tests had such a different pressure characteristic, that this was due to the absence of powder. Moreover, if the test conditions for CaO with and without powder are considered in isolation, this could suggest a significant and potential reaction when powder is included. However when the non-light emitting MgO results are also considered, this disproves any hypothesis relating to a chemical reaction being the cause. In summary, the mechanical characteristics of the diaphragm rupture and non-ideal behaviour of the CDST are the most likely cause.

4.4.9 Repeatability of Captured Light Emissions

In §4.14, the repeatability of the experiment was explored in terms of repeatability and reproducibility of the same test condition and overall precision of the methodology. It is noteworthy to mention the repeatability of captured light emission, particularly for tests with the largest sample sizes. The two conditions considered here are CaO + CO_2 (1173 K and 0.97 MPa) and CaO + N_2 (1058 K and 0.62 MPa). In total 5 repeats of the CaO + CO_2 condition, resulted in 3 occurrences of captured light emission. The sample size for the CaO + N_2 was more widely repeated as this unexpected result drove further investigation. A total of 20 repetitions was conducted; 8 of the repeat shots had issues with camera synchronisation and the photodiode was not always present and working. Based on experience working with this condition, it was highly likely that a light emission were present but not captured by the HSC due to incorrect triggering. The 'no-powder' tests comprised 2 in total, the first of the two had a small light emission, due to residual trapped in the CDST, captured on the photodiode, but no HSC image. The second no-powder shot had no light emission present. Finally the remaining 10 shots all had HSC images captured. After the issues with camera synchronisation were overcome, (mainly campaign 2), every CaO + N_2 shot produced a light emission. It can therefore be said that the CaO + CO_2 was less repeatable than the CaO + N_2 condition indicating a potential temperature threshold or sensitivity, but for this to be conclusive a larger sample size for the CaO + CO_2 condition would be necessary.

4.4.10 Shock Tube Tailoring

The 'test time' in a shock tube is the maximum time, where a quiescent slug of test gas at the target temperature and pressure created by a reflected shock-wave interacts with the following gas stream. So-called tailoring of the experiment, seeks to tune this behaviour to create a readily repeatable condition to allow the exploration of chemical kinetics in a shock tube. The shock tube is a reactor that can instantaneously provide high temperature and pressure, ideally recreating a constant volume reactor conditions post reflected shock [98]. In shock tubes that cannot be extended, driver gas tailoring can be used to extend the test time. A well tailored driver gas, the contact interface between the driver and reflected shock wave can be tailored so that no reflected wave processes are generated in the post reflected shock region [98]. From the same paper, specifically focussing on pressure in this example (similar behaviour can be seen with temperature), Figure 4.29 shows examples of under-tailored, tailored and over-tailored situations.

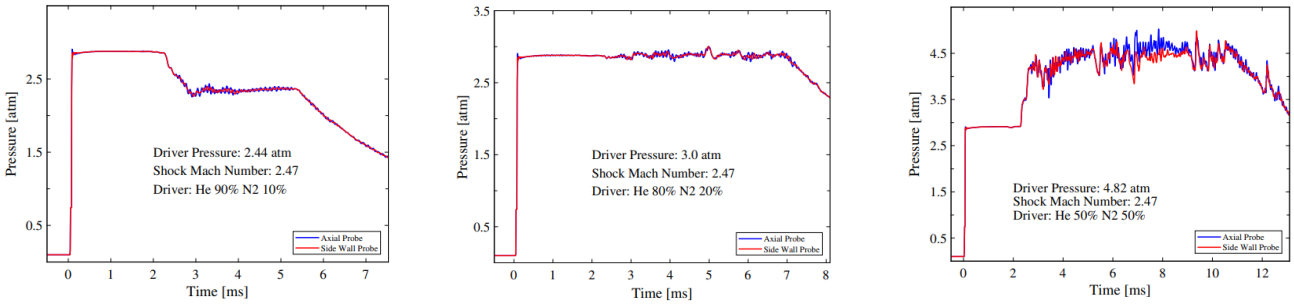

(a) Under-tailored (b) Tailored (c) Over-tailored

Figure 4.29: Examples of shock tube pressure tailoring [98].

The CDST does not provide well tailored conditions in the present experiments. It can be seen from 4.29, that (a) under and (c) over tailoring we experienced, but no (b) tailored (with the exception of the Argon test, which is quite close 4.24). Most of the tests in all three campaigns were over-tailored, an interesting characteristic of this situation is that the temperature, initially peaks post-test time then reduces dramatically due to the driver gas mixing with the driven gas. In the case of this work, the reduction in temperature appears not to have had a significant negative impact, however this could introduce air later in the shot. Whist this shouldn't be a factor for the initial gas composition and hence light emission, it could play a part in the long duration of glowing particles, analogous to sparks in a fire. Further experiments with different gas compositions would be required to explore this further and determine if a form of oxidation was occurring. This could be relevant particularly

for the CaO tests where initially there was rapid cloud-like light emissions, however discovered much later with further analysis, particle based light emissions late in the experiment which may point to a secondary oxidation reaction with air. Other considerations, mentioned previously, were problems due to non-idealities resulting from the creation of boundary layers and their interactions, [99]. This can lead to errors in the reaction temperature. Variability in the diaphragm rupture has also had a significant effect on this work, as its the likely cause of the unusual, potentially under-tailored behaviour experiences on shots #57 and #58 (no-powder). It is recommended for any future work that time is taken to tailor the experimental design to elongate the test time plateau, improve repeatability and understand the effects of any post test gas mixing.

4.5 Discussion

This work set out to investigate the hypothesis introduced in Chapter 3 conceived by Moriyoshi and co-workers [82] [83] of Chiba University, Japan. Whereby, the carbonation of CaO with CO_2 leads to an exothermic reaction with sufficient heat release to trigger LSPI. Whilst light emissions were captured a number of times at the highest temperatures tested, it was not a readily repeatable condition and not present at lower temperatures i.e. at the end of compression stroke in an ICE, or 'engine-like' conditions. The images captured using a HSC were initially cloud-like in early frames, moving to particle-like behaviour later in the experiment. Particle size was mentioned as a factor for consideration by Moryoshi *et al.*, but was not included in this current work. Visually at least, the results captured using the CDST differ from the measured pre-ignition in an engine running at a condition where LSPI could occur. Endoscopic measurements previously captured by Chiba University illustrate examples of how LSPI manifests inside a running engine [83]. The images are 'particle based', rather than a glowing cloud. The upper images in Figure 4.30 marked 'A' show glowing particles, in this case emanating from the piston top land crevice at approximately 10 °CA BTDC, once established this becomes extremely bright. The lower images in Figure 4.30 marked 'B', show LSPI occurring on the exhaust side of the combustion chamber.

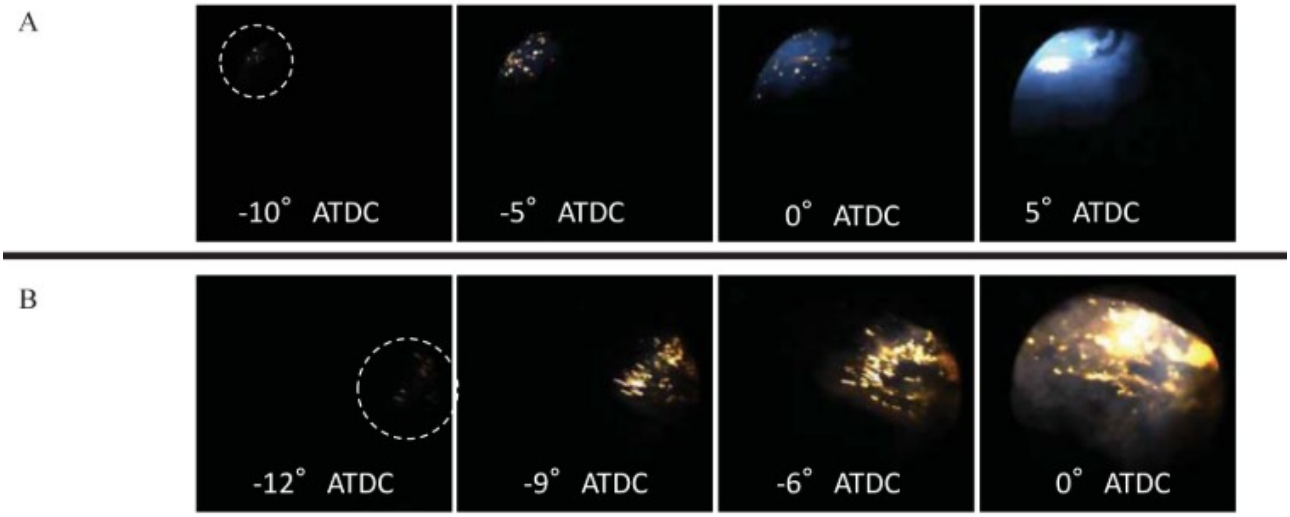

Figure 4.30: Endoscopic images of in-cylinder LSPI. A) Shows local luminescence around the piston crevice 10 °CA BTDC. B) Pre-ignition occurs on the exhaust side of the engine, 12 °CA BTDC [83]

Some of the CaO + N_2 tests exhibited cloud like behaviour e.g. shot #39, similar to the early frames of the CaO with CO_2 e.g. shot #37. However in contrast, there were tests for CaO + N_2 that were purely particle based. It can be seen in figure 4.18 (shot 145) a notable example of a visible light emission from CaO + N_2; starting from a completely dark condition, follows a single, then an increasing number of glowing and energetic particles were captured that lasted for tens of milliseconds, Figure 4.21. Once repeatable behaviour was established, the temperature was reduced to determine if light was emitted approaching 'engine-like' conditions (shot 154). On first impressions, it was thought that CaO + N_2 did emit light at significantly lower temperatures than CaO + CO_2, but this was later disproved as despite the condition approaching 750 K the light emission did not occur at the target conditions during the test time, rather not until the temperature in the CDST reached a critical level where light could be emitted, Figure 4.20. Further images of pre-ignition were collected by Fang *et al.* [100] from Tianjin University using a specially designed optical engine located at Brunel University, UK. The experiment was specifically targeted at capturing oil induced PI, by injecting oil into to the fully warm engine running a fixed speed and spark timing.

The engine has a unique optical window in the cylinder head and the intake and exhaust valves are horizontal. This physical engine configuration presents some challenges for combustion. It can be seen in cycle 70, in Figure 4.32 that the 'normal' combustion cycle has some spots of diffusive combustion, probably due to poor mixing of air and fuel that would lead to increased particle emissions. These spots are not to be confused with the oil based PI from injected oil which can be seen to trig-

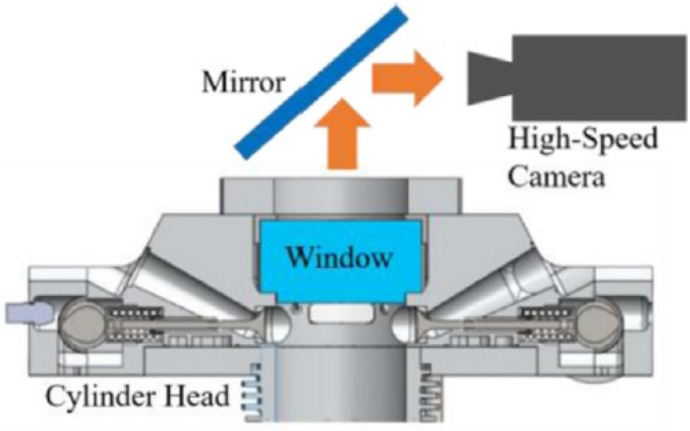

Figure 4.31: Schematic of the Brunel University optical engine and high speed imaging system [100]

ger PI 7.2 - 9.6 °CA BTDC in cycles 57 and 75, remembering that the spark timing was fixed at TDC. It stated in the paper that some image processing was used to enhance the images to aid the calculation of flame speed. This was why the image colour differs from the PI captured in 4.30. In figure 4.32, cycle 57, the PI occurred from the location that the oil was injected, the highlighted aspect of this image at 12 °ATDC shows some bright spots (highlighted in red) said to be exothermic centres in the unburned zone. In cycle 75, figure 4.32 shows multiple yellow 'particle like' spots of burning oil. Additionally a highlighted image at 3.6 °ATDC, was said to be an additional semi-separate combustion zone formed (highlighted in red). This cycle differed from cycle 57 in that the autoignition occurred near the expanding flame front rather than near the cylinder wall. It was also stated in this paper that a single drop of oil, whilst confirmed to initiate PI, cannot be the only cause of the other oil droplet or spots observed during this experiment and these are likely to be the result of pressure waves in the combustion chamber due to the extremely fast burn rates displacing oil from the top land crevice. In this alternative study, cloud-like areas form in addition to purely particle based light emissions. These are more similar in appearance to both the results captured in the CDST for CaO + CO_2 and some occurrences of when CaO + N_2 was tested. This suggests that there may be a level of variability in how CaO interacts with the surrounding gasses and the resulting optical behaviour. Of course the environment inside to combustion engine is considerable more complex than the CDST, containing fuel and oxygen from the air, water from complete combustion and residual gas from the previous cycle. The results presented to date, neither unambiguously disprove or prove the 'Chiba hypothesis'. However, a new, unexpected, vigorous reaction of CaO powder when shock heated in a N_2 gas atmosphere, does suggest the existence of an, as yet unidentified, alternative reaction

pathway for CaO to trigger LSPI. The highly repeatable behaviour of CaO + N_2 and nitrogen as a pathway was confirmed by the absence of a light emission when it was replaced with argon.

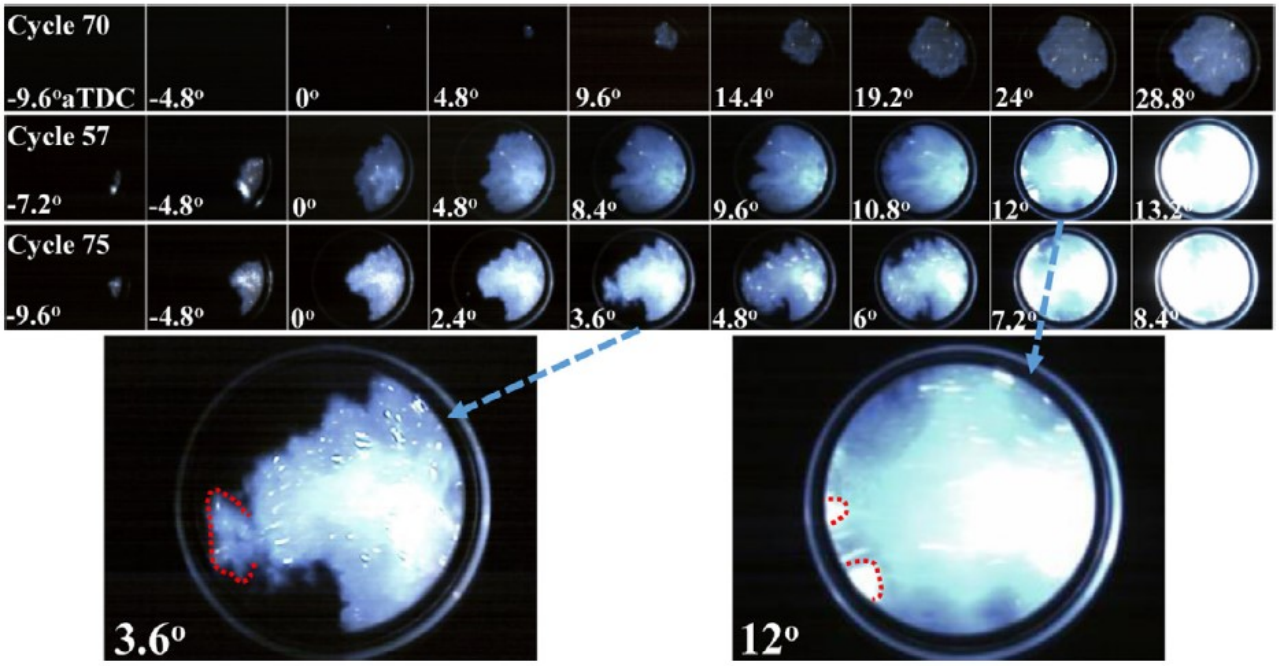

Figure 4.32: Endoscopic images of in-cylinder LSPI, 1200 rpm, ignition timing fixed at TDC. Cycle 70 is the engine running 'normal SI combustion'. Cycle 57 and 75 are PI cycles that result from oil injection. [100]

Whist investigating the potential reasons for why the unexpected behaviour of CaO + N_2 occurred, "could oxygen be present?" was explored. Is there sufficient air leakage (O_2) into the shock tube to create an oxidation reaction between either the CO_2 or N_2, which in turn could cause a light emission? The CDST was evacuated prior to each test using a vacuum, the filled with the desired driven gas for the test. The vacuum pump has a rated power capability and can remove most of the gas, well below atmospheric pressure, but not absolute zero pressure. The quantity that cannot be removed is assumed not to participate in the next test as the volumetric quantity would be very small in contrast to the test gas. The driven gas is filled to the target pressure, further increasing the charge density of the desired gas, and displacing any residual gas. Once the CDST is 'ready to fire' a number of tasks remain e.g. safety checks, which means that there was still an opportunity for air to leak into the test section despite countermeasures e.g. bespoke sealing grease, to prevent this (the test pressure is still below atmospheric pressure). The Oxford CDST driven section is 0.1 m diameter and 8.4567 m long, which equates to a geometric volume of 0.0664 m^3 or 66.4 L. The fill pressure, 'as set' was recorded in the test logbook, then the same pressure was again recorded at the

point of firing. Shot #109 was chosen to evaluate the estimated leakage. The set pressure was 0.0201 MPa or 20100 Pa, by the time the CDST was fired the pressure had risen to 0.0208 bar or 20800 Pa.

$$PV = MRT \tag{4.19}$$

Using the rearranged ideal gas Equation (4.19) the mass of gas was calculated for the set condition (N_2, 15.3 g) and the pressure at CDST firing (N_2 + leaked air, 16.4 g), and the difference equated to 1.1 g or 7.03%. As air comprises approximately 75.523% nitrogen and 23.133% oxygen by mass (excluding argon, CO_2 and other minor elements) the mass of O_2 in the CDST was therefore approximately 0.24 g. In contrast to the N_2, 15.2 g at the set pressure, making the overall percentage of air in the CDST at the point of firing 1.62%. The areas for leakage in the CDST comprise; the diaphragm(s), the clamps at each tube connection, each pressure transducer location and the plug at the end of the test section where the knife blade is located. Specific care is taken to reduce leakage using sealing compounds and grease and it is felt by the author that this level of leakage is extremely low and unlikely that O_2 is taking part in the visible phenomenon that was recorded. This reduces the likelihood of nitrogen oxides forming as the oxygen concentration and temperature during the CDST experiment are below the levels where thermal NO_x is readily formed (typically above 1573 K [101]). The nature of the cause of a light emission remains unknown and unexpected as despite an in-depth investigation into reference books and published literature, a plausible chemical reaction between CO_2 and N_2 was not found. Nitrogen is very stable at temperatures below 1600 K due to the triple bond between the atoms. Its possible that the nitrogen is not actually taking place in a chemical reaction, instead creating an environment where something can enable the calcium oxide to emit light when heated. Potential chemical compounds of calcium and nitrogen could be calcium nitrate (4.20) [102], calcium nitride (4.21) [102] or calcium cyanamide (4.22) [103] .

$$\mathrm{CaCO_{3(s)} + 2\,HNO_{3(l)} \longrightarrow Ca(NO_3)_{2(s)} + CO_{2(g)} + H_2O_{(l)}} \tag{4.20}$$

$$\mathrm{3\,Ca_{(s)} + N_{2(g)} \longrightarrow Ca_3N_{2(s)}} \tag{4.21}$$

$$\mathrm{CaO_{(s)}} + 3\,\mathrm{C_{(s)}} + \mathrm{N_{2(g)}} \longrightarrow \mathrm{CaCN_{2(s)}} + \mathrm{CO_{(g)}} \tag{4.22}$$

Calcium nitrate is a fertiliser produced by treating limestone ($CaCO_{3(s)}$) with nitric acid (HNO_3), which is then neutralised with ammonia. During the process (CO_2) and water (H_2) are formed. As there is no hydrogen or calcium carbonate in the experimental work, this is not a feasible outcome. Calcium nitride is created when calcium is burnt in air which forms calcium oxide and calcium nitrate, based on the composition of air (79% nitrogen/21% oxygen, by volume) [104]. The only form of calcium introduced into the experiment was in oxide form, so doesn't fulfil the chemical reaction. However, if with the temperatures in the CDST experiment, the calcium could form calcium nitrate, this would be very interesting. Saltpetre is typically produced using potassium and was used in gunpowder and as an ingredient in cigarettes to keep the tobacco alight. Lime saltpetre (calcium nitrate) was created in medieval times as a component of gunpowder, but was claimed to not ignite very well at ambient temperature and pressure. If this compound was heated, for example in a shock tube, maybe it is more readily ignitable. In modern times calcium nitrate is a component used in fertiliser as it readily reacts with water to form ammonia. Finally, calcium cyanamide is another nitrogen fertiliser. Produced at high temperatures (above 1273 K) in the presence of a reducing agent, in this case coal, typically requires an electric arc furnace. Again, the absence of direct carbon is a problem satisfying this chemical equation. The CDST tubes in the driven section are manufactured from AISI 4145H low-alloy steel for hardenability, strength and toughness and considered a medium carbon steel 0.30 – 0.60 % carbon. Whilst its not impossible, but unlikely that the chemical reaction can access carbon embedded in crystalline structure of the steel. In summary, the similarity of the way the CaO interacts with the N_2, to the images of LSPI occurring captured with endoscopic imaging is remarkable. To the authors knowledge, this is the first time this had been observed. Significant focus was placed on the temperature environment for the powder – gas reactions, starting with engine like temperatures, then increasing to temperatures where light emissions could be observed. However, in contrast the test pressures were lower than 'engine like' conditions. This was due to concerns of running high pressures (4 – 6 MPa) as despite the CDST being rated to 15 MPa it hadn't been run at those pressures. During the commissioning phase the pressures realised were accepted as baseline and allowed to vary between tests. In future work a recommendation would be

to control pressure to levels seen in the engine. It could be that increased pressure may reduce (or could indeed increase) the temperature at which a light emissions could occur and important factor in refining this causal mechanism for LSPI.

4.5.1 Advances in LSPI Research

Whilst there is general agreement in the literature that calcium concentration in the lubricant oil promotes LSPI, more recent research by Splitter *et al.* [105], suggests linkages between nitrogen compounds and oil nitration when combined with calcium detergent as a trigger for LSPI. Due to the combustion process in an engine, oxides of nitrogen and nitric acid are formed. Exposure to, and accumulation of, these compounds in the oil could potentially react with the oil detergent. Independently, this work and the work of Splitter *et al.* at Oak Ridge National Laboratories (ORNL) are converging on the significance of the role nitrogen plays in combination with calcium as a trigger for LSPI. Specifically, an ORNL LSPI literature and theory review [71] highlights the following directly linked and supporting information;

- Oxides of nitrogen, via crankcase blowby at elevated loads, could be a source of lubricating oil nitration and an associated source of ignition energy for LSPI promotion. NO_2 + heat + fuel fragments = nitro ester
- A "Goldilocks" criterion is needed for LSPI; not too hot, not too cold, just right!
- Oil volatility has a greater influence on LSPI than reactivity
- Piston top ring zone (TRZ) sampling shows oxidation of lubricant as a function of load, hence the TRZ is more reactive than the sump. The TRZ is a unique "reactor" in the engine. Ring zone samples collected by Busch *et al.* found that the oil viscosity and TAN increased and that there was no time to the onset of oxidation. This gives the material in the TRZ potential for unique properties and chemistry
- Used oil from engine tests showed the presence of acid, hydroxyl, carbonyl, nitrate, and nitro groups. There were variations in the relative intensities dependent upon the fuels used. The ignition delay of nitro compounds is significantly reduced.

- Nitro compounds have a strong effect on the high-temperature oxidation process, hence strongly promote pre-ignition, Downs *et al.*, 1950
- Nitro esters have an accelerated decomposition in the presence of alkali metal oxides ($CaCO_3$ and MgO), Toland *et al.*, 2003
- Increasing the quantity of $CaCO_3$ in calcium ammonium nitrate (CAN) fertilizer reduces the activation energy and chemical decomposition process Poplawski *et al.*, 2016
- Zinc + acid reduces nitrate esters. The anti-wear additive zinc dialkyl dithiophosphate (ZDDP) has been shown to reduce LSPI, Almog and Zitrin, 2009

Whilst the work reported in this thesis was not definitive in finding a clear chemical pathway to explains nitrogens role in LSPI, it has contributed to new findings which must form a part of the puzzle. Existing chemistry texts do not readily yield a explanation, but by testing with carbon dioxide and argon, isolates and confirms a link between these elements ($CaO + N_2$) when temperature is increased. Gas temperature was an important factor, this research proved that the end of compression temperature is insufficient to promote any form of visible output. This therefore suggests that in a running engine trapped residual gas must be present, locally heating the in-cylinder charge to 800 – 1100 K to create a 'Goldilocks criterion', then a oil droplet containing thermally decomposed calcium carbonate to calcium oxide must pass through this and ignite the premixed charge. This would also be considered irregular and thus aligns with the stochastic nature of LSPI.

4.6 Conclusion

In conclusion, it can be seen that; the results presented to date, neither unambiguously disprove or prove the 'Chiba hypothesis'. Exciting new data was presented, suggesting a yet unidentified reaction pathway between $CaO + N_2$ as a potential causal mechanism for LSPI. This work concluded that by this mechanism, end of compression temperature was insufficient to trigger a visible light emission from $CaO + N_2$. Due to the temperature dependency, local heating of the premixed charge, most likely due to trapped internal residual gas, is required to raise the gasses in the region of 800 – 1000 K to observe a light emission from the calcium oxide. Testing with argon confirmed that

N_2 is participating in some way to the light emission from CaO, in a way that's not present when argon was used. The chemical kinetic timescales are very short, CDST 'test time' was less than 3 ms, during and following this time, significant light emissions were observed for extended durations. As no readily available chemical reaction was found that fits this observation, the energy released is not quantifiable. This would have been useful to explore in terms of identifying the ignition energy present when light is emitted to quantify if it was sufficient to trigger LSPI. It was also confirmed that magnesium oxide, doesn't respond in a similar manner as calcium oxide in shock heated nitrogen or carbon dioxide gas environment, hence supports the hypothesis it does not cause LSPI.

Chapter 5

Top Land Crevice Sampling

5.1 Introduction

In the previous chapter, shock tube experiments, introducing metal oxide powders into a range of gasses, investigated the fundamentals of oil detergent chemical pathways in relation to LSPI. The comprehensive literature and theory research undertaken by Splitter and co-workers [71], points to the next area of enquiry, the accumulated material in the top land crevice (TLC), also referred to as the top ring zone (TRZ). This area of the combustion chamber often identified as a crevice, provides a unique space for fuel and oil to mix in a cyclic, high temperature and pressure environment. Splitter referred to the TRZ as a unique 'reactor' and previous sampling reported in the literature highlights local oil changes not seen in the oil sump. The objective of this work was to collect a sample from the top land crevice of a running engine using oils with calcium and magnesium detergents and analyse the composition, to build on the shock tube experiments and gain further understanding of potential LSPI mechanisms.

5.2 Top Land Crevice Material

In previous sections of the literature review there have been many references to fuel properties [38] and the effect of oil detergent additives [26, 33, 38, 72–77] and their proposed influence on the likelihood of LSPI. Based on the work of Dahnz [29] and the observations of Thomason [34], control of the oil entering the combustion chamber has a direct link to the occurrence of LSPI. So far its has been the Author's observation that whilst this published work substantiates these as credible

observations, no explanation as to why this causes LSPI has been provided in almost all cases. The papers relating to the impact of metallic detergents in the oil, leave little doubt that the treat rate and type of additive has a strong correlation to LSPI tendency. Again no explanation as to why this causes LSPI at the fundamental chemical kinetic or thermodynamic basis has been provided. Kalghatgi [40] makes reference to a potential catalytic reaction of the metallic oil additives (p164), but doesn't provide any further explanation of a mechanism. This highlights a gap in the current understanding of LSPI.

5.2.1 Top Land Crevice Sampling

A patent (No.# 13/718392, 19/08/2014) can be found relating to a means of dynamic sampling the top land crevice via a bespoke valve, owned by South West Research Institute (SWRI). The purpose of this system is to develop the understanding of the chemical mechanisms leading of LSPI, as a function of fuel and oil reacting in the top land crevice [106]. A schematic of the layout can be seen in Figure 5.1.

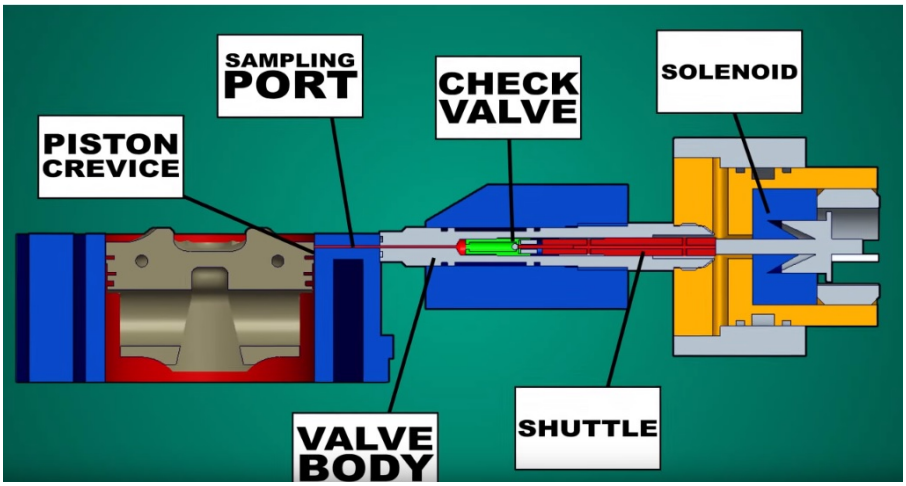

Figure 5.1: Schematic of the SWRI Crevice Sampling Valve, shown sampling from the piston top land crevice.

An alternative method of crevice sampling was used by Lee *et al.* [107] for tribological analysis of the material collected for the top land. A Ricardo Hydra single cylinder engine was modified to enable top land crevice sampling. A 0.5mm hole was drilled through the top land of the piston, above the top compression ring. Polytetrafluoroethylene (PTFE) tubing was connected to the drilling and routed through a steel tube mounted on the connecting rod and a lateral restraint was provided to limit

excessive movement of the tube when the engine was running. The sample pipe was passed though a fitting in the crankcase to allow a sample to be collected, whilst retaining the lubricating oil in the sump. The approach was to run the engine for approximately 40 hours, determined experimentally, to obtain a passive 25ml sample from the top land crevice. This technique relies on the pressure differential between the ring groove, created by the in-cylinder pressure and atmospheric pressure where the sample bottle is sited. This is considered to be a very simple alternative to the complex SWRI alternative, however the passive system can't sample at a selectable point in the engine cycle, which may or may not be a drawback.

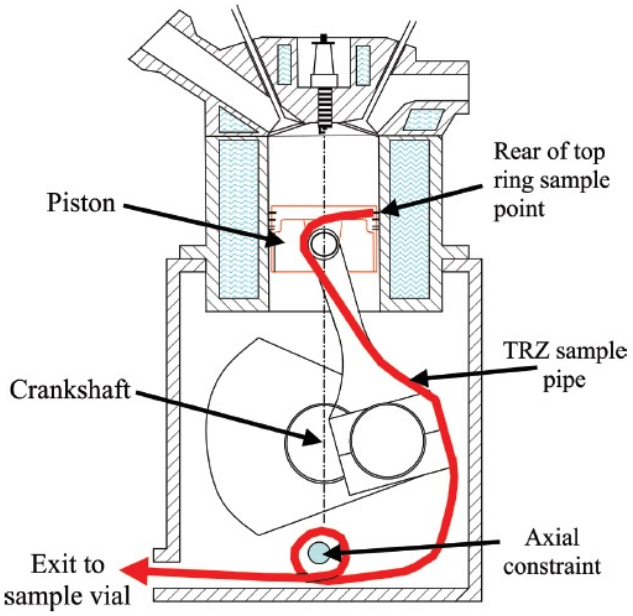

Figure 5.2: Top Ring Zone (TRZ) sampling, Lee *et al.* [107]

Note on authorship and collaborative working

The work described in this chapter is a result of the collaborative efforts of the author, Dr Navin Kalian of Jaguar Land Rover, Dr Mark Barrow and Mrs Latifa Alostad of Warwick University, and the BP-Castrol laboratories. The author conceived the methodology based on a modification of the approach used by Lee and co-authors. Dr Kalian oversaw the running of the SCE which was conducted during COVID 19 lockdown. The author defined the test matrix, operating conditions, test durations and conducted all of the result analysis. The initial laboratory oil analysis was conducted at BP Castrol laboratories in Pangbourne, also during lockdown. The selection of the oil analytical

techniques was a collaboration between the author, Dr Martin Gold and Duncan Leetch, of BP Castrol. Later, further oil analysis was conducted by Mrs Alostad using the Petroleomics techniques and supervised by Dr Barrow, in the laboratory at Warwick University. Subsequent further analysis of the results and findings was conducted by the author.

5.3 Experimental Set-up

The Ricardo Hydra single cylinder engine was chosen to collect a suitable top land crevice sample. This is due to the fact that there is relatively easy access through the crankcase and it is a more cost effective solution compared to a multi-cylinder engine and dynamometer test cell. A schematic of the piston modifications required to obtain an oil sample is shown in Figure 5.3.

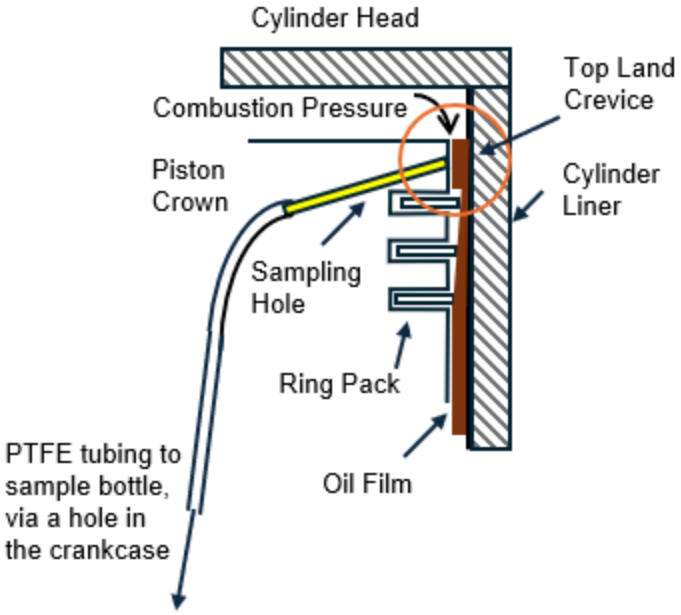

Figure 5.3: Piston top land crevice sampling schematic

A 3 mm hole was drilled through the piston crown to access the area above the top piston ring, highlighted in yellow in Figure 5.3. A PTFE tube was routed through the crank-case, guided by steel tubes attached to the connecting rod and fixed to a spigot on the rear of the hole in the piston crown. A 35ml glass vial was mounted to the crank-case and the PTFE tube was inserted into the vial. The operating principle is that the accumulated oil flows through the hole in the piston and into the vial outside the engine. The pressure in the combustion chamber is higher than the atmospheric pressure for most of the engine cycle and this will drive oil into the vial.

Engine Specification

A Ricardo Hydra single cylinder engine was fitted with a piston, liner and cylinder head with the specification detailed in Table 5.1. The piston, connecting-rod and crankcase were modified to facilitate top land crevice sampling, as shown in Figure 5.4. Despite LSPI occurring at high BMEP and low engine speed, it was concluded early that the sampling system would be insufficiently durable under these conditions to successfully and relatability collect a crevice sample. Replicating this operating condition would have also necessitated the addition of a pressure charged system, not possible without significant modification. Therefore, the objective became dynamically capturing a TLC sample at 1500 rpm, 9 bar BMEP. Based on the previous experience of Lee *et al.* [107], it was suggested that the engine should be run for circa 40 - 50 hours to generate a suitable sample, targetting 50 ml.

Table 5.1: Combustion system specification

Combustion System	Spray Guided, Direct Injection
Valve-train	Double over-head cam, variable int & exh phasing, continuously variable timing and lift
Aspiration	Naturally-aspirated
Cyl Displacement [cm^3]	499.2
Compression Ratio	10.5:1
Bore [mm]	83.00
Stroke [mm]	92.00
Fuel [RON/Ethanol Content]	95/E10
Oil Type	Castrol 0W 20

Engine Settings

Detailed operating conditions for all of the engine actuators can be found in Table 5.2. The settings were fixed for the duration of each test, and controlled using a closed loop controllers for both the dynamometer test bed and engine actuators.

Table 5.2: Engine actuator settings used during testing.

Variable	Set Point	Units
Speed	1500	rev/min
Load (BMEP)	7	bar
Coolant Temperature	90	°C
Oil Temperature	90	°C
Ignition Timing	12	°CA [BTDC]
Start of Injection Timing	300	°CA [BTDC]
Inlet Valve Opining (IVO) at 1mm lift	23	°CA [ATDC]
Inlet Valve Closing (IVC) at 1mm lift	77	°CA [ABDC]
Exhaust Valve Opining (EVO) at 1mm lift	57	°CA [BBDC]
Exhaust Valve Closing (EVC) at 1mm lift	9	°CA [BTDC]
Intake Manifold Pressure (Abs)	920	mbar
Exhaust Back Pressure	6	mbar

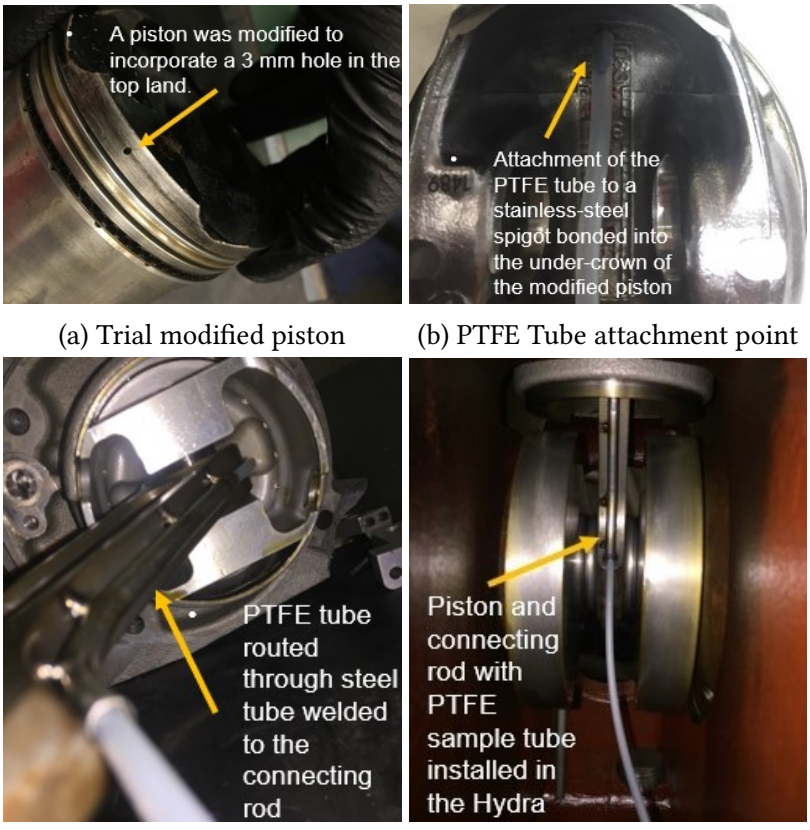

(a) Trial modified piston (b) PTFE Tube attachment point

(c) PTFE Tube routing (d) Sampling system installed

Figure 5.4: Component modifications for top land crevice sampling, based on the approach taken by Lee *et al.* [107]

5.3.1 Methodology

The engine was motored at 800 rpm, no-load, to check the sampling system was robust and the speed was gradually increased to 1500 rpm motoring with no firing. Once confident, fuel was injected and the ignition system was fired, until the engine was running stably at 1500 rpm, 5 bar BMEP. The engine was warmed up for 30 mins, again to assess the durability of the sampling system when firing loads were exerted on the piston and the PTFE sample tube was moving freely in the crankcase. With the coolant at the desired temperature of 90°C, the top land sampling trial commenced, with engine running successfully for 10 hours. A new sample bottle was fitted and testing commenced, with the engine set to 1500 rpm, 9bar BMEP. The engine ran at these conditions for a further 8.5 hours before the first sample line failure. There were multiple sample-line failures, detachments from the piston crown and failures of the attachment point to the piston during the early stages of testing, detailed are provided in Appendix B. The specific operating conditions became a variable in successfully capturing a top land crevice sample. It was established that the temperature of the gas flowing in the sample line was sufficient, when coupled with the movement of the tube in the crankcase, to cause the sample line to melt or collapse due to thermoplastic behaviour of PTFE (melting point ~327 °C). The piston was further modified to include a section of stainless steel tubing attached to the sample hole. Figure 5.5, shows the successful sampling system that was capable of running for a duration of approximately 50 hours. The final step necessary to gain this reliability was to reduce the load to 7 bar BMEP, vs. the original set-point of 9 bar BMEP. An additional problem encountered was condensate management. Whist accumulating a top land crevice oil sample, the sample line could fail multiple times. When this occurred there was a tendency to pull condensate into the sample bottle. Unfortunately this meant that there was some contamination of the oil sample with water. An aspect of the chemical analysis will establish evaluate the effect of water contamination on the chemistry of the TLC sample. In total, ten sample bottles containing crevice oil samples were collected and supplied to BP for analysis. Two further barrels containing the aged sump oil (magnesium and calcium based detergent oils), were also captured, to evaluate this oil in contrast to the top land samples. Finally, a fuel sample was also included, to allow fuel dilution of the oil to be investigated. Details of each sample can be found in Table 5.3.

(a) Sample tube reinforcement (b) High tensile cap-head screw

(c) Guide plates (d) Piston pipe routing

Figure 5.5: Top land crevice oil sampling - successful experimental set-up

5.4 Analytical Techniques

This section describes the laboratory tools and techniques used at BP and University of Warwick to analyse the samples collected from the single cylinder engine top land crevice sampling. These techniques were chosen in collaboration with Dr Martin Gold and Duncan Leetch of BP Castrol. The majority of the techniques are standard for elemental oil analysis e.g. ICP, XFS and CG (all acronyms are explained in the following subsections). Additional more specialised techniques were also employed e.g. ^{31}P NMR for detection of phosphorus and HT SIMDIS for determination of boiling point of a sample. These techniques were largely the full extent of that available in the BP Castrol's Pangbourne laboratory. Later, more specific fuel and lubricant fingerprinting was conducted using FTICR MS at the University of Warwick.

Table 5.3: Sample identification

Sample Number	Detergent/ Oil Type	Speed [rpm]/ BMEP [bar]	Running Hours	Comments
1	Calcium/0W 20	N/A	N/A	New oil, batch:BOT936
2	Calcium/0W 20	1500/5	10	TLC sample
3	Calcium/0W 20	1500/9	8.5	TLC sample
6	Magnesium/0W 20	1500/7	49.5	TLC sample
7	Magnesium/0W 20	N/A	N/A	New oil. Batch: E1553A/057A
8	Calcium/0W 20	N/A	N/A	New oil. Batch: BOT936
9	Calcium/0W 20	1500/7	51	TLC sample
11	N/A	N/A	N/A	95 RON E10 Gasoline
Barrel 1	Magnesium/0W 20	1500/7	62	Sump oil
Barrel 2	Calcium/0W 20	1500/7	51	Sump oil

5.4.1 Inductive Coupled Plasma Spectroscopy (ICP)

ICP is an analysis technique commonly used for identifying elemental concentrations in oil. The principle of operation is; oil is injected into a high temperature argon plasma. The atoms are vapourised and the resulting excitation releases a light emission. The light is focussed into a spectrometer containing a diffraction grating that splits the light into discrete wavelengths as a result of the angle of diffraction. The intensity of light from each angle of the grating referred to as a 'channel' is measured using a photodiode. The output voltage is converted into a concentration using a calibration process. A limitation of this technique is that it can only measure particles less than 3 microns in size. An variation of this technique is a rotating disc electrode (RDE) instrument. It has the capability to measure larger particles in the size range 3 - 10 microns, therefore whilst the accuracy of both machines is similar, they may give a different results as a function of the particle size of the metals or other contaminants [108]. ICP is a frequently used technique to measure oil composition and for wear metal trend analysis. In this work ICP was used to take evaluate

the composition of new oil, sump oil and the top land crevice sample. ICP can identify individual chemical concentrations such a zinc, however it cant speciate the type i.e. zinc oxide. Whilst ICP oil analysis is highly effective for detecting trace elements, monitoring lubricant health and wear metal trend analysis, its limitations mean that it is used in combination with complementary techniques for a more comprehensive understanding of the oil condition. This analysis was conducted at BP Castrol.

5.4.2 X-Ray Florescence Spectroscopy (XRF)

XRF is a laboratory technique also used to conduct elemental analysis. A proton beam is used to excite the inner electrons of an element or range of elements. As the element becomes de-excited X-rays are released (florescence), which can be absorbed by a detector. This process is described as “electron shell resonance absorption" based on the Mössbauer effect; whereby emission and absorption gamma rays of certain atoms are embedded in certain materials [109]. The X-radiation emitted is referred to as the X-ray florescence spectrum. This technique allows for both speciation (channel) and concentration (counts) to be measured [110], making this suitable for both qualitative and quantitative measurement. XRF can be used in addition to ICP for quantitative elemental analysis, however in this work, XRF was used to examine the aqueous portion of the calcium TLC sample only, due to condensate contamination (the magnesium sample was unaffected). Details of the results will be discussed later in this chapter.

5.4.3 Phosphorus-31 Nuclear Magnetic Resonance (^{31}P NMR)

Nuclear Magnetic Resonance (^{31}P NMR) is a techniques that utilises a magnet, a radio-frequency (RF) transmitter or oscillator and an RF detector. A sample of material will consist of atoms who’s nuclei have, or have not, certain magnetic properties. When this sample is place between a magnetic pole gap and exposed to an oscillating magnetic field in the RF frequency range, absorption (resonance) of the RF energy occurs at certain combinations of frequency which is picked up by the detector. The output of the detector is measured at constant oscillator frequency as a function of the strength of the magnetic field [111]. Phosphorus-31 Nuclear Magnetic Resonance (^{31}P NMR) spectroscopy is a variation on the standard NMR specifically targeted at substances contain-

ing phosphorus. When applied to engine oils, it is used to evaluate additive depletion. In this work it was used to evaluate the anti-wear additive Zinc dialkyldithiophosphates (ZDDP). According to literature, ZDDP is considered a moderator for LSPI and its morphology in the top land crevice may help explain its role [112].

5.4.4 Gas Chromatography (GC) and High Temperature Simulated Distillation (HT SIMDIS)

Gas chromatography has been widely used in many fields of science for determining how many components and in what quantity are present in a sample. In gas chromatography the sample is introduced as molecules on a surface or as a liquid solution. As the sample is passed into the GC it is exposed to a high temperature (200 - 300°C) so that it vaporises and is mixed with a carrier gas of He, N_2 or H_2. The sample moves into a separation section called a chromatographic column which is typically a fused silica capillary covered with a thin polymer coating. As the sample passes through this column, analyte particles are carried by the gas and separated into stationary and mobile forms based on their chemical structure. At the end of the tube is a detector which typically detects thermal conductivity, flame ionisation or electron capture. Each of these detectors would output an electrical signal which is proportional to the amount of similar molecules. The result is a chromatogram which displays this varying signal vs. time. High Temperature simulated distillation uses a Gas Chromatograph with a high temperature vaporiser for quick determination of the boiling point distribution of a sample or 'simulated distillation'. The detector is typically a flame ionisation type, and the sample is injected into the system for analysis [113]. Due to their volatility this technique is particularly useful for analysing hydrocarbon fuels and lubricants [114]. In this work GC was used to quantify the fuel in oil dilution of the TLC and sump samples.

5.5 Results

The oil samples were supplied to the oil analysis laboratory at BP's site in Pangbourne. The samples were located in a cold store to prevent any degradation prior to analysis. The oil samples were subject to ICP, XRF, ^{31}P NMR, GC HT and SIMDIS analysis to establish key performance indicators

for the composition, condition and levels of wear metals/contaminants.

5.5.1 Pre-work (Calcium Detergent Oil Only)

Close to the end of the engine testing with calcium detergent there was a sample line failure which contaminated the top land crevice sample No. 9, with condensate from combustion. The pipe leading away from the oil sample bottle to the test cell extract system collected water and fuel vapour due to cooling and condensation. When the top land crevice sample pipe failed, due to melting in this case, the pipe was exposed to negative pressure from the crankcase depression. The pressure differential caused water to flow in the reverse direction contaminating the TLCS sample. To determine if this was a significant problem for the oil sample and if it rendered it unfit, it was decided to investigate the condensate portion of the sample separately, Figure 5.6 (a).

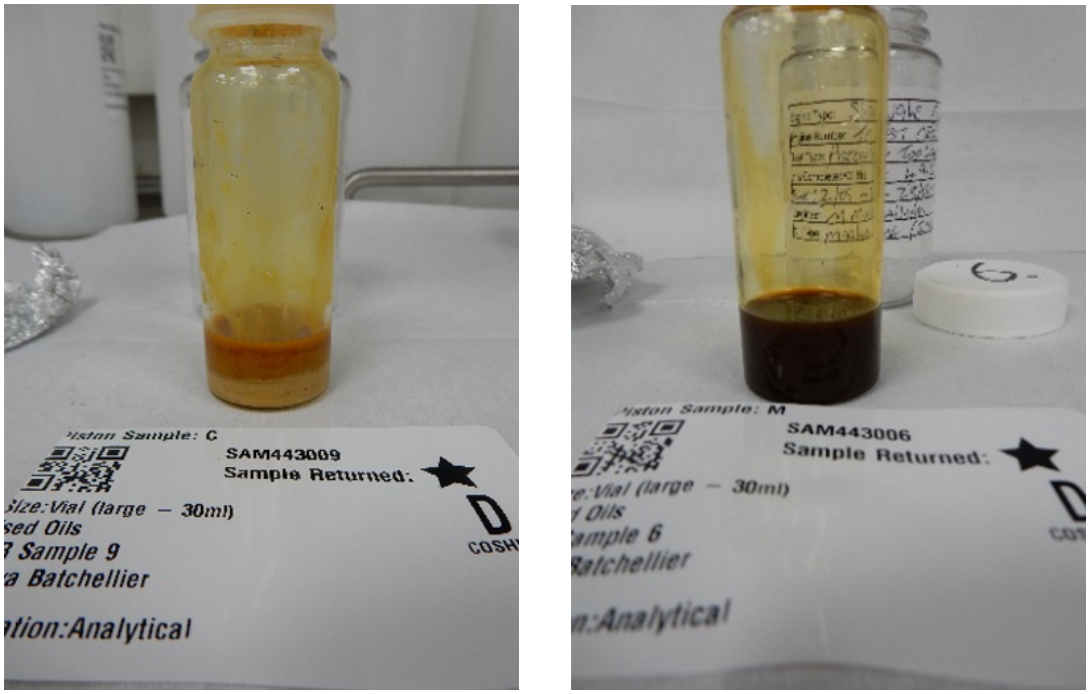

(a) Calcium Detergent Sample No. 9 (b) Magnesium Detergent Sample No. 6

Figure 5.6: Visual comparison of the top land crevice samples – Effect of water contamination.

X-Ray Florescence Spectroscopy, as described in section §5.4.2, was used to analyse the condensate portion of sample No. 9, prior to analysis of the oil portion to establish the impact of water contamination. This was a problem exclusively for sample No. 9 (calcium oil detergent). The effect of water addition has led to separation, emulsification and a change in colour of the sample, as shown in Figure 5.6 (a), when compared to the magnesium detergent top land crevice sample (b). The XRF

analysis found traces of the following elements; Calcium (Ca), Zinc (Zn), Sulphur (S), Phosphorus (P), Chlorine (Cl), Nickel (Ni), Iron (Fe), Copper (Cu) and Silicon (Si), Figure 5.7.

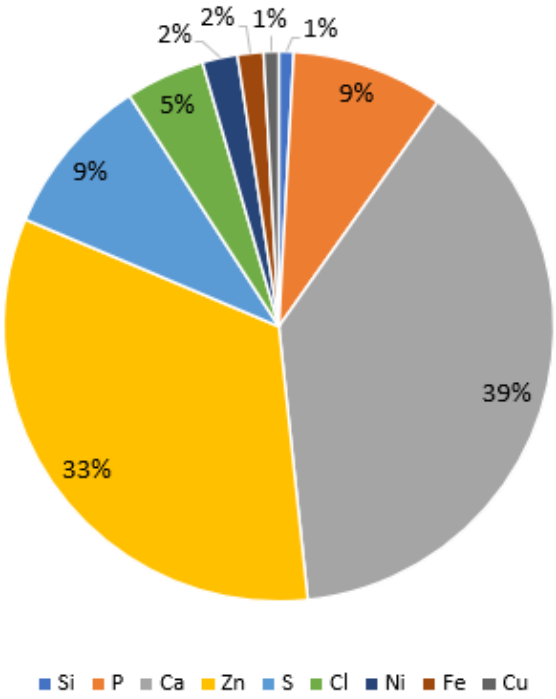

Figure 5.7: Qualitative XRF results - Aqueous portion of sample 9 (calcium oil detergent). Uncertainty ± 5% (ASTM E1621 and ASTM E177).

It must therefore be assumed that water contamination has had some effect on the properties of the sample. There is a minimum mass requirement for the XRF machine of 0.7g, however only 0.3g of aqueous solution was available. Therefore the BP laboratory recommended not to use the absolute values from this analysis directly. Instead a relative qualitative comparison was made in Figure 5.7, in terms of the concentrations relative to the overall sampled elements. It can be seen that calcium and zinc made up 74% of the sample, followed by phosphorus and sulphur both at 9% respectively. Calcium, zinc, sulphur and phosphorus are constituents of the additive pack, calcium as a detergent and zinc/phosphorus/sulphur for their anti-wear and oxidation resistance properties. There is a high concentration of chlorine, 5% of the sample (468 ppm). As a reference domestic tap water has 4 ppm maximum chlorine limit, so this is surprisingly high as the water is the product of complete combustion. The remaining elements; nickel, silicon, iron and copper are predominantly wear metals and in low concentration, 1 - 2%. The impact of the water contamination will be discussed in more detail in section §5.5.2. The positive outcome was that the oil could still be meaningfully analysed, but care was necessary when examining the results of Sample 9.

5.5.2 Results - Elemental Analysis

The first oil assessed was an SAE 0W 20 oil with 1850 ppm calcium carbonate detergent, batch; BOT936. A clean oil sample was taken and stored for comparison to the used oil generated by the engine testing. This oil was used to develop the sampling technique and generated samples No. 2 and No. 3 in Table 5.3. The remainder of this section will focus on the analysis results of sample No. 9 (top land crevice oil sample) compared to barrel 2 (sump sample) and No.8 (clean oil). As stated in §2.4 lubricating oil comprises a number of elements, namely the base oil and its additives, aimed at reducing friction, wear and maintaining oil condition between services. In used oil the base composition can be observed in addition to wear metals and contaminants. Figure 5.8 shows the comparative results of; clean oil, sump used oil and the dynamically sampled top land crevice oil.

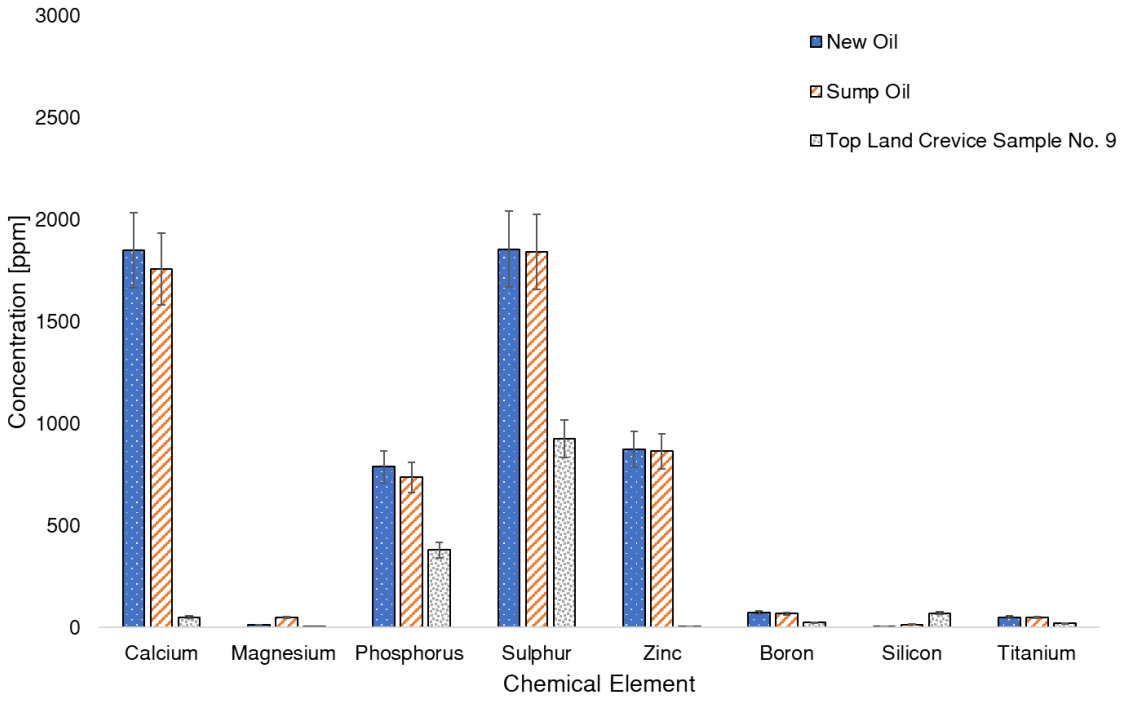

Figure 5.8: ICP analysis of SAE 0W 20 oil additives (calcium based detergent)). The error bars represent an uncertainty of ± 10% (ASTM D5185).

In Figure 5.8, the blue dotted bar shows the calcium carbonate detergent in the new oil at approximately 1850 ppm. The orange striped bar relates to the detergent concentration in the sump and shows that this has only reduced slightly to 1751 ppm or by 5%. This level of change is not surprising, as the oil has only been in the running engine for 50 hours and this is a small time compared to that in a passenger car between services, at approximately 320 hours. The significant change is in

the calcium level in the top land crevice sample, which has reduced to 50 ppm or by 97% compared to the new oil. As described in §5.5.1, the condensate contamination will have reduced the quantity calcium in the TLCS. No evidence could be found in the literature to describe detergent depletion directly, hence an alternative was required. It is known from §2.4.3, that the TBN is an indicator of the detergency of the oil and its ability to counter the build up of acid (quantified as TAN) from the products of combustion. It is therefore proposed to use the reduction of TBN as a surrogate to evaluate the rate of detergent reduction. Wolak [115] analysed 5 x 5w 30 oils with varying ACEA class and categories in a fleet of 25 vehicle, in order to characterise TBN vs. accumulated miles. Figure 5.9. It can be seen that oils CE, ME, MS and PE that there is an initial steep linear reduction in TBN, which then stabilises between 5,000 – 10,000 miles. PS is different in that it had a steady continuous relatively linear reduction vs. mileage.

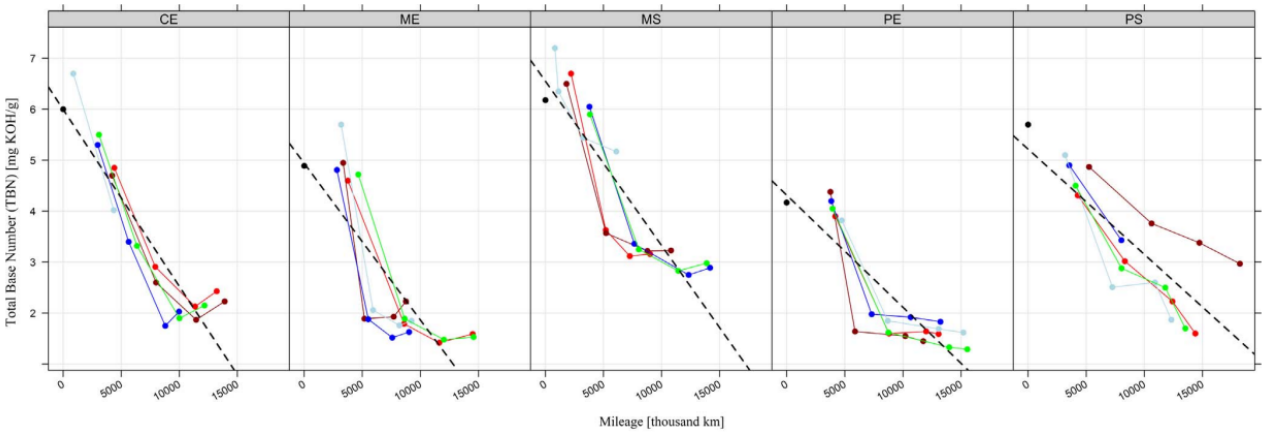

Figure 5.9: TBN reduction vs. vehicle mileage. Surrogate data to characterise potential detergent depletion. CE, ME, MS, PE and PS are anonymous identifiers for 5 different 5W 30 oils with varying base oil and additive compositions.

Further analysis shows the reduction in detergent plotted as; concentration vs. running hours for both the calcium and magnesium TLC samples Figure 5.10. The blue dashed line represents the measured reduction in calcium detergent in the TLC between 0 and 51 hours for the contaminated sample No. 9. The orange dashed line shows the detergent reduction vs. running hours for the magnesium oil sample No. 6. It can be seen that the consumption rate is lower than for the contaminated calcium sample. In order to estimate the reduction rate without contamination, the reduction rate of the magnesium sample was applied to the calcium sample. Based on the findings of Wolak [115], a simple linear model was applied using the gradient of the magnesium reduction rate (sample No. 6) and intercept of the calcium oil (Sample No. 9) at 0 run hours. The predicted reduction resulted

in a value at 51 hours that is approximately 8.6 times higher (432 ppm) than the actual measured sample. The reduction in calcium concentration measured at 10 hours for sample No. 2, lies close the predicted reduction trend line, giving some confidence that this is a reasonable approach. TBN could not be used directly for sample No. 9 as there was insufficient quantity of oil left to satisfy the requirements of ASTM D4739.

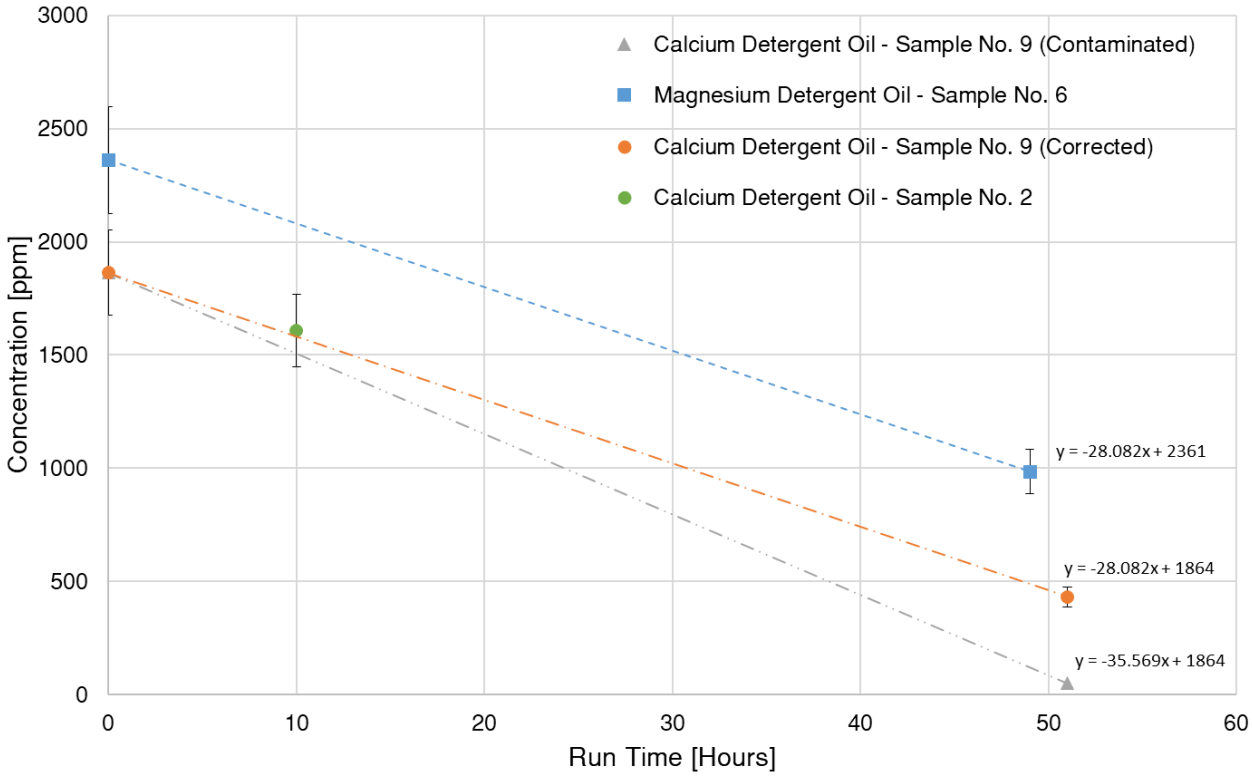

Figure 5.10: TLC calcium detergent reduction measured and predicted vs running hours, 1500 rpm, 7 bar BMEP. The error bars represent an uncertainty of ± 10% (ASTM D5185).

The underlying chemical composition of the oil containing calcium detergent had a very low concentration of magnesium, 12 ppm according to ICP analysis. The orange striped bar in 5.8 shows the sump concentration after 51 hours running has increased to 48 ppm. This is thought to be due to cross contamination from the testing of magnesium detergent oil prior to the testing of the calcium detergent oil. Despite flushing of the sump and oil coolers in the engine test cell between runs, its likely that this has accumulated in the sump. There are only small traces of magnesium in the TLCS, 2 ppm.

The second oil assessed was an SAE 0W 20 Castrol oil with approx. 2300 ppm magnesium carbonate detergent, batch; E1553A/507A, which was a special oil blended for this experiment. A clean oil sample was taken and stored for comparison to the used oil generated by the engine test 5.3.

Table 5.4: ICP analysis of the elemental components in ZDDP vs. sample location, calcium detergent oil. Items in curved brackets describe the percentage reduction compared to the fresh oil sample. Uncertainty ± 10% (ASTM D5185).

Sample	Fresh Oil [ppm]	Sump Oil [ppm] (% Reduction)	TLC Oil [ppm] (% Reduction)
Phosphorus	788	737 (6)	380 (52)
Sulphur	1856	1841 (1)	927 (50)
Zinc	873	864 (1)	5 (99)

Sample identification is as follows: No. 6 (top land crevice oil sample), barrel 1 (sump contents) and No.7 (clean oil). Again, ICP was used to determine the elemental composition of the clean oil, sump bulk used oil and the dynamically sampled top land crevice oil. From Figure 5.11 the following observations can be made: the yellow vertically striped bar shows the magnesium carbonate detergent in the new oil at approximately 2300 ppm. The blue horizontal stripped bar relates to the detergent concentration in the sump and shows that this has only reduced slightly to 2312 ppm or by 2%. This is not surprising as the oil has only been in the running engine for 49 hours. The significant change is the magnesium level in the top land crevice, which has reduced to 985 ppm or by 58% compared to the new oil. In contrast to the calcium detergent oil (sample No. 9), there was no contamination of this sample with tail line condensate. There is no stratification of the sample as shown in Figure 5.6. On this basis the reduction in the detergent levels are a true reflection of the reduction rate in the TLC (approx 28 ppm/hour), as shown in Figure 5.10. There is a small quantity of calcium present in the ICP analysis of the magnesium detergent oil, which is highest in the sump sample. Its is likely that this is due to cross contamination of the oil samples, despite flushing between runs. The single cylinder engine has been exclusively run on lubricating oils containing calcium based detergent oils for many years, so despite the cross contamination, this is seen a quite a low quantity and unlikely to have a negative effect on the results for the magnesium detergent oil. Figure 5.8 also shows a comparison of the ZDDP elements for fresh oil and the sump, for the calcium detergent oil. As with the calcium there have been only minor changes to the levels in the sump oil compared to new oil (1 - 6%) reduction. In contrast the TLCS shows significant reductions: phosphorus (52%), sulphur (50%) and zinc (99%).

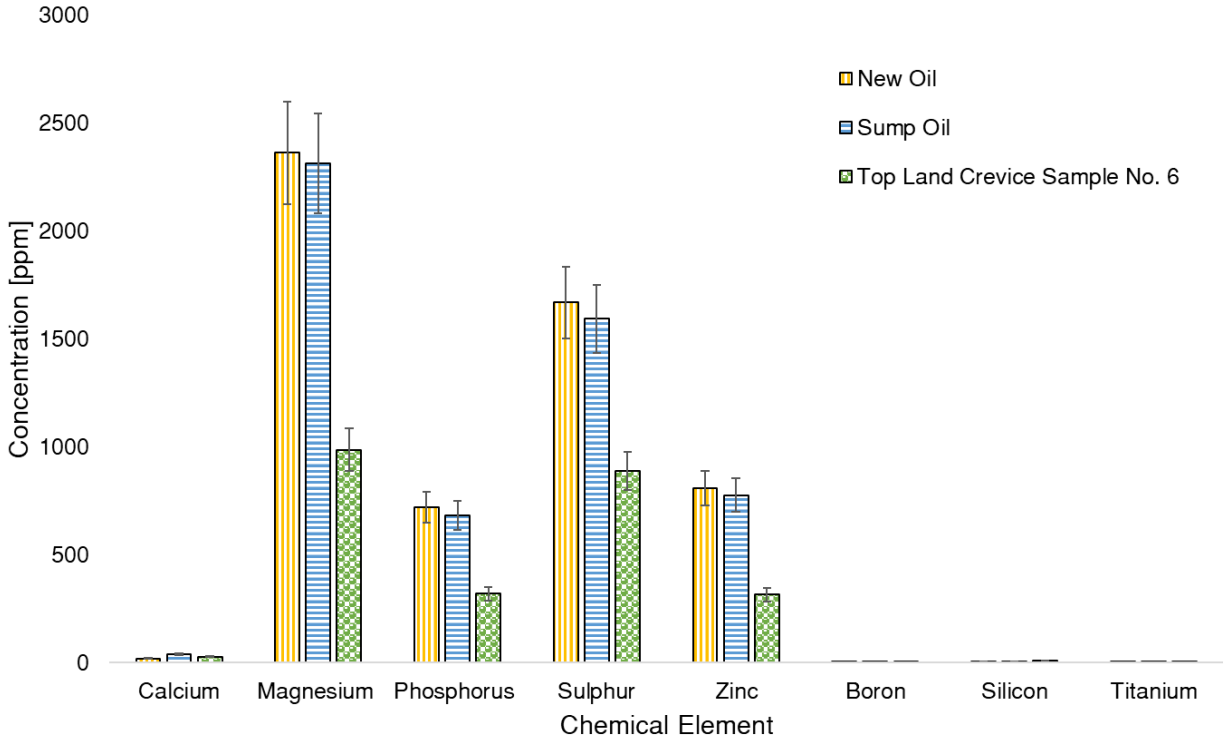

Figure 5.11: ICP analysis of SAE 0W 20 oil additives (Magnesium Based Detergent)). The error bars represent an uncertainty of ± 10% (ASTM D5185).

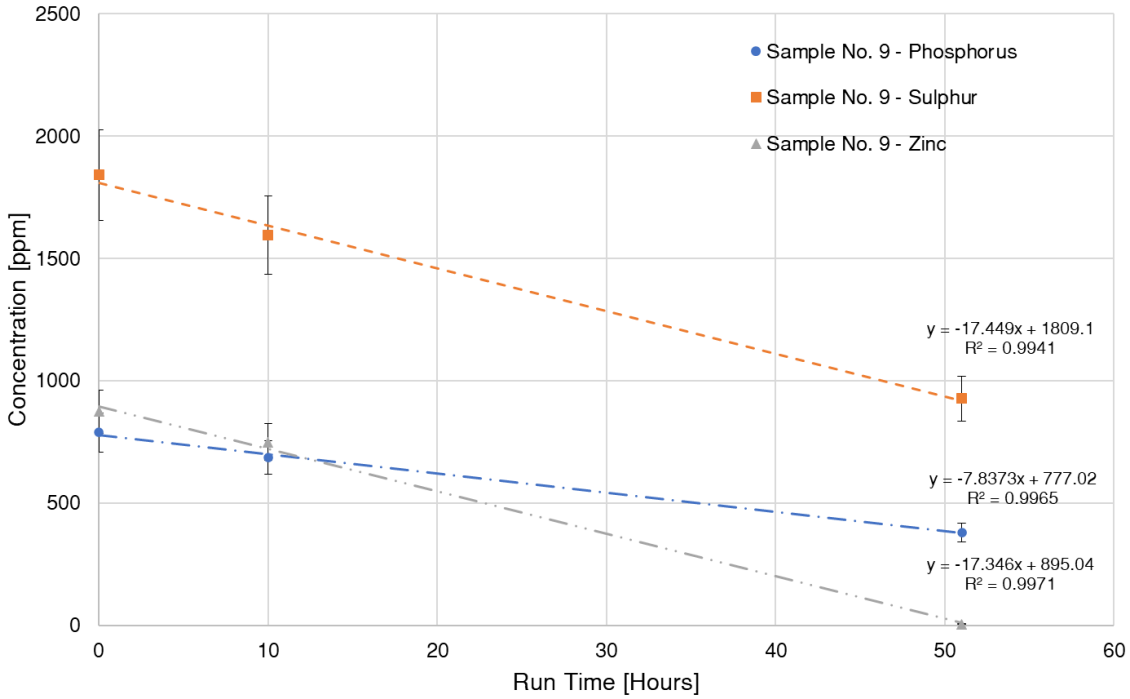

Figure 5.12: Reduction of the components in ZDDP vs. run time (1500 rpm, 7 bar BMEP). The error bars represent an uncertainty of ± 10% (ASTM D5185).

As with the calcium, the ZDDP components may have been affected by the water contamination described in §5.5.1. Figure 5.12 shows the reduction of the components within ZDDP from the TLCS vs. run time at 1500 rpm, 7bar BMEP. The question here is "have the components of ZDDP been affected by the water contamination?" If the qualitative XRF results in Figure 5.7 are considered; zinc was the second highest constituent in the aqueous portion of the TLCs at 33%, followed by phosphorus and sulphur being similar at 9%. When compared to the ICP results from Table 5.4 phosphorus and sulphur had reduced by approximately 50%. This indicatively suggests that the water contamination has had only a minor effect on the these components. However, the zinc is almost completely gone with only 1% or 5 ppm present in the TLCS, suggesting that the water contamination has affected the reduction rate of zinc in a similar way to calcium. If the second points, at approximately 10 hours in the graphs in Figure 5.12, are evaluated for phosphorus and sulphur, they are very close to the reduction trend lines vs run time. For zinc only, if the end point was removed, on the basis that the final value was influenced by water contamination, the new equation for the line (based on the first and second point only) would extend the run time to zinc depleted to approximately 70.4 hours. This is less than anticipated and suggests that the LSPI suppressing properties of ZDDP are degraded in the TLC of the engine, in the absence of water contamination. As the ZDDP is exposed to metallic surfaces the objective is for the phosphate to form a glassy smooth and tough layer so that it can provide anti-wear protection to the engine components lubricated by the oil. As the ZDDP encounters high temperatures and pressures within the engine, oxidation changes the ZDDP into dithiophosphate. The additive is still available to protect the engine, but with increasing exposure to oxygen at high temperature and pressures it changes into the two stages of thiophosphate as the bonding to the oxygen increase. Hereafter, the additive has changed into phosphate which is inactive and no longer able to provide oxidation and anti-wear protection. Further analysis of the ZDDP was conducted using Phosphorus-31 Nuclear Magnetic Resonance (NMR) as described in §5.4.3. This technique was able to go beyond the basic elemental analysis capability of ICP and XRF and evaluate the compounds within the ZDDP structure. This technique is primarily used to evaluate additive depletion. The compounds of interest are Phosphate (single bond with one oxygen and double bond with another oxygen (O-P=O)), Thiophosphate (single bond between the sulphur and phosphorus, double bond with the oxygen (S-P=O)), Thiophosphate (single bond between the oxygen and phosphorus, double bond with the phosphorus (S=P-O)) and Dithiophosphate (two double

Table 5.5: ZDDP evolution vs. sample location - Calcium detergent oil. Uncertainty ± 5% (ASTM E386).

	New oil [%]	Sump Oil [%]	TLC Oil [%]
ZDDP	97.1	87.3	12.3
Dithiophosphate (S=P=S)	1.8	10	73
Thiophosphate (S=P-O)	0.8	1.6	3.6
Thiophosphate (S-P=O)	0.3	0.2	5
Phosphate (O-P=O)	0	0.9	6.1
Total	100	100	100

bonds between the sulphur and the phosphorus (S=P=S).

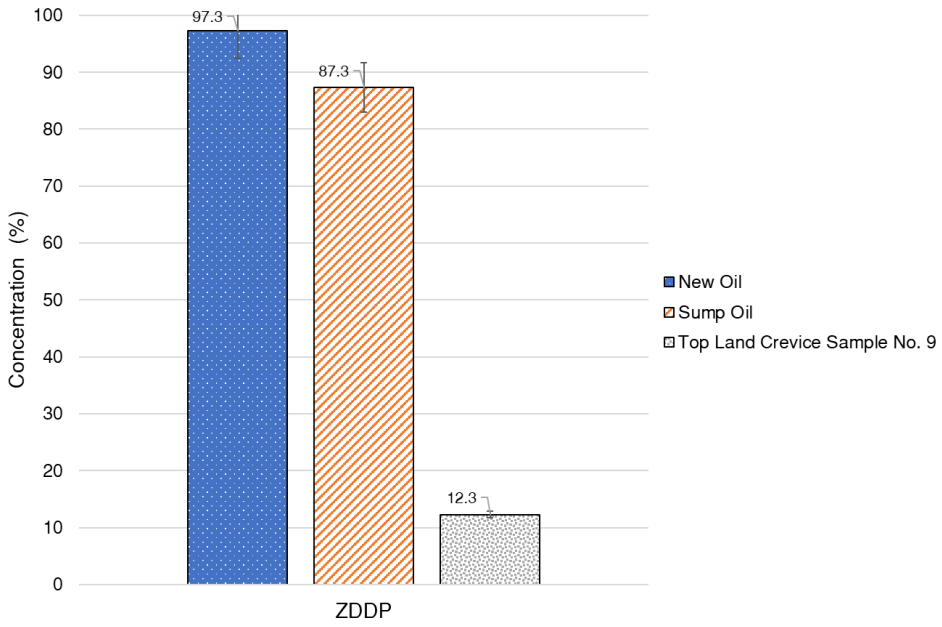

Figure 5.13: (^{31}P NMR) Review of the ZDDP additive pack vs. sample location. The error bars represent ± 5% uncertainty (ASTM E386).

The effect on ZDDP concentration in the three samples can be seen in Figure 5.13. The clean oil sample contains ZDDP at 97.3% of the target value which is within expected blending tolerances for a batch of production lubricant. The ZDDP in the additive pack had not yet been exposed to the running engine and is essentially ready for deposition on surfaces to facilitate its chemical anti-wear and anti-oxidation properties. Table 5.5 shows that the phosphate, thiophosphate and dithiophosphate levels are low, or practically zero. Moving from ZDDP to phosphate (top to bottom in Table 5.5 indicates oxidation and degradation) denotes the reduced capability for ZDDP to perform is role

in the additive pack. The ZDDP in the sump has dropped by 10 % and the dithiophosphate has increased proportionally in turn. This indicates that there is additive capacity in the bulk oil with the objective of delivering the benefits of this additive between services. However in the TLC there has been a more significant effect, the ZDDP has reduced to 12.3% and the dithiophosphate has increased to 73%. The other chemical compounds have increased more modestly, but this highlights that the oil in the TLC is exposed to high temperature and pressure environment this potentially accelerates the oxidation of ZDDP into dithophosphate. ZDDP is said to have an LSPI suppressing properties when the oil is new, and that this degrades with time in the engine. Based on the findings in this work, could be linked with the changing chemical properties of the ZDDP to phosphate and potentially why aged oil is worse for LSPI than new oil, independent of the calcium treat rate. The suppressing effect of ZDDP and alternative alkaline metal additives is discussed in the work of Elliot *et al.* [116]. It was noted that whilst ZDDP had an LSPI reducing effect with increasing concentration, that the total level was limited due to the negative impacts of phosphate ash on exhaust after-treatment. Alternative non-phosphate containing zinc compounds were also found to have a suppressing effect on LSPI. Moreover, Takeuchi and co-workers [78] investigated the effects of base oil composition and alkaline metal additives (various metals and anti-oxidants) namely calcium, zinc dialkyldithiophosphate (ZnDTP or ZDDP), molybdenum dithiocarbamate (MoDTC) and phenolic anti-oxidant (AO), poly-methacrylate (PMA). This work confirmed both the LSPI promoting effect of calcium treat rate and the LSPI suppressing effect of ZnDTP/ZDDP and MoDTC. A variation of this work was later repeated at SWRI [112], and whilst the findings were similar in that the LSPI suppressing effects of Mo and Zn the effect was inconsistent and almost negligible at low calcium concentrations. Table 5.6 shows a comparison of the ZDDP elements for fresh oil and the sump for the magnesium detergent oil. As with the magnesium there have been only minor changes to the levels in the sump oil compared to new oil for ZDDP (4 - 6%) reduction. In contrast the TLCS shows significant reductions: phosphorus (56%), sulphur (47%) and zinc (61%).

Figure 5.14, show the condition of the ZDDP vs. sample location. In contrast to the calcium detergent oil where the ZDDP was 97.3% in the new oil, there is only 80% ZDDP and 20% dithiophosphate. The other forms of phosphate are essentially zero as you would expect in new oil. This implies that either 20% dithiophosphate was intentionally added or a level of degradation due to oxidation has occurred The sump oil has also undergone a more extensive conversion to dithiophosphate compared to the

Table 5.6: ICP analysis of the elemental components in ZDDP vs. sample location, magnesium detergent oil. Items in curved brackets describe the percentage reduction compared to the fresh oil sample. Uncertainty ± 10% (ASTM D5185).

Sample	Fresh Oil [ppm]	Sump Oil [ppm] (% Reduction)	TLC Oil [ppm] (% Reduction)
Phosphorus	721	681 (6)	319 (56)
Sulphur	1668	1592 (5)	888 (47)
Zinc	809	775 (4)	316 (61)

calcium detergent oil (87.3%) vs. 13.5% for the magnesium detergent oil.

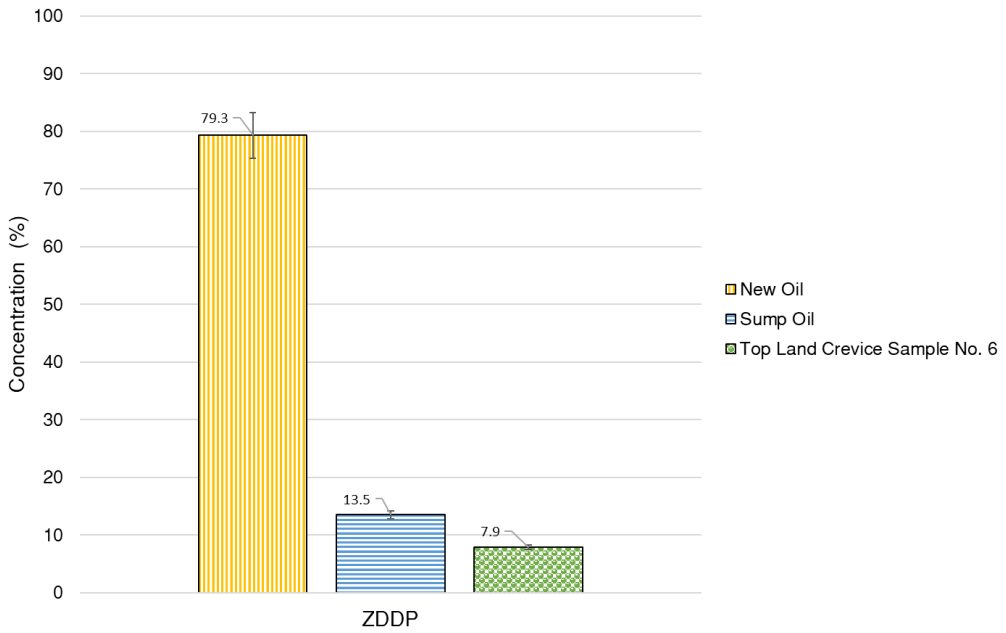

Figure 5.14: (^{31}P NMR) Review of the ZDDP additive pack vs. sample location. The error bars represent ± 5% uncertainty (ASTM E386).

Table 5.7: ZDDP evolution vs. sample location - Magnesium detergent oil. Uncertainty ± 5% (ASTM E386)

	New oil [%]	Sump Oil [%]	TLC Oil [%]
ZDDP	79.3	13.5	7.9
Dithiophosphate (S=P=S)	19.6	66.8	37
Thiophosphate (S=P-O)	0.0	8.9	4.4
Thiophosphate (S-P=O)	0.5	1.8	14.6
Phosphate (O-P=O)	0.7	9.0	36.1
Total	100	100	100

The thiophosphate (S=P-O) is considerably higher and there is phosphate present in the magnesium oil, but only trace in the calcium oil. This indicates high levels of degradation of the ZDDP in this oil due to oxidation, but this must also be an artifact of the oil starting life with 20% dithiophosphate in contrast to the calcium oil (1.8%). In the top land crevice the ZDDP levels are very low at only 8%. The dithiophosphate has reduced by approximately half, in favour of 'depleted' or inactive additives comprising thiophospahte (S-P=O) 14.6% and phosphate 36%. The fact that there is a more spread in the morphology of the ZDDP suggests that without the presence of water a more gradual depletion is likely. Hence in the case of Calcium, the ZDDP should be present for a longer duration, and allow more LSPI suppression whilst being gradually oxidised.

5.5.3 Fuel in Oil Dilution

Fuel in oil dilution (FiO) is the quantity of fuel present in the oil at the various sample locations of interest. Its significance in respect to LSPI is related to the reduction in oil viscosity and hence mobility of oil and fuel containing particles in the combustion chamber. Additionally, in §2.3.1 reference is also made to the fact that fuel properties have an affect on the propensity for LSPI and that certain calibration approaches exist, whereby for example, the injection timing can be varied that also have a significant effect on LSPI tendency. Figure 5.15 shows that there was no fuel in the clean oil sample and only 0.6% (g/g) in the sump. This is low and commensurate with the low running hours at low engine speed and load. In comparison, the TLC sample contains 23% (g/g) fuel. At 1500 rpm, 7 bar BMEP the engine speed and load are relatively low, with a air to fuel ratio of lambda = 1 and could be approximated to a steady cruise in a vehicle. At 23% (g/g) the fuel in oil from the TLC sample is substantially higher than expected from sump oil measurements. Under transient speed/load excursions where LSPI typically occurs the injected fuel mass will be significantly higher than the examined condition to achieve the load, and until recently eradicated by emissions legislation, enriched for higher performance potential. Therefore, potentially the fuel in oil dilution in the TLC, under LSPI promoting operating conditions, could be significantly higher than that measured in the current work.

Figure 5.15, also shows the FiO results for magnesium detergent oil: new oil (0%), the sump (0.6%) an in the TLC (23.5%), which are similar to the test with calcium detergent and reflects the good

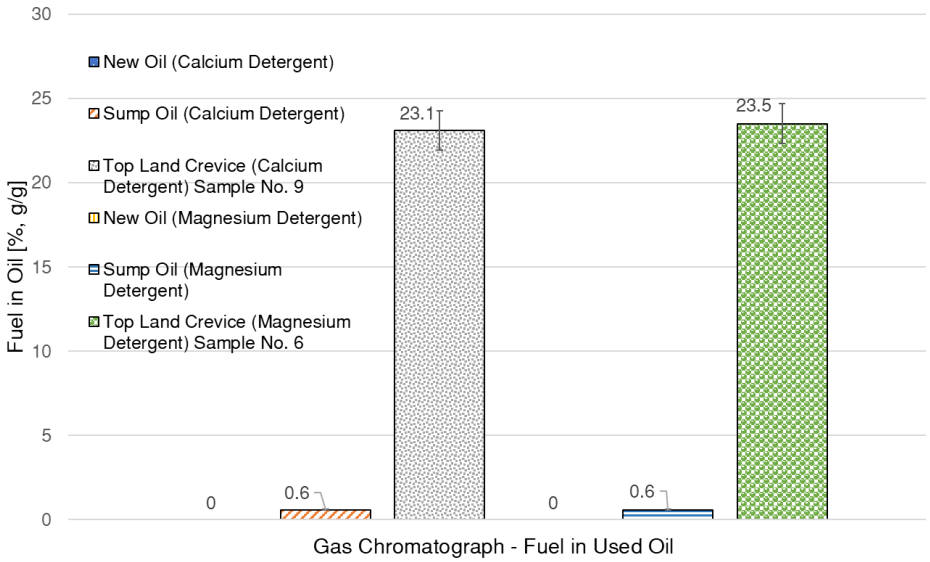

Figure 5.15: Fuel in Oil Dilution (%, g/g), Calcium Detergent Oil - 1500 rpm, 7 bar BMEP, 50 hours run time. Measured via Gas Chromatograph, uncertainty ± 5% (D2887).

test to test repeatability of the experiment. If the LSPI mechanism is assumed to be that proposed by Dahnz [29], then it is useful to evaluate the effect that FiO has had on the kinematic viscosity. There is little data in the open literature for gasoline FiO dilution (in contrast to diesel FiO dilution), that confirms the trend for reducing KV with increasing fuel dilution. An example of such a trend was available from the work of Kramer [117] conducted in 1915, whereby gasoline was added to a number of oils with varying starting viscosity and increasing quantities of gasoline to 20% v/v. These data were converted from viscosity in Saybolt Seconds at 130 °F to Centistokes (cSt) at 54.4 °C and compared to the SAE 0W 20 oil used in this work at 50 °C, Figure 5.16. It's important to note the effect that the absolute viscosity of the oil has on the apparent trend when fuel is added to the oil. Measured data from a fleet of engines running a range of durability tests using the SAE 0W 20 oil, enabled further investigation of the effect of FiO. The engine oil from 1915, evaluated in Figure 5.16 was twice the viscosity of the modern SAE 0W 20 oil at 0% FiO dilution. There is an initial steeper reduction in KV as the FiO dilution increases, the reduction rate then reduces with increased fuel addition. In contrast the 0W 20, has a lower starting KV and what appears to be a relatively flat response with increasing FiO dilution. If a similar comparison of KV is made for the 0W 20 oil, at 40 and 100 °C, Figure 5.17, a similar trend can been seen for the KV40, whereas the KV 100 appears relatively flat.

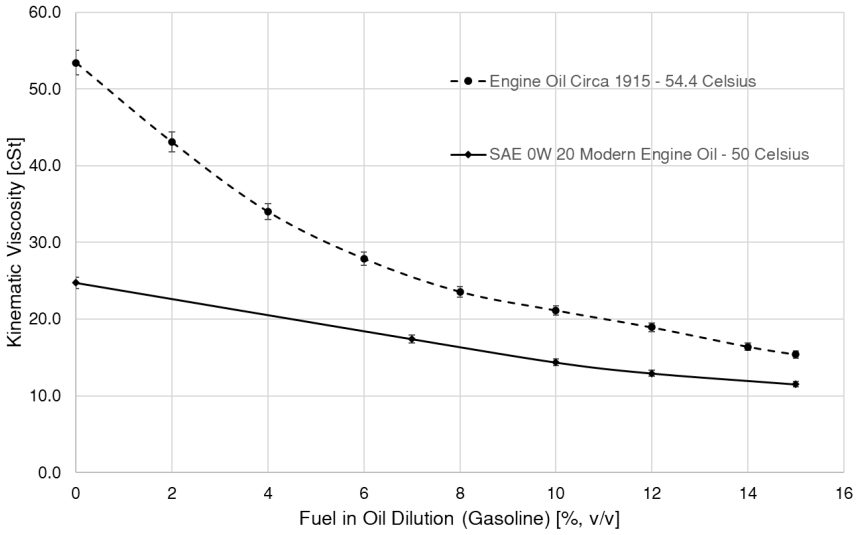

Figure 5.16: Comparison of KV of Measured Fuel in Oil dilution, [117]. The error bars represent ± 3% uncertainty (ASTM D445).

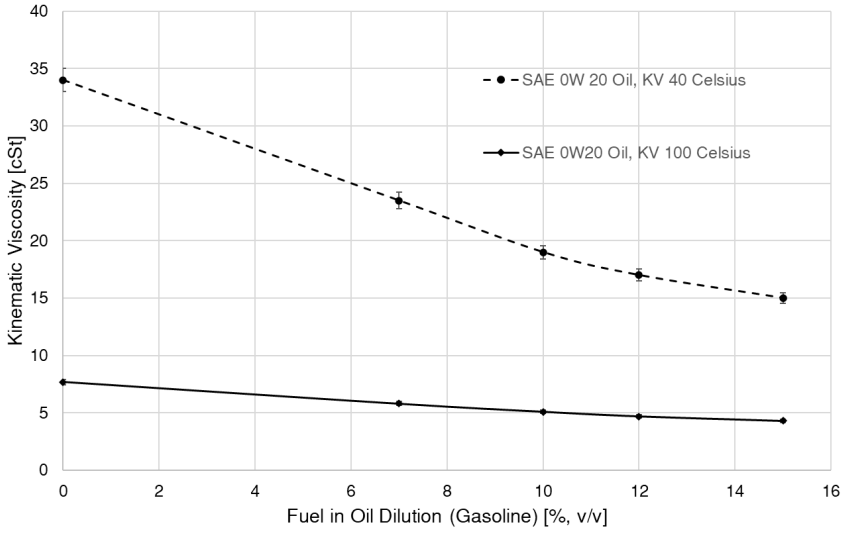

Figure 5.17: SAE 0W 20 Oil, Measured KV40 and KV100 vs. Fuel in oil dilution. The error bars represent ± 3% uncertainty (ASTM D445).

Moreover, the emphasis on understanding the trend of FiO vs. KV was to estimate of the KV resulting from the FiO dilution measured in the TLC sample. Therefore, empirical data from 5 oil samples collected from the measurements provided by JLR, was used to estimate the KV100 at higher FiO levels than the measured data. An initial estimated curve fit was applied to the measured data, then using the solver function in MS Excel, the coefficients of non linear curve fit were optimised to minimise the residual squared errors. The equation from the optimised curve fit was then used to predict the KV100 for the TLC sample for both oils which were in the range of approx 23 - 24%

FiO dilution. The detergent type doesn't influence the viscosity of the oil directly, but the level of detergency may influence the viscosity due to the particles in suspension, this is not accounted for in this model. The modelled curve predicted that the resultant KV100 would be approximately 3.42 cSt. When compared to the new oil the KV100 is 7.7 cSt, which indicates that the viscosity has reduced by 55%.

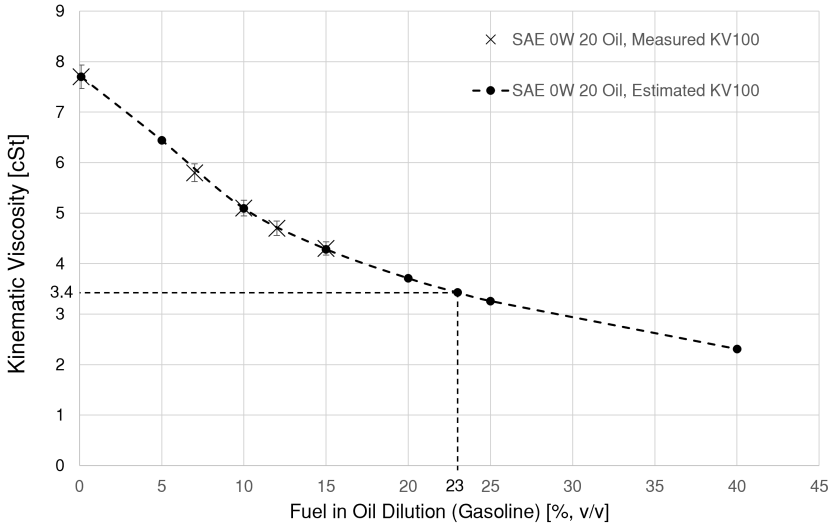

Figure 5.18: Measured and modelled KV100, SAE 0W20 oil from a fleet of 2.0L 4-cyl engines undertaking durability testing. The measurements were conducted at SynLab UK. The error bars represent ± 3% uncertainty (ASTM D445).

It can be seen by the shape of the curve that the gradient of the reduction in viscosity is initially steep up to around 15% FiO, thereafter the gradient is shallower. Based on the earlier comments regarding the fact that the speed and load conditions under which the TLC sample were collected were significantly lower than the conditions that LSPI is known to occur, it can therefore be assumed that the FiO dilution would be higher under LSPI conditions. This curve was then used to forecast KV at double the FiO than that of the measured TLC sample, at 40% FiO. It can be seen that the KV100 drops to 2.31 cSt, or by 70% compared to the new oil. Whilst the exact level of the FiO in the TLC under the LSPI conditions is unknown, the fact that the KV100 reduces significantly, supports the likelihood that this reduced viscosity oil can accumulate in the TLC and result in inertia driven particle mobility. Therefore this current work supports the hypothesis proposed by Dahnz [29] for oil droplet release due to reduced oil viscosity.

Finally, the simulated distillation (SIMDIS) analysis was evaluated for the TLC samples, it can be

seen that they comprises: group I mineral oil, group IV polyalphaolefin synthetic oil (PAO) and gasoline 'heavy ends', as shown in Figure 5.19 (the example shown is from sample No.#6 magnesium detergent, sample No.#9 for calcium detergent oil is similar).

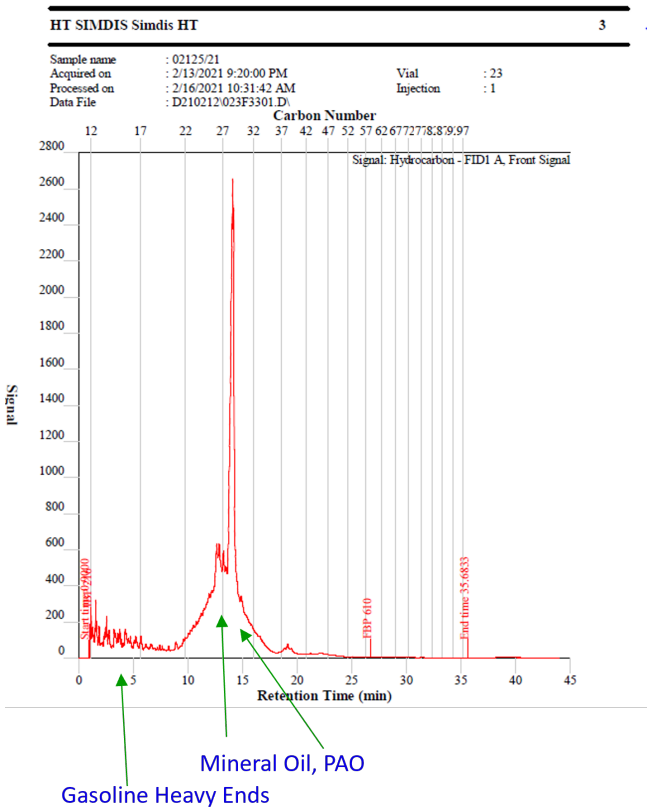

Figure 5.19: SIMDIS analysis, magnesium detergent oil, sample No.#6 - 1500 rpm, 7 bar BMEP, 50 hours run time. Uncertainty ± 5% (ASTM D6352 and D2887).

The fuel 'heavy end's' are identified by their carbon numbers. The carbon number range for EN228 automotive gasoline, typically fall between C4 and C12 but can contain heavier compounds. The significance for LSPI is that the heavier end's don't readily evaporate at the oil temperatures found in the top land crevice and hence accumulate. Figure 5.19 provides evidence of fuel components at carbon numbers of 12 - 17, with reducing concentration. EN590 automotive diesel comprises carbon numbers in the range C10 to C26, so there is evidence of the presence of more diesel like compounds in this sample although the vast majority is lubricating oil.

5.5.4 Total Base Number

The 'total base number' of used oil is an indication of the acidification level of the oil. A low TBN highlights additive depletion and the inability to counteract acid formation resulting from the com-

bustion process, §2.4.3. In this experiment TBN was assessed using a modification of ASTM D4739, which is a standard for assessment of used oil using potentiometric hydrochloric acid titration. The modification to this standard is a BP Castrol propriety method called the 'TBN estimator algorithm', which cannot be described in this thesis for intellectual property (IP) reasons. However, this can be used to make a relative comparison between the key sample locations, even if these values cannot be considered for absolute external comparison.

Table 5.8: Total Base Number - 1500 rpm, 7 bar BMEP, 50 hours run time. Uncertainty ± 5% (ASTM D4739).

	New Oil	Sump Oil (% Reduction)	TLC Oil (% Reduction)
TBN (Calcium detergent oil)	5.3	5.2 (1.9)	0.2 (96.2)
TBN (Magnesium detergent oil)	11.2	11 (1.8)	4.7 (58.3)

Table 5.8 shows that for the calcium detergent oil, the TBN of the new oil and the sump oil are very similar, with only a 1.9% reduction. In contrast, the TLC sample has a very low TBN, 0.2 which represents a 96% reduction and that locally the oil can no longer resist the acidity of combustion. As stated previously, the environment in the top land crevice is very harsh as has a profound effect on the additive pack in the oil. As calcium is the neutralising additive component, this implies that it has been consumed in countering the acidity from combustion. However as this is a dynamic system, new oil containing calcium will continually be replenished into the TLC. This could be a factor in why LSPI is stochastic, in that any droplets released from the top land crevice must contain calcium detergent which would not always be the case based on these results. It can also be seen from Table 5.8 that the TBN of the new and sump samples of the magnesium detergent have reduced by a similar amount to the calcium oil at 1.8%. The magnesium oil has a TBN in the TLC of 4.7 after 49 hours running and hence reduction of 58%. In contrast the calcium detergent oil has reduced by 96%, suggesting it is all but depleted locally in the TLC. The starting TBN of the calcium detergent oil was significantly lower than the magnesium detergent (5.3 vs 11.2) respectively. BP Castrol were asked for an explanation as to the reason for the differences in detergency between the Ca and Mg additives and the following feedback was provided: *The TBN calculator is based on the amount of Ca and Mg in the oil samples and doesn't account for the availability of detergent to do its job. Looking at*

the fresh oil results then the Ca oil is 8.3 mgKOH/g and the Mg oil is 13 mgKOH/g. Having looked at other batches of these oils and the results are consistent so we can assume they are correct. The difference is due to the amount of detergent present in the respective oils and the type of detergent. TBN values vary between different detergents so their contribution to the finished oil is also different hence you are not seeing the same TBN for the two oils here e.g. the Ca oil might have a 250BN detergent and the Mg oil might have a 350BN detergent so even if the treat rates are the same the measured TBN of each oil will be different.

5.5.5 Additive Treat Rate Comparison, Wear Metals and Contaminants

Whilst the detergent treat rates differ between the new oils: calcium oil 1800 ppm and magnesium 2300 ppm respectively, the overall additional additive content is similar at approximately 5500 ppm, Table 5.9.

Table 5.9: Total additive treat rate, new Ca and Mg oils. Uncertainty ± 10% (ASTM D5185).

	New Oil	Sump Oil (% Reduction)	TLC Oil (% Reduction)
Total Additive (Ca oil)	5505	5366 (3)	1408 (74)
Total Additive (Mg oil)	5582	5404 (3)	2540 (53)

These values were obtained by summing all of the additive components; Titanium (Ti), Boron (B), Barium (Ba), calcium or magnesium, phosphorous, sulphur and zinc. It can be seen, in a similar trend to previous sections in this chapter that the new and sump lubricants are typically similar, with only a minor reduction in the sump additives approximately 3% for both oils. In the TLC however, it can be seen that the additives have been significantly reduced. In the case of the magnesium oil this has reduced by 53%, whereas the calcium oil has reduced by 74%. Table 5.10 shows molybdenum to be the stand-out metal in Sample No.#6, magnesium detergent oil. It was checked and confirmed that neither oil contained molybdenum when manufactured. The only notable change was the molybdenum concentration in the magnesium detergent oil, starting at 3% or essentially 0% new, rising to 106 ppm in the TLC sample.

Table 5.10: Notable wear metal, Mg oil. Uncertainty ± 10% (ASTM D5185).

	New Oil [ppm]	Sump Oil [ppm]	TLC Oil [ppm]
Molybdenum (Mg oil)	3	10	106

Rather than a wear metal per se, the source of molybdenum is thought to originate from assembly grease used during the piston fitment in the engine first build, no alternative source of molybdenum is present in the engine. No significant molybdenum concentration was detected in the calcium detergent oil. In terms of contaminates, the main elements detected were sodium and silicon, neither of which were added during manufacture of the oils. Neither contaminant was present in the Mg lubricant in a significant quantity. Notable was the increase of silicon in the TLC for the Ca lubricant, of which the exact origin is unknown, but silicon is a well known sealant that may have been used somewhere in contact with the oil.

Table 5.11: Contaminants, Ca oil. Uncertainty ± 10% (ASTM D5185).

	New Oil [ppm]	Sump Oil [ppm]	TLC Oil [ppm]
Sodium (Ca oil)	3	2	10
Silicon (Ca oil)	3	16	80

There is no mention that could be found in the open literature that pointed to sodium or silicon as a significant contributors to LSPI. Molybdenum was found to have no or a moderating effect on LSPI.

5.6 Further Oil Analysis

The oil analysis presented thus far has given valuable insight into the condition of the engine lubricating oil, the engine wear metals, metallic components of the oil and fuel in oil dilution. Further analysis was undertaken in collaboration with University of Warwick in the field of 'Petroleomics', a molecular-level characterisation of the components of petroleum and petroleum products using ultra-high resolution mass spectrometry (UHR MS) [118] [119]. The objective was to identify chemical species present in the TLC sample that were not initially present in the lubricating new oil or

fuel.

5.6.1 Fourier Transform Ion Cyclotron Resonance Mass Spectrometry

The device used for this additional analysis was a Bruker 15 T Fourier Transform Ion Cyclotron Resonance Mass Spectrometer (FTICR MS) as shown in Figure 5.20.

Figure 5.20: Bruker 15 T Fourier Transform Ion Cyclotron Resonance Mass Spectrometry (FTICR MS), housed at the University of Warwick.

The operating principle of this device is a diluted sample is passed through an ionising source and the resulting gas-phase ions are introduced into an ion cyclotron cell embedded in a constant magnetic field. There a two main ionisation methods used in petroleomics based on the polarity and nature of the sample: Electrospray Ionisation (ESI) and Atmospheric Pressure Photoionisation (APPI). Depending upon the ionisation source and polarity, the following ions are produced: radical ions (M^+ (mostly radical cations) or M^-), protonated $[M+H]^+$, and de-protonated $[M-H]^-$ and these species can be detected in the spectra [119]. Each chemical element or compound is classified according to its mass-to-charge ratio *m/z*, where the total charge q is equal to the number of charges z multiplied by the charge of an electron e. Therefore, the output is a spectra of signal intensity plotted against *m/z* [119]. The mass spectrometry resolving power R, describes the mass spectrometers ability to distinguish between two ions with 'close' mass to charge ratios *m/z*. The resolving power is important, because it evaluates the performance of FTICR MS by making sure the peaks are well

separated and it is inversely proportional to full width at half maximum and directly proportional to acquisition time (T) as shown in (5.1).

$$R = \frac{m}{\Delta m_{50\%}} \propto \frac{q\mathbf{B}T}{mk} \tag{5.1}$$

Where m is mass of the ion in Daltons and $\Delta m_{50\%}$ is the full width at half maximum of the peak (FWHM, this defines the mass difference between two points on the peak where the intensity is 50% of the maximum), **B** is magnitude of the magnetic field, k is the peak width constant and T is the acquisition time. A higher R value indicates better resolution and hence ability to differentiate between closely spaced peaks more readily, Figure 5.21 and Equation (5.1).

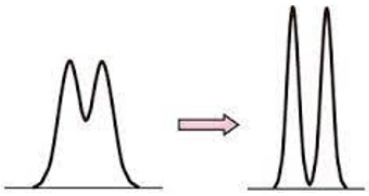

Figure 5.21: Ultra-high resolving power is required to resolve the peaks for petroleum mass spectrometry.

In addition to resolution, the mass accuracy is another important factor, in order to distinguish between molecular assignments within a mass spectrum and accurately assign molecular formulae, UHR MS can achieve sub-parts-per-million (ppm) or even parts per billion (ppb) levels, Equation (5.2) [119].

$$\text{Mass error} = \frac{m_{exp} - m_{calc}}{m_{calc}} \times 10_6 \tag{5.2}$$

Once the ions are generated, the analysis categorises them according to their *m/z* value. In FTICR MS, ions with the same *m/z* have the same cyclotron frequency (ω_c) which is dependent upon the magnetic field and is inversely proportional to *m/z* (5.3) [119].

$$\omega_c = \frac{q\mathbf{B}}{m} \tag{5.3}$$

To achieve the required high mass accuracy for complex mixtures containing hundreds of thousands molecular compositions with close mass differences the test is typically conducted over a wide *m/z* range. Therefore a mass split of 0.1 mDa must be resolved to assign unique molecular compositions up to 500 Da for samples containing C, H, N, O and S [119]. Hence, the mass resolving power of FTICR MS is defined by equations (5.1) and proportional to the resolving time T (5.4) [119].

$$T = \frac{N}{f_s} \tag{5.4}$$

Where N is data set size (typically in megawords e.g. 4M or 8M and so on) and f_s sample frequency, which is defined by the cut-off for detection.

5.6.2 Categorisation

Categorisation usually includes class, carbon number, and DBE. The assignment of elemental compositions typically take the form: C_c H_h N_n O_o S_s, where the lowercase letters indicate the number of each element. Figure 5.22 shows an example FTICR MS spectra from a NIST crude oil sample [119]. (a) denotes the class, which in organic chemistry defines any atoms that are not C or H, in this case examples include: O N S P. (b) Illustrates the double bond equivalent (DBE) or level of unsaturation, calculated using equation (5.5) .

$$\text{DBE} = c - \frac{h}{2} + \frac{n}{2} + 1 \tag{5.5}$$

Where c, h and n are the number of carbon, hydrogen and nitrogen atoms in the molecule. This concept is used to describe the number of rings and double or triple bonds that exist in a molecule. Integer values can be assumed for odd electron ions and half integer values for even electron ions. The Kendrick Mass Defect (KMD) [120] can aid the analysis of complex mixtures such as fuel and

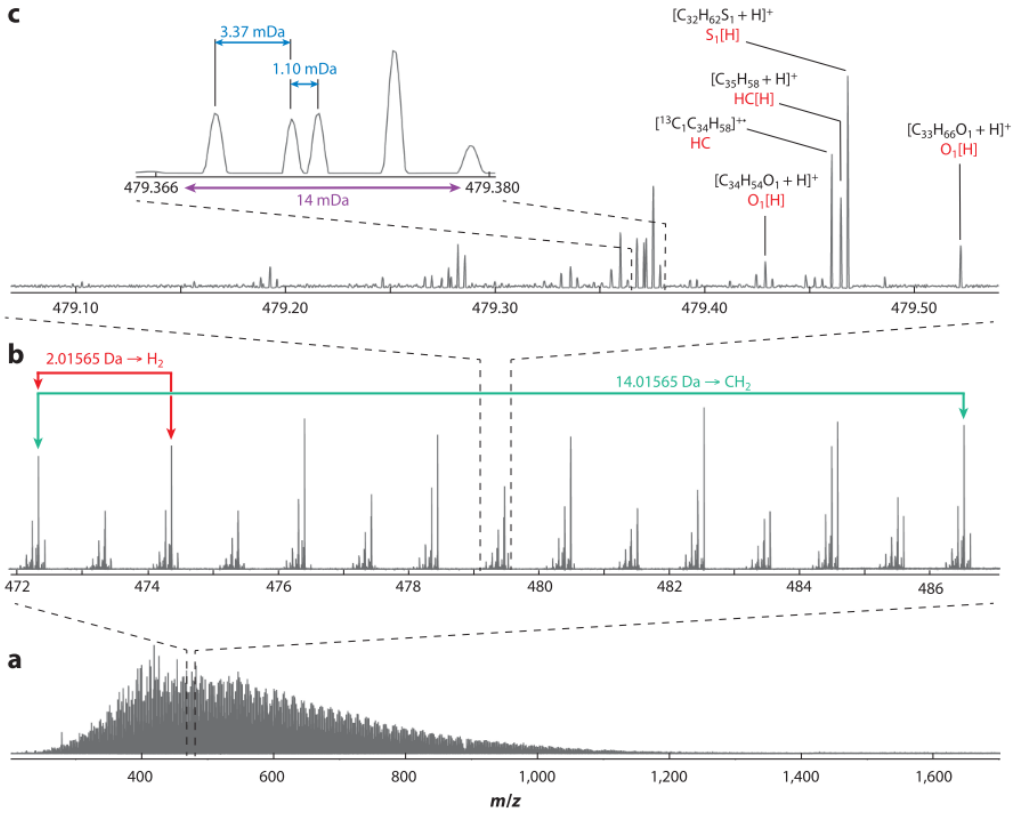

Figure 5.22: (a) FTICR MS of a NIST crude oil sample using APPI. (b) Petroleum species at m/z = 479, separated by 14.01565 Da and 2.01565 Da. (c) Highlighting selected assignments, class designations and common mass splits. The mass difference of 3.37 mDa corresponds to C_3 vs. H_4S and the mass difference of 1.1 mDa corresponds to C_4 vs. $^{13}CH_4S$ [119].

oil sampled from the TLC. This technique uses the repeating mass defect of the 14.01565 Da CH_2 alkyl, to sort members of the same heteroatom class and DBE into a homologous series. Figure 5.22 (b) shows the for H_2 (red arrows separated by 2.01565 Da) CH_2 (green arrows separated by 14.01565 Da). The KMD can be calculated using equations (5.6) and (5.7).

$$\text{exact KMD} = \text{IUPAC mass} \times \left(\frac{14}{14.01565} \right) \tag{5.6}$$

$$\text{KMD} = \text{nominal Kendrick mass} - \text{exact Kendrick mass} \tag{5.7}$$

Where the IUPAC mass typically refers to the atomic mass of an element as defined by the Interna-

tional Union of Pure and Applied Chemistry (IUPAC). Finally, (c) highlights selected assignments, class designations and common mass splits. The mass difference of 3.37 mDa corresponds to C_3 vs. H_4S and the mass difference of 1.1 mDa corresponds to C_4 vs. $^{13}CH_4S$. In addition to the mass spectra, the chemical class distribution and carbon number vs. DBE results are produced to allow for deeper understanding of the samples chemical 'fingerprint'. Figure 5.23 provides a sample class distribution for the NIST crude oil sample. The cyan arrow highlights the Sl chemical class, the scatter plot represents one molecular formula per point, where the x-axis is carbon number (moving from left to right represents the addition of CH_2)) and the y-axis is DBE.

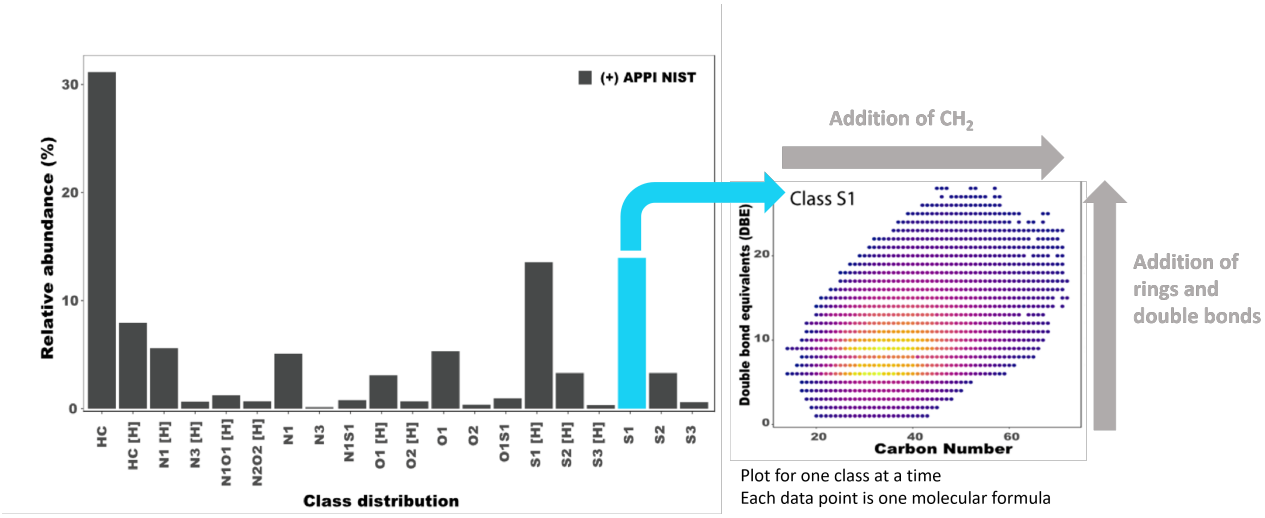

Figure 5.23: Class distribution and DBE characterisation, adapted from [119].

5.6.3 Results

To recap the objective of using FTICR MS in the field of 'Petroleomics' was for: new oil (Sample 8), new fuel (Sample 11) to be compared to the TLC (Sample 9), to identify any new molecules in the TLC sample that were not present in the new fuel or oil, i.e. that had been formed in the TLC 'reactor'. Figure 5.24 compares new oil (sample 8 – red lines) to the TLC (sample 9 – purple lines) over a broadband range of *m/z*. The first observation from the new oil is the number of peaks, intensity and *m/z* range occupied by its molecular composition. The mass spectrum acquired for the TLC sample exhibit lower intensity than the new oil sample, other than at a few locations, and a signifiant new peak around 470 Da. The basic shape characterises of the wide range Spectra 1 (a) are similar at lower *m/z*, this is symptomatic of reduction, depletion or contamination of the

elements in the additive pack, described in §5.5.2. Spectra 2 (b) is a zoomed in window of *m/z* 354 - 365. The repeating patterns are similar between the new and TLC sample, with notable increase in abundance in the TLC sample at approx 359.3 Da and 364.4 Da.

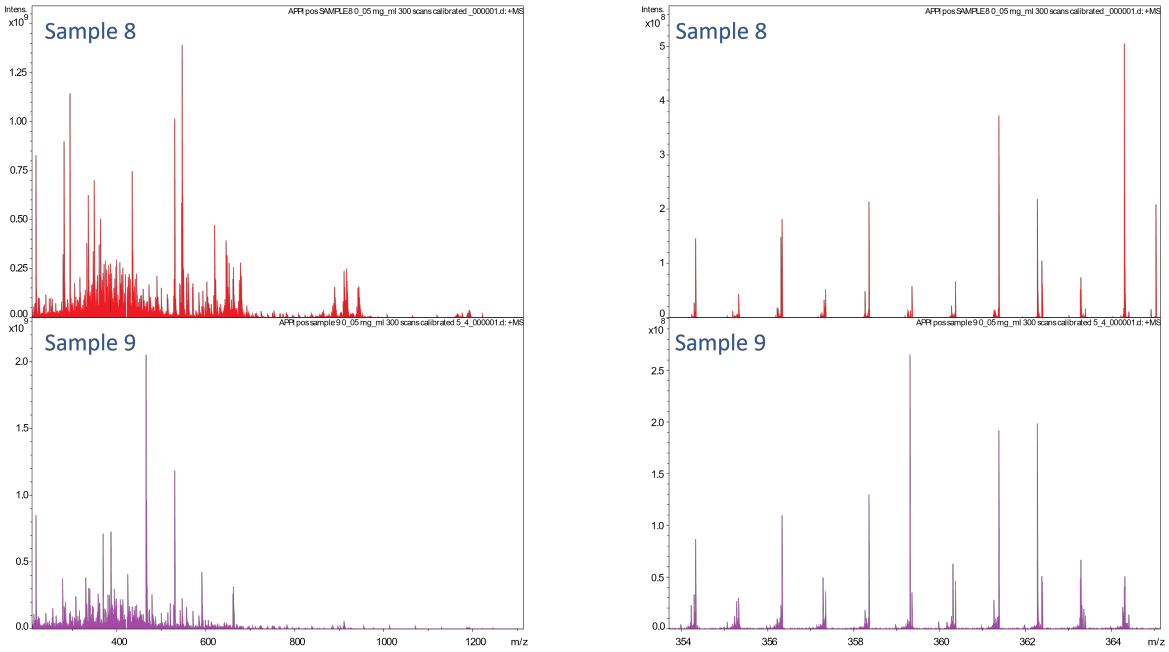

(a) Spectra 1: broadband range *m/z*.

(b) Spectra 2: zoomed in window 354 - 365 *m/z*.

Figure 5.24: (+) APPI – FTICR MS, comparison of new 0W 20 oil (sample 8 – red lines) vs. TLC (sample 9 – purple lines).

Figure 5.25 (a) is a zoomed window at 359 Da, with a 0.4 Da window and highlights a number of carbon-13 isotopes and hydrogen (protonated or radicals). Isotopes are a variant of a chemical element with the same number of protons, but and different number of neutrons in the nucleus, in the case of carbon-13 there are 6 protons and 7 neutrons. The process of protonation is where a molecule or atom gains a proton. Radicals are molecules or atoms that have an unpaired electron, making them highly reactive [121]. Whilst there are a number of complex compounds in the new oil, of note is the new isotope formed in the TLC between 359.0 – 359.25 Da, a new compound not present in the new oil. Moreover, if Spectra 4 (b) is examined, a new compound of interest in relation to the current work was apparent, $C_{22}H_{33}NO_3$ a radical cation. Created in the TLC, this could be a nitrate ion or a molecule containing one nitrogen atom and three oxygen atoms and part of a function group of: esters, carboxyls or nitro compounds, potentially consistent with the work of

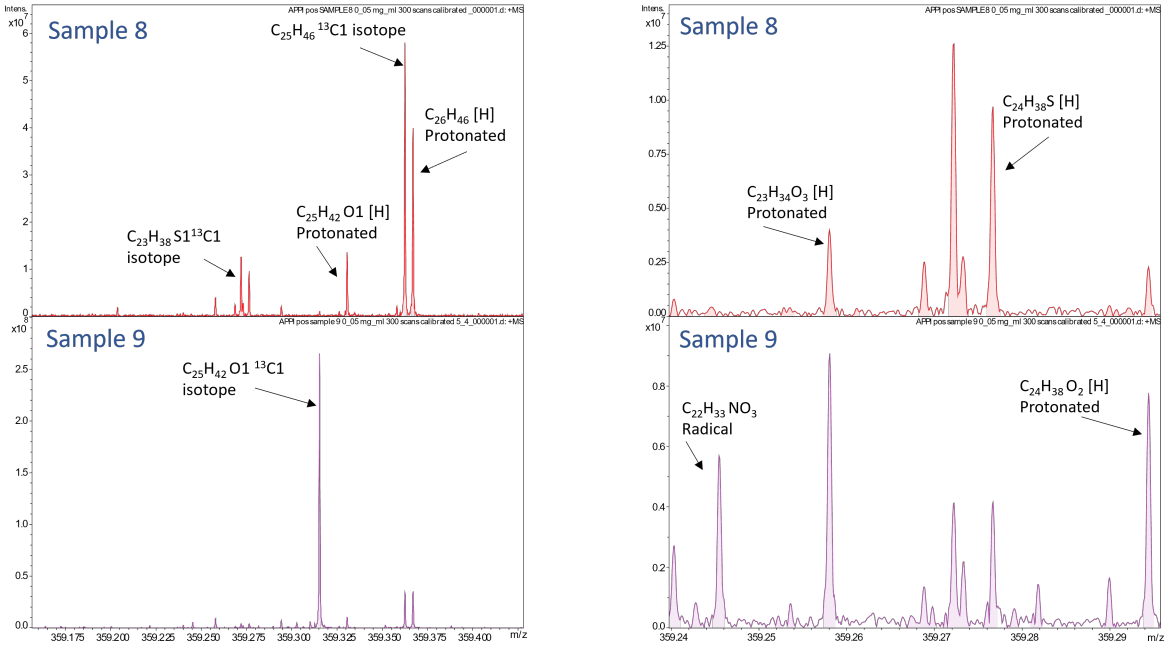

(a) Spectra 3: 0.4 Da window.

(b) Spectra 4: 0.05 Da zoomed in window.

Figure 5.25: (+) APPI – FTICR MS, comparison of new 0W 20 oil (sample 8 – red lines) vs. TLC (sample 9 – purple lines). *m/z* range example 359.175–359.40.

Splitter [105] and the observations of an apparent nitrogen reaction in the CDST §4.4.5. A similar analysis was completed for the fuel vs. the TLC (sample 9). It can be seen from Figure 5.26 (a), that the fuel is 'simpler' in terms of it's molecular composition, and was observed at lower *m/z*. The highest intensity was centred around 200 Da, with an addition large peak at 530 Da and a smaller one at 565 Da. In contrast the TLC oil has a much wider spread, and contains molecules not present in the fuel sample. This is not surprising as despite both being hydrocarbons from crude oil, fuel and oil have different carbon numbers. However, if Figure 5.26 (b) is considered, there are some common molecules in the 208 - 218 Da range, with slight differences in the intensity of the peaks. Figure 5.27, show two areas of interest at: 217 Da (0.016 Da window) and 218 Da (0.014 Da window). (a) Spectra 7 highlights a number of common compounds found in both the new fuel and TLC sample. As with the previous oil spectra, radicals, aromatic ketones, PAH's, and pyrene were present and all were known products of combustion. Figure 5.27 (b), highlights a notable observation, the presence of $C_{13}H_{15}NO_2$ [H] protonated. Whilst this compound itself is unremarkable and appears to be phenylethylamine derivative from a group of psychoactive substances, the effect of nitration

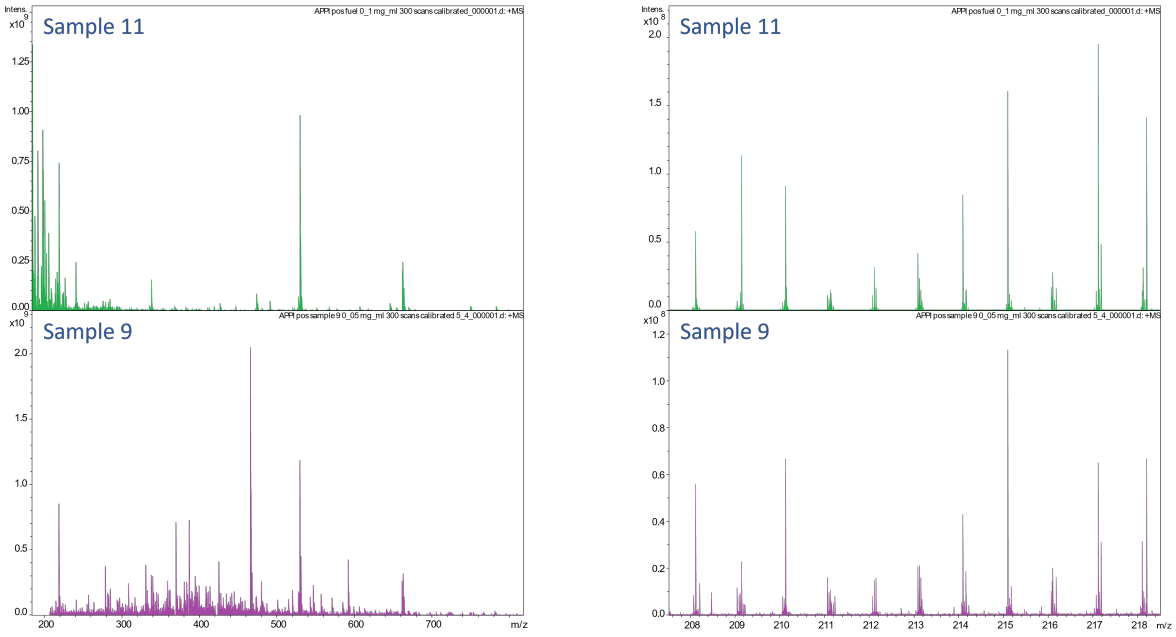

(a) Spectra 5: broadband *m/z*.

(b) Spectra 6: zoomed in window 208 - 218 *m/z*.

Figure 5.26: (+) APPI – FTICR MS, comparison of new E10 Gasoline fuel (sample 11 – green lines) vs. TLC (sample 9 – purple lines).

to create the NO_2 indicates the presence of nitro compounds. The analysis presented thus far, is a small subset of the potential capability of FTICR MS. The extremely high resolving power means that complex hydrocarbons can be investigated in extremely fine detail, but its also helpful if you know what you are looking for in order to refine the search into a narrower field of enquiry.

Figure 5.28 shows the number of compounds present on the mass spectra, vs. the chemical class on the x-axis. The red bars show the molecular class distribution for the new 0W 20 oil. The majority of the compounds are in the HC, HC [H], N_xO_x [H], O_x and O_x [H] classes. The components of the additive pack, mainly the components of ZDDP were detected in significant quantities. The blue bars represent the TLC sample, of note are the significant effects of oxidation and nitration, enclosed by the orange rectangle. There were large increases in N_xO_x [H], O_x, O_x [H], and most notably $N_x\,O_x$, whereby there is none present in the new oil. The oxidation and depletion of the ZDDP can also be seen, where there are no $O_xP_xS_xZn_x$ or $O_xP_xS_xZn_x$ [H] classes present in the TLC sample.

The final comparison of samples 8 (new oil) and sample 9 (TLC sample) can be seen in Figure 5.29. In sample 8, there were a total of 5311 assigned molecular formulae, whereas sample 9 had 10,859,

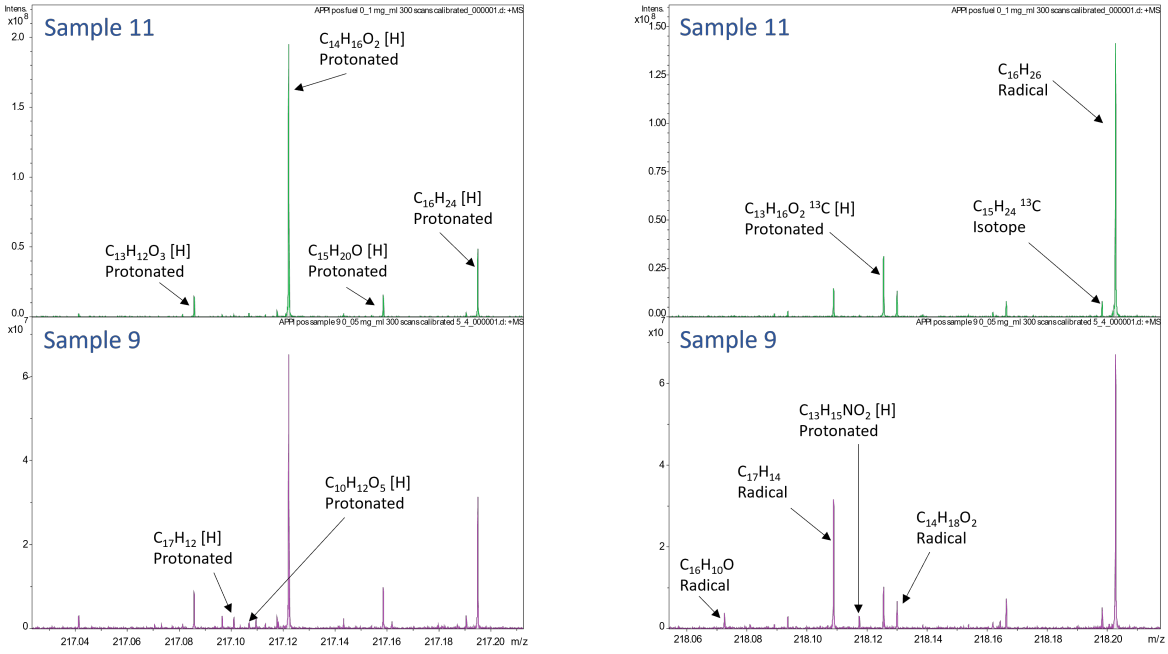

(a) Spectra 7: 0.016 Da window.

(b) Spectra 8: 0.014 Da window.

Figure 5.27: (+) APPI – FTICR MS, comparison of new E10 Gasoline fuel (sample 11 – green lines) vs. TLC (sample 9 – purple lines).

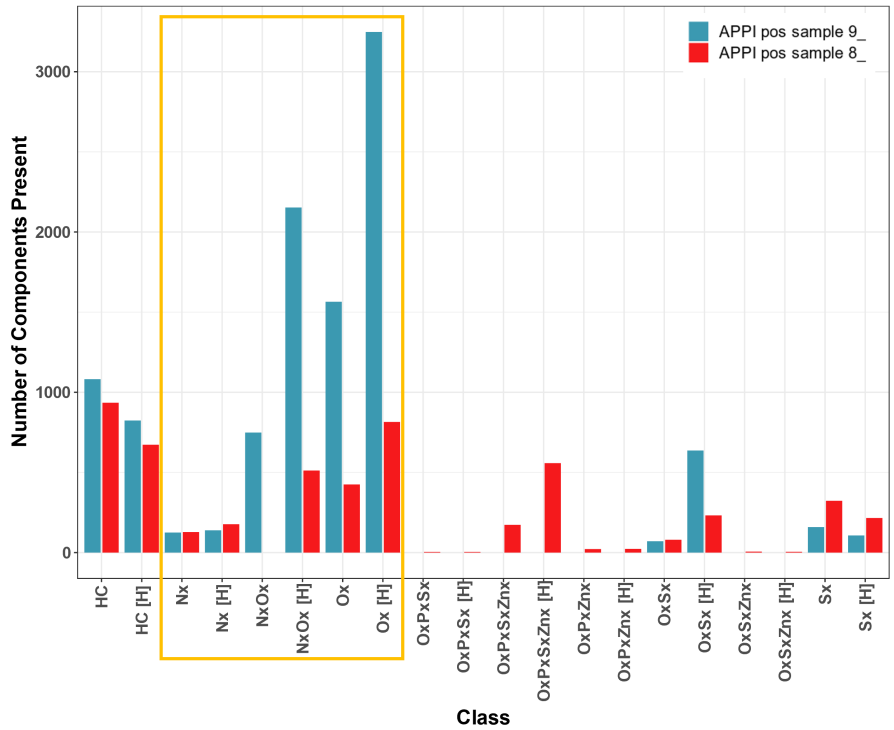

Figure 5.28: Number of compounds present vs. chemical class, by L. Alostad (Warwick University). The red bars refer to the clean oil (sample 8) and the blue bars refer to the TLC (sample 9).

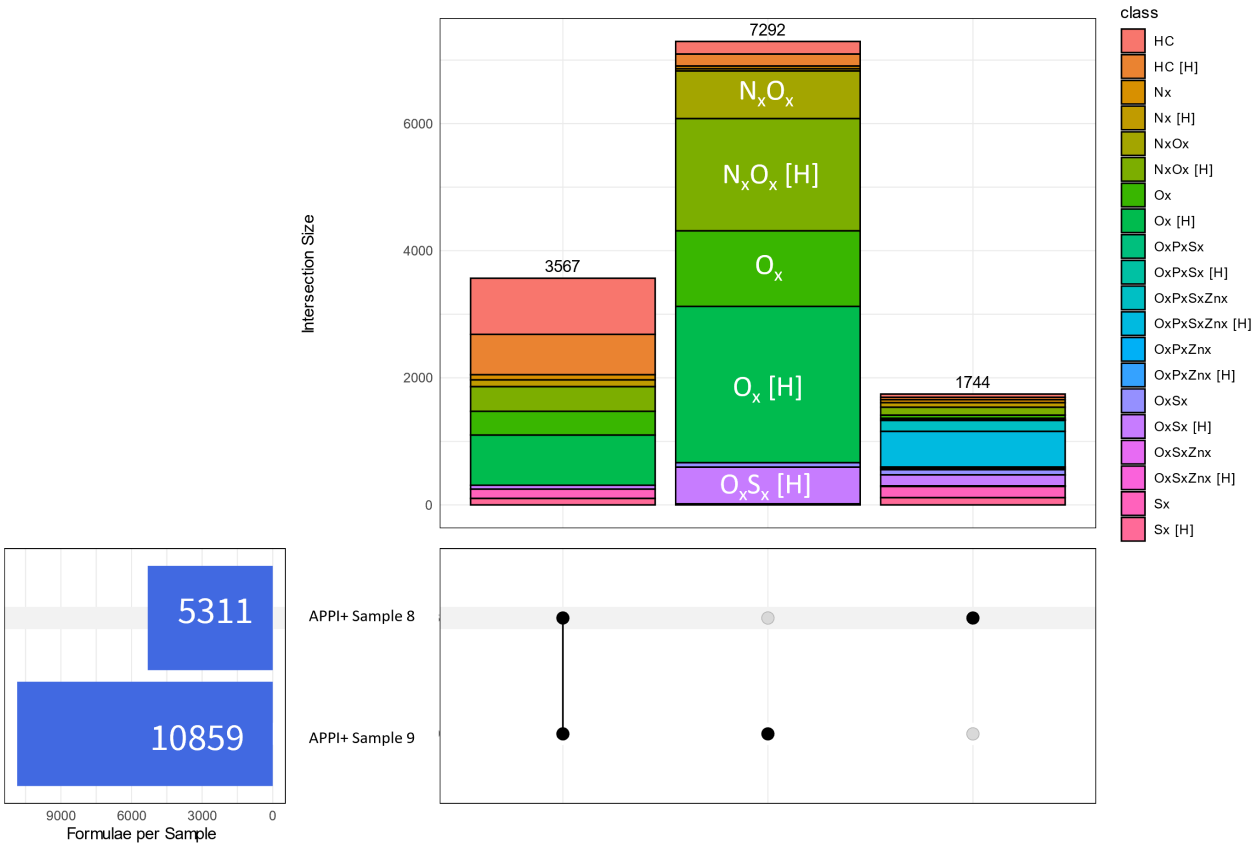

Figure 5.29: Upset plot of identical and unique compounds, by L. Alostad (University of Warwick).

almost double. There were 3567 common molecular compounds present in both samples 8 and 9 respectively. In sample 8, there were 1744 unique compounds in the new oil not present the TLC (sample 9). Most notable were the compounds unique to the TLC (sample 9). The total number of unique molecular compounds totalled 7292, mainly comprising: O_xS_x [H], O_x [H], O_x, N_xO_x [H] and N_xO_x classes.

5.7 Discussion

A suitable sampling methodology was defined that allowed multiple top land crevice samples to be collected from a running engine, based on the approach of [107], but with modifications to overcome reliability issues. Analysis of the extracted samples, using advanced laboratory techniques was conducted at BP Castrol's Pangbourne laboratory. ICP, XRF, ^{31}P NMR and GC MS (inc. HT SIMDIS). Due to an unforeseen sample line failure, the key TLC (sample 9) was contaminated with condensate. This added uncertainty to the analysis of this sample, but some meaningful results were obtained. XRF analysis of the aqueous portion of sample 9 revealed larger than typical levels of Ca

and Zn in solution and this would have very likely led to faster than normal depletion. The ICP elemental analysis highlighted interesting data showing the changes in the additive pack that occur locally in the TLC. This highlighted significant reductions in detergent for both oils that illustrate how, when exposed to the combustion process, this is locally naturalised. However, by making some assumptions and creating a simple model, it was possible to predict the potential reduction rate that may show how detergent is depleted, had it not been contaminated with water. Based on the work of Wolak [115], using TBN reduction rates as a surrogate to estimate the uncontaminated detergent depletion rate. Some cross contamination was present between tests when different oils were used, although this was minimal, despite care being taken to flush the system with the desired oil to minimise this effect. The effects on the additive pack, specifically ZDDP were evaluated for both oils as significant degradation/depletion was present in the TLC samples. ZDDP's known LSPI suppressing effect, which appears to reduce with oil ageing could be related to the observation of local depletion in the TLC, linked to a larger effect in used oil. Another significant outcome of this work was the quantification of fuel dilution of TLC samples. It is known from literature that increases in fuel in oil, in particular the heavier ends of gasoline, are known to increase LSPI tendency [122]. A simple model was created to predict the reduction in kinematic viscosity at 100°C, vs. fuel in oil dilution quantity, based on the trends observed by Kramer [117]. This could allow a potential future forecasting of the reduction in KV100 to be made for fuel in oil quantified under LSPI promoting engine conditions. It also provides further data to aid interpretation of the mechanism for oil accumulation and release (due to local reduced viscosity in the TLC) reported as the main recognised hypothesis for oil based LSPI proposed by Dahnz [29]. The SIMDIS analysis of the TLC sample also confirmed that reported in literature, of the oil in the top land containing the 'heavy ends' of the fuel distillation. Assessment of additional oil condition indicators, such as TBN, additive treat rate, wear metals and contaminants of the oils were also assessed. In sample 6, TLC sample for the magnesium detergent, contamination with molybdenum was found. This was thought to be due to grease used during assembly of the piston and did not affect the calcium detergent oil.

In addition to the work conducted at BP Castrol, the oil samples were also subject to UHR analysis using 'Petroleomics' at Warwick University. This FTICR MS ultra high resolution mass spectrometry technique provided insight into the molecular composition of the samples tested. A form of chemical fingerprinting, this advanced approach of MS can be used to detect differences in compounds with

very small mass differences at resolutions approaching 'parts-per-billion' levels. The objective of this work was to identify new chemical compounds present in the TLC that were not present in the new fuel or oil. It could be seen that the fuel was much simpler in terms of molecular composition than the oil. Key characteristics of the TLC (sample 8) oil could also be seen in the FTICR MS that has previously been observed in the ICP analysis. There was strong evidence to support the oxidation and nitration of the TLC sample, which was also observed in the ^{31}P NMR analysis of ZDDP, particularly for the calcium detergent oil. Finally, a macro analysis of all of the molecular compounds present highlighted 7292 unique molecular compounds in classes present in the TLC sample not present in the new fuel or new oil.

5.7.1 Advances in LSPI Research

Building on the the observations in §5.7.1 this work adds to the evidence relating to the presence of nitro compounds in the oil once exposed to combustion in the TLC 'reactor'. Examining a small range of *m/z* from the FTICR MS analysis, evidence was found of nitro compounds present in the TLC not present in either new fuel or oil. In a further publication Splitter *et al.* [123], described dynamic oil sampling from the TRZ, found FiO levels in the region of 21.9%, albeit under a no-load condition, similar to the results measured in this current work (23%). The tribological work of Lee *et al.* [107], which used the same sampling technique to the current work and that used by Splitter, suggested that the accumulation of 'volatiles' (fuel) in the TLC typically stabilised after approximately 15 mins of engine running. This suggests that there is also a potential 'time at level' element to the accumulation of fuel in the TLC and this was a factor not explored in this current work.

5.8 Conclusion

In conclusion, it can be seen that: A modified version of the technique used by Lee *et al.* [107], was successfully used to extract a TLC sample dynamically from a running single cylinder engine. Advanced laboratory techniques were utilised to explore in detail oil from the TLC crevice samples for both test oils, and compared to new fuel and oil to observe the impact of exposure to combustion in the TLC. This work highlighted significant differences in composition of the oil in TLC

when compared to the sump and the new lubricating oil. Specifically major changes in terms of degradation and depletion of the additive pack, observed using ^{31}P NMR analysis of ZDDP. Simple models were created to overcome issues with contamination of the TLC sample from the calcium oil, based on the performance of the magnesium detergent oil. Also a further model was built using empirical data to forecast FiO dilution and hence predict the reduction in KV100 in the TLC. This provides further evidence to support the prime LSPI mechanism hypothesis proposed by Dahnz [29], in terms of accumulation and inertial release of oil droplets into the combustion chamber due to reduced local viscosity. HT SIMDIS of the TLC sample also confirmed the presence of fuel 'heavy ends' in the TLC known to exacerbate LSPI, and consistent with the work of Jatana *et al.* [124]. Finally, a molecular-level characterization of the samples was performed using FTICR MS, and used to compare the molecular composition of the TLC sample to the new fuel and oil. In total 7292 new molecular assignments were identified in the TLC sample, that were not present in the fuel or the oil. Of note were the nitro compounds in the TLC sample. These findings add further to a growing body of evidence, linking to the significance of the role of nitrogen in the context of LSPI.

Chapter 6

Multi-cylinder Engine Testing of Fuels Containing Methylcyclopentadienyl Manganese Tricarbonyl (MMT)

6.1 Introduction

The current work has focussed on establishing the root cause of abnormal combustion, linked to metal oxide detergents, at a fundamental level using the CDST. This work led to sampling of the top land crevice of a running engine. Of note was the high level of fuel in oil dilution in the TLC, when the mechanism for oil droplet accumulation proposed by Danhz et al [29] is considered, FiO dilution leading to local viscosity reduction of the oil may support this. The work so far has been entirely focussed on oil and oil additives, with the discovery of FiO levels as an additional factor. Chapter 6 considers the fuel, specifically the effect of adding an alkaline metal oxide. Section §2.3 describes the fuels properties known to exacerbate LSPI, without the addition metal oxide additives. Also, section §2.3.3 introduced the use of metal oxide octane boosters. Methylcyclopentadienyl Manganese Tricarbonyl (MMT) was used in gasoline fuel as an alternative to Tetra-ethyl Lead (TEL). It was later marketed as octane booster in the late 1970's and early 1980's. Due to awareness of the public heath concerns relating to use of metallic additives in road transport fuel it's use has been steadily reducing, today only appearing in certain (mostly developing) markets, namely Africa, Pakistan and some parts of Asia and South America. There is very little recently published material relating to

MMT in the literature, as in large global markets e.g. the USA it was completely phased out, due to problems with deposits and contamination/poisoning of engine after-treatment, namely oxygen sensors and catalysts. MMT is known to promote LSPI more readily than fuels that do not contain MMT, although there are additional factors that must be considered, for example the underlying fuel quality. The objective of this experimental campaign was to characterise the behaviour of fuels known to promote LSPI, with the addition of MMT in quantities based on dedicated in-market sampling. The addition of MMT octane booster increased the RON of the fuel, this was not corrected in the base fuel. Engine testing would also allow for deposit sample collection, of specific interest was the fuel injector tip.

6.2 Background

OEM's observed significant engine warranty replacements due to what appeared to be abnormal combustion, in markets with fuels containing MMT. Examination of failed engine parts indicated evidence of LSPI and mega-knock damage similar to the photographs in Figure 2.9 in addition to heavy carbonaceous deposits. Analysis of fuel samples highlighted high concentrations of MMT, typically around 50 ppm. Figure 6.1 shows a world map produced by the Japan Automobile Manufacturers Association (JAMA), illustrating MMT concentration in fuel samples. Pakistan had the highest MMT concentration at 140 ppm.

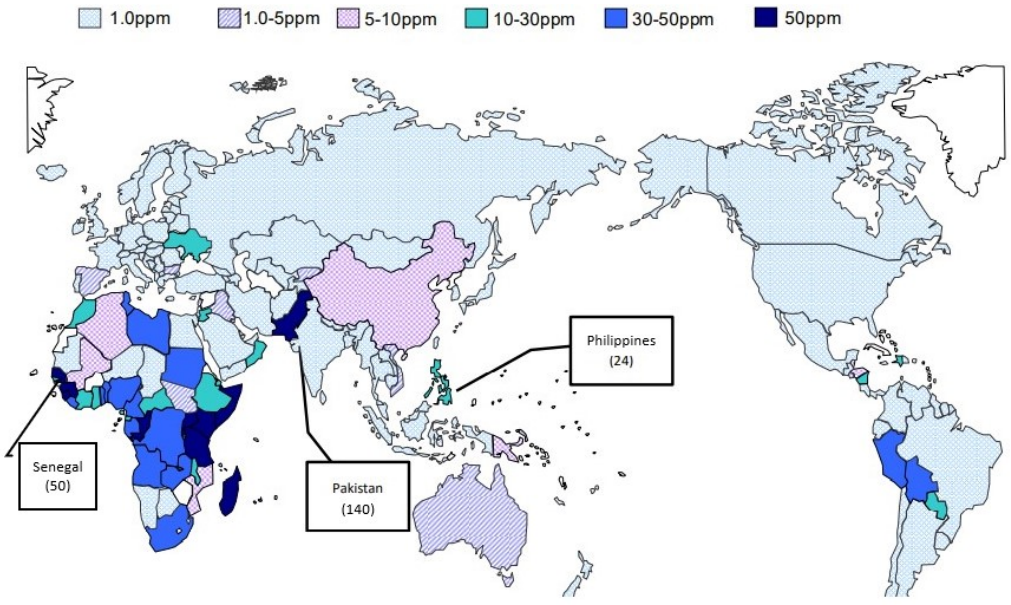

Figure 6.1: JAMA – Manganese Concentration by Geographical Location - Adapted From [125]

6.3 Properties of MMT

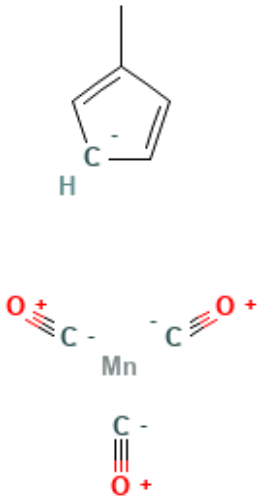

Figure 6.2: Chemical Structure Depiction of MMT

Figure 6.2 provides a depiction of the chemical elements and bonds for MMT. It can be seen that a triple bond exists between the carbon and oxygen elements for the tricarbonyl, which are chemically difficult to break.

Table 6.1: Chemical Properties of MMT.

Methylcyclopentadienyl Manganese Tricarbonyl		
Chemical Formula		$C_9H_7MnO_3$
Molar Mass	g/mol	218.09
Appearance		Pale yellow to dark orange
Odour		Faint, pleasant
Melting Point	°C / °F / K	-1 / 30 / 272
Boiling Point	°C / °F / K	232 - 233 / 450 - 451 / 505 - 506
Solubility in Water	ppm	Low
Solubility		Hydrocarbons (Gasoline), ether, alcohol
Vapour Pressure	mmHg at 100 °C	7

Table 6.1 presents some the chemical and physical properties of MMT. Of note is the boiling point, when compared to the fuel distillation curves in Figure 2.12, it can be seen that this corresponds with the final boiling point of the 'heaviest back-end' distillation fuel at 235.5 °C. This could mean that

MMT's likely to accumulate with the fuel in the TLC, in addition to the fuel 'heavy-ends'. As the abnormal combustion mechanism for MMT is unknown, this would be a factor in its LSPI behaviour.

6.4 Potential Hypotheses

A link between fuel quality and MMT concentration has been proposed by Nomura *et al.* [56] as a cause of LSPI. This work proposes two main mechanisms:

- The first is related to the fact that fuels using MMT as an octane booster have low base volatility as they tend to be in lower fuel quality.
- Manganese oxide in scattered droplets supplies the ignition energy to ignite the droplet, which is a mixture of fuel and lubricating oil. Within this hypothesis, two chemical ignition mechanisms are proposed related to exothermic heat release from further oxidation of manganese oxides.

$$\mathrm{MnO_{(s)}} \; + \; 1/4 \; \mathrm{O_{2(g)}} \; \longrightarrow \mathrm{Mn_2O_{3(s)}} \qquad (743\mathrm{K\ to\ 813K}) \tag{6.1}$$

$$\mathrm{Mn_3O_{4(s)}} \; + \; 1/4 \; \mathrm{O_{2(g)}} \; \longrightarrow 3/2 \; \mathrm{Mn_2O_{3(s)}} \qquad (853\mathrm{K\ to\ 1073K}) \tag{6.2}$$

As limited data is available in the current body of knowledge and the linkages to the current work regarding alkaline metal additives in oil, it was logical to evaluate the abnormal combustion behaviour of MMT using specially selected fuels, in combination with clean and used lubricating oils in a multi-cylinder engine.

6.5 Experimental Set-up

A modern high specification multi-cylinder engine, test bed with an AVL Gigabit Indimaster, combustion analyser and the ability to run barrelled fuels was available, and there was interest in conducting the work at BP Castrol, Pangbourne. The engine specification is defined in Table 6.2. The engine was fitted with in-cylinder pressure sensors in all cylinders and the measurement system

was calibrated once the engine was installed onto the engine test bed. The engine control unit (ECU) was a development type to allow for the required modifications to the knock system, otherwise the engine ran the production calibration. The engine was configured for temperature and pressure measurement for both test bed controls (e.g. coolant and oil temperature) and health checks (e.g. exhaust port temperatures, oil pressure and crankcase pressure).

Table 6.2: Multi-cylinder Engine specification

Combustion System	High tumble, spray guided, direct injection
Valve-train	Double over-head cam, variable int & exh phasing, continuously variable timing and lift
Aspiration	Turbocharged
Cyl Displacement [cm^3]	499.2
Cylinder Count	Inline 4
Compression Ratio	10.5:1
Bore [mm]	83.00
Stroke [mm]	92.00
Fuel [RON/Ethanol Content]	See fuels matrix
Oil Type	Castrol 0W 20 (New and Used)

Also available to support this work was access to laboratory facilities allowing the analysis of the lubricants and chemical deposits in the engine. The engine calibration was practically as per the production release, with the exception of minor modifications to the knock control retard authority (determined by the first 'aggressive' test fuel) which was extended this to manage the severe behaviour of the lower RON fuels, resulting is extremely retarded combustion phasing.

Figure 6.3 (a) shows the test cell equipment and (b) shows the test engine installed in the test cell in Pangbourne. The LSPI test detailed in Figure 2.6, was used to assess all fuels, due to its ability to provoke both particle and oil droplet based LSPI mechanisms.

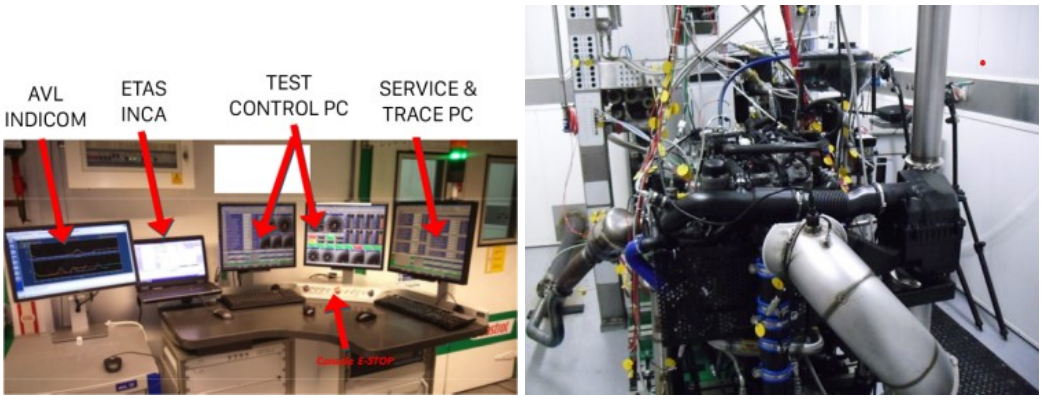

(a) Test Cell Equipment (b) Engine Installation

Figure 6.3: Test Cell Equipment and Engine Installation

6.6 Fuels Matrix

Table 6.3 show the test fuel matrix used to evaluate the effect of adding MMT to LSPI promoting fuels. The results of in-market fuel sampling in Africa and China highlighted the fuel was generally of 'poor' quality, characterised by low RON ($\leq$ 92), elevated low, mid and back-end evaporation temperature, high aromatic content and MMT. Varying concentrations of MMT were observed, on average 30 ppm was typical and representative of a Senegalese (African) forecourt fuel. With reference to Figure 6.1, this concentration does not represent the highest levels of MMT recorded in Senegal, but is acceptable to allow for characterisation of abnormal combustion due to MMT. A 95 RON E10 (10% ethanol) fuel reference used for general engine combustion system and calibration development, based on EN228, but without seasonal volatility changes and containing 10% ethanol, was used to baseline the engine performance. A second 102 RON E0 (0% ethanol) was also used to characterise the baseline LSPI level and to periodically assess the health of the engine between the LSPI testing. Analysis results for this fuel were not available for proprietary reasons and are omitted in the following fuel analysis results.

Coryton Advanced Fuels (CAF) provide a number of LSPI promoting fuels, synthesised based on their own fuel knowledge, market sampling, and referred to as 'China Bad' and 'High LSPI'. China Bad, is a CAF reference fuel based on in-market Chinese worst case characteristics for LSPI testing. It had the highest final boiling point of all of the fuel at 200 °C. High LSPI is a 96 RON reference fuel created by CAF to promote LSPI, as a result of it's high mid and back-end distillation curve. CAF were asked to blend a new fuel to represent African in-market fuel samples, with 30 ppm MMT,

Table 6.3: Test Fuel Matrix

Name	MMT [ppm]	Description
95RON E10	0	EN228 based reference fuel, 10% ethanol
102RON E0	0	High RON reference fuel, 0% ethanol
China Bad	0	CAF Chinese market representative fuel
High LSPI	0	CAF LSPI promoting reference fuel for LSPI testing
Africa Bad MMT	30	CAF synthesized fuel based on Senegal market sampling
High LSPI MMT	55	CAF High LSPI fuel with added MMT
China Bad MMT	55	CAF China Bad fuel with added MMT

named 'Africa Bad MMT'. A version of this fuel with MMT added was included to understand the difference that the addition of MMT made to a fuel designed to excite LSPI (China Bad MMT). Based on in-market data from China, 55 ppm MMT was added to China Bad to create a version with MMT. Similarly 55 ppm MMT was also added to LSPI High fuel to make a comparable fuel at the equivalent MMT treat rate at the China Bad fuel.

Octane Rating

When designing a fuels matrix there are typically fuel parameters that can be fixed or varied depending upon the desired outcome. When assessing LSPI, it has already been discussed in §2.3.2, that octane number itself does not increase the propensity for LSPI, but does impact the severity of mega-knock if this occurs. Other fuel properties such as the evaporation behaviour can also have a promoting effect on LSPI. Figure 6.4, shows the RON, MON and AKI for the fuels in the test matrix. No fuel analysis data was available for the 102 RON reference fuel, hence it is not included in the analysis.

Due to the fact that RON does not have a promoting effect on LSPI, it was acceptable for the ON to vary with the addition of MMT. The reference fuel and the High LSPI fuel has similar RON (95 - 96), MON (85 - 86) and hence AKI (90 - 91) values. With the addition of MMT in the High LSPI fuel the RON was increased to 99.7. The Africa Bad MMT had a relatively low RON (92), MON (84) and AKI (88). China Bad had the lowest RON, MON and AKI at (90, 80 and 85) respectively. The addition

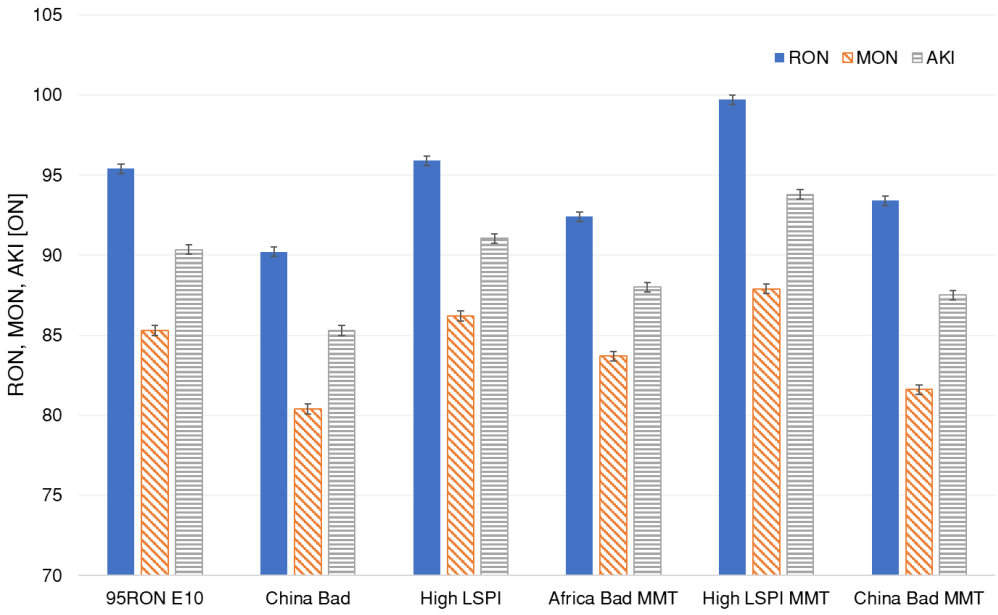

Figure 6.4: Octane Rating – RON ASTM D2699, MON ASTM D2700, uncertainty for the same test laboratory $\pm$ 0.3 RON, MON and AKI.

of MMT had the effect of increasing ON by approximately 2 - 3 RON. Across the fuel matrix the sensitivity, calculated using equation (2.7), was in the range of 9.7 - 11.8, Figure 6.5.

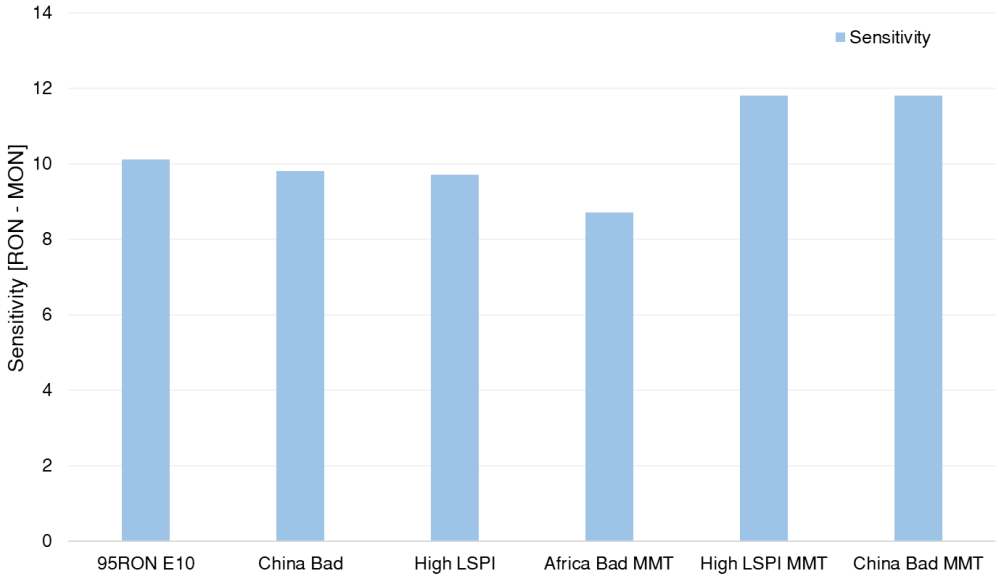

Figure 6.5: Sensitivity, RON - MON, for the fuel matrix.

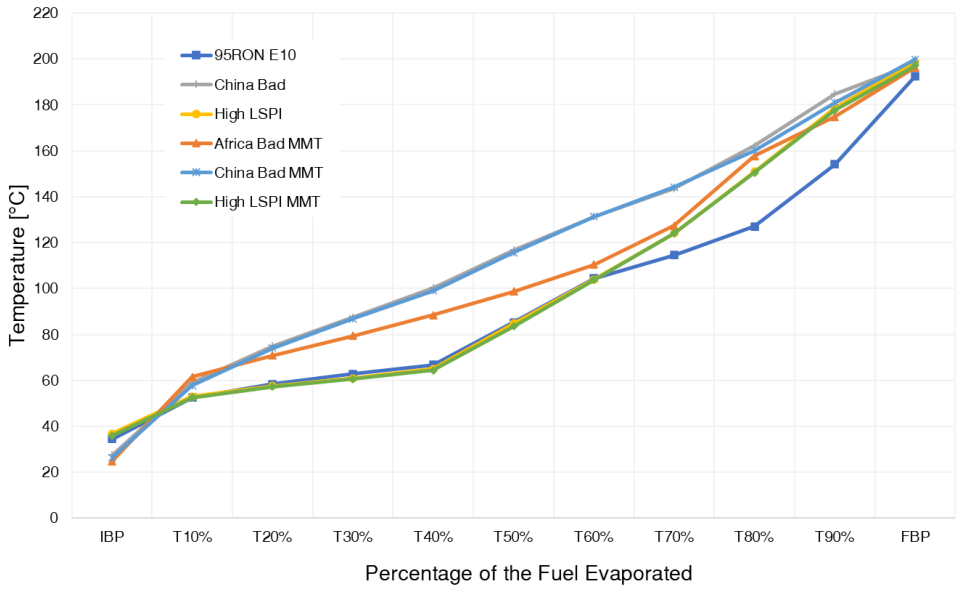

Figure 6.6: Fuel evaporation curves, ASTM D86, uncertainty for the same test laboratory, at T50% ± 2 °C.

Evaporation Behaviour

As stated in §2.3.1, it has be demonstrated that the evaporation behaviour of a given fuel has a strong link to the LSPI tendency. Fuels most likely to excite LSPI tend to have higher mid and back-end evaporation temperatures. The worst fuels also tend to have high final boiling points 200 - 220 °C. As the maximum oil sump temperature in an engine does not generally exceed 150 °C, and is more typically between 90 - 120°C, in some cases as much as 25% of the mid and heavier ends of the fuel could be present in the lubricating oil. As shown in §5.5.3, from experiments conducted at relatively low engine speed and load, the fuel in oil dilution in the top land crevice was appropriately 23%. Thus, fuel can enter the combustion chamber from the bulk sump oil via lubrication of the cylinder liner and also the fuel caught in the TLC. It is likely and therefore consistent with the model presented in Figure 5.18, that this could lead to a reduction in the local oil viscosity in the top land crevice. In the market fuels (representative and worst case) the evaporation temperature is high throughout the curve, and is generally indicative of poor base fuel quality. The high LSPI fuel, having been deliberately designed by CAF is consistent with an EN228 or typical European fuel until T65%, thereafter it has been chemically engineered to behave like a market fuel with high back end evaporation temperatures.

PIONA Analysis

Paraffins, Iso-paraffins, Olefins, Naphthenes and Aromatics (PIONA) make up the list of components assessed in a 'PIONA' fuel analysis. The term alkane has replaced the term paraffin, however for this analysis is still referred to as a PIONA for historic reasons. Fuels containing higher alkane concentrations tend to have a lower RON and higher evaporation temperatures.

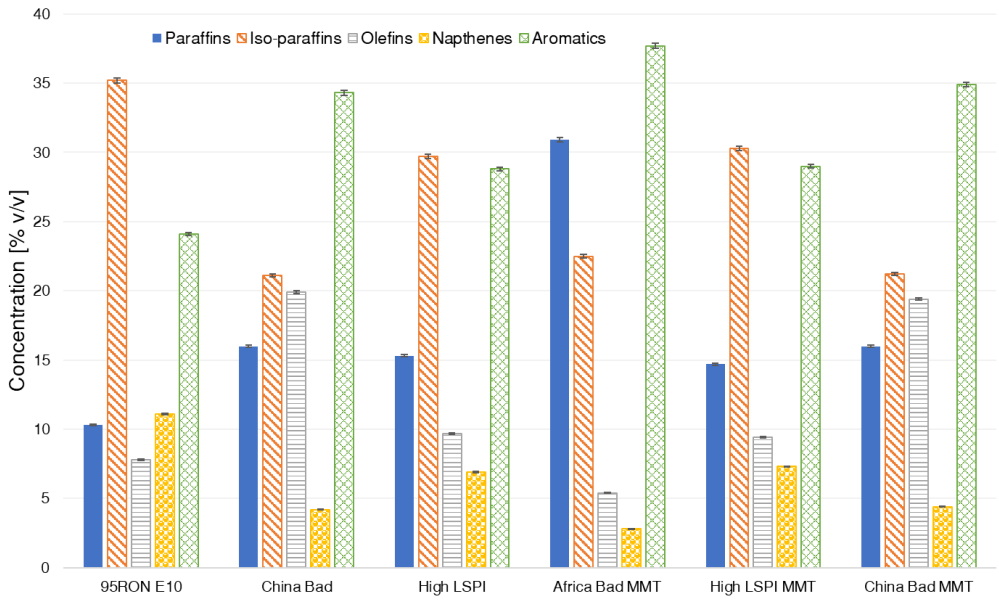

Figure 6.7: PIONA analysis, ASTM D6730 (GC MS), single laboratory uncertainty ± 0.5% v/v.

Figure 6.7, shows Africa Bad fuel has significantly higher alkane and iso-alkane concentration when compared to the 95 RON E10 fuel. This is also evident in the evaporation curve in Figure 6.6. The High LSPI fuel has a high iso-alkane content. All of the LSPI promoting fuels have high aromatic content, compared to the EN228 95RON E10 fuel. As stated in section §2.3, fuels high in aromatics tend to be worse for particle emissions, have a high final boiling point and therefore have the tendency to excite a particle based or fuel/oil LSPI trigger mechanisms. Naphthenes are cyclic alkanes that have a ring shaped structure and are desirable in the base gasoline as these tend to deliver higher RON. The 95RON E10 and High LSPI fuels, have the highest naphthene content and both have the highest RON (95 - 96). The market and worst case LSPI fuels have lower naphthene levels in the base fuel and lower RON, the addition of MMT raised the RON by approximately 2 - 3 points. Olefins are a base building blocks for gasoline fuel and they also contribute to the base octane. Whilst some of the fuels that promote higher LSPI tendency have higher olefin levels than the

'better' fuels, Africa bad has the lowest olefin content. There does not appear to be a strong trend relating to olefin concentration as a particular benefit or penalty.

Fuels Test Sequence

The fuel test sequence is shown in Table 6.4. To evaluate the effect of used oil in addition to MMT, tests were conduced with new (clean) and used oil.

Table 6.4: Fuel Test Sequence

Name	Oil Type	Description
102RON E0	Clean Oil	Baseline
102RON E0	Clean Oil	Baseline (repeat)
95RON E10	Clean Oil	Baseline
95RON E10	Used Oil	Baseline
China Bad	Clean Oil	
China Bad	Used Oil	
102RON E0	Clean Oil	Re-baseline and health check
China Bad MMT	Clean Oil	
High LSPI	Clean Oil	
High LSPI	Used Oil	
102RON E0	Clean Oil	Re-baseline and health check
High LSPI MMT	Clean Oil	
102RON E0	Clean Oil	Re-baseline and health check
Africa Bad	Clean Oil	
Africa Bad	Used Oil	
Africa Bad MMT	Clean Oil	
102RON E0	Clean Oil	Re-baseline and health check

Four repeat tests were targetted to enable repeatability and averaging to be assessed. Following the initial engine performance testing and baseline to confirm that the installation was successful, testing then moved to the 'safe' 102 RON fuel. The engines 'health' was regularly assessed using the 102 RON fuel to ensure that the affects of accumulated damage were not impacting the test results. An additional objective of running periodic reference tests, was to utilise the potential cleaning

effect via removal of deposits, with the objective of returning the combustion chamber surfaces to their original condition. This was seen as a pragmatic approach to manage this in the most effective way. Bore scope images were also collected and recorded between tests to evaluate this visually.

6.7 Engine Hardware and Lubricants

The following section details hardware considerations also evaluated in the engine testing. As previously stated, the engine testing was planned to evaluate the behaviour of fuel containing MMT, with both new and used lubricant.

Engine Hardware

In addition to the hypotheses proposed in §6.4, the question was raised as to whether, MMT does not directly cause LSPI by a particle or metallic catalytic means, rather the LSPI is triggered by component damage (injectors, spark plugs or lambda sensors). To evaluate this phenomena the injectors, spark plugs and lambda sensors were all replaced each time the LSPI promoting fuel type was changed.

Lubricants

A total of 140 kg of used 0W 20 oil was collected from serviced vehicles and sent to BP Castrol for consolidation into a single batch and chemical analysis. Table 6.5 shows an analytical comparison of new vs. used oil. The KV100 reduced by 1 cSt going from new to used oil. Using the KV100 vs. FiO dilution model in Figure 5.18, this reduction in viscosity is consistent with the predicted reduction in KV100 for 3.75% FiO dilution (found in the used oil), which serves as additional validation data. ICP elemental analysis found that there were increases in typical wear metals for an ICE in terms of aluminium, copper and iron. Of note was the 56 ppm manganese present in the used oil. UK fuel is blended to EN228, and as such there would be no manganese present. The engine manufacturer was consulted to identify the source of manganese from the engine and it was found to be present in the crankshaft and timing chain material, hence in the oil due to component wear. A small reduction of calcium was observed (1801 - 1781 ppm), indicating the detergent levels are still high and able to counter acid formation. Minor oxidation and some nitration had occurred, but this is typical for

used oil. Overall, the consolidated mixture used oil was in good condition and suitable for testing.

Table 6.5: Comparison of new vs. used SAE 0W 20 Castrol oil. KV (ASTM D445) uncertainty ± 3%. Elemental analysis ICP (ASTM D5185) uncertainty ± 10%. FiO GC MS (ASTM D2887) uncertainty ± 5%. Nitration: new oil (ASTM D5762), used oil (ASTM D5763). Oxidation: new oil (ASTM D7528), used oil (ASTM D7414). Overall uncertainty for FTIR MS ± 10%.

Description	Unit	New Oil	Used Oil
Kinematic Viscosity at 100 °C	cSt	7.6	6.6
Kinematic Viscosity at 40 °C	cSt	34.1	29.1
Viscosity Index		199	195
Aluminium	ppm	<1	6
Iron	ppm	<1	50
Copper	ppm	<1	24
Manganese	ppm	<1	56
Calcium	ppm	1801	1781
Magnesium	ppm	<1	6
Silicon	ppm	3	17
Fuel Dilution	%	0	3.75
Nitration (1630 FTIR Peak)	Abs/cm	0	13
Oxidation (1720 FTIR Peak)	Abs/cm	0	4

6.8 LSPI Classification

No consensus exists regarding LSPI classification criteria to date in industry or academia, however there are common themes between those in the literature. When making a relative comparison of factors influencing LSPI behaviour, a set of deterministic criteria must be applied, however a level of manual inspection is also recommended to minimise the likelihood of 'miss detection' of LSPI events. Based on the known characteristics of LSPI, it is therefore a fair assumption that if an alternative classification criteria were applied to the same data, that the absolute number of 'events' could be different. When a test generates large numbers of LSPI events a small difference, due to the classification method, is not critical to the overall outcome of the experiment. In the case where the results of two tests, with different noise factors, generated the results: 0 and 1 events, this would not be valid as it would not be possible to interpret the results with sufficient statistical confidence. To

account for this, where possible, four repeat tests were conducted, hence the overall quoted number of LSPI events in the results is the average four tests. In some cases, where the LSPI observed was so severe, it was not possible to run four repeat tests, typically either the engine or the in-cylinder pressure sensors were damaged. The classification method chosen for the current work were those used by Leach *et al.* [38], namely the BP Castrol triggers detailed in Figure 6.8. This approach allowed for 'windowing', where events captured by early AI02 or high PMAX allowed identification of PI events. Using a standard deviation window allowed for separation of 'normal' cyclic variability from abnormal combustion.

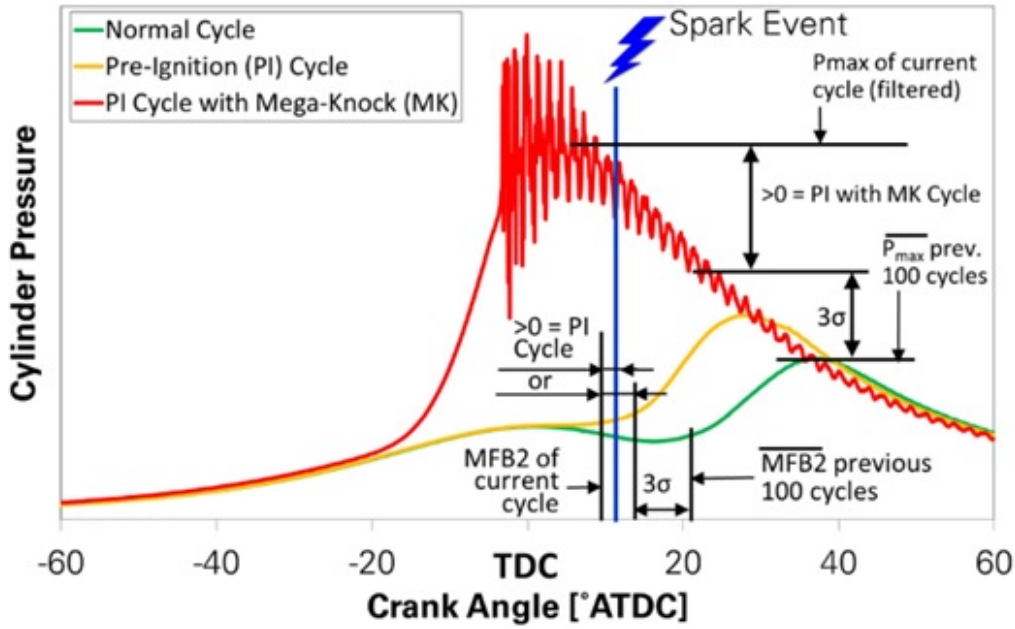

Figure 6.8: BP Castrol abnormal combustion triggers and LSPI classification[38]

MATLAB was used to post process the Indimaster indicating files to extract the files that were captured by these 'triggers'. A LSPI event can trigger on one or more of criteria classed as an LSPI event. When using less aggressive LSPI provoking fuels, adopting these triggers (as defined) works well to identify LSPI cycles. However, with the fuels tested in this work, high levels of cyclic variability was experienced due to the extremely advanced combustion phasing. This resulted in lots of LSPI mis-detection due to the cyclic variability, confusing the mathematical rules implemented in the script. The simplest way to improve this was to increase the standard deviation to 4σ (from 3σ), for the moving average AI02 and the PMAX criteria (as shown in the list on the following page).

- Trigger if; $\theta_{MFB2i} < [\sum_{i=-101}^{-1} \frac{MFB2i}{100} - \mathbf{4} \cdot \sigma MFB2i]$

- Trigger if; $\theta_{MFB2i} < \theta_{ign}$

- Trigger if; $\theta_{PMAXi} < [\sum_{i=-101}^{-1} \frac{PMAXi}{100} - \mathbf{4} \cdot \sigma PMAXi]$

6.9 Results

A general summary of all of the engine testing results can be found in Figure 6.9. The first reference test was 102 RON fuel and clean oil, and found to have an average of 6 LSPI events. The following test was a 102 RON fuel available at BP Castrol, not in the test matrix. This result was included as it illustrates well, the fact that two fuels with the same RON can have different LSPI tendency (everything else being equal). The fuel was changed to 95 RON E10 and tests conducted firstly with new oil (2 events), then followed by used oil (3 events). Whilst the test with used oil is on average 1 event higher, this thought not significant as the absolute number of events are low. Given the test cycle is deigned to provoke LSPI behaviour, the levels of events experienced using these fuels was deemed good and acceptable to proceed with testing of the more extreme fuels.

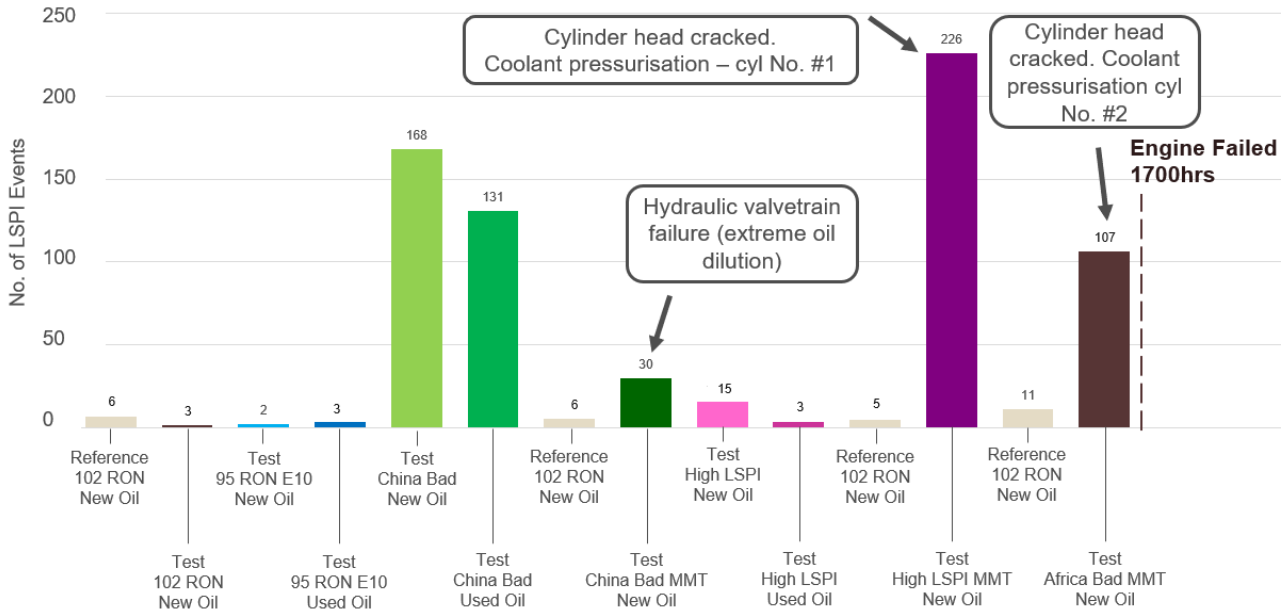

Figure 6.9: Test summary - Number of LSPI events per test (average of 4 tests) using fuel from the fuels matrix. Note, for China Bad MMT fuel with new oil (dark green bar), the engine failed in one test, hence this result is not an average of 4 tests.

Results for the LSPI provoking fuels will be discussed in the following seperate sections of the results, and with reference to Figure 6.9.

Interpretation of the LSPI Result Plots

A MATLAB script was created to analyse results of files captured using the AVL Indimaster. The combustion analyser was operated in a continuous buffer mode whilst running the LSPI test. Any cycles that exceeded some or all of the 'trigger' criteria were automatically saved for later post processing. The MATLAB script loads the raw Indimaster .dat file (also know as Ifiles), plots the cylinder pressure from 30 °CA BTDC – 90 °CA ATDC. Filters are then applied to identify which trigger(s) caused the file to be logged. Figure 6.10 shows an example plot where the post-processing has been applied. The key at the top of the chart indicate which triggers and which cylinder or cylinders have triggered.

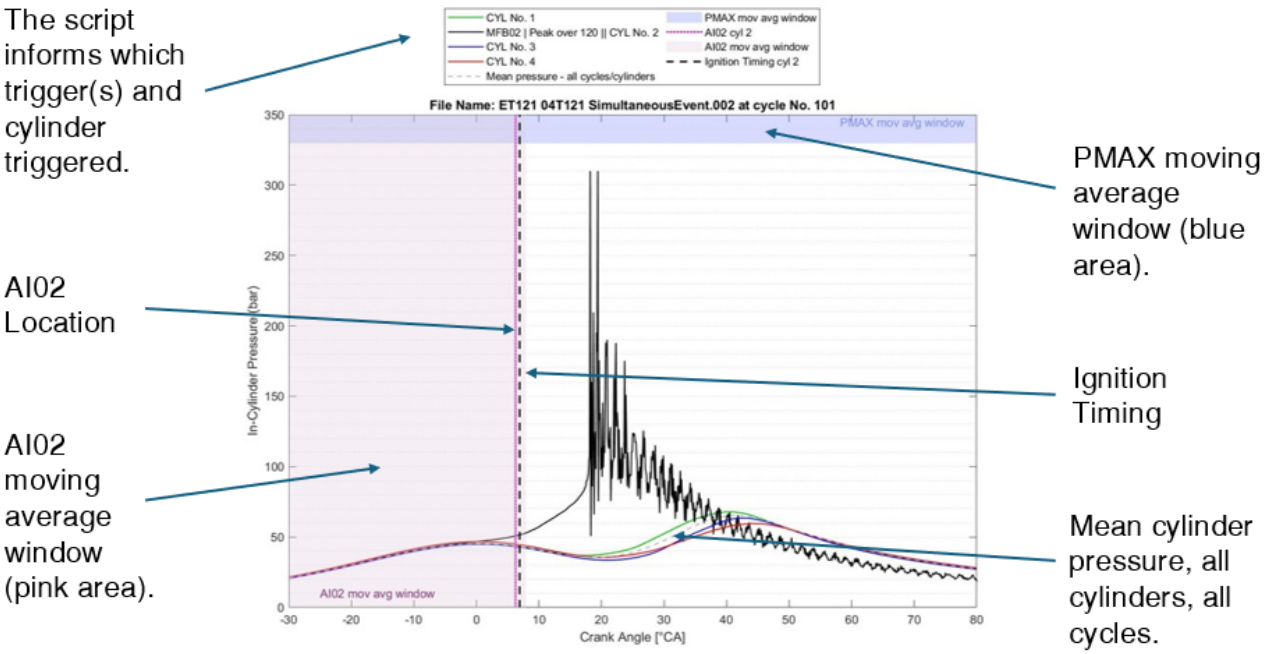

Figure 6.10: Result plot and triggers explanation. X-axis is crank angle, Y-axis is cylinder pressure. The significant of the lines and shaded areas are explained in the captions.

The least reliable trigger was the location of AI02. This is notoriously difficult parameter to determine, during heat release analysis, due to the very shallow gradient change at the start of combustion. Its can be seen in the examples included in this chapter that the location of AI02 is after the spark despite it being a clear LSPI cycle on manual inspection. Hence the use of all triggers was necessary to capture as many cycles as possible without significant quantities of mis-detection. In the example shown in Figure 6.10, it can be seen that cylinder 2 (black) has experienced pre-ignition

and mega-knock. Examining the plot from left to right: the location of AI02 is just before the ignition timing, given there is a finite ignition delay even for PI cycles, this infers that PI has occurred. The trigger identified by the script was PMAX >120 bar. The start of the pressure rise is inside of the AI02 moving average window, again further indication of PI. Looking at the cylinders with typical pressure traces, it can be seen that the combustion is retarded (PMAX is approx. 40 °CA ATDC, despite the ignition timing being 7 °CA ATDC).

China Bad Fuel

China Bad fuel, in combination with clean oil, produced very high levels of LSPI events with 168 observed, Figure 6.9, compared to the reference fuels. This was expected on the basis that this is a fuel designed to increase LSPI tendency based on Chinese market fuels with known LSPI promoting characteristics. The absence of repeated or run-away events points to this being most likely attributed to the oil accumulation and release mechanism. The following test with China Bad fuel and used oil. This test yielded 131 captured events, Figure 6.9, an unexpected result. Based on the understanding thus far, the addition of used oil was expected to have increased the number of events rather than reduce them. This fuel had a particularly low RON (90.2) in contrast to the 102 RON reference fuel, resulting the very late combustion phasing. The effect on the calibration, was very active knock control, increased exhaust temperature resulting from retarded ignition, which in-turn required increased fuel enrichment. Four example LSPI cycles of particular interest were extracted from the 168 files captured and shown is Figure 6.11.

- **Example (a)**, shows a typical and fairly mild pre-ignition event, triggered by PMAX >120 bar. AI02 is after the ignition timing, due to the finite ignition delay the actual pre-ignition event must have been just before the ignition. The retarded spark timing for the cylinders with normal combustion resulted in a mean peak cylinder pressure of approximately 50 - 60 bar, in contrast to the PI cycle which has an approximate mean peak of 90 bar and acoustic ringing from the mega-knock which peaked at 260 bar.

- **Example (b)**, is an aggressive example of LSPI and mega-knock, when compared to similar examples of LSPI from literature [29], [31], [126]. Cylinder 2 (black) has triggered on both MFB02 and peak pressure >120 bar. This was a pre-ignition cycle as AI02 was 12 °CA before

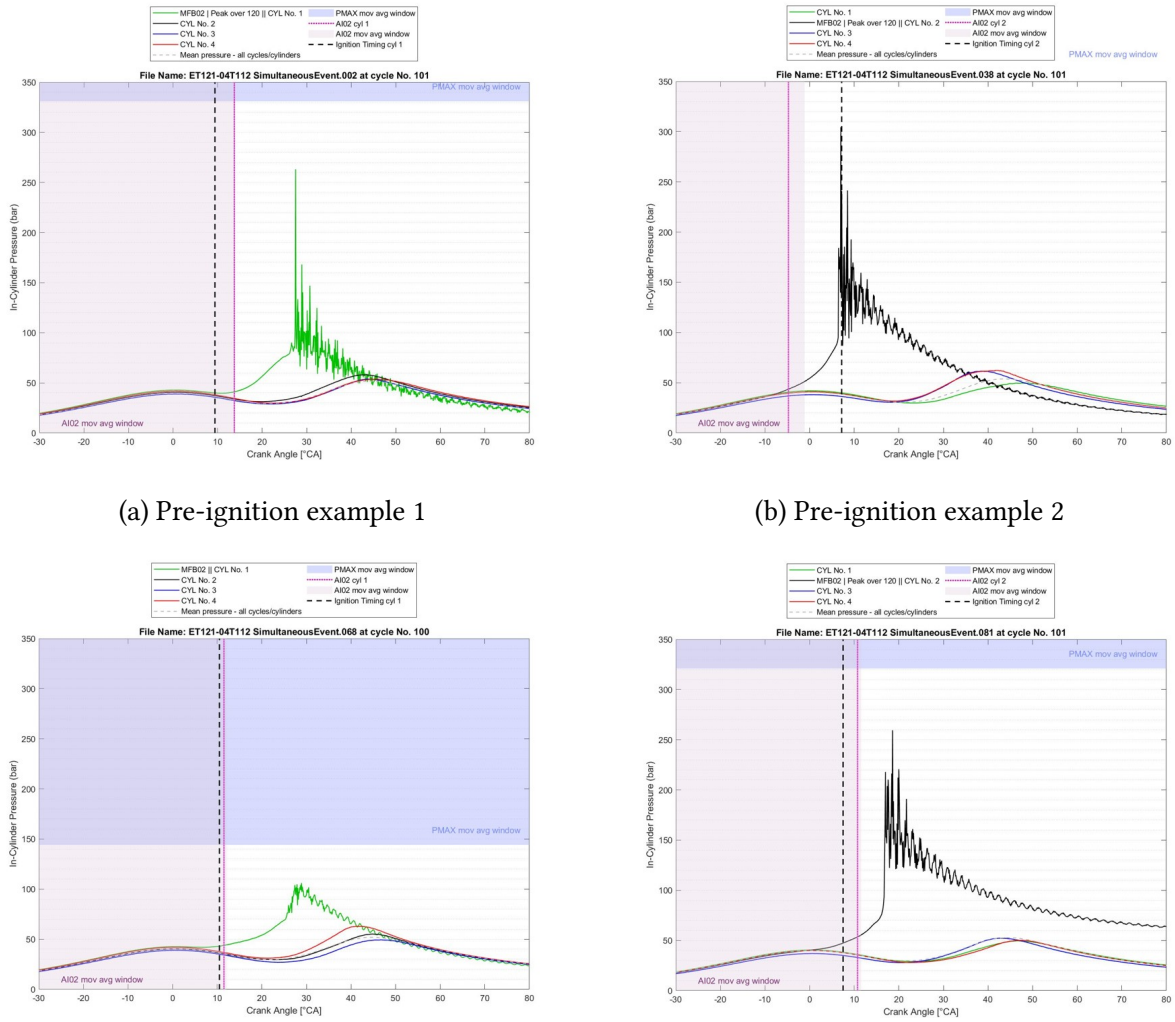

(a) Pre-ignition example 1

(b) Pre-ignition example 2

(c) Pre-ignition example 3

(d) Pre-ignition example 4

Figure 6.11: China bad fuel, clean oil, examples of pre-ignition events captured from the continuous log file.

the ignition timing and the cylinder pressure was rising significantly before the spark timing. The rate of pressure increase was relatively smooth until approx. 8°ATDC whereafter the rate of pressure was vertical, leading to aggressive mega knock by 10°ATDC. Based the work of Kalghatgi [40] on mega-knock, this is likely to be developing detonation (DD). The mean peak pressure of the normal combustion cylinders was 60 - 70 bar, whereas the mean peak of the abnormal cylinder was 150 bar. The acoustic ringing of the mega-knock peaked at over 300 bar.

- **Example (c)** is a relatively mild event pre-ignition event, this particular example was chosen as there was only light knocking and no evidence of mega knock. The mean peak pressure

was around 100 bar and the knocking is that described in Section 2.2.1.

- **Example (d)** was chosen as it characterised the vertical rate of pressure rise of DD around 18 °CA ATDC, similar to *Example (b)*, but less aggressive in terms of the resulting mega-knock. The pre-ignition occurred around TDC, which phased the PMAX around 20 °CA ATDC. These results illustrate that in addition to the stochastic nature of LSPI, the output is very variable in terms of the resulting pressure profile that occurs. This is likely to be due to a number of factors; namely the position and number of PI initiating particles or droplets, the position of the piston in terms of the volume of the cylinder, the timing of the PI event and the in-cylinder conditions (temperature and pressure of the charge) at the point of ignition. The example LSPI events (*a, b & d*) all have high mean cylinder pressures and the peaks of the acoustic ringing above 250 bar. Analysis of these data suggests that their characteristics are consistent with the mechanisms previously described in §2.2.2.

China Bad Fuel 55 PPM MMT

A reference test was conduced between each fuel to check the health of the engine, from Figure 6.9, it can be seen from the second 102 RON reference test that 6 events occurred, which was consistent with the baseline test and the engine health being maintained despite exposure to 315 PI event until this point. Next test was a fuel with China Bad base fuel specification, with the addition of 55 ppm MMT, in combination new oil. The testing commenced but had to aborted after only a quarter of the first test was completed. Investigation of the engine hardware found that this was due to failure of the electro-hydraulic valve-train. Oil analysis of the sump oil confirmed extremely high levels of FiO dilution (15%), which in turn led to reduction in viscosity and hence oil film thickness which caused the mechanical failure. FiO dilution will be discussed in more detail later in this chapter. The prevalence of LSPI with China Bad fuel, as stated in the previous test may have triggered an 'anti-runaway PI' calibration strategy, that prevents this by adding significant enrichment to cool the combustion chamber with fuel. Using the Ifiles from the 30 events that were captured it was possible to evaluate the characteristics of the first fuel containing MMT, Figure 6.12 shows four examples of LSPI captured before the valve-train failure.

- **Example (a)** shows a fairly typical LSPI event similar in characteristic to the previous examples from literature.

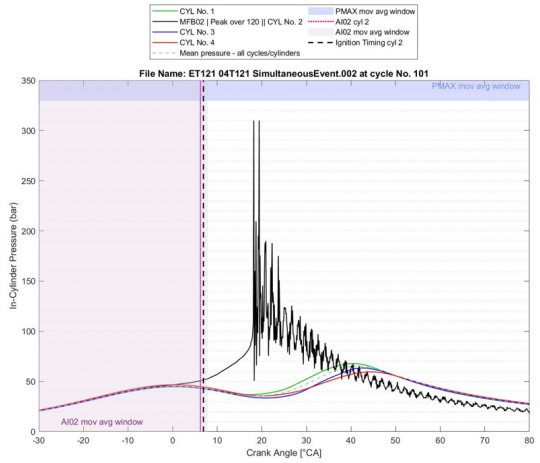

(a) Pre-ignition example 1

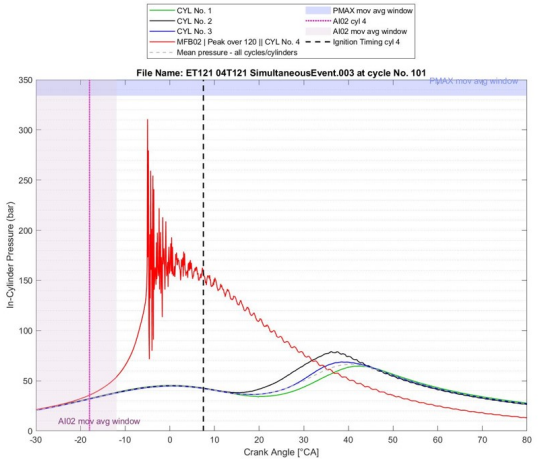

(b) Pre-ignition example 2

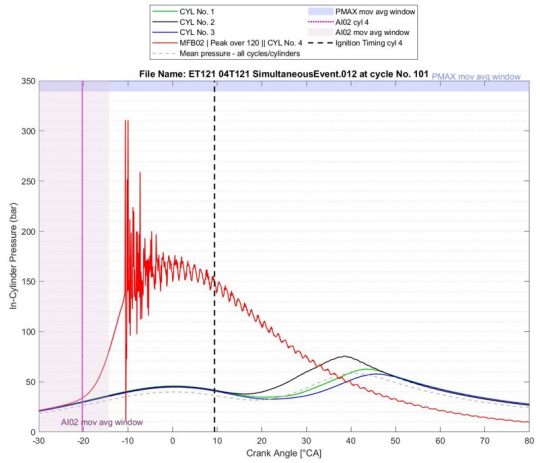

(c) Pre-ignition example 3

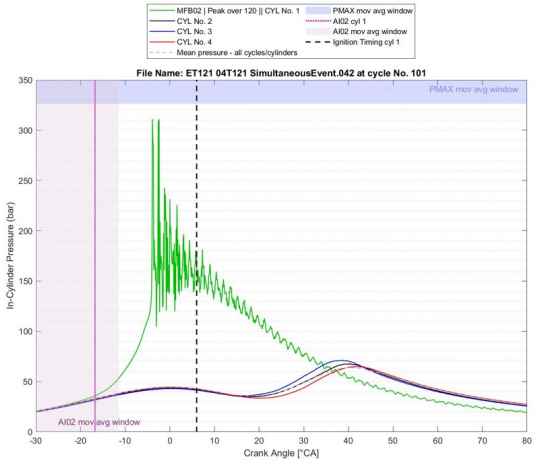

(d) Pre-ignition example 4

Figure 6.12: China bad fuel with 55 ppm MMT. Examples of pre-ignition events captured from the continuous Indimaster log files.

- **Example (b)** of note is the PI event on cylinder 4. This triggered on AI02 and PMAX >120 bar. This is believed to characterise a new behaviour for fuel containing MMT not previously observed. The first point of note, was the extremely early start of combustion, which is around 21 °BTDC. When this is compared to the requested ignition timing, this was 28°CA before the spark timing. This is potentially different to oil or particle based LSPI, which tend to be closer to the spark timing. The resulting peak cylinder pressure of 160 - 170 bar occurred close to TDC, for reference the design pressure limit of the engine is 120 bar. The peak pressure of the acoustic ringing was 310 bar, which represents the more extreme mega-knock events.

- **Example (c) and (d)** were quite similar, with (c) occurring on cylinder 4 (red) and (d) occurring on cylinder 1 (green) respectively, both triggering AI02 and PMAX >120 bar. It is proposed that the high pressure was the result of DD and the combustion occurring in a reducing cylinder volume as the piston approaches TDC.

It is highly likely the available results presented do not reflect the full LSPI potential behaviour of this fuel due to the hardware failures limiting the testing. It expected that if this was retested in the future that the number of events would be significantly higher.

High LSPI Fuel

As detailed in §6.6, 'High LSPI' fuel is generated by CAF a reference LSPI fuel with known promoting attributes. According to the test sequence, Table 6.4 clean oil was used. The result was an average of 15 PI events observed over 4 repeat test cycles, which aligned with previous testing of this fuel (when compared to existing data/experience). The events captured were consistent with a typical LSPI and hence not included in the section for further discussion. The test which followed, was High LSPI fuel in combination with used oil. Again the result was lower than with clean oil (3 events) which was unexpected. So low in fact, that it was compatible with 95 RON E10 fuel. Moreover, consistent with the trend from 'China Bad' in combination with used oil, again inconsistent with the literature [38] and cannot be logically explained on the basis of the causal mechanism.

High LSPI Fuel 55 ppm MMT

The next set of results were the most interesting observed during the multi-cylinder testing campaign. The 102 RON reference test was run prior to testing this fuel and the result of 5 events was consistent with the engine being healthy and fit to proceed with the testing, despite having been exposed to an approximate 374 significant PI events. During the first test the engine reached 226 PI events before having to be halted prematurely due to cooling system pressurisation. After investigation the problem was found to be due to a cracked cylinder head, cylinder-2, exhaust side as shown in Figure 6.13. The deposits on the chamber roof on physical inspection appeared to be 'damp' due to coolant leakage in the region close to the visible cracks, highlighted in yellow. Also of note, is the red discolouration of the exhaust valves, consistent with manganese oxide deposits.

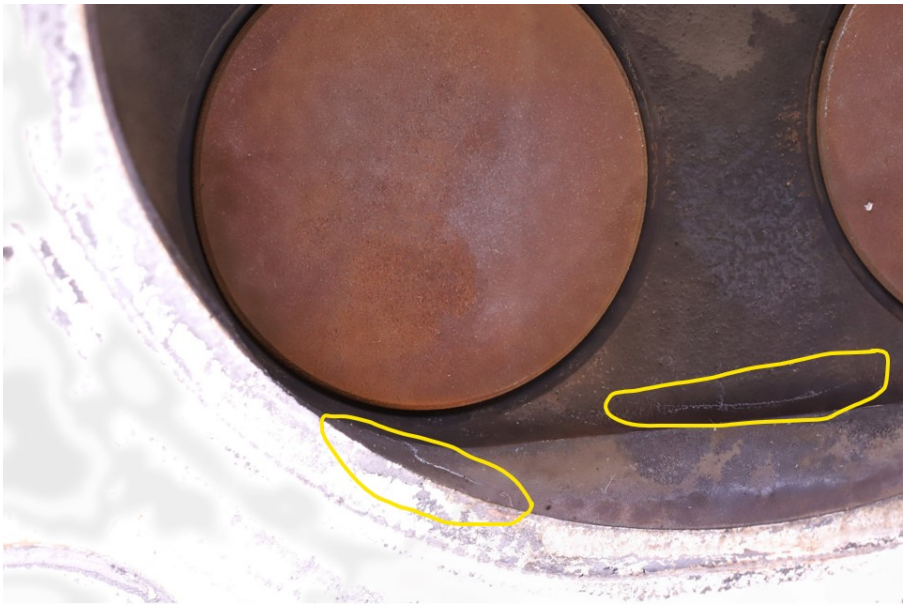

Figure 6.13: Cracked cylinder head, cylinder 2 exhaust side - High LSPI Fuel 55 ppm MMT

To the authors knowledge this is the first observed case as there have been no publicly reported cases of cracked cylinder heads, due to LSPI, reported in the literature. The most commonly recorded damage due to LSPI being associated with the pistons and spark plugs as detailed in Section 2.9. It can be seen from Figure 6.14 that very severe LSPI events were encountered with High LSPI fuel containing MMT.

- **Example (a)** has triggered on cylinder 1 (green) for PMAX greater than 120 bar. The resulting mean peak cylinder pressure was 160 - 170 bar, with a peak mega-knock pressure of 250 bar. The start of combustion was extremely early, estimated to be 28 °CA BTDC, with the corresponding requested ignition timing of 2 °CA ATDC, 30 °CA later. The resulting rise in pressure in the reducing cylinder volume, as the piston moves towards TDC results in a high peak cylinder pressure, before TDC.

- **Example (b)** has a very similar, early start of combustion, but the curve shape is more rounded and the mean peak pressure is in the same range (160 - 170 bar). The resulting mega-knock is not as severe as (a), and the peak pressure occurs before TDC.

- **Example (c)** is almost identical in nature to (b), but the start of combustion is a degree or two earlier.

- **Example (d) and (e)** return to a more typical LSPI form, similar to (a), with a very early start

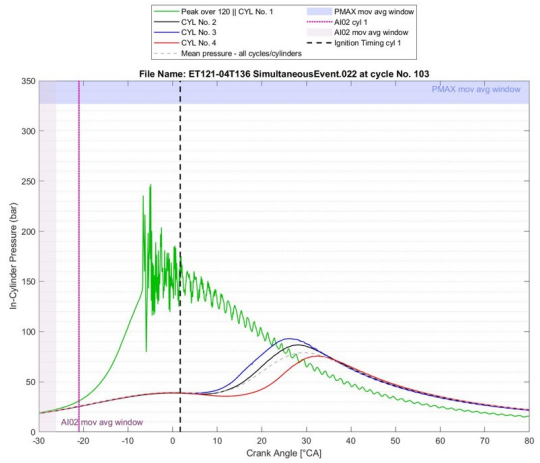

(a) Pre-ignition example 1

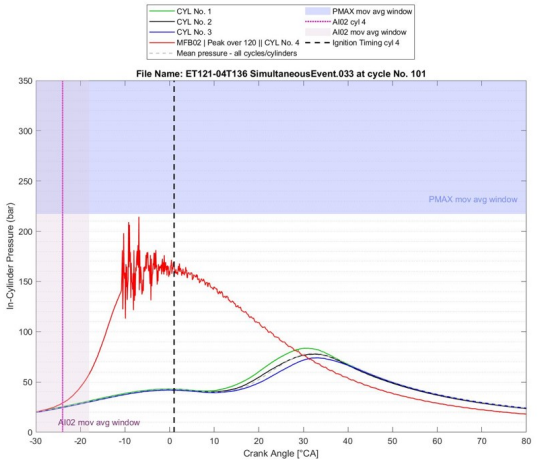

(b) Pre-ignition example 2

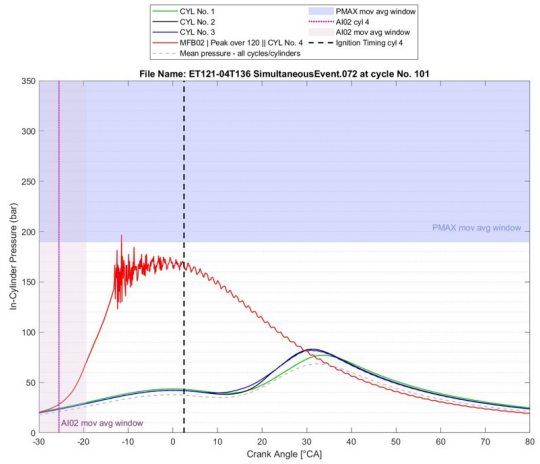

(c) Pre-ignition example 3

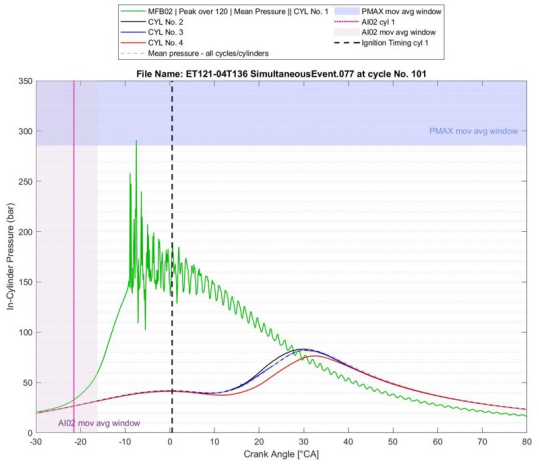

(d) Pre-ignition example 4

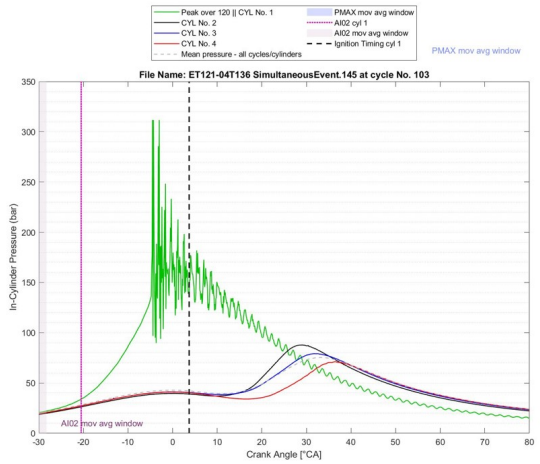

(e) Pre-ignition example 5

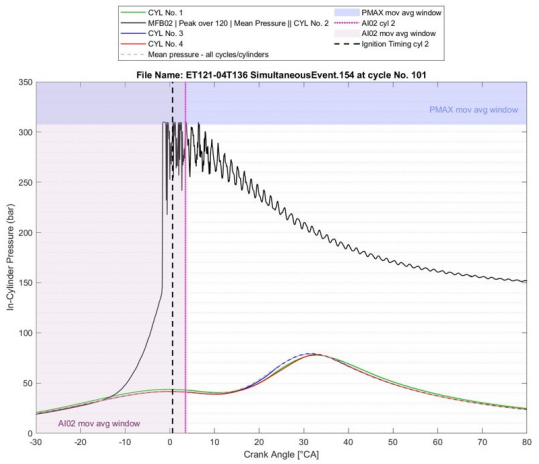

(f) Pre-ignition example 6

Figure 6.14: High LSPI fuel with 55 ppm MMT, examples of pre-ignition events captured from the continuous Indimaster log file.

of combustion.

- **Example (f)** is most remarkable cycle captured. Interestingly, the start of combustion is later, at approximately 15 °CA BTDC. When the rising cylinder pressure reaches 3 °CA BTDC a DD occurs and the pressure rise is vertical. The mean peak pressure reached 280 - 290 bar PMAX, the magnitude of the mega-knock is unknown, but is well in excess of 300 bar (the signal was clipped at 310 bar), possibly up to 350 bar.

In four out of the six examples the AI02 rolling average that triggers the continuous logging to capture the LSPI event as a result of the very early start of combustion. The resulting extreme pressures before TDC, are effectively counteracting the rotating inertia of the engine as the piston approaches TDC. Engines aren't designed to withstand the pressure levels recorded, not least peak pressure regimes before TDC, likely to result in the engine damage experienced. A potential explanation for the cylinder cracking: analogous to connecting rod bending due to LSPI, is the fact that the connecting rod angle is almost vertical at TDC and hence the forces will be acting through the piston crown directly into the connecting rod, via the gudgeon pin. Assuming the piston , pin, con-rod and crankshaft in the vertical position, there is a large upward bending moment due to the high in-cylinder pressure. In most cases its the AI02 rolling average that triggers the continuous logging to capture the LSPI event as a result of the very early start of combustion. A replacement cylinder head was fitted to the engine, following inspection of the bottom-end of the engine, it was confirmed OK to rebuild. Once the engine was re-installed on the test-bed, a 102 RON reference test confirmed that the engine heath was deemed OK to proceed with caution, as the LSPI count was the highest until this point at 11 events per test.

Africa Bad Fuel 30 ppm MMT

This fuel had similar behaviour to all of the fuels containing MMT, namely: very early start of combustion, high mean pressure and very high acoustic ringing. The severity of in-cylinder pressure peaks from mega-knock events of 300 - 350 bar with this fuel, were so extreme that engine failed again after just 107 events. This was an estimate due to sensor damage, constant errors from the indicating system and due to being a single test result does not allowing for any averaging. The engine was inspected and after the cylinder head was removed and pressure tested it was confirmed

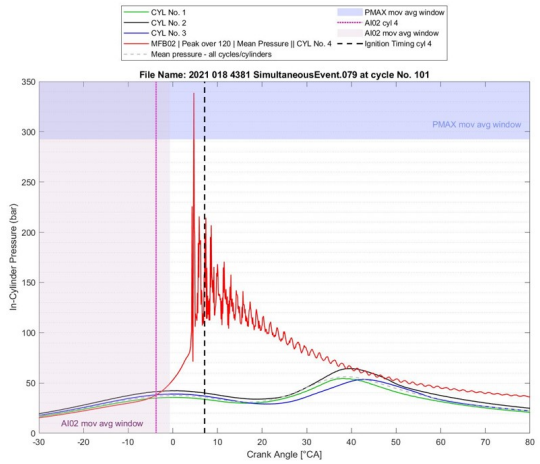

(a) Pre-ignition example 1

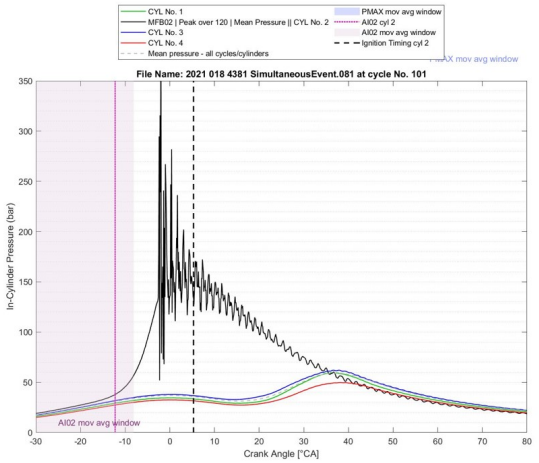

(b) Pre-ignition example 2

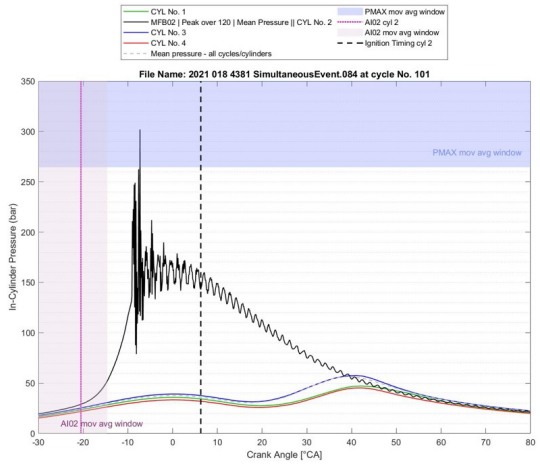

(c) Pre-ignition example 3

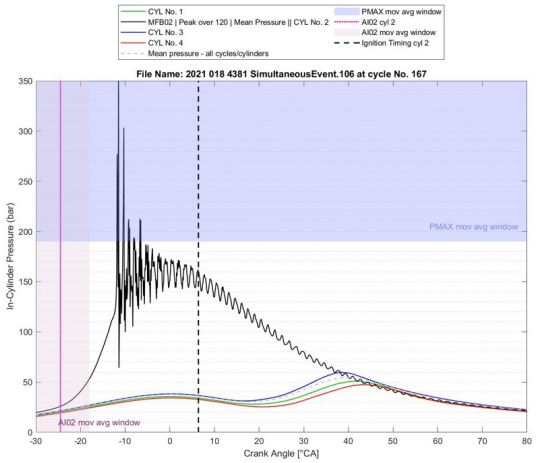

(d) Pre-ignition example 4

Figure 6.15: Africa Bad fuel with 30 ppm MMT, examples of pre-ignition events captured from the continuous Indimaster log file.

that again micro cracks were the cause of failure. This was surprising as this was a new cylinder head which hadn't accumulated the hours of damage that the previous cylinder has been exposed to. This could lead to the conclusion that this is more likely to be caused by overload rather than fatigue. It was determined that the frequency and severity of LSPI fuels containing MMT was so bad, that engine would need to be repaired or replaced after each fuel. This was not possible within the scope of this project, at which point the investigation was ended, prior to collecting a complete data set. A secondary observation from Africa Bad fuel testing, was the amount of damage occurring to the in-cylinder pressure transducers. Typically, all of the pressure traces on the indicating system are aligned during induction and compression stroke, thereafter there is a general divergence due to the cyclic variability from SI combustion. Figure 6.15 illustrates this in examples (*a* - *d*). Whereby,

there is a spread in the traces during compression, which is due to mechanical damage of the transducer diaphragms, affecting the pressure measurements. This error, resulting in the variability of 1 - 2 bar in 350 bar, between cylinders, is only 0.4% error deemed acceptable for the current work. Pressure sensor robustness became an issue throughout the testing, with the sensors regularly being replaced between tests. Assistance was sought from the sensor supplier and some higher pressure rated motor-sport sensors were supplied free of charge for evaluation. Whist they lasted longer than standard sensors, they also fail due to the severity of the maximum pressures experienced, in particularly those with fuels containing MMT.

6.9.1 Run-away LSPI Events

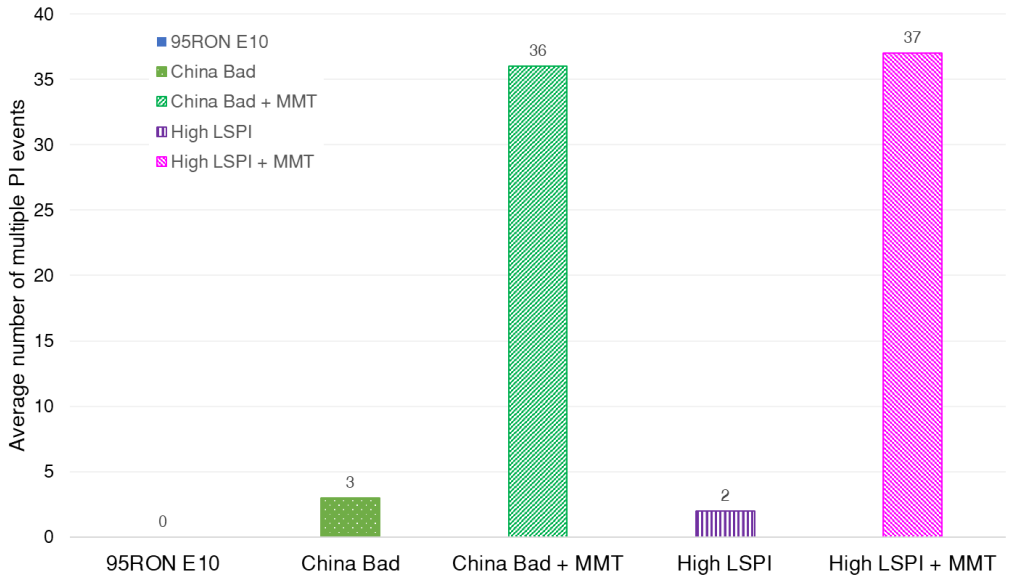

Figure 6.16: Comparison of run-away LSPI event tendency of fuels, with and without MMT.

A stand-out feature of the fuels containing MMT were run-away LSPI events. This phenomenon was described in §2.2.2, where Okada et all [31] present a particle based ignition hypothesis as the cause of LSPI. Figure 6.16 shows an approximate number of multiple LSPI events recorded. It can be seen that no runaway events were present when using the 95 RON pump fuel. A very small number of consecutive or run-away events were also recorded for China Bad and High LSPI fuels. In contrast, the same fuels but with the addition of MMT, exhibit similar high numbers of consecutive or run-away events. Unfortunately test results from the Africa bad fuel could not be included as the

pressure sensors were damaged and the resulting number of events inaccurately captured due to indicating system synchronisation errors, meant that most runaway events were lost or corrupted. It is however proposed by the author, but unproven, that similar large numbers of consecutive or run-away events would have been observed. A proposed hypothesis is that an oil or hot particle based LSPI causes a PI event, leading to the so-called 'snow shaker' effect named by the author [1], whereby the first LSPI triggered by the release of an oil droplet resulting in LSPI, dislodges particles on the combustion chamber surface that heat up and are retained. These particles then go on to cause run-away behaviour. This typically does not occur for a long time thereafter, as the surface particles would need time to reform.

6.9.2 Fuel in Oil Dilution MMT Fuels

Following the failure of the valve-train, oil samples were analysed at BP for fuel in oil dilution using GC MS. This was only conducted for 95 RON and China bad fuel, with new and used oil, Figure 6.17. It can be seen that fuel in oil is relatively low for a dedicated LSPI test cycle (3.5 & 3.7 respectively), due to lower levels of knock retard and fuel enrichment. In contrast, China bad fuel resulted in very retarded ignition timing and fuel enrichment, leading to very high fuel in oil levels (15.2 & 18.2 respectively). This would also have triggered the pre-ignition run-away protection in the engine ECU, reducing λ to as low as 0.6 for 10s to cool the combustion chamber and regain control of combustion. Repeated triggering of this feature would lead to high fuel in oil dilution. Whilst the data is not available, it is anticipated the the fuel in oil levels for the other fuels test would be at least as high as China bad, but potentially higher. An addition observation from these data in Figure 6.9, it can be seen that the total number of LSPI events observed was lower with used oil, despite this having the highest FiO dilution. This contradicts the expected behaviour (as with the number of LSPI events). This remains unexplained and requires further evaluation. Based on guidance from the manufacturer a value of 9% FiO dilution in the sump oil is considered excessive and puts the engine at risk of severe damage due to the reduction in kinematic viscosity. The KV100 is shown in Table 6.6 for 95RON E10 and China Bad fuels, and illustrates the resulting difference between the KV100 at the start of test vs. the end of test.

[1] (named after the desk ornament which is shaken for snow particles to fall on the subject in a closed volume)

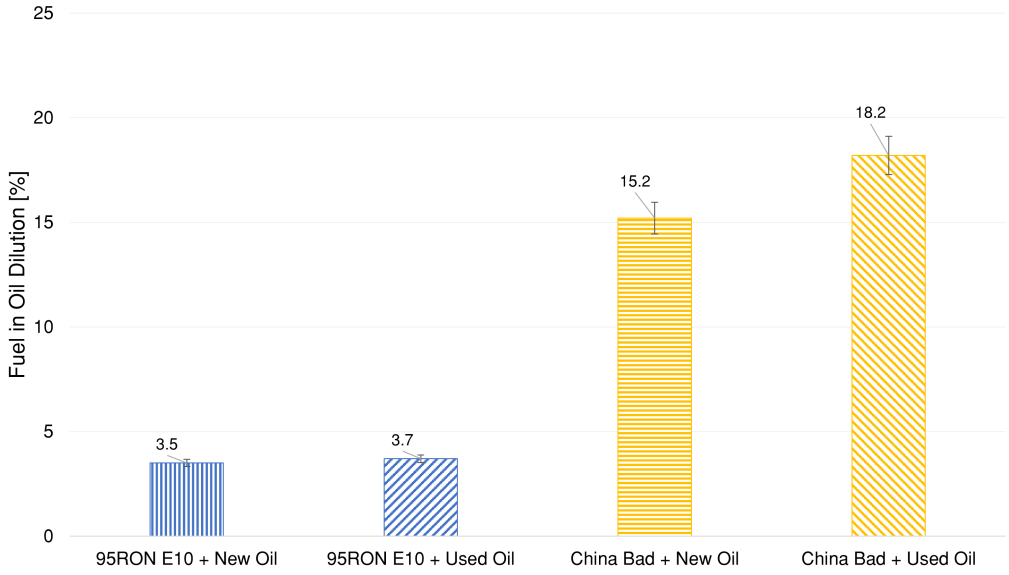

Figure 6.17: Fuel in Oil Dilution, 95 RON vs China Bad Fuel, new and used fuel. Measured via GC MS, uncertainty ± 5% (D2887)

Table 6.6: Comparison of 95RON E10 vs. China Bad fuels, KV100 at the start and end of test. KV (ASTM D445) uncertainty ± 3%.

	Start of Test [cSt]	End of Test [cSt]	Delta [cSt]
95RON E10 + New Oil	7.7	6.6	1.1
95RON E10 + Used Oil	6.6	6.6	0
China Bad + New Oil	7.7	5	2.7
China Bad + Used Oil	6.6	4.5	2.1

It can been seen for the 95 RON E10 fuel that there is a drop of KV100 between the start of test to the end of test of 1.1 cSt. This is due to the new oil being diluted slightly with fuel, 3.5 %, Table 6.6. It is known from Figure 6.9 that only 2 events/test occurred and the resulting FiO dilution was comparable from the service oil (3.75%), Table 6.5. When used oil was tested with the 95 RON fuel only 3.25 events/test occurred and there was no change in the KV100. China Bad fuel had a high PI propensity with extremely high fuel in oil dilution. When new oil was tested there was a reduction in KV100 to 2.7 cSt, vs used oil 2.1 cSt respectively. Whilst there was a significant reduction in KV100 overall, the final viscosity of the used oil was only 0.5 cSt lower in the used oil than the new oil. There is therefore no evidence in the current work that used oil is worse than new oil.

6.10 Analysis of Indicating Data

The cylinder pressure vs. crank angle data captured via the combustion analyser, often referred to as 'indicating data' was interrogated and filtered for errors and outliers. As mentioned previously, due to the aggressive pressure behaviour of the fuels containing MMT the in-cylinder pressure transducers experienced pressure magnitudes and frequency of events that they weren't designed to withstand and this resulted in damaged, unwanted breaks in pressure measurement, pressure offsets and ultimately failed sensors. As stated previously, in normal engine operation LSPI is stochastic and rare in occurrence, however when a specifically designed cycle and fuels are used LSPI can be readily encouraged to occur and does. It was concluded by the author that its not imperative to capture all events in order to draw a conclusion and that with the data captured this was deemed sufficiently conclusive to provide directional data for further investigation into LSPI.

Indicating Parameters

The parameters chosen were not exhaustive, but felt by the author were able to provide clear direction as to data trends present from the testing conducted. They were as follows:

a. **AI02 [CAD]** - The crank angle at which 2% mass fraction of the premixed charge has burned. This was determined via the calculated heat release curve, propriety to AVL List GmbH, the manufacturer of the combustion analyser but typically using a function known as 'Thermodynamics 1A'.

b. **SPA [CAD]** - The angle of spark advance which is a mapped parameter in the engine ECU. For the reference fuels 95 RON E10 and the 102 RON fuel these parameters were fixed to reduce the number of variables in the experiment and active knock control was disabled as the engine was able to run the cycle safely. However, for the aggressive low RON and LSPI promoting fuels it was necessary to allow the ECU to utilise active knock detection and an ECU controlled run-away LSPI prevention strategy, that when triggered enriched the lambda to 0.6, adding extra fuel to provide in-cylinder cooling the charge and reducing the likelihood of runaway LSPI.

c. **PMAX [Bar]** - This is the maximum cylinder pressure observed in the triggered cycle and can be used to optimise the engines efficiency.

d. **APMAX [CAD]** - This is the crank angle that the maximum pressure occurred in the triggered cycle.

e. **AI50 [CAD]** - The crank angle at which 50% mass fraction of the premixed charge has burned. This was determined via the calculated heat release curve, propriety to AVL List GmbH, the manufacturer of the combustion analyser but typically using a function known as 'Thermodynamics 1A'.

f. **KPPK [Bar]** - This parameter is also propriety to AVL, but is based on the difference between a estimated notional mean pressure and the peak knocking pressure amplitude, for the cycle of interest. Its purpose was to estimate the knock intensity, for example low levels of KPPK pressure indicates light knock and the opposite is true for high KPPK values.

g. **RMAX [Bar/°CA]** - This variable is the gradient of the rise in pressure due to combustion. High RMAX or steep rate of pressure rise is typical of aggressive combustion and is often linked to high levels of combustion noise. Abnormal combustion, due to LSPI normally results in high RMAX, but this is not necessarily always lead to high PMAX, other than the acoustic 'ringing' that is typically observed during LSPI cycles.

h. **ARMAX [CAD]** - ARMAX is the crank angle at which the highest rate of pressure rise is observed. This can influence the interaction between the gas and the piston impacting piston secondary motion.

Data Analysis

The objective of the following section was to identify trends is the combustion data captured for the range of fuel and oil combination examined. MATLAB was used to calculate the Weibull 'probability event analysis' to plot the likelihood of occurrence for the parameter of interest using Equation (6.3).

$$P_m = \frac{m}{N+1} \tag{6.3}$$

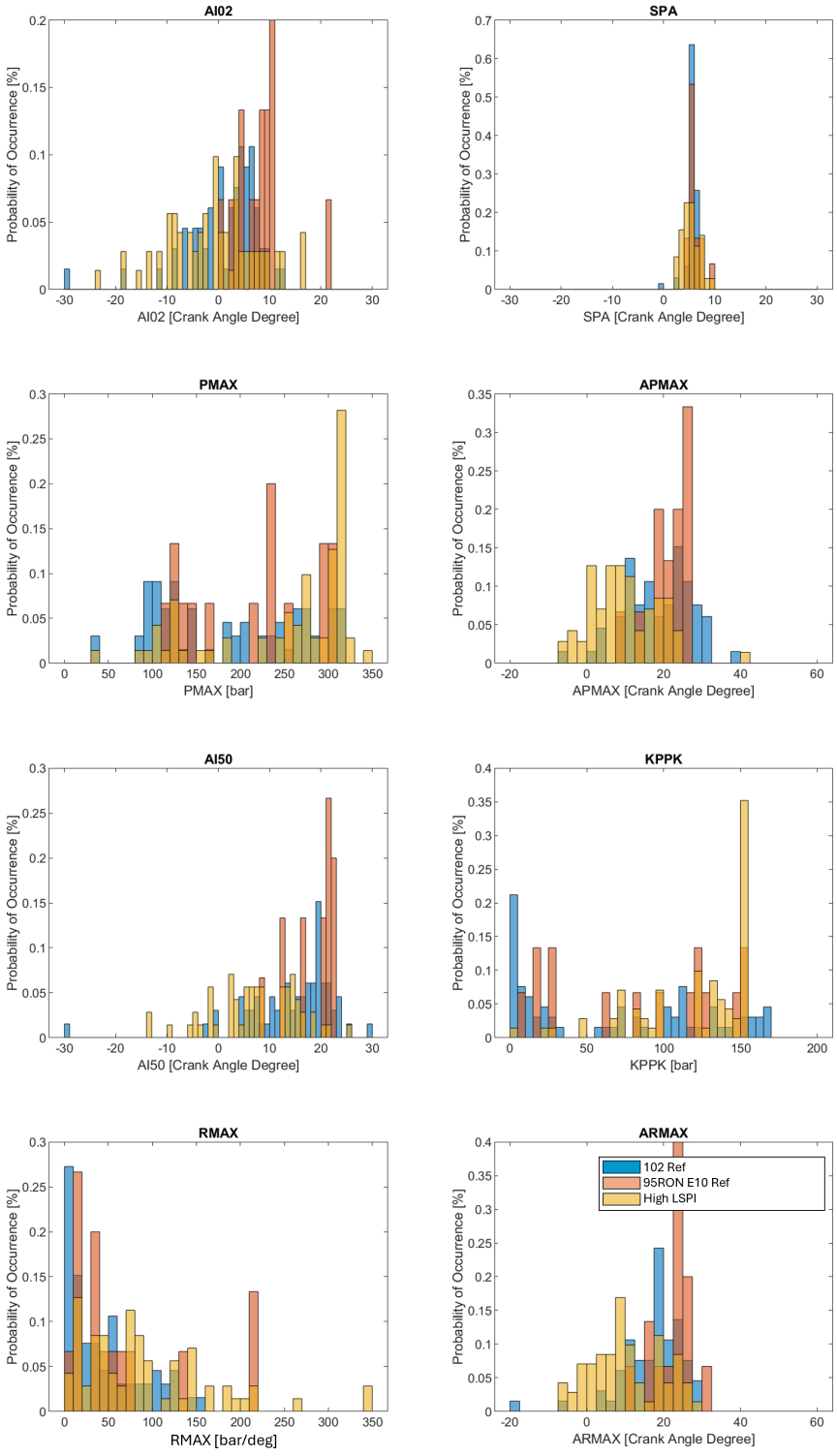

Figure 6.18: Comparison of attributes characterising LSPI: 102 RON (Blue), 95 RON E10 (Red), High LSPI (yellow), new oil.

Where m is the rank of the data point (1 for the highest, 2 for the next highest etc.), N = total number of data points and P_m is the estimated probability of occurrence. This was also normalised such that 1 = 100 %, and 0 °CA represents TDC for the charts with CAD x-axes. Plotted for each

metric, a spread in the data or very early/late phasing as a result of varying fuel properties can be identified. The data was pre-filter to remove erroneous points and obvious outliers due to known pressure sensor issues. Figure 6.18 show a comparison between 95RON E10, 102 RON reference fuel and High LSPI fuels (all with new oil). *AI02* occurs much earlier and has higher variability for High LSPI fuel in comparison to the reference fuels. Due to the fact this fuel was designed to excite abnormal combustion, early and fast burning cycles are typically present. *SPA* was fixed for the 95RON E10, 102 RON reference fuel so there is no variation in angle location, with knock control active for the High LSPI there is a small variation in crank angle. *PMAX*, this chart shows the distribution and prevalence of maximum cylinder pressure. All of the fuels have a wide spread in PMAX, with High LSPI having the widest and highest pressure events, with the largest peak at approx 310 bar. *APMAX* for High LSPI fuel has a large spread in occurrence, with the events biased earlier than the reference fuels. AI50 is typically in the region of 10 – 20 °CA ATDC, whereas the High LSPI fuel is phased earlier and larger spread. No clear trend exits for *KPPK*, this is spread over a wide range of pressures. *RMAX* is typically bias towards lower rise rates as the majority of events are bad but not extreme. As seen in most of the other parameters, LSPI Bad had the most extreme events. Finally *ARMAX* are also spread over a range of crank angle values, with the High LSPI followings the similar tend as with the other metrics of being phased early.

Figure 6.19 shows 102 RON reference fuel vs. High LSPI fuel with and without MMT (all with new oil). The inclusion of MMT had a dramatic effect on the combustion parameters. Of note was *AI02* which displayed very advanced phasing and was spread over approximately 35 CAD. *SPA* for 102 RON remained fixed, LSPI High had a slight spread, but with similar phasing to 102 RON due but was 96 RON, High LSPI with MMT retarded by 5 °CA, despite the highest RON of the aggressive fuels, Figure 6.4. *PMAX*, the addition of MMT had the effect of significantly increasing the occurrence of higher pressure events. There was a particular cluster between 310 - 320 bar. *APMAX* also highlighted a significant shift for High LSPI with MMT to much earlier events. *AI50* similarly retarded in phasing, the large spread indicative of higher cyclic variability. *KPPK* shows an increase in higher peak amplitudes, with a cluster around 150 bar. *RMAX* is similar to with or without the addition of MMT. *ARMAX* is similar, with a slighty earlier phasing with the addition of MMT.

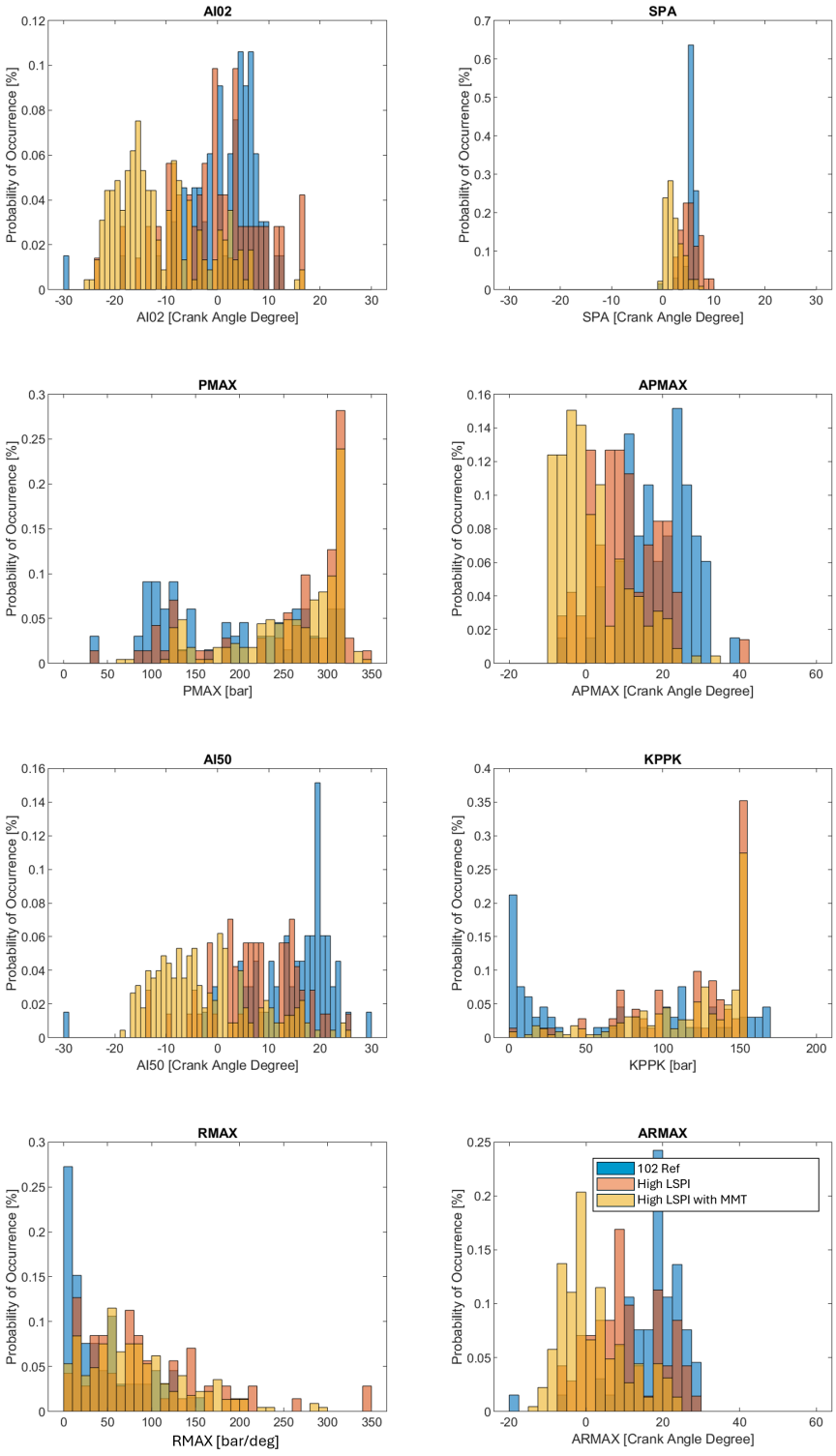

Figure 6.19: Comparison of attributes characterising LSPI - 102 RON (Blue), High LSPI (Red), High LSPI MMT (yellow), all new oil

A similar comparison was made for China Bad fuel with and without MMT, all new oil, Figure 6.20.

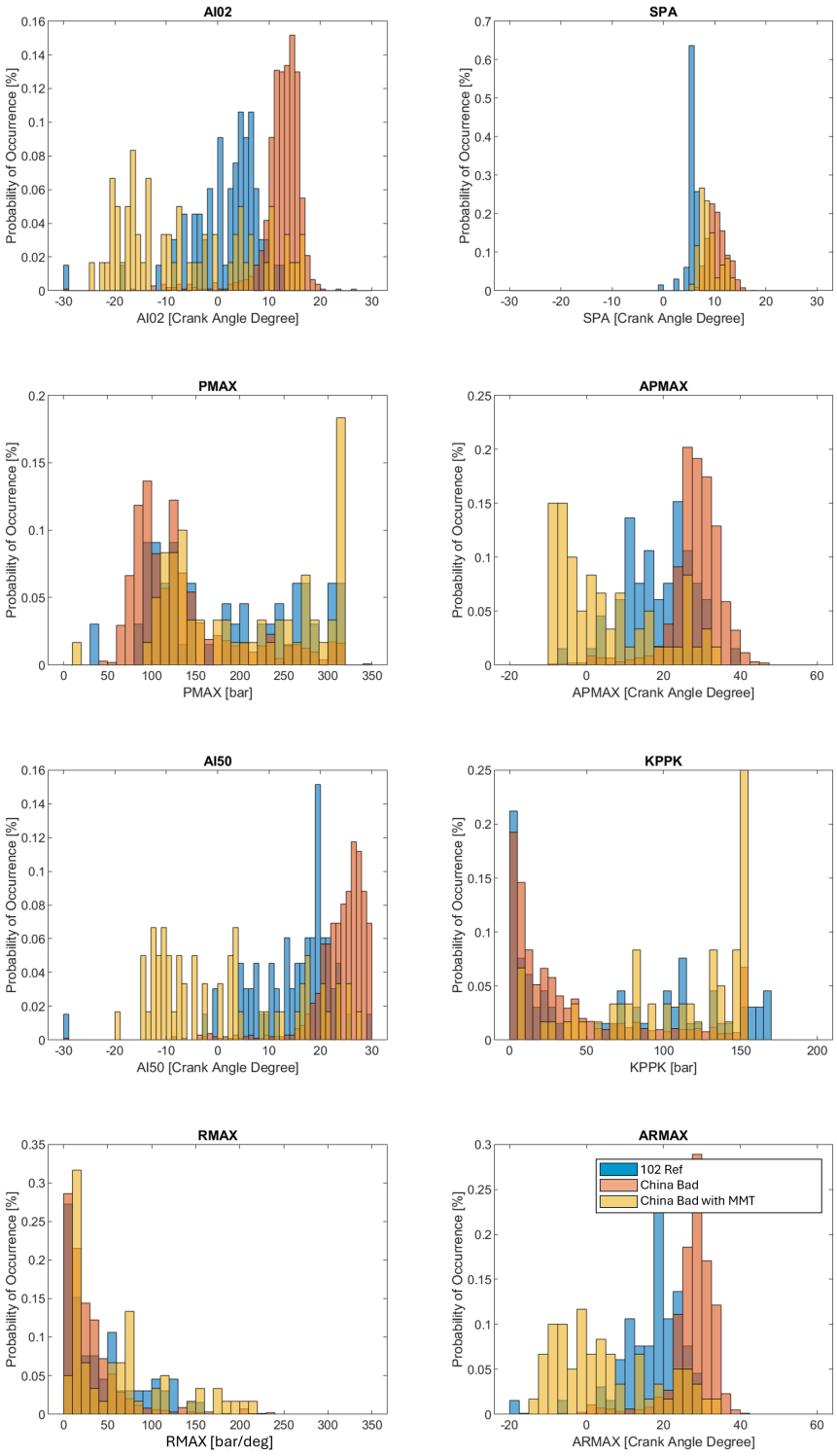

Figure 6.20: Comparison of attributes characterising LSPI - 102 RON (Blue), China Bad (Red), China Bad MMT (yellow), all new oil.

Starting with *SPA* , it can be seen that the effect of lower RON China Bad fuel retards ignition 5 – 8 degrees. This can also been seen in the *AI02* plot, however the addition of MMT significantly advances this parameter due to LSPI, more so than the fuel without the addition on MMT. *PMAX*

has a similar trend with or without MMT, with the exception of a small cluster at 320 bar. As seen with the High LSPI fuel, *APMAX* is earlier due to the LSPI events. As with *AI02*, a similar trend can be observed with *AI50*. There is a retardation with knock control active due to the lower RON of this fuel, and due to abnormal combustion the phasing of this fuel with the addition of MMT leads to more advanced combustion phasing. *KPPK* is similar with and without MMT, with a slight indication of higher peak amplitudes with the addition of MMT due to a cluster around 150 bar. *RMAX* is similar, again there is a slight tendency for higher gradients with the addition of MMT. *ARMAX* displays again the effect RON and increased LSPI tendency with the addition of MMT. Figure 6.21 includes the effect of new and used oil in addition to the inclusion of MMT. For the reasons described in Figure 6.9 it was not possible to complete a test using China Bad fuel with MMT and used oil. Hence this comparison was only made for High LSPI fuel. As Figure 6.19 already made a comparison between High LSPI with and without MMT this will not be covered again. This section will focus solely on the effect of used oil which was tested only with High LSPI fuel without MMT, the effect of MMT is added for comparison purposes. In general the addition of used oil tended to have a very similar effect on all parameters, there were no clear adverse trends (red vs. blue bars). Why the addition of used oil did not have a promoting effect for LSPI, as detailed in the literature, remains unknown.

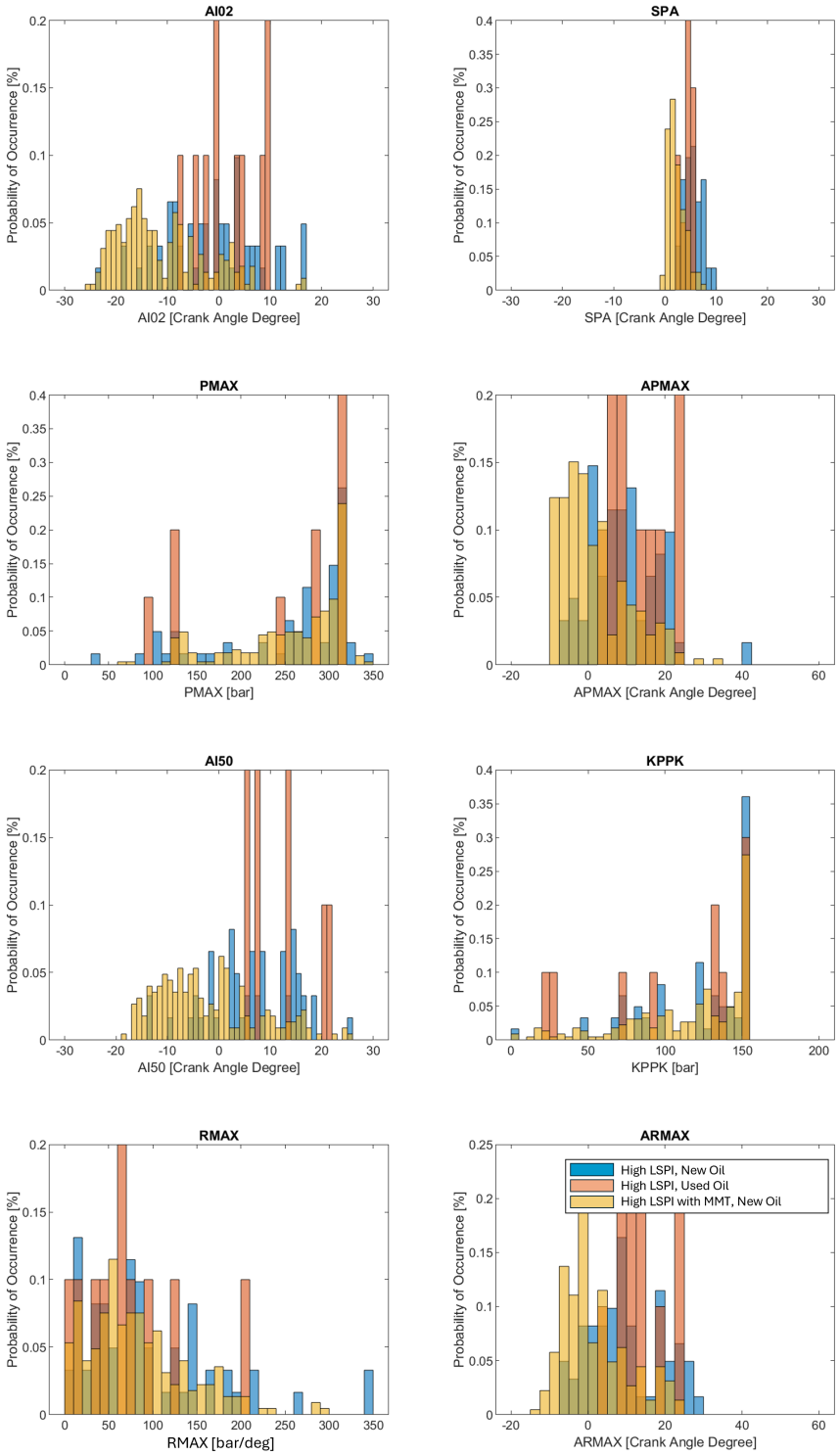

Figure 6.21: Comparison of attributes characterising LSPI - High LSPI New Oil (Blue), High LSPI Used Oil (Red), High LSPI MMT New Oil (yellow).

6.11 The Effect of MMT on Engine Hardware

It was proposed that the cause of LSPI with fuels containing MMT, was due to injector hardware damage or errors in engine lambda control. An objective of the current work was to investigate this hypothesis, hence for each fuel tested, the injectors and lambda sensors were changed and the engine was inspected. It was not possible to collect borescope image for all fuels, however a comparison between 102 Ref and China bad was available. Figure 6.22 compares images of the piston crowns for 102 RON fuel vs. China Bad fuel. It can be seen that after the 102 RON testing the combustion chamber was clean and deposit free.

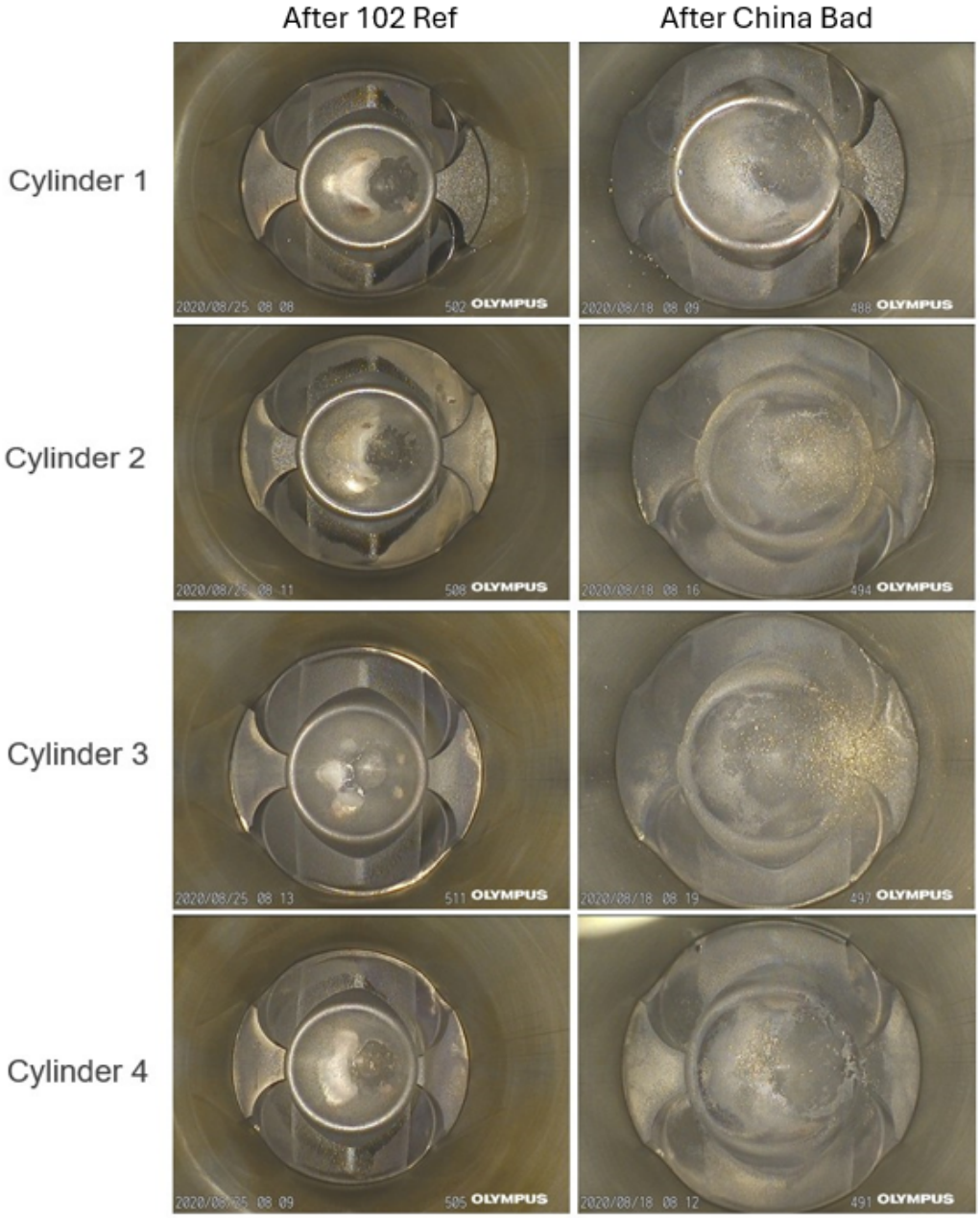

Figure 6.22: Borescope comparison of pistons, post testing: 102 RON vs. China Bad fuel.

In contrast, post test running China Bad fuel, the piston crowns are coated in deposits. Pistons 2 – 4 have what appears to be evidence of knock damage (erosion) or bright yellow deposits. The China bad fuel had the lowest RON at 90.2, which would result in significant knock in addition to the LSPI propensity previously discussed. As MMT is known to create a range of coloured oxide deposits, from yellow through to brown, yellow deposits on the piston crown are plausible. However, erosion is of the piston material is also feasible. The quality of the pictures does not allow for a definitive conclusion to be made. In general, knock tends to preferentially occur where the end gas is spacially located in the cylinder [127]. In this case the location of knock appears to be on the intake side of the engine if the bright areas on the piston crown are consistent with damage. Figure 6.23 shows images of the thrust (intake) side of the liner. The yellow appearance was due to the light source rather than MMT in the fuel. The 102 RON fuel resulted in a small amount of lacquering from oil consumption, in the area above the top ring reversal (which is normal). The liner honing is visible on all four cylinders, which confirmed the engine was in good condition. In contrast, the China Bad fuel created significant brown lacquer deposits in the top land crevice area, on all cylinders. The most affected was cylinder 3 where the highest occurrence of brown deposits was present. This could indicate that cylinder 3 had the highest liner temperatures, increasing knock tendency and promotion of deposits. This was also consistent with the piston images in Figure 6.22, whereby piston 3 had the highest evidence of deposit accumulation or knock damage. The remaining cylinders were in the early stages of similar deposit accumulation. Also of note, was the removal of deposits above the top ring reversal, a known LSPI mechanism and potential related to the run-away behaviour detailed in Figure 6.16. Completing the borescope assessment of the engines internals, Figure 6.24 compares the intake and exhaust valves running 102 RON vs. China Bad fuel. The image quality is not consistent in terms of viewing position as the bore-scope was turned through 180°to view the valves. The exhaust valves are characterised by having a flat face interface with the combustion gasses, whereas the intake valves have a ‘dish shaped’ feature in the face of the valve. The exhaust valve have a similar colouration for both fuels and hence are unremarkable. When running on 102 RON fuel, the intake valves have light transient soot deposits. In contrast, China Bad fuel resulted in significantly more soot deposits. Additionally, there appeared to be more soot on the combustion chamber when running China Bad fuel. All of the LSPI promoting fuels are high in aromatic content, Figure 6.7, and therefore have higher soot promoting tendency.

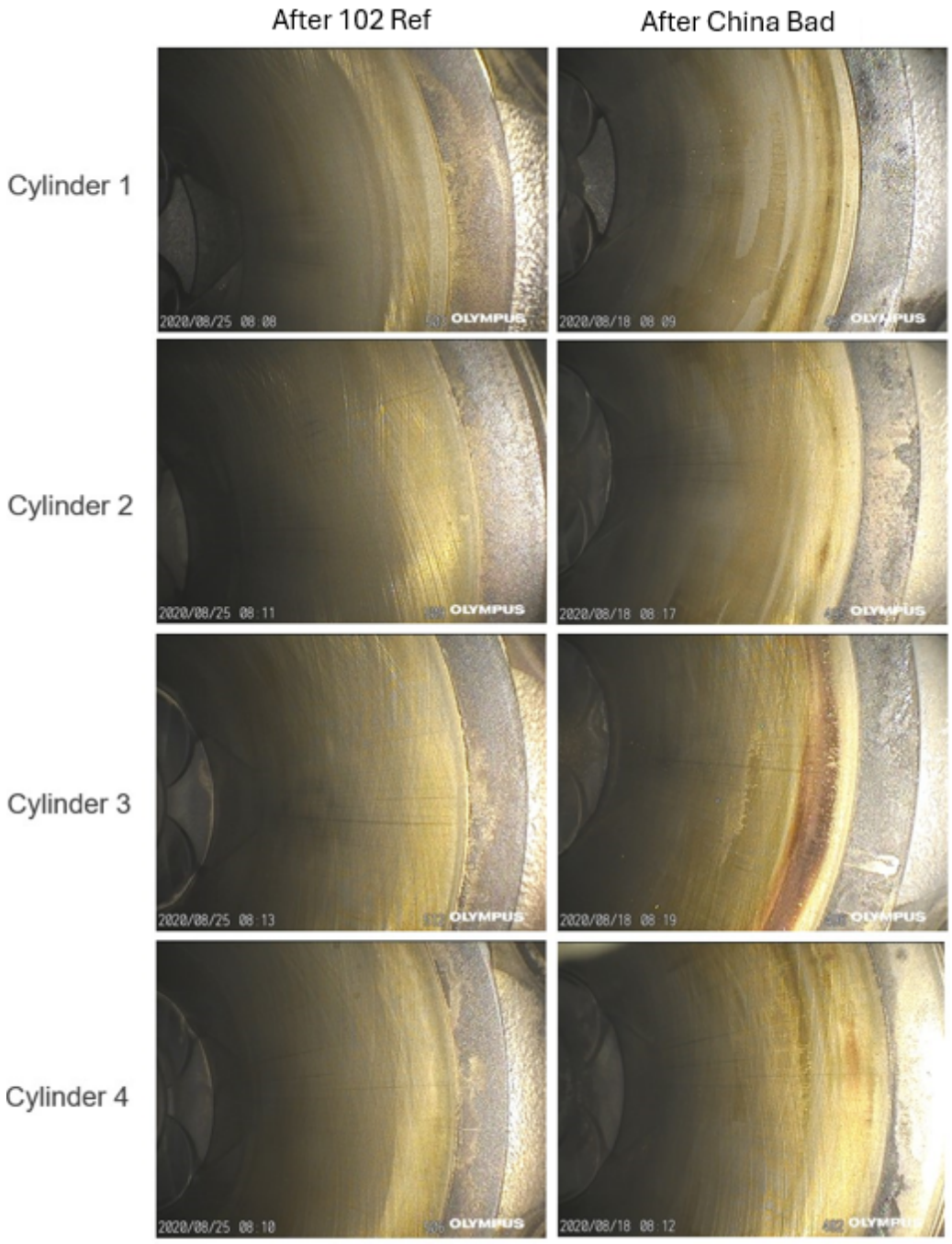

Figure 6.23: Borescope comparison of liner (thrust side), post testing: 102 RON vs. China Bad fuel.

The deposits present in the cylinder are therefore a potential combination of manganese oxide deposits and soot particles. Based on the literature both particle types have the propensity to instigate LSPI albeit via different mechanisms. The most likely cause for the soot particles is analogous to a glowing particle from a fire. The mechanism is not clear for the manganese oxide particle, but it has been suggested that a potential catalytic effect could be the cause of LSPI when this fuel is used. To exacerbate the problem when using fuel containing MMT is the likelihood that the base fuel is

low quality and has lower RON, increasing the knock tendency and opportunity to liberate particles from the combustion chamber surfaces.

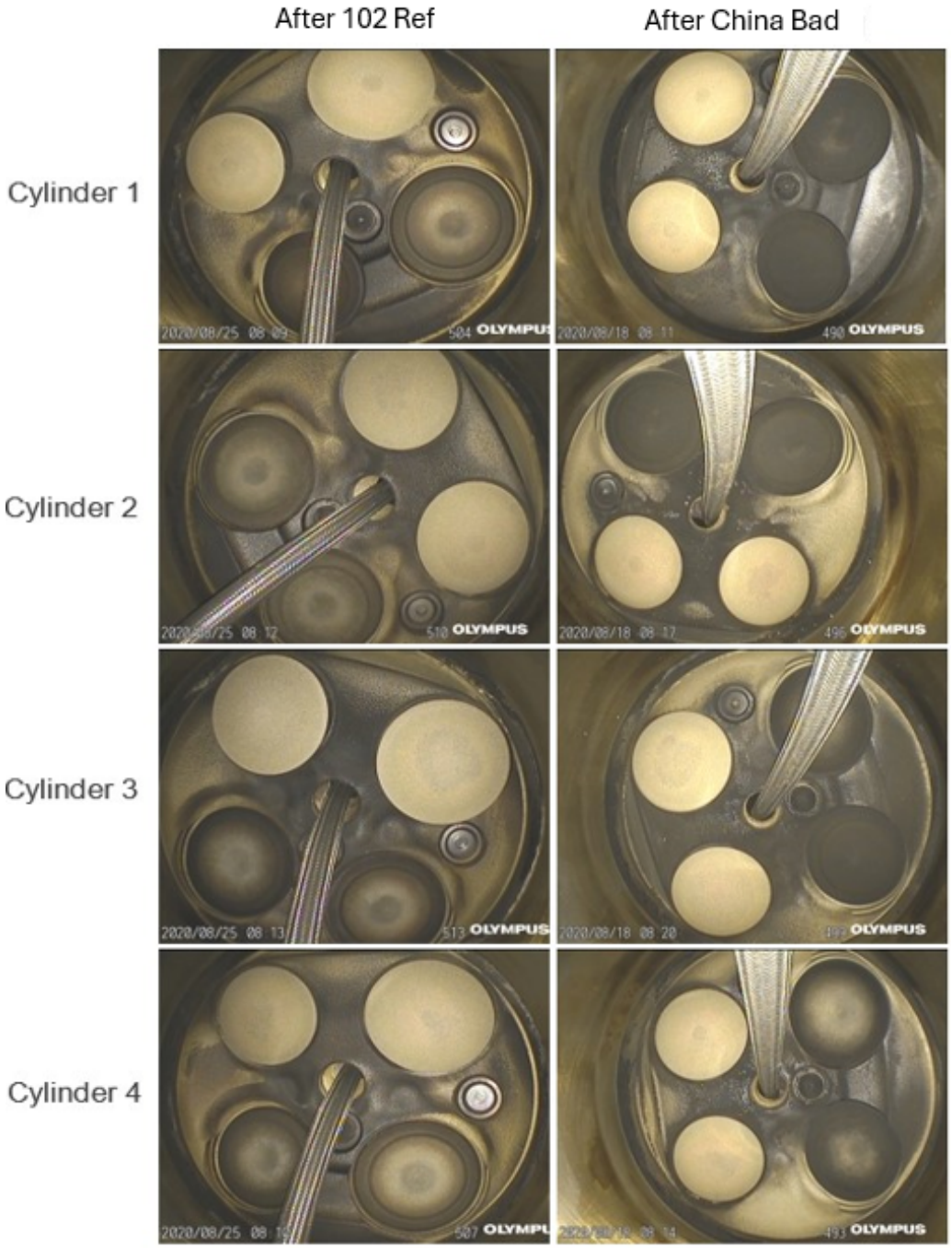

Figure 6.24: Borescope comparison of the valves, post testing: 102 RON vs. China Bad fuel.

Examination of the Fuel Injector Tip, Africa Bad Fuel with MMT

The fuel injectors are mounted in the cylinder head with the tips exposed to the combustion process on a cyclic basis. As a result the injector tip temperature will vary with the running condition of the engine. This is controlled to an extent by the resulting fuel flow having a cooling function. The fluid dynamics of the injector opening and closing behaviour, in conjunction with the geometric features of the injector tip, result in 'tip wetting'. Over time, the tip wetting in combination with in-cylinder cyclic temperature and pressure variation can result in tip deposit accumulation [128]. Figure 6.25 (a) shows deposit accumulation whereby the hard sponge like structure can retain fuel, which when burnt in a low oxygen environment results in diffusive high soot combustion and high particle number count.

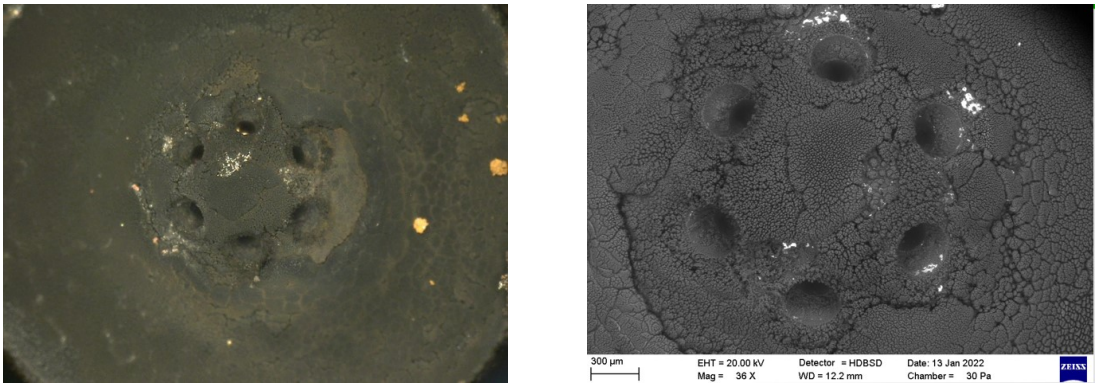

(a) Africa Bad fuel with MMT, 50 x magnification. (b) Africa Bad fuel with MMT, SEM.

Figure 6.25: Bosch HDEV5, 6-hole, injector tip coking.

The same injector was also examined using a scanning electron microscope (SEM), Figure 6.25 (b). The SEM highlights a cellular structure of the tip deposit, the spaces being able to retain fuel. The injector holes, when clean have a so-called 'step-hole' or annular machining so that the outer hole is larger than the spray hole itself. This is an anti-clogging feature, the SEM shows that deposit has covered the inner corner of the machining to form a natural conical shape. The spray holes themselves are clear of deposit due to the fuel pressure which was 150 bar for the majority of the the LSPI test. To determine if there was a significant manganese deposit on the injector tip, a Scanning Electron Microscopy with Energy Dispersive X-ray Analysis (SEM-EDX) technique was used due to its ability to perform elemental analysis on surfaces. The SEM-EDX process produces a high resolution images by rastering a focussed electron beam, then detecting the backscattering electron signal [129]. Figure 6.26 upper image shows the SEM-EDX mapping pictures that provide the surface

elemental analysis. The lower image in Figure 6.26, shows a histogram of elements, the x-axis is Kiloelectronvolts (keV) and the y-axis is the elemental energy level in 'counts'. It can be seen that the dominant element is carbon, this is undoubtedly a product of combusting a hydrocarbon fuel. The second much smaller peak of manganese and trace quantities of O, Zn, Cr, Cu, Co, C+O, F, Fe, Al, Si, P and were also detected.

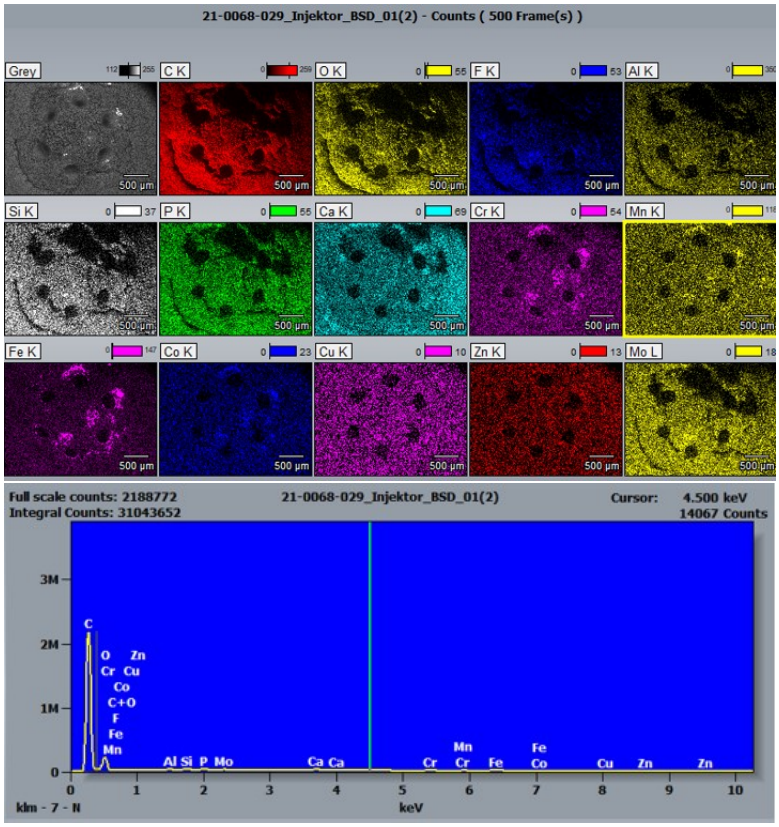

Figure 6.26: Bosch HDEV5, 6-hole injector, Africa Bad fuel: injector tip analysis via SEM-EDX.

This technique was able to detect elements from the fuel, possibly calcium from the lubricating oil and the metallic surface of the injector itself. The SEM-EDX technique apportions a colour to each element allowing for qualitative overlaying or mapping, Figure 6.27. The upper image shows Mn, the brighter intensity showing the highest concentration. The middle image shows the addition of O in blue, and the lower picture shown Fe in pink. The injector is made of stainless steel, of which iron is the highest content element. The presence of Mn is not surprising due to its presence in the fuel. The injector deposits are known to be transient in nature, hence could readily detach and go on to create LSPI. Not included in the section, but available for review, are images of the injectors and spark plugs for 95 RON E10 and China Bad fuel, which can be found in Appendix C. Of note is the fact that the spark plugs insulators did not sustain and damage from the extreme pre-ignition

and mega-knock experienced with this fuel.

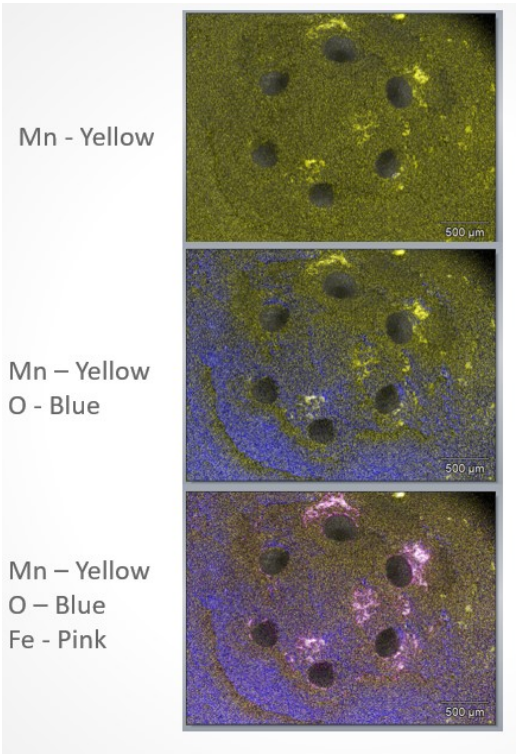

Figure 6.27: Bosch HDEV5, 6-hole injector, Africa Bad fuel: injector tip analysis via SEM-EDX mapping overlay.

Examination of the Oxygen Sensor

As with the hypothesis that damaged fuel injectors cause LSPI, a similar hypothesis was proposed that damage to the oxygen sensors could be the cause of LSPI when using fuels containing MMT. This hypothesis was based on the possibility the damage to the oxygen sensor could again result in incorrect fuel delivery for the operating condition leading to LSPI. To remove this noise factor the oxygen sensors were replaced for each test when the fuel changed at the same time the injectors and spark plugs were changed. It can be seen in figure 6.28 (a), that universal heated exhaust gas oxygen sensor (UHEGO), catalyst brick and the surrounding metal work were covered in an orange powder, extremely likely to be manganese oxide [130]. The visible deposit on the outside of the oxygen sensor is fairly light, in contrast the deposit accumulation on the front face of the catalyst brick is more significant and was appearing to form in the wake of the UHEGO sensor 6.28 (b). It was not possible to have the UHEGO sensors tested by the supplier post engine test. It can however be confirmed that there were no error codes or indications that the closed loop lambda

control was adversely affected by this deposit accumulation.

(a) Pre-catalyst UHEGO sensor, High LSPI fuel. (b) Starter Catalyst, High LSPI fuel.

Figure 6.28: Mn oxide powder deposits on the UHEGO and front face of the starter catalyst.

Evidence is present in the literature regarding the long term effect Mn oxide powder has on the UHEGO sensors, spark plugs and clogging of the catalyst brick [131]. As the total test time of the catalysts was relatively short, despite the presence of Mn oxide deposits on the front face of the catalyst, no increase in exhaust back pressure was observed.

6.12 Discussion

Testing of LSPI promotion fuels with and without MMT

The test cycle chosen to investigate the effect of MMT, was the LSPI test cycle detailed in §2.6, due to the fact that this test is able to discriminate between droplet vs. particle LSPI mechanisms. The inclusion of clean vs. used oil was to determine if there was a further aggravating effect of used oil reported in literature. Based on the analysis in the current work, it is hypothesised by the author that a deposit based mechanism is more likely cause of LSPI when MMT is added to the fuel, than an oil droplet based mechanism. However, the unexplained effect of reducing LSPI tendency ob-

served with used oil, is inconsistent with the literature. A similar hypothesis was loosely proposed by Nomura [132], but not precisely the same, as only limited testing was conducted. The results of the current work confirm the aggressive LSPI promoting effects of MMT. Due to the extremely aggressive LSPI behaviour observed, there were limits as to the tested that could be completed when MMT was present. Based on the combinations of tests that were successfully completed, a number of observations could be made. The re-baseline using 102RON fuel after each candidate fuel test proved decisive in monitoring engine health throughout the testing. It was noteworthy that for the last reference test, this was successfully used to discriminate that the overall engine health had deteriorated and despite a new cylinder head being fitted, the engine failed prematurely. The contrast in results between the 102RON fuel and 95 RON E10 fuels was useful to characterise the baseline knock and LSPI behaviour, which whilst was inconsequential for these fuels, later became significant factor for the LSPI targetting fuels, resulting in modifications to the adaptive knock control strategy. The most noteworthy findings of the current work was capturing previously unseen examples of LSPI resulting from the addition of MMT to LSPI promoting fuels. China Bad and LSPI High fuels were most extensively characterised, both leading to extremely high levels of LSPI occurrence the engine experienced. The detailed analysis of the cylinder pressure indicating data highlighted key feature of fuels containing MMT, namely extremely early LSPI events (characterised by advanced *AI02*), high rates of pressure rise (*RMAX*) and occurrences of *APMAX* on or just before TDC. This exerted extreme levels of mechanical stress on the engine components, ultimately leading to multiple mechanical failure of the cylinder head. Also of note was the unexpected and as yet unexplained reducing effect on LSPI frequency testing with used oil. There was an significant effect of MMT that resulted in increased levels of run-away LSPI events, not experienced in so prevalently in the fuels without MMT. The high levels of the fuel in oil dilution observed in the fuels testing was significant. The results presented in Figure 6.17 show post test FiO dilution levels with 95 RON E10 fuel of 3.5% in the sump oil, however when running with fuel containing MMT this rose 5 to 6 fold, ultimately leading to engine damage due to low oil viscosity and reduced lubricity.

Effects on engine hardware of fuels with and without MMT

Evidence of increased soot and either Mn deposits was present on the piston crowns with the addition of MMT to the fuel. There was a clear trend in deposit accumulation on the liner, and removal

of deposits, due to knocking from the area above the top ring reversal. The intake valves appeared to accumulate greater levels of soot deposits with MMT containing fuels, thought to be the result of higher aromatic content in the base fuel and rich operation due to retarded combustion phasing and run-away LSPI strategies. It was possible to disprove the hypothesis that MMT does not directly cause LSPI, rather degraded fuel injector and oxygen sensor damage. No evidence of injector or UHEGO damage, resulting in incorrect AFR, was present when testing fuels containing MMT, in the presence of aggressive LSPI. Accumulation of manganese oxide in the exhaust was evident, consistent with the literature. Publications reviewed, also described orange or reddish brown deposits on engine and after-treatment components after operating on fuels containing MMT [130–133], Figure 6.29. Due to the relative short time scales in terms of catalyst life, no damage occurred to either the UHEGO or blocking of the catalyst brick during this work.

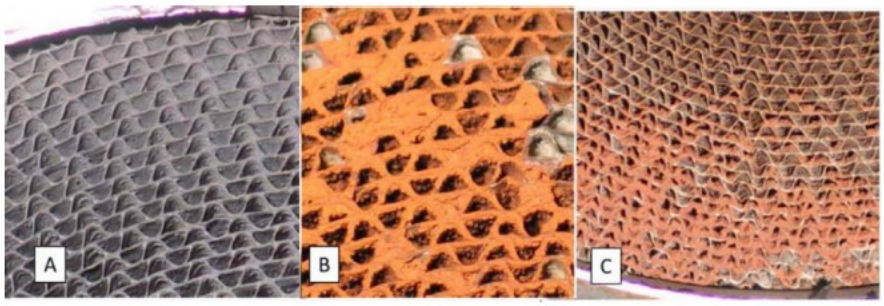

Figure 3. Color photographs of the front faces of the Porsche Carrera catalysts after durability testing. (A) Starter catalysts with Super-Plus, (B) Starter catalyst with Super Plus and MMT, (C) Main catalyst with Super-Plus and MMT.

Figure 6.29: Example deposits observed on catalysts where fuels containing MMT were used during durability testing [130].

6.13 Conclusion

In conclusion, it can be seen that: LSPI promoting fuels with and without MMT were successfully tested to investigate the LSPI behaviour of MMT octane booster. The frequency and magnitude of LSPI events of fuels containing MMT was significant and led to engine damage as a result of mechanical stress. Due to the severity of events encountered, it was not possible to test all of the planned fuel and oil combinations in the test matrix due to the engine hardware damage, ultimately ending the test campaign prematurely. A significant observation, was the distinct difference in

the type and phasing of LSPI in fuel containing MMT, characterised by very early *AI02* and *PMAX* before TDC. In general the average levels of *PMAX* weren't significantly higher than fuels without MMT, despite the highest recorded events being when MMT was present. The gradient of *RMAX* was steeper with MMT present than without. There were also occurrences of *APMAX* before TDC leading to high pressure events whilst the piston was travelling upwards. The inclusion of used oil in the testing of fuels containing MMT did not display the same effect previously presented in literature for oil based LSPI mechanisms. Fuel in oil dilution was extremely high in tests where MMT was added to the fuel. The resulting reduction in oil viscosity was such that mechanical failures of the valve train components occurred. An increased tendency for run-away LSPI events was observed when using fuels containing MMT vs no MMT. The severity of damage observed in this test campaign has not been reported in literature and the cylinder head cracking is the first time this has been seen by the Author. It was demonstrated with reasonable certainty that the cause of LSPI, when MMT is included in the fuel, was not related to injector wear or mis-reading oxygen sensors. It is possible that these factors could lead to increased LSPI tendency to occur over extended engine lifetime, but are not the primary causal mechanism for increase LSPI frequency with MMT.

Chapter 7

Conclusions, Claims of Originality and Further Work

7.1 Conclusions

This thesis comprises three key areas:

Fundamental Investigation in to Oil Detergent as the Cause of LSPI

This work focussed on investigating the previously reported observation "calcium detergent promotes LSPI, whereas magnesium detergent does not", at a fundamental level away from the ICE. In practice this proved to be far from simple and commissioning and developing the test methodology was extremely challenging. However, this yielded new exciting observations of an as unreported path way involving nitrogen, which whilst remaining unexplained in terms of the chemistry, was extremely repeatable. It was also informative in examining the CaO + CO_2 carbonation hypothesis proposed by the university of Chiba as unlikely, but not conclusively disproven. Utilising Argon a truly inert gas, it was proven that CaO powder does not simply fluoresce at high temperatures and requires N_2 for a light emission to occur. As no chemical equation could be found to describe this observation, it was not possible to calculate the enthalpy of reaction and confirm that sufficient heat was released to ignite the un-burnt charge in an engine. The testing completed using magnesium oxide power was also important, as it demonstrated that the same visible light emission was not present with this metal oxide. This finding supports to the fact that magnesium oxide does not

promote LSPI.

Top Land Crevice Sampling

The first task was to obtain top land crevice samples from a running engine, which was successfully completed and led to new data being presented describing the chemical composition of this material. A range of laboratory analytical techniques were used to understand the chemical composition of the TLC material, giving new insight in the context of LSPI. Similarly it was the first time that Petroleomics was used to analyse a top land crevice oil sample and present new insight into compounds accumulated in the top land crevice that are not present in the new fuel or oil. This work was generously funded by the Warwick University Seed-corn funding mechanism, which successfully facilitated collaboration between universities in new areas, hence allowing access 'instrument time' on the Fourier transform ion cyclotron mass spectrometry and the vast expertise of the department.

Multi-cylinder Engine Testing of Fuels Containing Methylcyclopentadienyl Manganese Tricarbonyl

The final topic for consideration was to utilise previously gathered data to explore the hypothesis developed by the author; 'could an alkaline metal octane booster in the fuel promote LSPI in a similar way to alkaline metal detergents in the oil?'. The engine testing produced excellent data allowing for detailed analysis to characterise the behaviour of LSPI promoting fuels with the addition of MMT. The new findings being that the LSPI behaviour of fuels containing MMT is quite different to LSPI promoting fuels. The LSPI behaviour of fuels with deliberately formulated distillation characteristics to promote LSPI, follow an expected behaviour based on multiple published papers. In contrast the LSPI behaviour of the same fuels with the addition of MMT, led to very different behaviour. The pre-ignition moved to very early in the combustion cycle and the aggressivity of the pressure curves are the worst seen by the author and also in published material. The LSPI frequency was significantly higher than when no MMT was present. When MMT was added the tendency for run-away LSPI was increased, this is thought to be due to the first event dislodging particles similar to a 'snow shaker', leading to subsequent hot spot retained particle pre-ignitions. The damage caused by fuels containing MMT was worse than anything in the public domain, so bad in this case that the damage

was unsustainable, leading to significant engine failures and multiple failed in-cylinder pressure transducers.

7.2 Claims of Originality

The stated objective of this DPhil was to provide insights into abnormal combustion, investigated at a fundamental level. The original findings were as follows:

1. *Successfully conducted testing of shock-heated metal oxide powders in a range of gases:*
    - Light emissions were observed under the specified conditions for the Chiba hypothesis. Whilst light emissions were present they were inconsistent and diffusive in appearance. These results neither unambiguously prove nor disprove the Chiba hypothesis.
    - This work provides the first experimental evidence of a new potential LSPI promoting mechanism – a strong light-emitting reaction between shock-heated $CaO + N_2$ occurring at significantly lower temperatures than for $CaO + CO_2$.
    - The observation that no light was emitted at engine-representative temperatures, led to the conclusion that an additional source of heat is required to trigger an LSPI event, in addition to the presence of calcium detergent.
    - In contrast to CaO, when MgO powder was shock-heated under similar conditions, no light emissions were observed, confirming that magnesium does not take part in LSPI.
2. *Successfully collected TLC samples of oils with magnesium and calcium based detergents from a running engine:*
    - This work identified that the composition and evolution of the oil in the TLC was significantly different, chemically, from the bulk sump oil due to local conditions in this 'reactor' zone in the engine.
    - The local reduction in detergency of the oil in the TLC was quantified and analysed in contrast to the bulk sump oil.
    - Characterisation of the evolution of ZDDP into its derivatives was described and quantified, in contrast to the levels in the bulk sump oil.

- Quantification the fuel-in-oil dilution provided a simple mathematical model for the reduction in local KV100 due to fuel-in-oil dilution, supporting the oil accumulation and release mechanism proposed by Dahnz *et al.* [29].
- The new and emerging technique of Petrolomics FTICR MS was applied to the TLC sample of a passenger car engine oil for the first time. This identified chemical compounds present in the TLC, not in either the new fuel or oil.

3. *Successfully conducted multi-cylinder engine testing of LSPI-promoting fuel with and without MMT, and with new and used oil:*

   - Characterised the extreme LSPI behaviour of fuels containing MMT vs. the baseline LSPI behaviour of reference fuel and LSPI-promoting fuels without MMT.
   - Identified new and unseen in the open literature LSPI behaviour of fuels containing MMT, characterised by extremely early *AI02*, steep *RMAX* gradients, and APMAX occurrence before TDC.
   - Presents the first evidence in the open literature of severe cylinder head damage due to abnormal combustion when MMT was added to LSPI promoting fuels.
   - Quantified extreme, damaging, levels of fuel-in-oil dilution when fuel containing MMT was used, which led to previously unreported valve-train issues in the open literature.

7.3 Further Work

For all three experimental chapters, extensive suggestions for targeted future work has been proposed, based on the observations and limitations of this research. Several 'firsts' have been put forward by this work, but due to the complexity of LSPI even after circa 100 years of abnormal combustion appearing and disappearing, and in the last 10 years of intensive research in this field, a full explanation of the cause of LSPI has still not been reported. This work adds further knowledge to the topic of LSPI, but it is felt by the Author that at least one further doctorate, building on the foundations of this work, is necessary to develop the ideas further and explore the chemistry in more detail.

Oxford CDST

Whilst this work has presented new data that could be linked to the trigger for LSPI in engines, as with most research it leaves many questions. Commissioning the CDST and developing a experimental methodology consumed a significant amount of time. A new cleaning procedure or removal/sealing of crevices is required to eradicate contamination between experiments. The number of shots conducted was significantly more that intended at the kick off for the experiment. In total 169 shots were fired, representing many months of work. In order to investigate this area further the following gas and powder combinations could be considered:

- CaO + Air.
- CaO + NO_x ·
- $CaCO_3$ + N_2 ·
- $CaCO_3$ + Air.
- $CaCO_3$ + Air.
- MnO_x + Air.

Additional instrumentation such as gas sampling of the shock tube post test to speciate the gas would be a very useful addition to the experiment. Optical diagnostic techniques could be part of a future tool chain to provide further information to validate the experimental results. An analysis technique which eluded this test campaign was a method to speciate the calcium. Whilst ICP was used to conduct a general elemental analysis of the oil, a fairly standard test, it proved very difficult via the avenues explored to find an appropriate measurement technique. If such an analysis had been available then it would have been useful to have a sample of residual powder from the shock tube post test analysed for its chemical composition. Another area the Author would have liked to explore was introducing manganese oxide into the CDST. This would have given insight into whether manganese oxide behaves in a similar way to calcium oxide and nitrogen. It was not possible to include this powder in the shock tube experimental campaign, although this was considered as very desirable. To further link the CDST experiments to the ICE, a parametric analysis of particle

sizes (shock tube – optical engine – multi-cylinder engine). This would address areas not covered in the current CDST work, and look to identify the particle sizes of the compounds of interest. Future work may also benefit from a researcher with a chemistry background. Despite it being typical for a combustion and performance engineer to deal with the consequences of LSPI in an engine OEM setting, this research topic headed in the direction of chemical specialism.

TLC Sampling

Conducting this work during COVID19 lockdown, was an unexpected added complexity to what is already a complex topic. The limitations in the number of tests that could be completed under the circumstances meant that issues such as oil sample contamination, due to failure of the sampling system, had to be accepted into the analysis and overcome. This aspect of the project would have benefited from repeat sample collection. Whilst the analysis conducted provided valuable insight in the composition of the TLC material, the next step would be to build on this work and conduct more focussed analysis in specific areas. As mentioned in the previous subsection, speciation of the calcium in the TLC material would have confirmed if the detergent had thermally decomposed to CaO as per the Chiba hypothesis. The addition of the FTICR MS Petroleomics analysis provided valuable additional insight in to the new chemical compounds present in the TLC sample, but not present in the new fuel or oil. A significant number of nitrogen compounds were classified, in particular nitro compounds, which are worthy of more targetted investigation not possible in the current work.

Testing of fuels containing MMT

As previously stated, it wasn't possible to test all fuel and oil combinations due to the severity of the damage that occurred to the engine. It is felt that the testing of the muli-cylinder engine in this research project was sufficient to provide new insight in this field and characterise the extreme combustion behaviour that occurs when MMT is present in the fuel. It was the view of the Author that further multi-cylinder dyno test work unlikely to yield more conclusive data that would significantly influence the understanding of this LSPI mechanism beyond the approach used. Further data analysis could be performed on the cycles leading up to and immediately after abnormal cycles to understand the intensities and decay rates of pressure related to PI events. There could also be a sig-

nificant benefit from the addition of optical diagnostics, such as endoscopy, to observe and identify the origin of the PI events. Moreover, a more fundamental approach could be beneficial to further research this area. It would be very interesting to design a test campaign to explore the response of Manganese oxide powder in combination with the gases used to investigate the CaO powder in the shock tube. If MnO_x powder and N_2 gave a similar reaction to CaO powder and N_2 this could link the chemical kinetic mechanisms despite the difference in LSPI behaviour observed.

7.3.1 COVID 19 Statement

This research commenced in September 2018, then in 2020 the UK was subject to a series of lockdowns to control the spread of the corona virus. The last of the lockdowns finished in March 2021. The top land crevice sampling and oil analysis occurred during this period. These factors caused a number of restrictions and limitations to what could be carried out during this time. It severely limited physical interaction, in the authors case leading to long periods of isolation. The Author would like to thank his supervisor, Dr Martin Davy for his continued support throughout this challenging time.

Appendix A

CDST Test Result Summary

Table A.1: CDST test result summary.

Campaign	Test	Operator	Powder	Test Gas	Target Temperature	Actual Temperature	Target Pressure	Actual Pressure	Comments
No.#	No.#				K	K	MPa	MPa	
Shots 1 – 31 were all used for setting up the CDST, no results were recorded									
1	32	RPG	CaO	CO_2	1173		0.92		Data recording issues
1	33	RPG	CaO	CO_2	1173		0.92		Data recording issues
1	34	RPG	CaO	CO_2					Powder dispersal test
1	35	RPG	CaO	CO_2	1173		0.92		Data recording issues
1	36	RPG	CaO	CO_2	1173		0.92		Photodiode added
1	37	RPG	CaO	CO_2	1173	1253	0.92	0.98	First recoded light emission on HSC with DAQ data
1	38	RPG	CaO	CO_2	1173		0.92		Aborted test
1	39	RPG	CaO	N_2	1173	1107	0.92	0.84	Light emission with N_2 at CaO + CO_2 target boundary conditions
1	40	RPG	CaO	CO_2	1173	1204	0.92	1.3	Repeat of test No. #37
2	41	LLP/LD	None	CO_2	1173		0.92		Aborted test – pressure too high
2	42	LLP/LD	None	CO_2	1173		0.92		Aborted test – pressure too high
2	43	LLP/MMc	None	CO_2	1173		0.92		Aborted test – pressure too high
2	44	LLP/MMc	None	N_2	1093	1096	0.84	0.92	Fill pressure too high
2	45	LLP/MMc	None	CO_2	1173		0.92		High speed camera didn't trigger
2	46	LLP/MMc	None	CO_2	1173	1148	0.92	0.96	High speed camera didn't trigger
2	47	LLP/MMc	None	N_2	1093	1053	0.62	0.64	High speed camera triggering issues
2	48	LLP/MMc	CaO	CO_2	1173	1181	0.92	0.99	High speed camera triggering issues
2	49	LLP/MMc	CaO	N_2	1093	1062	0.62	0.66	High speed camera triggering issues
2	50	LLP/MMc	CaO	N_2	1093	1064	0.62	0.60	High speed camera triggering issues
2	51	LLP/MMc	CaO	N_2	1093	1053	0.62	0.60	High speed camera triggering issues
2	52	LLP/MMc	CaO	N_2	1093	1034	0.62	0.56	High speed camera triggering issues
2	53	LLP/MMc	CaO	N_2	1093	1054	0.62	0.65	High speed camera triggering issues
2	54	LLP/MMc	CaO	N_2	1093	1046	0.62	0.61	High speed camera triggering issues
2	55	LLP/MMc	CaO	N_2	1093	1045	0.62	0.60	High speed camera triggering issues
2	56	LLP/MMc	CaO	CO_2	1173	1185	0.92	0.98	High speed camera triggering issues
2	57	LLP/MMc	None	N_2	1093	1088	0.62	0.66	High speed camera triggering issues
2	58	LLP/MMc	None	N_2	1093	1064	0.64	0.61	High speed camera triggering issues
2	59	LLP/MMc	None	CO_2	1173	1181	0.92	0.93	Camera issues resolved. Light emission from particles half way through the video
2	60	LLP/MMc	CaO	N_2	1093	1066	0.62	0.65	Light emission captured
2	61	LLP/MMc	CaO	CO_2	1173	1164	0.92	1.0	No light emission present
2	62	LLP/MMc	CaO	N_2	773	810	1.8	1.8	No light emission present
2	63	LLP/MMc	CaO	N_2	773	772	1.8	1.64	No light emission present
2	64	LLP/MMc	CaO	N_2	753	756	1.9	1.94	No light emission present
Shots 65 – 89 CDST was used for an alternative project									
Shots 90 – 104 CDST upgrade, new pressure transducers and DAQ configuration									
Continued on next page									

Campaign	Test	Operator	Powder	Test Gas	Target Temperature	Actual Temperature	Target Pressure	Actual Pressure	Comments
No.#	No.#				K	K	MPa	MPa	
3	105	LLP/TN	CaO	N_2	1058	1096	0.62	0.69	High speed camera issues
3	106	LLP/TN	CaO	N_2	1058	1018	0.62	0.58	High speed camera issues
3	107	LLP/TN	CaO	N_2	1058	1054	0.62	0.65	Issue related to HSC aperture, light emission captured
3	108	LLP/TN	CaO	N_2	1058	1068	0.62	0.67	Light emission captured
Shots 109 No data collected									
3	110	LLP/TN	CaO	N_2	1058	1054	0.62	0.65	Light emission captured
3	111	LLP/TN	CaO	N_2	1058	1054	0.62	0.62	Light emission captured
3	112	LLP/TN	CaO	N_2	1058	1029	0.62	0.60	Light emission captured
Shots 113 – 123 No data collected									
3	124	CW/MMc	MgO	N_2	773	834	1.62	1.56	No light emission
3	125	CW/MMc	MgO	CO_2	1179	803	0.97	0.66	No light emission
Shot 126, No data system pre-trigger									
3	127	CW/MMc	MgO	N_2	1058	1079	0.62	0.66	Light emission?, confirmed incorrect powder used in error (CaO)
Shots 128 – 144, CDST being used for other experiments									
3	145	CW	CaO	N_2	1058	1025	0.62	0.59	Light emission captured
Shots 146 – 153, CDST being used for other experiments									
3	154	CW	CaO	N_2	873	870	0.62	0.85	Light emission captured (glowing particles)
Shots 155 – 159, CDST being used for other experiments									
3	160	CW	MgO	N_2	1058	965	0.62	0.52	Light emission captured (small number of glowing particles), CaO contamination from crevices despite tunnel being cleaned
3	161	CW	MgO	N_2	1058	1016	0.62	0.58	Light emission captured (small number of glowing particles, fewer than previous test), CaO contamination from crevices despite tunnel being cleaned, reducing as consumed
Shots 162 – 165, set up with mylar diaphragms									
3	166	CW	CaO	Ar	1058	876	0.62	0.53	No light emission captured, temperature did not meet target due to slow shock speed
3	167	CW	CaO	Ar	1058	876	0.62	0.53	No light emission, temperature did not meet target due to slow shock speed
3	168	CW	MgO	Ar	1058	866	0.62	0.53	No light emission, temperature did not meet target due to slow shock speed
3	169	CW	MgO	Ar	1058	873	0.62	0.53	No light emission, temperature did not meet target due to slow shock speed

Appendix B

Failures in top land crevice sampling system

The following images were included to illustrate the type of failures encountered whilst developing a suitable TLC sampling solution. Figure B.1 (a) shows melting and detachment of the PTFE tube. It was unsuitable to have the PTFE close to the sample point as the hot combustion gasses exceeded the maximum temperature of the tube. The connection to the sampling point was replaced with 6mm stainless steel tubing, approximately 300mm long, as shown in Figure B.1 (b). This allowed for external splash oil cooling of the tube, prior to the sample entering the PTFE section. However, the additional mass of the stainless steel tube required a bolt into the gudgeon pin bush, via an additional tab on the tube, and two screws in the underside of the piston crown. Initiall the bolt used was mild steel and this failed after a short time. The final solution was the use of a high-tensile cap-head bolt. Figure B.1 (c), is a further illustration of both melting (collapse) and potential mechanical damage due to the moving components in the crankcase. Once the PTFE reached its transition temperature plastic deformation occurred. This was ultimately solved by the inclusion of a stainless steel section and guide plates, detailed in Figure 5.5 in Chapter 5.

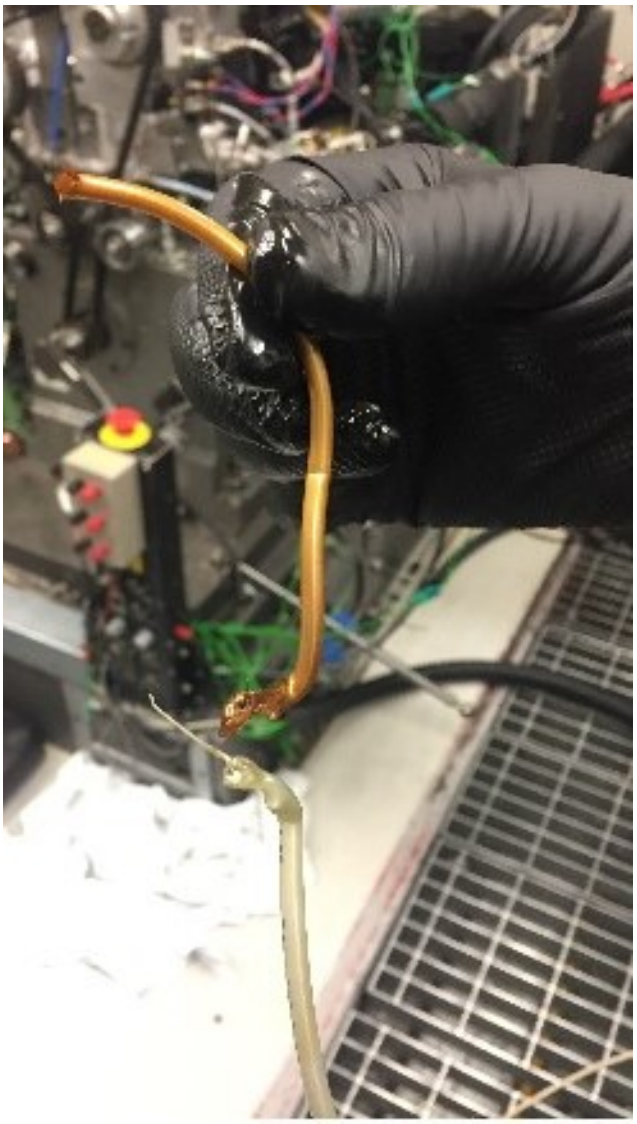

(a) Pipe failures (melted and detached)

(b) Broken stainless steel sample tube

(c) Melted sample tube

Figure B.1: Sample line failures and detachments

Appendix C

Injector and Spark plug Images

The images in Figure C.1 show the baseline condition of the injector tips and spark plugs, following running on 95 RON E10 reference fuel. They are deemed to be in good condition with typical levels of deposits.

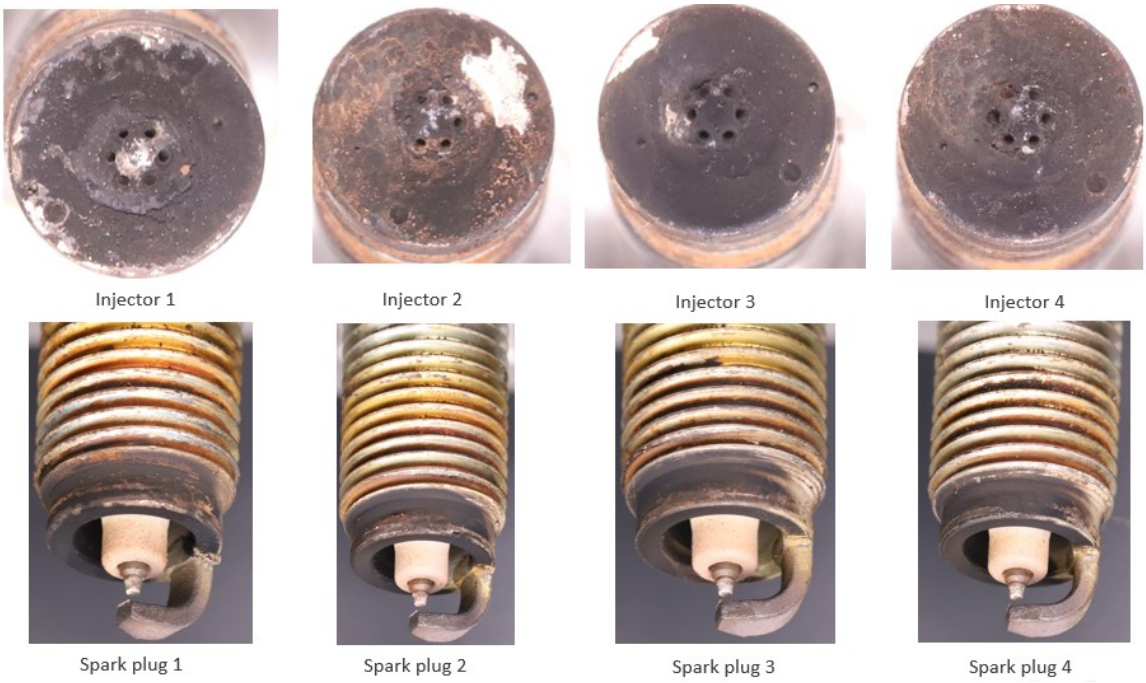

Figure C.1: 95 RON E10 Injectors and Spark Plugs

Figure C.2, shows the spark plugs following the referencing, 4 tests with 3 repeats (12 total runs). The change in lighting may impact the observation of the deposits, however it appears that they have changed following the subsequent tests. Most notable was injector 2, which appears to have lost some hard deposit, and injector 4 which has changed significantly both losing deposit from the

spray hole region and the main deposit appears smoother. In both cases this doesn't seem to have impacted the LSPI testing. The spark plugs remain unchanged.

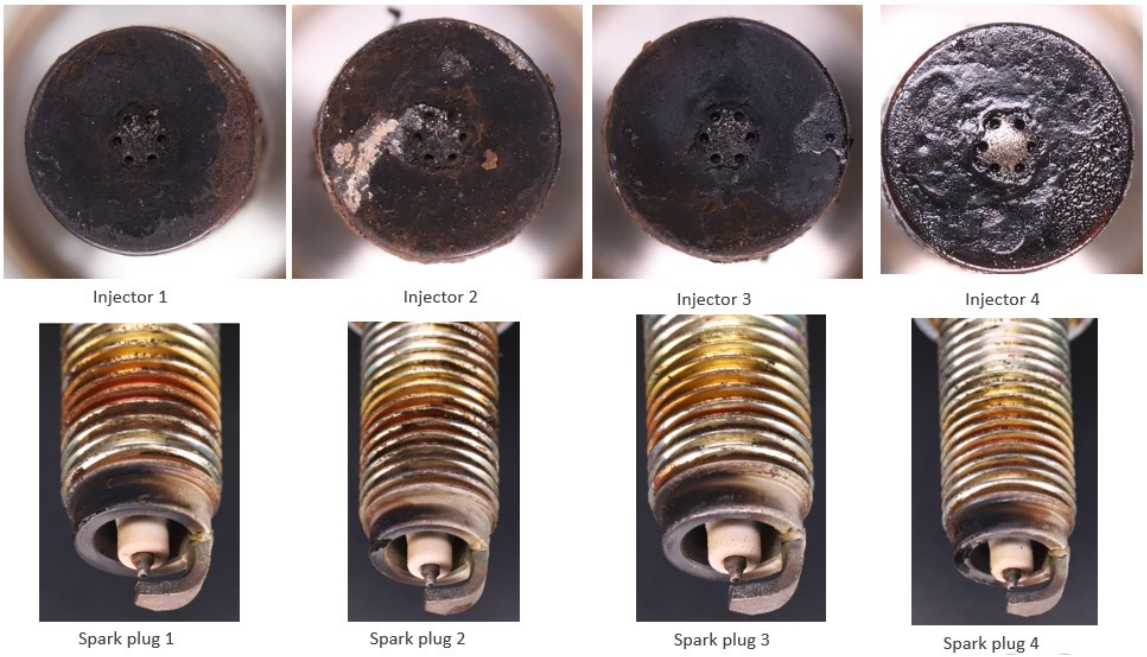

Figure C.2: 95 RON E10 Injectors and Spark Plugs, End of Referencing

Finally, Figure C.3, the injectors and spark plugs are pictured following running with China bad fuel. Despite the extreme LSPI behaviour encountered by the injectors and spark plugs were in good condition. No damage detailed in Figure 2.10 (b), in Chapter 2 was found on the spark plugs.

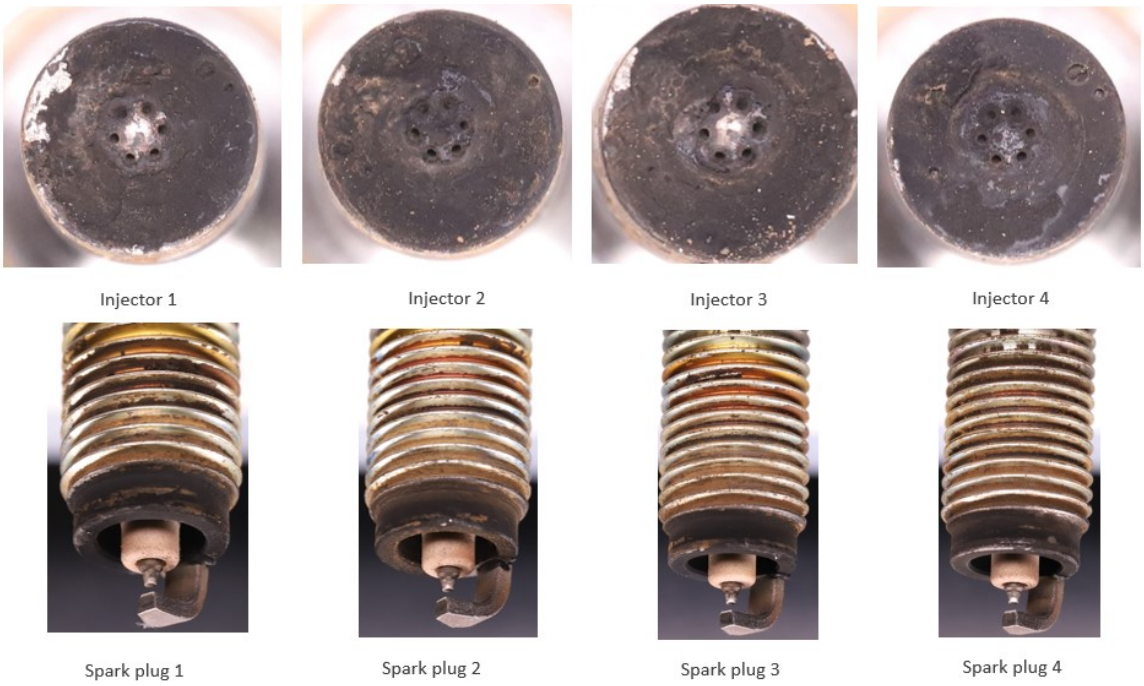

Figure C.3: Injectors and Spark Plugs After China Bad Fuel

Nomenclature

γ	Ratio of Specific Heats
λ	Non-dimentional ratio of measured to stoichiometric air to fuel ratios
ρ	Density
ρ_a	ρ of State 'a'
ρ_b	ρ of State 'b'
σ	Standard deviation
$\tau^{'}$	Time Available for Autoiginition
$\mathbf{B}$	Magnetic Field Strength
ξ	Non-dimensional Resonance Parameter
e	Electron Charge
f_s	Sample Frequency
k	Peak Width Constant
m	Mass
N	Data Set Size
n_R	Number of crank revolutions for each power stroke
P_b	Brake power
P_m	Estimated Probability of Occurrence

P_s	Specific power
q	Total Charge
R	Resolving Power
T	Acquisition Time
T_s	Specific torque
V_d	Volume displaced
z	Charge
β	Zeldovich Number
δ	Laminar Flame Thickness
ϵ	Dimentionless Reactivity Parameter
μ	Dynamic Viscosity
ϕ	Equivilance Ratio
τ_e	Excitation Time for Autoignition Heat Release
R_f	Critical Flame-ball Radius
r_o	Radius of the Hotspot
T_b	Temperature of the Burned Gas
T_u	Temperature of the Unburned Gas
U_a	Autoignition Propogation Velocity, Relative to the Unburned Gas
$Ca(NO_3)_2$	Calcium Nitrate
Ca_3N_2	Calcium Nitride
$CaCN_2$	Calcium Cyanamide

$CaCO_3$	Calcium Carbonate
CaO	Calcium Oxide
CO_2	Carbon Dioxide
CO	Carbon Monoxide
H_2	Hydrogen
H_2S	Hydrogen sulphide
HC	Hydrocarbon
He	Helium
$MgCO_3$	Magnesium Carbonate
MgO	Magnesium Oxide
N_2	Nitrogen
NOx	Oxides of Nitrogen
H	Enthalpy
m	Rank of the Data Point
N	Total Number of Points
AI02	The angle of 2% mass fraction burned
AKI	Antiknock Index
Al	Aluminium
AO	Phenolic Anti-oxidant
APPI	Atmospheric Pressure Photoionisation
Ar	Argon

ASTM	American Society for Testing and Materials
B	Boron
B	Cylinder bore
b	Distance from the centre of the crank shaft to the dynamometer load cell
Ba	Barium
BEV	Battery Electric Vehicle
BMEP	Brake Mean Effective Pressure
C	Carbon
CA	Crank Angle
Ca	Calcium
CAF	Coryton Advanced Fuels
CFD	Computational Fluid Dynamics
Cl	Chlorine
Co	Cobalt
CR	Compression ratio
CR	Compression ratio
Cr	Chromium
cSt	Centistokes
Cu	Copper
D	Daltons, a unit of mass to express atomic and molecular weights
DAQ	Data Aquisition System

DBE	Double Bond Equivalent
DD	Developing Detonation
dP	Differential Pressure Across the Diaphragm
E	Activation Energy
ECU	Engine Control Unit
EGR	Exhaust Gas Recirculation
ESI	Electrospray Ionisation
F	Flurorine
F	Force
Fe	Iron
FiO	Fuel in Oil
FPS	Frames Per Second
FTICR MS	Fourier Transform Ion Cyclotron Resonance Mass Spectrometry
GC	Gas Chromatography
ICE	Internal Combustion Engine
ICP	Inductive Coupled Plasma Spectroscopy
IP	Intellectual Property
IUPAC	International Union of Pure and Applied Chemistry
JAMA	Japan Automobile Manufacturers Association
JLR	Jaguar Land Rover
KMD	Kendrick Mass Defect

KV	Kinematic Viscosity
L	Length of the driven section
L	Stroke length
L1	Distance From the Diaphragm to the Measurement Section of the Shock Tube
Le	Lewis Number
LSPI	Low Speed Pre-Ignition
M_a	Mach Number for State 'a'
M_b	Mach Number of State 'b'
M_r	Mach Number of the Reflected Shock
M_s	Mach Number of the Shock
MATLAB	Matrix Laboritory Software
MFB50	50% Mass Fraction Burned
mgKOH/g	milligrames of Potassium Hydroxide required to neutralise 1 g of sample (in TAN and TBN titration)
mmHg	Pressure in Millimeters of Mercury
MMT	Methylcyclopentadienyl Manganese Tricarbonyl
Mn	Manganese
Mo	Molybdenum
MoDTC	Molybdenum Dithiocarbamate
MON	Motor Octane Number
N	Rotational engine speed
NI	National Instruments

Ni	Nickel
NIST	National Institute of Standards and Technology
O	Oxygen
OEM	Original Eqipment Manufacturer
OI	Octane Index
ON	Octane Number
ORNL	Oak Ridge National Laboratories
OTI	Oxford Thermal Institute
P	Phosphorus
p	Pressure
p_a	Pressure of State ‘a’
p_b	Pressure of State ‘b’
PAO	Polyalphaolefin Oil
Pn	Particle Number
PPM	Parts per million
Pr	Prandtl Number, ratio of momentum diffusivity to thermal diffusivity
PTFE	Polytetrafluoroethylene
R	Universal Gas Constant
RDE	Real Driving Emissions
RDE	Rotating Disc Electrode Spectroscopy
RON	Research Octane Number

RVP	Reid Vapour Pressure
S	Sensitivity
S	Sulphur
s(1).γ	Initial Ratio of Specific Heats of Driven Gas
s(1).ρ	Initial Density of the Driven Gas
s(1).a	Speed of Sound of the Driven Gas
s(1).p	Initial Pressure of Driven Gas
s(1).R	Initial Gas Constant of Driven Gas
s(1).T	Initial Temperature of Driven Gas
s(1).u	Initial Velocity of the Driven Gas
s(2).γ	State 2 Ratio of Specific Heats
s(2).ρ	State 2 Density
s(2).p	State 2 Pressure
s(2).R	State 2 Gas Constant
s(2).T	State 2 Temperature
s(3).γ	State 2 Ratio of Specific Heats
s(3).ρ	State 3 Density
s(3).p	State 3 Pressure
s(3).R	State 3 Gas Constant
s(3).T	State 3 Temperature
s(4).γ	Initial Ratio of Specific Heats of Driver Gas

s(4).ρ	Initial Density of the Driver Gas
s(4).a	Speed of Sound of the Driver Gas
s(4).p	Initial Pressure of Driver Gas
s(4).R	Initial Gas Constant of Driver Gas
s(4).T	Initial Temperature of Driver Gas
s(4).u	Initial Velocity of the Driver Gas
s(5).γ	Reflected Shock Ratio of Specific Heats
s(5).ρ	Reflected Shock Density
s(5).p	Reflected Shock Pressure
s(5).R	Reflected Shock Gas Constant
s(5).T	Reflected Shock Temperature
SC	Supercharger
SEM	Scanning Electron Microscope
SI	Spark Ignited
SI	Spark Ignited
Si	Silicon
SWRI	South West Research Institute
T	Torque
t	Time
T_a	Temperature of State ‘a’
T_b	Temperature of State ‘b’

TAN	Total Acid Number
TBN	Total Base Number
TC	Turbocharger
TEL	Tetraethyl lead
Ti	Titanium
TRZ	Top Ring Zone
TTL	Transistor-Transistor Logic (Trigger)
u_a	Velocity of the Gas Ahead the Shock Wave, Relative to the Shock Wave (u_a is used for State '2' and State '5')
u_b	Velocity of the Gas Behind the Shock Wave, Relative to the Shock Wave (u_b is used for State '2' and State '5')
u_r	Reflected Shock Velocity
$u_s(1)$	Velocity of the Gas Behind the Wave of the Driven Gas
UHEGO	Universal heated exhaust gas oxygen sensor
UHR MS	Ultra High Resolution Mass Spectrometry
Us1	Average Measured Shock Speed
VI	Viscosity index
WOT	Wide Open throttle
XRF	X-Ray Florescence Spectroscopy
ZDDP/ZnDTP	Zinc Dialkyldithiophosphate
Zn	Zinc
eSC	Electric Supercharger

References

[1] M. K. Tran, A. Bhatti, R. Vrolyk, D. Wong, S. Panchal, M. Fowler, and R. Fraser, "A review of range extenders in battery electric vehicles: Current progress and future perspectives", World Electric Vehicle Journal 12, DOI: 10.3390/wevj12020054 (2021).

[2] *Webpage: UK Government - Phasing out sales of new petrol and diesel cars from 2030, https://www.gov.uk/government/news/government-takes-historic-step-towards-net-zero-with-end-of-sale-of-new-petrol-and-diesel-cars-by-2030 [cited Feburary 2025]*, 2020.

[3] G. Kalghatgi, "Is it the end of combustion and engine combustion research? Should it be?", Transportation Engineering **10**, 100142 (2022).

[4] D. C. Beddows and R. M. Harrison, "PM10 and PM2.5 emission factors for non-exhaust particles from road vehicles: Dependence upon vehicle mass and implications for battery electric vehicles", Atmospheric Environment, DOI: 10.1016/j.atmosenv.2020.117886 (2021).

[5] H. A. Rakha, M. Farag, and H. Foroutan, "Electric versus gasoline vehicle particulate matter and greenhouse gas emissions: Large-scale analysis", Transportation Research Part D: Transport and Environment 140, DOI: 10.1016/j.trd.2025.104622 (2025).

[6] *Webpage: European Council - Euro 7: Council and Parliament strike provisional deal on emissions, https://www.consilium.europa.eu/en/press/press-releases/2023/12/18/euro-7-council-and-parliament-strike-provisional-deal-on-emissions [cited Feburary 2025]*, 2023.

[7] N. Wicks, *The evolution of gaseous EU emission limits (unpublished work, JLR)*, tech. rep. (2018).

[8] N. Turner, "An Investigation into the Effects of Engine Displacement and Geometric Compression Ratio on Downsizing of a Direct-Injection Spark-Ignition Engine", PhD thesis (University of Bath, 2020).

[9] M. J. McAllister and D. J. Buckley, "Future gasoline engine downsizing technologies - CO2 improvements and engine design considerations", Institution of Mechanical Engineers - Internal Combustion Engines: Performance, Fuel Economy and Emissions, pp. 19–26 (2009).

[10] *Webpage: European Union - Regulation for setting CO2 emissions standards, https://eur-lex.europa.eu/legal-content/EN, [cited Feburary 2025]*, 2019.

[11] J. B. Heywood, *Internal Combustion Engine Fundamentals, ISBN 0-07-100499-8* (McGraw-Hill, 1988).

[12] Bosch, *Automotive Handbook, ISBN 978-0-7680-8152-7*, 9th Ed (Robert Bosch GmbH, 2014).

[13] D. Talué, P. Whitwood, G. Page, M. McAllister, F. Borean, and R. Penfold, "Introducing the Ingenium SI Engine: Jaguar Land Rover's New Four-Cylinder Gasoline Engine", 38. Internationales Wiener Motorensymposium, pp. 43–62 (2017).

[14] K. Clasen, L. Koopmans, and D. Dahl, "Homogeneous Lean Combustion in a 2lt Gasoline Direct Injected Engine with an Enhanced Turbo Charging System", SAE Technical Papers, DOI: 10.4271/2018-01-1670 (2018).

[15] B. Sendyka, *Advances in Internal Combustion Engines and Fuel Technologies* (IntechOpen, 2013) Chap. 3.

[16] A. Cairns, H. Blaxill, and G. Irlam, "Exhaust gas recirculation for improved part and full load fuel economy in a turbocharged gasoline engine", SAE Technical Papers, DOI: 10.4271/2006-01-0047 (2006).

[17] T. Wandschneider, K. Wiege, and W. Gottschalk, "Holistic Evaluation of CO2 Saving Potentials for New Degrees of Freedom in SI Engine Process Control Based on Physical Simulations", SAE Technical Papers, DOI: 10.4271/2018-01-1654 (2018).

[18] M. McAllister, "Future Gasoline Engine Downsizing Technologies – Fuel Economy Improvements and Engine Design Considerations, (MSc Dissertation), Loughborough University, Dept. Automotive and Aeronautical Engineering", (2008).

[19] F. W. D. S. Tuckmantel, F. Nonato, and T. C. D. Freitas, "Chamshaft Vibration Characteristic Assessment when Applying Needle Roller Bearings as Solution for Efficiency Increase", SAE Technical Papers, DOI: 10.4271/2012-36-0628 (2012).

[20] L. C. Canale, G. Xu, H. Liang, J. Liu, and G. E. Totten, "Surface engineered coatings and surface additive interactions for boundary film formation to reduce frictional losses in the automotive industry: A review", SAE Technical Papers, DOI: 10.4271/2005-01-2180 (2005).

[21] R. Stone, *Introduction to Internal Combustion Engines, ISBN 978-0-230-57663-6*, 4th Ed. (Red Globe Press, 2012).

[22] M. Marr, J. S. Wallace, S. Memme, S. Chandra, L. Pershin, and J. Mostaghimi, "An investigation of metal and ceramic thermal barrier coatings in a spark-ignition engine", SAE Technical Papers, DOI: 10.4271/2010-01-2090 (2010).

[23] *Webpage: FEV - Customised test bench flow investigation, https://magazine.fev.com/en/fev-customized-test-bench-flow-investigation, [cited March 2019]*, 2017.

[24] I. Glassman, *Combustion, ISBN 978-0-12-407913-7*, 4th Ed. (Academic Press, 2008).

[25] Coordinating Research Council, *Terms for Use in Otto Cycle Engine Combustion*, tech. rep. (1954).

[26] E. M. Chapman and V. S. Costanzo, "A Literature Review of Abnormal Ignition by Fuel and Lubricant Derivatives, pp. 107 - 142", SAE International Journal of Engines, DOI: 10.4271/2015-01-1869 (2015).

[27] L. G. Pless, "Surface Ignition and Rumble in Engines", SAE International Automotive Engineering Congress and Exposition, DOI: 10.4271/650391 (1965).

[28] B. Sturgis, "Abnormal Combustion Problems in Gasoline Engines", SAE Technical Papers, DOI: 10.4271/610401 (1961).

[29] C. Dahnz, K. M. Han, U. Spicher, M. Magar, R. Schiessl, and U. Maas, "Investigations on pre-ignition in highly supercharged SI engines", SAE Technical Papers, DOI: 10.4271/2010-01-0355 (2010).

[30] A. Zahdeh, P. Rothenberger, W. Nguyen, M. Anbarasu, S. Schmuck-Soldan, J̈. Schaefer, and T. Goebel, "Fundamental Approach to Investigate Pre-Ignition in Boosted SI Engines, pp. 246-273", SAE International Journal of Engines, DOI: 10.4271/2011-01-0340 (2011).

[31] Y. Okada, S. Miyashita, Y. Izumi, and Y. Hayakawa, "Study of Low-Speed Pre-Ignition in Boosted Spark Ignition Engine, pp. 584-594", SAE International Journal of Engines, DOI: 10.4271/2014-01-1218 (2014).

[32] T. Kuboyama, Y. Moriyoshi, and K. Morikawa, "Visualization and Analysis of LSPI Mechanism Caused by Oil Droplet, Particle and Deposit in Highly Boosted SI Combustion in Low Speed Range, pp. 529-537", SAE International Journal of Engines, DOI: 10.4271/2015-01-0761 (2015).

[33] K. Tamura, T. Utaka, H. Kamano, N. Hayakawa, T. Miyasaka, T. Ishino, A. Iijima, and H. Shoji, "Abnormal Combustion Induced by Combustion Chamber Deposits Derived from Engine Oil Additives in a Spark-Ignited Engine, pp. 200 - 205", SAE International Journal of Engines, DOI: 10.4271/2014-32-0091 (2014).

[34] D. Thomason, *Green Belt Project Report Integrated Problem Solving Using Six Sigma Methodology Reducing the Occurrence of LSPI in a Four-Cylinder Gasoline Engine (Unpublished work, JLR)*, tech. rep. (2016).

[35] Z. Wang, Y. Qi, X. He, J. Wang, S. Shuai, and C. K. Law, "Analysis of pre-ignition to super-knock: Hotspot-induced deflagration to detonation", Fuel **144**, pp. 222–227 (2015).

[36] X. Luo, H. Teng, T. Hu, R. Miao, and L. Cao, "An Experimental Investigation on Low Speed Pre-Ignition in a Highly Boosted Gasoline Direct Injection Engine, pp. 520 - 528", SAE International Journal of Engines, DOI: 10.4271/2015-01-0758 (2015).

[37] J. M. Zaccardi and D. Escudié, "Overview of the main mechanisms triggering low-speed pre-ignition in spark-ignition engines, pp. 152 - 165", International Journal of Engine Research, DOI: 10.1177/1468087414530965 (2015).

[38] B. Leach, A. Smith, R. Pearson, J. Williams, R. Yates, and C. Ritchie, "Management of Low Speed Pre-Ignition via Fuel and Lubricant Formulation", Aachen Colloquium Automobile and Engine Technology, pp. 333–348 (2017).

[39] H. Teng, R. Miao, L. Cao, X. Luo, T. Hu, and M. Wu, "Characteristics of Abnormal Combustion in the Scavenging Zone for a Highly-Boosted Gasoline Direct Injection Engine", SAE Technical Papers, DOI: 10.4271/2017-01-1721 (2017).

[40] G. T. Kalghatgi, *Fuel/Engine Interactions, ISBN 978-0-7680-6458-2* (SAE International, 2014).

[41] D. Bradley and G. T. Kalghatgi, "Influence of autoignition delay time characteristics of different fuels on pressure waves and knock in reciprocating engines", Combustion and Flame **156**, pp. 2307–2318 (2009).

[42] J. Zheng, D. R. Overton, C. Eiden, and P. P. Treier, "Dielectric test methods for evaluating sparkplug insulators", SAE Technical Papers, DOI: 10.4271/2019-01-0928 (2019).

[43] T. Inoue, Y. Inoue, and M. Ishikawa, "Abnormal combustion in a highly boosted SI engine-the occurrence of super knock", SAE Technical Papers, DOI: 10.4271/2012-01-1141 (2012).

[44] NASA, *SPARK PLUG DEFECTS AND TESTS*, tech. rep. 51 (1920).

[45] Z. Wang, H. Liu, T. Song, Y. Qi, X. He, S. Shuai, and J. Wang, "Relationship between super-knock and pre-ignition, pp. 166-180", International Journal of Engine Research, 16, DOI: 10.1177/1468087414530388 (2015).

[46] A. B. Mansfield, E. Chapman, and K. Briscoe, "Effect of market variations in gasoline composition on aspects of stochastic pre-ignition", Fuel **184**, pp. 390–400 (2016).

[47] P. Richards, *Automotive Fuels Reference Book, ISBN 978-0-7680-0638-4* (SAE International, 1995).

[48] *Webpage: Overlap of Hybrid Orbitals, https://chem.libretexts.org/Courses/College-of-the-Canyons/Chem-General-Chemistry-Theories-of-Chemical-Bonding/Overlap-of-Hybrid-Orbitals, [cited April 2021]*, 2020.

[49] T. A. Albahri, M. R. Riazi, and A. A. Alqattan, "Octane number and aniline point of petroleum fuels", ACS Division of Fuel Chemistry, pp. 710–711 (2002).

[50] *Webpage: Properties of Ethanol, https://www.iea-amf.org/content/fuel-information/fuel-info-home/ethanol/e10/ethanol-properties, [cited September 2021]*, 2018.

[51] J. H. Shrader, "Tetra-Ethyl Lead and the Public Health", American Journal of Public Health **15**, pp. 213–216 (1925).

[52] D. G. Robinson, "Tetra-Ethyl Lead Poisoning", British Medical Journal **2**, p. 837 (1946).

[53] W. Zhang, G. G. Zhang, H. Z. He, and H. M. Bolt, "Early health effects and biological monitoring in persons occupationally exposed to tetraethyl lead", International Archives of Occupational and Environmental Health **65**, pp. 395–399 (1994).

[54] *Webpage: Chronology of Leaded Gasoline / Leaded Petrol History, http://www.lead.org.au/Chronology-Making-Leaded-Petrol-History, [cited December 2024]*, 2011.

[55] *Webpage: United Nations - Era of leaded petrol over, eliminating a major threat to human and planetary health, https://www.unep.org/news-and-stories/press-release/era-leaded-petrol-over-eliminating-major-threat-to -human-and-planetary-health, [cited March*, 2021.

[56] T. Nomura, H. Ueura, Y. Tanaka, Y. Iida, Z. Yuan, and A. Ando, "The Effect of Gasoline Metallic Additives on Low Speed Pre-Ignition", SAE Technical Papers, DOI: 10.4271/2018-01-0936 (2018).

[57] M. Amann, T. Alger, B. Westmoreland, and A. Rothmaier, "The Effects of Piston Crevices and Injection Strategy on Low-Speed Pre-Ignition in Boosted SI Engines, pp. 1216 - 1228", SAE International Journal of Engines, 5, DOI: 10.4271/2012-01-1148 (2012).

[58] F. Leach, R. Stone, and D. Richardson, "The influence of fuel properties on particulate number emissions from a direct injection spark ignition engine", SAE Technical Papers, DOI: 10.4271/2013-01-1558 (2013).

[59] V. Mittal and J. B. Heywood, "The shift in relevance of fuel RON and MON to knock onset in modern SI engines over the last 70 years, pp. 1 - 11", SAE International Journal of Engines, 2, DOI: 10.4271/2009-01-2622 (2010).

[60] Kalghatgi, "Fuel Anti-Knock Quality - Part I. Engine Studies", SAE Technical Papers, DOI: 10.4271/2001-01-3584 (2001).

[61] M. C. Kocsis, G. Anderson, and T. Briggs, "Real Fuel Effects on Low Speed Pre-Ignition", SAE Technical Papers, DOI: 10.4271/2018-01-1456 (2018).

[62] A. Kar, A. Huisjen, A. Aradi, J. Reitz, A. Iqbal, K. Haumann, J. Kensler, K. Hardman, R. Mainwaring, and S. Remmert, "Assessing the Impact of Lubricant and Fuel Composition on LSPI and Emissions in a Turbocharged Gasoline Direct Injection Engine", SAE Technical Papers, DOI: 10.4271/2020-01-0610 (2020).

[63] G. Kalghatgi, I. Algunaibet, and K. Morganti, "On Knock Intensity and Superknock in SI Engines, pp. 1051 - 1063", SAE International Journal of Engines, 10, DOI: 10.4271/2017-01-0689 (2017).

[64] G. Kalghatgi and R. Stone, "Fuel requirements of spark ignition engines", Proceedings of the Institution of Mechanical Engineers, Part D: Journal of Automobile Engineering **232**, pp. 22–35 (2018).

[65] Y. Zeldovich, "Mathematical theory of combustion and explosions", Combustion and Flame Vol 67, DOI: 10.1016/0010-2180(87)90152-0 (1985).

[66] F. Incropera, *Fundamentals of Heat and Mass Transfer, ISBN 978-0-4713-1272-7*, 6th Ed. (John Wiley & Sons, 2007).

[67] Infinium, *Infinium Lubricating Oil Additives Seminar* (2015).

[68] H. Spikes, "The history and mechanisms of ZDDP", Tribology Letters **17**, pp. 469–489 (2004).

[69] W. Van Dam, D. H. Broderick, R. L. Freerks, V. R. Small, and W. W. Willis, "TBN retention - Are we missing the point?", SAE Technical Papers, DOI: 10.4271/972950 (1997).

[70] D. R. Coultas, "The Role of NOx in Engine Lubricant Oxidation", SAE Technical Papers, DOI: 10.4271/2020-01-1427 (2020).

[71] D. Splitter, V. Boronat-Colomer, S. Neupane, and B. Partridge, *Overview of LSPI Literature and Theory*, tech. rep. (Oak Ridge National Laboratory, 2020).

[72] Z. Wang, H. Liu, and R. D. Reitz, "Knocking combustion in spark-ignition engines", Progress in Energy and Combustion Science **61**, pp. 78–112 (2017).

[73] N. Hayakawa, K. Miura, T. Miyasaka, T. Ishino, A. Iijima, H. Shoji, K. Tamura, T. Utaka, and H. Kamano, "A Study on the Effect of Zn- and Mo-Based Engine Oil Additives on Abnormal SI Engine Combustion using In-Cylinder Combustion Visualization, pp. 214 - 220", SAE International Journal of Engines, 8, DOI: 10.4271/2014-32-0096 (2014).

[74] K. Miura, K. Shimizu, N. Hayakawa, T. Miyasaka, A. Iijima, H. Shoji, T. Utaka, K. Tamura, and H. Kamano, "Influence of Ca-, Mg- and Na-Based Engine Oil Additives on Abnormal Combustion in a Spark-Ignition Engine, pp. 452 - 457", JSAE International Journal of Engines, 9, (2016).

[75] T. Miyasaka, K. Miura, N. Hayakawa, T. Ishino, A. Iijima, H. Shoji, K. Tamura, T. Utaka, and H. Kamano, "A Study on the Effect of a Calcium-Based Engine Oil Additive on Abnormal SI Engine Combustion, 206 - 213", SAE International Journal of Engines, 8, DOI: 10.4271/2014-32-0092 (2014).

[76] K. Shimizu, S. Takahata, K. Miura, H. Shoji, A. Iijima, T. Utaka, and K. Tamura, "Influence of Calcium-Based Additives with Different Properties on Abnormal Combustion in an SI Engine", SAE Technical Papers, DOI: 10.4271/2016-32-0007 (2016).

[77] K. A. Fletcher, L. Dingwell, K. Yang, W. Y. Lam, and J. P. Styer, "Engine Oil Additive Impacts on Low Speed Pre-Ignition, pp. 612 - 620", SAE International Journal of Fuels and Lubricants, 9, DOI: 10.4271/2016-01-2277 (2016).

[78] K. Takeuchi, K. Fujimoto, S. Hirano, and M. Yamashita, "Investigation of Engine Oil Effect on Abnormal Combustion in Turbocharged Direct Injection - Spark Ignition Engines, pp. 1017 - 1024", SAE International Journal of Fuels and Lubricants, 5, DOI: 10.4271/2012-01-1615 (2012).

[79] S. Hirano, M. Yamashita, K. Fujimoto, and K. Kato, "Investigation of engine oil effect on abnormal combustion in turbocharged direct injection - Spark ignition engines (Part 2)", SAE Technical Papers, DOI: 10.4271/2013-01-2569 (2013).

[80] K. Fujimoto, M. Yamashita, S. Hirano, K. Kato, I. Watanabe, and K. Ito, "Engine Oil Development for Preventing Pre-Ignition in Turbocharged Gasoline Engine, pp. 869 - 874", SAE International Journal of Fuels and Lubricants, 7, DOI: 10.4271/2014-01-2785 (2014).

[81] K. Onodera, T. Kato, S. Ogano, K. Fujimoto, K. Kato, and T. Kaneko, "Engine Oil Formulation Technology to Prevent Pre-ignition in Turbocharged Direct Injection Spark Ignition Engines", SAE Technical Papers, DOI: 10.4271/2015-01-2027 (2015).

[82] Y. Moriyoshi, T. Yamada, D. Tsunoda, M. Xie, T. Kuboyama, and K. Morikawa, "Numerical Simulation to Understand the Cause and Sequence of LSPI Phenomena and Suggestion of CaO Mechanism in Highly Boosted SI Combustion in Low Speed Range", SAE Technical Papers, DOI: 10.4271/2015-01-0755 (2015).

[83] Y. Moriyoshi, T. Kuboyama, K. Morikawa, T. Yamada, Y. Imai, K. Hatamura, and M. Suzuki, "A Study of Low Speed Preignition Mechanism in Highly Boosted SI Gasoline Engines, 98 - 106", SAE International Journal of Engines, 9, DOI: 10.4271/2015-01-1865 (2015).

[84] M. North, "What is CO2? Thermodynamics, Basic Reactions and Physical Chemistry, ISBN 978-0-444-62746-9", in *Carbon dioxide utilisation: closing the carbon cycle:* (Elsevier B.V., 2015) Chap. 2, pp. 3–17.

[85] E. Bisceglia, G. M. Longo, and S. Longo, "Thermal decomposition rate of MgCO3 as an inorganic astrobiological matrix in meteorites", International Journal of Astrobiology **16**, pp. 130–136 (2016).

[86] J. Camm, M. Davy, X. Fang, L. Doherty, M. McGilvray, and F. Foerster, "The Oxford Cold Driven Shock Tube (CDST) for Fuel Spray and Chemical Kinetics Research", SAE Technical Papers, DOI: 10.4271/2018-01-0222.

[87] J. D. Anderson, *Modern Compressible Flow, ISBN 0-07-001673-9* (McGraw-Hill, 1990).

[88] T. Bazyn, N. Glumac, H. Krier, T. S. Ward, M. Schoenitz, and E. L. Dreizin, "Reflected shock ignition and combustion of aluminum and nanocomposite thermite powders", Combustion Science and Technology **179**, pp. 457–476 (2007).

[89] P. Jacobs, *Shock Tube Modelling with L1d, University of Queensland, Australia*, tech. rep. (1998).

[90] P. L. Collen, L. J. Doherty, M. McGilvray, I. Naved, R. P. Geraets, T. Hermann, R. G. Morgan, and D. E. Gildfind, "Commissioning of the t6 stalker tunnel", AIAA Scitech 2019 Forum, DOI: 10.2514/6.2019-1941 (2019).

[91] P. A. Jacobs, "Quasi-one-dimensional modeling of a free-piston shock tunnel, " AIAA Journal **32**, pp. 137–145 (1994).

[92] H. Ning, J. Wu, L. Ma, W. Ren, D. F. Davidson, and R. K. Hanson, "Chemical kinetic modeling and shock tube study of methyl propanoate decomposition", Combustion and Flame **184**, pp. 30–40 (2017).

[93] A. M. Ferris, A. J. Susa, D. F. Davidson, and R. K. Hanson, "High-temperature laminar flame speed measurements in a shock tube", Combustion and Flame **205**, pp. 241–252 (2019).

[94] A. Birkigt, K. Michels, J. Theobald, T. Seeger, Y. Gao, M. C. Weikl, M. Wensing, and A. Leipertz, "Investigation of compression temperature in highly charged spark-ignition engines, pp. 282 - 292", International Journal of Engine Research, 12, DOI: 10.1177/1468087411399216 (2011).

[95] D. Vuilleumier, N. Kim, M. Sjöberg, N. Yokoo, T. Tomoda, and K. Nakata, "Effects of EGR Constituents and Fuel Composition on DISI Engine Knock: An Experimental and Modeling Study", SAE Technical Papers, DOI: 10.4271/2018-01-1677 (2018).

[96] J. P. Szybist, S. W. Wagnon, D. Splitter, W. J. Pitz, and M. Mehl, "The Reduced Effectiveness of EGR to Mitigate Knock at High Loads in Boosted SI Engines, pp. 2305 - 2318", SAE International Journal of Engines, 10, DOI: 10.4271/2017-24-0061 (2017).

[97] E. Randolph, K. Fieseler, G. Conway, T. Alger, and C. Chadwell, "The Effects of EGR Composition on Combustion Performance and Efficiency", SAE Technical Papers, DOI: 10.4271/2020-01-2052 (2020).

[98] D. Coombs and B. Akih-Kumgeh, "Numerical investigation of the impact of tailored driver gases and driver inserts on shock tube flows", Shock Waves **28**, pp. 1097–1107 (2018).

[99] A. Lifshitz, "Shock Tube Techniques", Annual Review Physics and Chemistry **41**, pp. 559 – 599 (1990).

[100] D. Feng, K. Buresheid, H. Zhao, H. Wei, and C. Chen, "Investigation of lubricant induced pre-ignition and knocking combustion in an optical spark ignition engine", Proceedings of the Combustion Institute **37**, pp. 4901–4910 (2019).

[101] E. P. A, *Nitrogen oxides (NOx), why and how they are controlled, EPA-456/F-99-006R* (DIANE Publishing, 1999).

[102] F. Ullmann, *Ullman's Encylopedia of Industrial Chemistry, ISBN 978-3-527-30673-2* (Wiley-VCH Verlag GmbH & Co, 1984).

[103] G. Miessler and D. A. Tarr, *Inorganic Chemistry, 2nd Edition, ISBN 0-13-841891-8* (Prentice-Hall, 1999).

[104] G. Brauer, *Handbook of Preparative Inorganic Chemistry, ISBN 9-780-3231-6129-9* (Academic Press, 1963).

[105] D. Splitter, B. Kaul, J. Szybist, L. Speed, B. Zigler, and J. Luecke, "Fuel-Lubricant Interactions on the Propensity for Stochastic Pre-Ignition", SAE Technical Papers, DOI: 10.4271/2019-24-0103 (2019).

[106] T. Alger, *Patent No.# 13/718392 - SWRI Crevice Sampling Valve*, 2014.

[107] P. M. Lee, M. Priest, M. S. Stark, J. J. Wilkinson, J. R. Lindsay Smith, R. I. Taylor, and S. Chung, "Extraction and tribological investigation of top piston ring zone oil from a gasoline engine", Proceedings of the Institution of Mechanical Engineers, Part J: Journal of Engineering Tribology **220**, pp. 171–180 (2006).

[108] V. A. Fassel and R. N. Kniseley, "Inductively Coupled Plasma-Optical Emission Spectroscopy", Analytical Chemistry **46**, pp. 1110–1120 (1974).

[109] G. Principi, "The mössbauer effect: A romantic scientific page", Metals, 10, DOI: 10.3390/met10080992 (2020).

[110] G. Choppin, J.-O. Liljenzin, J. Rydberg, and C. Ekberg, *Radiochemistry and Nuclear Chemistry, ISBN 9-780-1239-7868-4* (Academic Press, 2013).

[111] F. A. Gunther, "Nuclear Magnetic Resonance: Applications to Organic Chemistry", Journal of Agricultural and Food Chemistry, 7, DOI: 10.1021/jf60105a607 (1959).

[112] M. C. Kocsis, T. Briggs, and G. Anderson, "The Impact of Lubricant Volatility, Viscosity and Detergent Chemistry on Low Speed Pre-Ignition Behavior, pp. 1019-1035", SAE International Journal of Engines, 10, DOI: 10.4271/2017-01-0685 (2017).

[113] C. Wang, R. Firor, and A. Technologies, *High-Temperature Simulated Distillation System Based on the 6890N GC, https://www.agilent.com/cs/library/applications/5989-2727EN.pdf*, 2005.

[114] D. G. Gillen, “Recent advances in gas chromatography”, Journal of Colloid and Interface Science **39**, pp. 442–443 (1972).

[115] A. Wolak, “TBN performance study on a test fleet in real-world driving conditions using present-day engine oils”, Measurement: Journal of the International Measurement Confederation **114**, pp. 322–331 (2018).

[116] I. Elliott and R. Cherpeck, “Alternative Engine Oil Formulating Solutions to Reduce Low Speed Pre-Ignition Amir Maria , Theresa Gunawan”, JSAE/SAE Powertrains, Fuels and Lubricants, DOI: 10.4271/2019-01-2153 (2019).

[117] G. A. Kramer, “DILUTION OF ENGINE LUBRICANTS BY FUEL, pp. 232-257”, SAE Automotive Lubrication, Vol. 10 (1915).

[118] A. G. Marshall and R. P. Rodgers, “Petroleomics: Chemistry of the underworld”, Proceedings of the National Academy of Sciences of the United States of America **105**, pp. 18090–18095 (2008).

[119] D. Lozano, M. J. Thomas, H. E. Jones, and M. P. Barrow, “Petroleomics : Tools , Challenges , and Developments”, Annual Review of Analytical Chemistry, DOI: 10.1146/annurev-anchem-091619-091824 (2020).

[120] E. Kendrick, “A Mass Scale Based on CH_2 = 14 . 0000 for High Resolution Mass Spectrometry of Organic Compounds, pp. 2146 - 2154”, Analytical Chemistry, 13, DOI: 10.1021/ac60206a048 (1963).

[121] J. Clayden, N. Greeves, and S. Warren, *Organic Chemistry, ISBN 9-780-1992-7029-3* (OUP Oxford, 2012).

[122] E. Chapman, R. Davis, W. Studzinski, and P. Geng, “Fuel Octane and Volatility Effects on the Stochastic Pre-Ignition Behavior of a 2.0L Gasoline Turbocharged DI Engine, pp. 379 - 389”, SAE International Journal of Fuels and Lubricants, 7, DOI: 10.4271/2014-01-1226 (2014).

[123] D. Splitter, B. Burrows, and S. Lewis, “Direct Measurement and Chemical Speciation of Top Ring Zone Liquid during Engine Operation”, SAE Technical Papers, DOI: 10.4271/2015-01-0741 (2015).

[124] G. S. Jatana, D. A. Splitter, B. Kaul, and J. P. Szybist, "Fuel property effects on low-speed pre-ignition", Fuel **230**, pp. 474–482 (2018).

[125] *Fuel Information and Trend in Asia, (unpublished work, Japanese Automotive Manufacturers Association, JAMA)*, tech. rep. (2019).

[126] P. Haenel, D. Tomazic, H. Kleeberg, and J. Ciaravino, "Fuel Properties and Their Impact on Stochastic Pre-Ignition Occurrence and Mega-Knock in Turbocharged Direct-Injection Gasoline Engines", SAE Technical Papers, DOI: 10.4271/2020-01-0614 (2020).

[127] D. J. Corrigan and S. Fontanesi, "Knock: A Century of Research, pp. 3 - 15", SAE International Journal of Engines, 15, DOI: 10.4271/03-15-01-0004 (2021).

[128] A. Berndorfer, S. Breuer, W. Piock, and P. Von Bacho, "Diffusion combustion phenomena in GDi engines caused by injection process", SAE Technical Papers, DOI: 10.4271/2013-01-0261 (2013).

[129] *Webpage: Lucideon Scanning Electron Microscopy (SEM), https://www.lucideon.com/testing-characterization-techniques-sem-edx, [cited November 2024]*, 2023.

[130] S. K. Hoekman and A. Broch, "MMT Effects on Gasoline Vehicles: A Literature Review, pp. 322 - 343", SAE International Journal of Fuels and Lubricants, 9, DOI: 10.4271/2016-01-9073 (2016).

[131] W. P. Boone, C. P. Hubbard, R. E. Soltis, Y. Ding, and A. Chen, "Effect of MMT® fuel additive on emission system components: Detailed parts analysis from clear- and MMT®-fueled escort vehicles from the alliance study", SAE Technical Papers, DOI: 10.4271/2005-01-1108 (2005).

[132] T. Nomura, H. Ueura, Y. Tanaka, Y. Iida, Z. Yuan, and A. Ando, "The Effect of Gasoline Metallic Additives on Low Speed Pre-Ignition", SAE Technical Papers, DOI: 10.4271/2018-01-0936 (2018).

[133] J. W. Roos, D. P. Hollrah, G. H. Guinther, and L. J. Cunningham, "A peer-reviewed critical analysis of SAE Paper 2002-01-2894 the Impact of MMT Gasoline Additive on Exhaust Emissions and Fuel Economy of Low Emission Vehicles (LEV)", SAE Technical Papers, DOI: 10.4271/2002-01-2903 (2002).